Neutron stars as fragmentary records of supernova explosions

Proefschrift

ter verkrijging van de graad van doctor
aan de Radboud Universiteit Nijmegen
op gezag van de rector magnificus prof. dr. J.H.J.M van Krieken,
volgens besluit van het college van decanen
in het openbaar te verdedigen op donderdag 21 december 2017
om 9:30 uur precies

door

Andrei Petrovich Igoshev

geboren op 28 maart 1990
te Zlatoust (Rusland)

Promotor:	Prof. dr. F.W.M. Verbunt	
Manuscriptcommissie:	Prof. dr. A.V. Kimel	
	Prof. dr. M. van der Klis	(UvA)
	Prof. dr. H.D.E. Falcke	
	Prof. dr. G.A. Nelemans	
	Dr. G.H. Janssen	(ASTRON, Dwingeloo)

Neutron stars as fragmentary records of supernova explosions
Thesis, Radboud University Nijmegen
Illustrated; with bibliographic information and Dutch summary

ISBN: 978-94-0280831-5

Contents

Introduction

> "Zwei Dinge erfüllen das Gemüt mit immer neuer und zunehmender Bewunderung und Ehrfurcht, je öfter und anhaltender sich das Nachdenken damit beschäftigt: Der bestirnte Himmel über mir, und das moralische Gesetz in mir."
>
> – Immanuel Kant, Kritik der praktischen Vernunft

The supernova explosion apart from being a very spectacular and energetic event, produces a significant amount of heavy elements [Burbidge et al., 1957] such as Cu, Zn[1] and Se which eventually constructs the biological molecules and proteins which serve as the base of our life. An understanding of the supernova can help us to better constrain distances in the Universe, trace heavy elements in the Galaxy and uncover the physical properties of the matter in extreme conditions.

The physics of the supernova explosion is far from completely understood. The implosion centre is deep in the star, so the extended envelope obscures the process. Only two witnesses survive the explosion and are ready to testify about the physics involved: neutrinos which leave the supernova without any interactions with outer layers and a compact remnant.

The neutrino flux is measured only from the supernova SN1987A [Arnett et al., 1989]. Moreover, the neutrino is weakly sensitive to some key components of the explosion such as the explosion asymmetry, fall back, turbulence scale and the magnetic field.

A neutron star, the compact remnant of the supernova keeps most of this information deeply encoded into its properties. The temperature, spin, strength and configuration of the magnetic field and velocity of the neutron star are only elusive evidence of the violent supernova explosion which survives Myrs and are ready to tell this story. E.g. if the fall-back is strong, the pulsar activation is postponed which results in the observational diversity of neutron stars.

During decades different scenarios of the supernova explosion were assumed (e.g. Janka 2012; Bethe & Wilson 1985). The scenarios which lead to the formation of the neutron stars are the basic core collapse supernova and potentially the electron capture supernova explosion [Podsiadlowski et al., 2004]. The latter scenario is often discussed in the context of low-velocity neutron stars. The neutron stars are found in close binaries (i.e., double pulsar) and in globular clusters where

[1] Zinc is the second most abundand trace metal in the human body [Coleman, 1992]

the weak gravitational potential is capable of retaining objects only if their natal kick velocity is less than ≈ 60 km/s.

If a significant amount of the envelope is removed prior to the explosion it should strongly decrease the ejecta mass. Smaller ejecta mass leads probably to smaller natal kick [Janka, 2017]. A mass removal occurs in close binaries. This alternative explosion channel should manifests itself in the observed population of the neutron stars.

Below I introduce all objects (neutron stars, radio pulsars, millisecond radio pulsars) which are involved in this thesis in some detail.

Neutron stars

Inside a massive star ($\approx 8 - 15\,M_\odot$) elements are fused from hydrogen till iron in a sequence of thermonuclear reactions. At earlier times a heat released in such reactions supports the gas pressure and the star stability. However, when a significant part of the massive star core has turned into iron, the following reactions cannot provide heat, so the gas pressure in the star core cannot overcome the gravity anymore. At this moment protons capture the electrons and form neutrons and neutrinos. The matter becomes neutron rich. The neutrons obey the Pauli exclusion principle. That is why the neutron gas become degenerate and provide the pressure which stops the collapse. A compact remnant with a radius around 10 km and mass in the range from 1.4 till $\approx 3M_\odot$ which keeps the equilibrium because of the neutron degeneracy is called a neutron star.

The protoneutron star is accelerated by hydrodynamical and gravitational forces in an interaction with slower and dense part of the inner ejecta [Scheck et al., 2008]. The inner ejecta are defined as a stellar matter which is between the shock wave and the surface of the protoneutron star. The acceleration can last up to a few seconds after the beginning of the explosion. The final acceleration depends strongly on asymmetries in the ejecta matter and its mass as well as the explosion energy [Janka, 2017]. A probe for neutron star velocity distribution gives a direct insight into these parameters.

The structure of the neutron star is shown in Figure 1. The outer layers (atmosphere and the crust) are understood quite well [Chamel & Haensel, 2008], while the inner core still requires careful investigation.

Neutron star crust

Due to the strong gravitational force, the dynamical equilibrium is reached on a relatively short timescale at the neutron star surface. The lightest available elements (hydrogen, carbon or iron) float to the surface, and all remaining heavy elements sink. The size of an atmosphere ranges from 0.1 till 10 cm [Zavlin & Pavlov, 2002].

The crust consists of the outer and the inner crust that in total extends to 1 km size. Its density ranges from $10^7\,\mathrm{g/cm^3}$ to $10^{14}\,\mathrm{g/cm^3}$. Nuclei with a large number of neutrons mostly compose the outer crust. Deeper to the NS centre these nuclei form a lattice allowing some space for the degenerate electron gas. The shape of the lattice is modified due to the local magnetic field and defects which can be parametrized by the impurity parameter Q. This parameter is one of the essential factors which determine the magnetic field decay timescale for neutron stars.

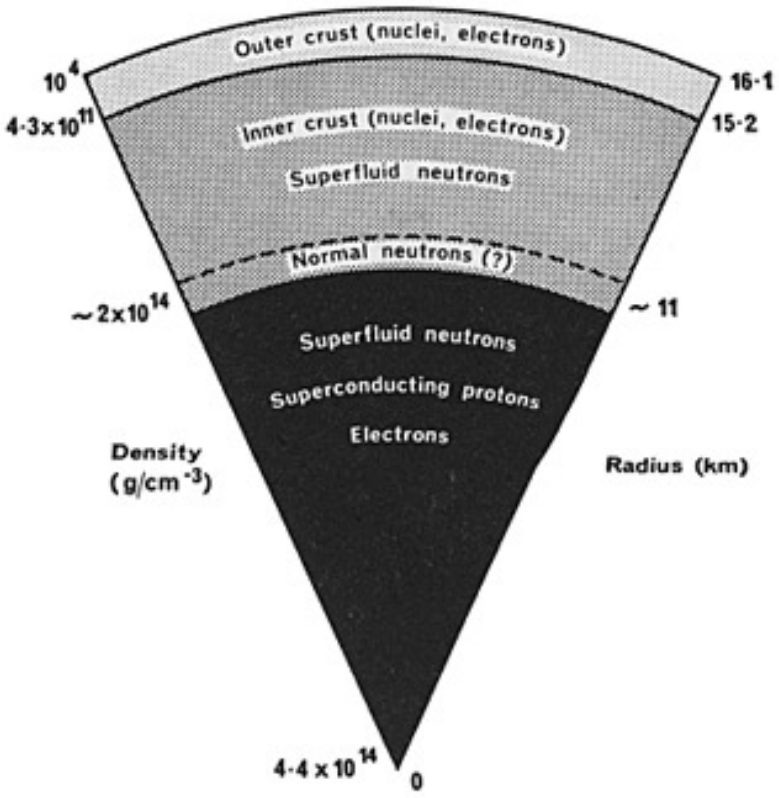

Figure 1: The structure of the neutron star. Courtesy of https://heasarc.gsfc.nasa.gov/docs/objects/binaries/neutron_star_structure.html

The electron flow is also strongly affected by a local magnetic field which might exceed 10^{14} G. The electron gas efficiently transports the heat outwards and the electric current in the crust except for the direction perpendicular to the magnetic field. It complicates the task to study the magnetic field evolution and makes magnetic field to be coupled to the heat transfer.

High conductivity occurs in the neutron star crust due to a large number of charge carriers available (number of electrons available is proportional to the matter density).

Radio pulsar mechanism

Due to the high conductivity of the neutron star crust, the electric current can survive Myrs without significant change. Therefore if the proto-neutron star is submerged into the fossil magnetic field or some magnetic field is generated on the place due to high convection through the dynamo mechanism, the neutron star keeps this magnetic field for Myrs after the crust is solidified. A fast rotation and presence of the magnetic field make a neutron star very suitable place for the operation of the pulsar mechanism.

Radio pulsars were first discovered by Hewish et al. [1968] as a sequence of bright radio impulses which are separated by a constant time interval. The emission process was described by Ruderman & Sutherland [1975]. The rotation of the magnetic field dipole in a vacuum creates a strong electric field with a strength proportional to the magnetic field and inversely proportional to period, see eq. (2) in Ruderman & Sutherland [1975]. Such an electric field efficiently accelerates charged particles dragged from the neutron star atmosphere up to highly relativistic speeds. Neutron stars with the shortest periods (young and millisecond radio pulsars) are the most efficient accelerators which is confirmed in γ-ray observations.

The radio emission originates at larger distances from the neutron star surface up to 10 neutron star radii. Its formation requires a sufficient supply of secondary plasma which is formed due to pair formation in the curved magnetic field. The exact plasma instability which is responsible for the coherent radio emission from pulsars is not yet identified.

The periodic pulses allow us to learn multiple properties of the neutron stars which operate in the radio pulsars mode such as rotational period, period derivative (a measure of the dipolar magnetic field). The VLBI measurements help to estimate the proper motion and distance.

More than 2600 radio pulsars are known by this moment (the ATNF catalogue v 1.56 Manchester et al. 2005)[2]. The period–period derivative for different types of neutron stars is shown in Figure 2.

Millisecond radio pulsars

Contrary to the young radio pulsars the recycled ones are necessarily formed in binaries or in the dense environment of globular clusters. The formation channel is shown in Figure 3. The more massive stars evolve first and form a neutron star after the supernova explosion. This neutron star is gravitationally bound with its companion and acts like a young radio pulsar for a period probably less than 10 Myr. After this time the neutron star crosses the death line at period–

[2]http://www.atnf.csiro.au/research/pulsar/psrcat

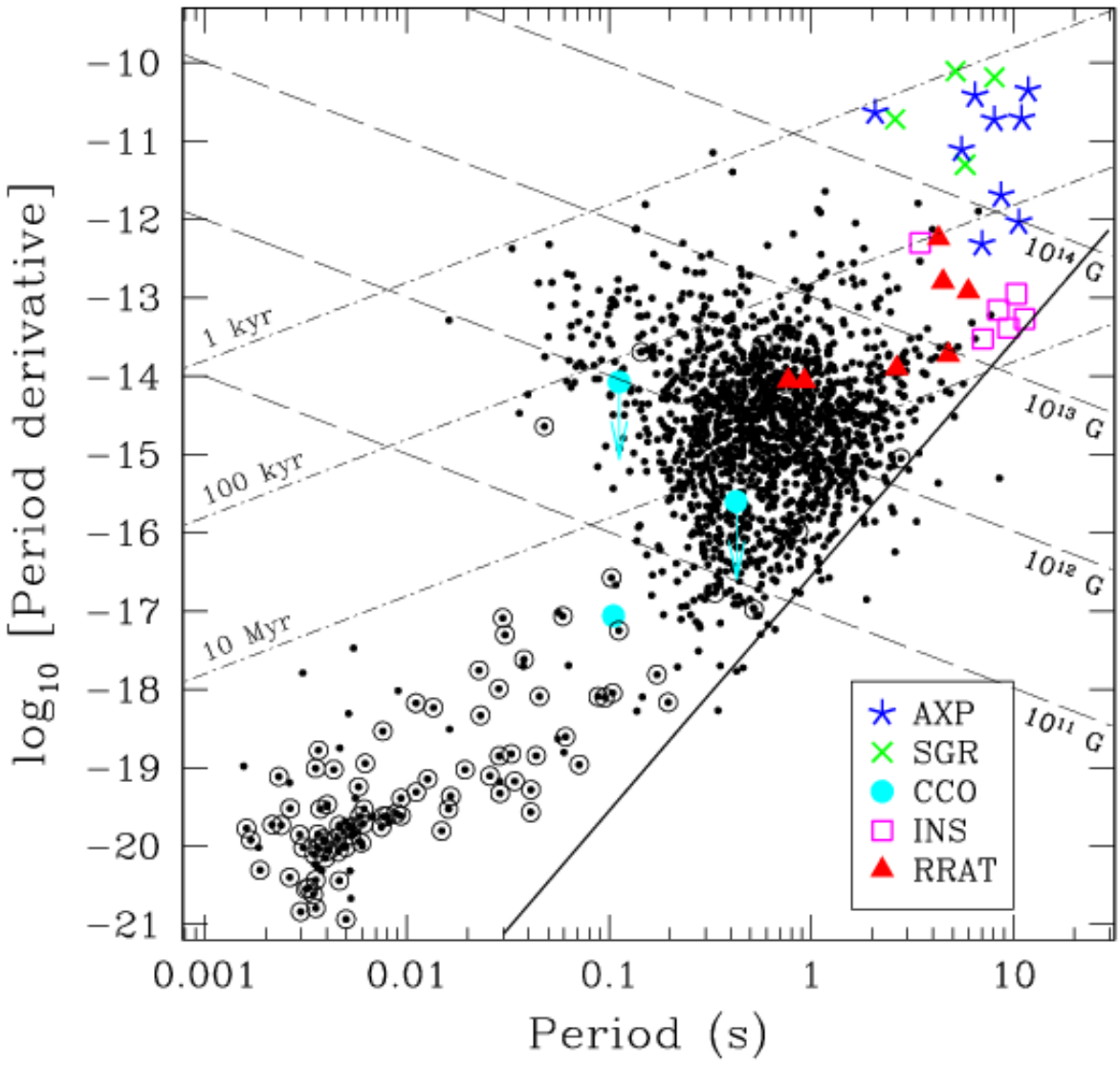

Figure 2: The distribution of period – period derivative for different types of neutron stars. Courtesy of http://inspirehep.net/record/854264/plots

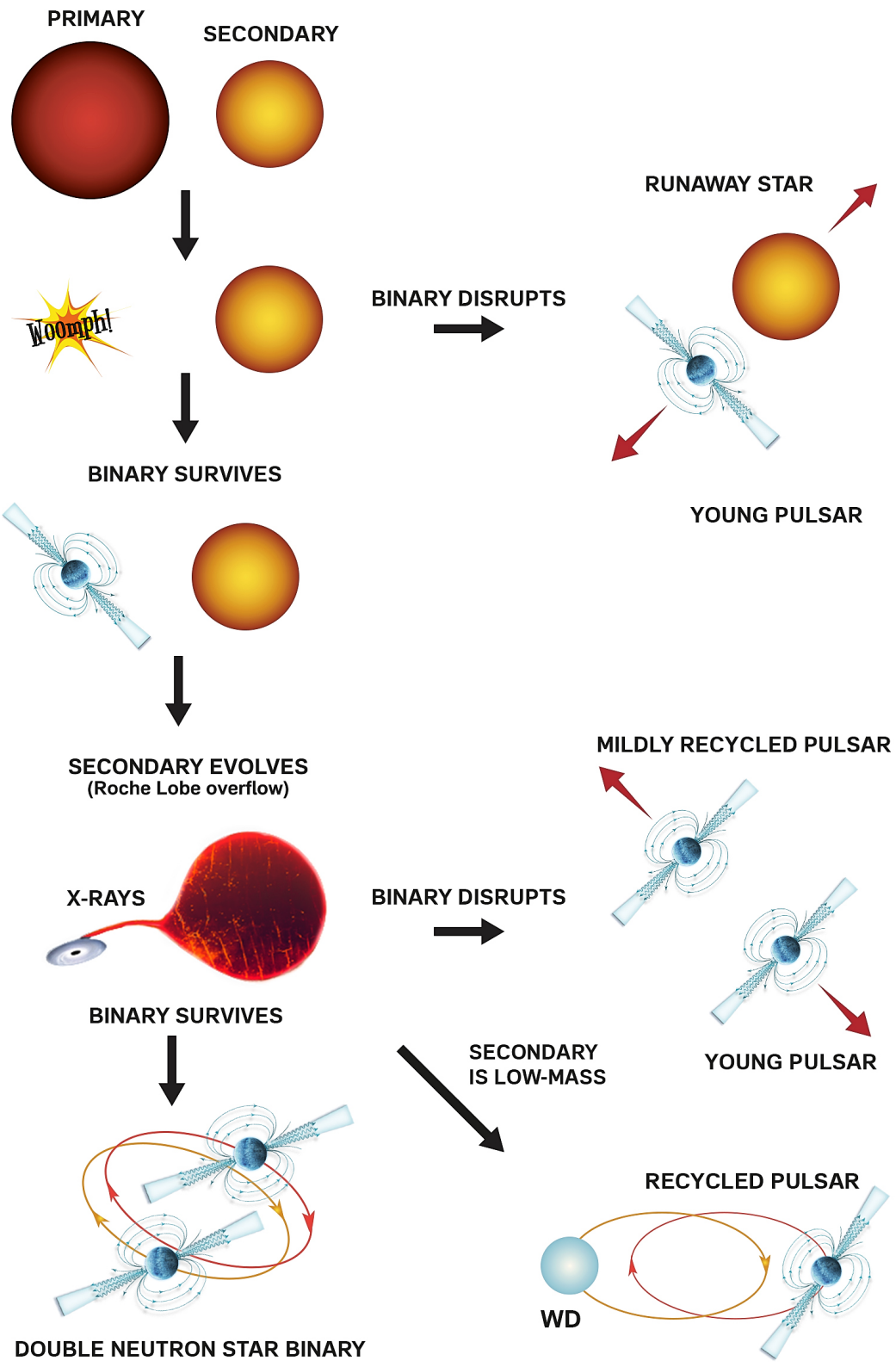

Figure 3: Formation of the millisecond radio pulsar. Courtesy of Alice Froll.

period derivative diagram and the pulsar mechanism stops operating, so no radio emission can be detected.

When the secondary star leaves the main sequence, it expands and fills its Roche lobe which leads to the mass transfer on the neutron star. Because of the orbital motion, the transferred matter has a significant angular moment which leads to the formation of the accretion disk around the neutron star. The system manifests itself as an X-ray binary. If the magnetic field has decayed sufficiently or the accretion rate is very large, the accretion onto neutron star surface becomes possible. Therefore the orbital angular momentum of the gas is transferred into the angular moment of the neutron star which leads to a spin up and further decay of magnetic field.

The accretion is usually stopped when the neutron star has been spun up to a spin period of a few milliseconds. A neutron star with this small period is again above the death line and can operate as the radio pulsar. The mass transfer stops when the secondary turns into a white dwarf which leads to a formation of a millisecond radio pulsars with a white dwarf companion. Sometimes no companion for millisecond radio pulsar is found which might indicate an evaporation of the companion by strong radiation from the pulsar. A more rare evolution path leads to the formation of double neutron stars, in particular, the double pulsar PSR J0737-3039, see Figure 3

The millisecond radio pulsars are ideal test particles for the low-velocity kicks. The high-velocity natal kick leads either to a disruption of the binary or the binary leaves the Galaxy. If the low-velocity neutron stars are formed more often in binaries such objects should be strongly overrepresented in the sample of the recycled radio pulsars.

Natal kick formation

The nascent neutron star receives a significant kick of velocity sometimes as large as 1000 km/s, e.g. the pulsar in the Guitar Nebula PSR B2224+65. Such a large velocities cannot possibly occur from a binary disruption. The typical orbital velocities in binaries ranges from 10 to 100 km/s. Many alternative scenarios were suggested for an exact mechanism which leads to the formation of the natal kick, see review by Lai [2001]. One of them is the hydrodynamically driven kicks described in previous section.

A few alternative mechanisms of the neutron star acceleration are related to neutrino transport in the magnetic field. The strong local magnetic field can change the matter opacity for the neutrino. This mechanism requires in general magnetic fields of order $10^{15} - 10^{16}$ G. The magnetic field can also locally suppress the convection driven by the neutrinos.

An electromagnetic acceleration of the neutron star because of the off-center dipole is also considered as one of the sources for the natal kick. Such a mechanism leads necessarily to a conclusion that older pulsars should be in general faster than the young ones.

Usually in the discussion of the neutron star kicks researchers distinguish the core collapse supernova and the electron capture supernova explosion. The essential difference is the neon ignition [Nomoto, 1984]. The ignition of neon in the core of the massive star happens if the core mass exceeds $1.37 M_{\odot}$. It necessarily leads to neon burning and ignition of heavier elements. This path results in a classical core collapse supernova explosion.

If the core mass is not enough to ignite neon a neutron star can still be formed. The core

loses stability and collapses because magnesium and neon capture the electrons. In particular, the accretion-induced white dwarf collapse can occur through this channel. This scenario can happen more often in binaries compared to isolated massive stars [Podsiadlowski et al., 2004]. The mass transfer from a primary removes a significant amount of envelope and does not allow the carbon core to overgrow the limit. If the natal kick formed through hydrodynamic instabilities, the electron capture supernova is a natural source of the low natal kicks because of the explosion symmetry.

Diversity of neutron stars and fall-back

Neutron stars show an unprecedented variety of behaviour ranging from isolated neutron stars to magnetars and accreting objects. Among other, the central compact objects – isolated neutron stars found exclusively in supernova remnants – deserve special consideration. This type of neutron stars emits only soft thermal X-ray radiation and show no signs of radio emission.

Even though these sources are in a region of period-period derivate diagram which is occupied by very old radio pulsars with a weak magnetic field $10^{10} - 10^{11}$ G, see Figure 2, their association with supernova and thermal emission indicate extremely young age $10^3 - 10^4$ years. The absorption feature in an X-ray spectrum, if it is interpreted as the electron cyclotron line, corresponds to the magnetic fields around 10^{11} G [Gotthelf & Halpern, 2009]. On the other hand, the pulse fraction which found in some of these objects might be only explained by a very strong crustal toroidal magnetic field $\propto 10^{14}$ G [Shabaltas & Lai, 2012]. Such magnetic fields block the heat transfer across but favour it along the field. No objects with similar properties are found so far among high mass X-ray binaries with neutron stars [Chashkina & Popov, 2012] which indicates that central compact objects evolve on timescale $10^4 - 10^5$ years.

One of the explanations for such contradictory properties can be found in a model of fall-back by Bernal et al. [2013]. An episode of a fall-back occurs soon after the supernova explosion when a part of supernova ejecta receives insufficient velocity to leave the compact remnant. The material falls back with an instantaneous accretion rate up to 100 $M_\odot$/yr. Such a strong accretion rate makes it possible to bury a part of the magnetic field in the crust at a first few moments after the neutron star crust solidified. The fall-back continues up to an year with accretion rate which drops dramatically. The total mass added to neutron star does not exceed $10^{-3} - 10^{-4} M_\odot$.

The magnetic field hidden under new layers of crust can still control the heat transfer which could explain the unprecedented large pulse fraction of Kes 79. However, such magnetic field does not manifest itself through the pulsar braking. A short lifetime of the central compact objects is explained in this scenario with the natural magnetic field re-emergence episode which occurs at $10^4 - 10^5$ years. The re-emerged magnetic field make it possible to start the radio pulsar mechanism. So, such object will be hardly distinguished from an ordinary old radio pulsar.

This Thesis

In this thesis, I study the velocity distribution of young and millisecond radio pulsars with an ultimate goal to find evidence in favour of the separate channel of the supernova explosion which

leads to the formation of low-velocity neutron stars.

In this thesis, I put new constraints on the velocity distribution of young and old neutron stars as well as analyse the observational appearance of hidden but potentially numerous group of neutron stars which experiences significant fall-back of a matter. Both these evidence allows us in the future to calibrate a relation between the ejecta mass (or neutron star mass or fall back) and the neutron star velocity i.e. to establish a relation between a turbulence scale in the supernova and its mass at the explosion. My study also shed light on a variety of the supernova explosion mechanisms.

In Chapter 1 a Bayesian approach for distances is developed and verified in a series of Monte Carlo simulations. The distances are crucial for the study of velocities because they are estimated using parallax and proper motion measurements.

In Chapter 2 the velocity distribution of isolated radio pulsars is studied. These objects show the velocity distribution at the moment of their formation.

In Chapter 3 the observed velocity distribution of millisecond radio pulsars is studied with the parametric maximum likelihood technique. A few isotropic and anisotropic velocity distributions are analysed.

In Chapter 4 the evolutionary path of central compact objects is studied. The high order multipoles are responsible for the pulsar mechanism operation. Their evolution under fall-back is essential for better understanding of the central compact objects.

In Chapter 5 the impurity parameter for the neutron star crust is studied based on the high mass X-ray binaries with extreme magnetic fields. The Bayesian techniques is developed to estimate the kinematic age of the magnetar 4U0114+65.

Chapter 1

The distance and luminosity probability distributions derived from parallax and flux with their measurement error

Andrei Igoshev, Frank Verbunt, Eric Cator

A&A, 2016, 591, 10

Abstract

We use a Bayesian approach to derive the distance probability distribution for one object from its parallax with measurement uncertainty for two spatial distribution priors, viz. a homogeneous spherical distribution and a galactocentric distribution – applicable for radio pulsars – observed from Earth. We investigate the dependence on measurement uncertainty, and show that a parallax measurement can underestimate or overestimate the actual distance, depending on the spatial distribution prior. We derive the probability distributions for distance and luminosity combined, and for each separately, when a flux with measurement error for the object is also available, and demonstrate the necessity of and dependence on the luminosity function prior. We apply this to estimate the distance and the radio and gamma-ray luminosities of PSR J0218+4232. The use of realistic priors improves the quality of the estimates for distance and luminosity, compared to those based on measurement only. Use of a wrong prior, for example a homogeneous spatial distribution without upper bound, may lead to very wrong results.

1.1 Introduction

Distance determinations are fundamental in astronomy. The study of spatial distributions and source number densities is the most direct application. Together with proper motion measurements, distances form the basis of velocity measurements and kinematic studies. Combined with flux measurements they provide luminosities.

A standard method of distance determination is the measurement of the trigonometric parallax. The conversion of the measured parallax into the most probable actual parallax is not straightforward, as is evident from the excellent historical survey given by Sandage & Saha (2002). Most of the papers discussed in that survey use parallax and apparent magnitude measurements to derive absolute magnitude distributions, or statistical corrections between apparent and absolute magnitudes. In a much cited paper, Lutz & Kelker (1973) derive the probability distribution of the real parallax as a function of the measured parallax and its measurement error. Since that paper, there has been some debate as to whether or not their equation is applicable when only one object is observed (as reviewed by Sandage & Saha 2002).

In a study of radio pulsars, Faucher-Giguère & Kaspi (2006) give a probability distribution of actual distances as a function of the measured parallax, reproduced as Eq.1.21 below. In an important paper Verbiest et al. (2012) develop a Bayesian method to combine various distance-related measurements and their uncertainties to find the probability distribution of distances, and show the importance of the choice of priors. Verbiest & Lorimer (2014) apply this method in a study of the gamma-ray luminosity of the millisecond pulsar PSR J0218+4232. Alas, they make the same error as Faucher-Giguère & Kaspi (2006) in deriving the probability distribution of actual distances as a function of the measured parallax, and make a similar error in the equation for the probability distribution of luminosity as a function of measured flux and parallax.

Much of the confusion in the existing literature arises because of the failure to dicriminate between what technically are called the frequentist approach and the Bayesian approach, leading to the incorrect conclusion that a measurement by itself provides a probability density distribution centered on the measured value. We briefly explain this error in Sect.1.1.1, where we also discuss the related confusion on whether population priors must be taken into account in the study of single objects. In contrast to statements in several previous papers (e.g. Feast 2002, Francis 2012, and references therein), the answer is yes if a probability density is required. A more detailed explanation is given in Sect.1.3. In that Section we repeat some results by Bailer-Jones (2015) that appeared as we were finalizing our paper, but we differ in that we use a spatial distribution appropriate for pulsars.

The structure of our paper is as follows. In Sect.1.2 we describe the spatial distributions and the luminosity distributions that we use, and explain our notation. In Section 1.3 we describe in some detail the derivation of the correct conversion of measured parallax to probability distribution of actual distances, for the case of a known (or assumed) distribution in space. We consider a homogeneous distribution, and a galactocentric distribution observed from Earth. The latter is applied to the case of PSR J0218+4232. In Sect.1.4, we consider objects for which both parallax and flux are measured to determine the probability distributions for distance and luminosity, and illustrate our results for PSR J0218+4232. The gamma-ray luminosity of PSR J0218+4232 is discussed in Sect.1.5. Finally, in Section 1.6 we briefly discuss the assumptions that we have made,

and the expected consequences of relaxing these.

1.1.1 Confidence intervals and probability densities

Consider an object whose parallax is measured with accuracy σ, i.e. the measured value ϖ' is a draw from a gaussian centered on its real parallax ϖ_1 with standard deviation σ. The probability that a draw leads to a measured value ϖ' such that $|\varpi' - \varpi_1| < \sigma$ is then (roughly) 68%, which corresponds to a 68% probability that the real value ϖ_1 is in the range given by $\varpi' - \sigma < \varpi_1 < \varpi' + \sigma$. Similarly, if the real parallax is ϖ_2 there is a 68% probability that the real value ϖ_2 is in the range given by $\varpi' - \sigma < \varpi_2 < \varpi' + \sigma$, and so for every real distance ϖ_i. Thus, no matter what the real distance is, we can state that there is a 68% probability that it is in the range bounded by $\varpi' - \sigma$ and $\varpi' + \sigma$. Analogously, for each frequency of occurrence, e.g. expressed in percentage x%, on may derive the corresponding range: between $\varpi' - n_x\sigma$ and $\varpi' + n_x\sigma$, where $n_x = 1.645$ for 90%, $n_x = 2$ for 95.5%, etc. Hence the name frequentist approach. The measured value ϖ' does *not*, however, provide the probability distribution within these ranges.

To obtain such a probability distribution one must compute the relative contribution that each possible real parallax ϖ_i makes to the probability of measuring ϖ', i.e. follow the Bayesian approach. As an illustration, consider a population of 10 sources, 9 of which have $\varpi = 5$ mas, and 1 has $\varpi = 3$ mas. We select one source from this population for a parallax measurement with accuracy 1 mas, and measure $\varpi' = 4$ mas. The real parallax answers to the 68% probability of lying within 1 mas of the measured value. A real parallax of 5 mas has a probability of 90%, a real parallax of 3 mas of 10%, and other parallaxes have probability zero. The probability distribution of the real distance ϖ is *not* given by a gaussian centered on the measured value ϖ'. Also for the case of a more realistic, continuous intrinsic distribution, the probability distribution of ϖ in general can *not* be stated to be given by a gaussian centered on the measured value ϖ'. Therefore, the use of realistic priors improves the quality of the estimate for the distance, compared to that based on one measurement only. The same is true for the estimate of the luminosity.

Finally, consider a series of measurements ϖ'_i made from a single object, each with its own accuracy σ_i. Each measurement is a draw from a distribution centered on the actual distance of the object. The best estimate of ϖ', and its accuracy σ can be determined by averaging these measurements with appropriate weighting of the individual measurements, without reference to the population priors. The resulting values ϖ' and σ are the best estimate of the parallax *measurement* and its error. They may be used in a frequentist approach to determine a confidence interval. To determine a probability density, they must be combined with a population prior.

1.2 Ingredients and notation

The analysis in this paper is based on measurements of parallax and flux, combined with an intrinsic spatial distribution, which is assumed to be known, and an intrinsic luminosity distribution, also assumed known. The measurement errors lead to probability distributions for measured values that we denote with g_D and g_S for parallax and flux, respectively. The intrinsic spatial and luminosity distributions are denoted with f_D and f_L, respectively. To illustrate the general methods, we discuss two spatial distributions and two luminosity distributions.

1.2.1 Measurements

A parallax measurement is subject to measurement error σ. The measurement error distribution $g_D(\varpi'|D)$ gives the probability of measuring a parallax ϖ' when the actual distance is D. $g_D(\varpi'|D)$ may follow a gaussian distribution (Eq.1.2), but in general, it may also have a different, non-gaussian form.

We will assume that the distance D is given in kiloparsecs, and the parallax ϖ and measurement error σ in milliarcsec, hence $\varpi = 1/D$, and we will assume that the parallax measurement errors follow a gaussian distribution, centered on zero and with width σ, i.e. that the probability of measuring a parallax ϖ' for an actual parallax ϖ is given by a gaussian:

$$g_D(\varpi'|\varpi)\Delta\varpi' = \frac{1}{\sqrt{2\pi}\sigma}\exp\left[-\frac{(\varpi-\varpi')^2}{2\sigma^2}\right]\Delta\varpi' \tag{1.1}$$

In this equation ϖ is fixed, so with $\varpi = 1/D$ we rewrite it as

$$g_D(\varpi'|D)\Delta\varpi' = \frac{1}{\sqrt{2\pi}\sigma}\exp\left[-\frac{(1/D-\varpi')^2}{2\sigma^2}\right]\Delta\varpi' \tag{1.2}$$

where $g_D(\varpi'|D)$ is normalized over the range $-\infty < \varpi' < \infty$. (Note that, whereas the real parallax is by definition positive, the measured value may be negative.) Our results for spatially homogeneous distributions will be identical for D in parsecs with ϖ and σ in arcsecs.

We furthermore assume that the probability of a measured flux S' for an actual flux S is given by

$$g_S(S'|S)\Delta S' = \frac{1}{\sqrt{2\pi}\sigma_S}\exp\left[-\frac{(S-S')^2}{2{\sigma_S}^2}\right]\Delta S' \tag{1.3}$$

A flux S for a source at distance D corresponds to a luminosity $L = L_o D^2 S$. We introduce the factor L_o to discriminate isotropically emitting sources, for which $L_o = 4\pi$, and pulsars, for which traditionally the luminosity is defined with $L_o = 1$. It may also be used to indicate the effect of interstellar absorption, in which case L_o itself depends on D.

1.2.2 Spatial distribution

To avoid unnecessary duplication, we subsume the two spatial distributions that we discuss in one equation:

$$f_D(D)\Delta D \propto D^2\mathcal{F}(D)\Delta D \tag{1.4}$$

For a homogeneous distribution in space, $f_D(D) \propto D^2$, and $f_D(D)$ cannot be normalized. In realistic applications, however, the spatial distribution is always bounded: for stars by the finite extent of the galaxy. For illustrative purpose, we consider the (in general non-realistic) case where the distribution is homogeneous up to a maximum distance $D_{\max}$, and zero beyond it; and write

$$\mathcal{F}(D) = \begin{cases} 1 & \text{for } D < D_{\max} \\ \\ 0 & \text{for } D > D_{\max} \end{cases} \tag{1.5}$$

Verbiest et al. (2012) consider the observations made from Earth on a galactocentric distribution, which results in a heliocentric distribution given in our notation by (cf. Eq. 21 of Verbiest et al. 2012):

$$\mathcal{F}(D) = R^{1.9} \exp\left[-\frac{|z(D,b)|}{h} - \frac{R(D,l,b)}{H}\right] \tag{1.6}$$

Here a cylindrical galactocentric coordinate system is adopted with R and R_o the distance of the pulsar and of Earth to the galactic center, projected onto the galactic plane, and z the distance of the pulsar to that plane. h and H are the vertical and radial scaling parameters. With D the distance of the object to Earth, and l, b its galactic coordinates, we have

$$z = D \sin b; \text{ and } R = \sqrt{{R_o}^2 + (D\cos b)^2 - 2D\cos b\, R_o \cos l} \tag{1.7}$$

The last equation shows that z and R are functions of D, l and b. and thus $\mathcal{F}(D)$ and through it $f_D(D)$ are functions of l and b.

1.2.3 Luminosity functions

The luminosity function $f_L(L)$ gives the relative numbers of sources as a function of luminosity L, in the range between minimum luminosity $L_{\min}$ and maximum luminosity $L_{\max}$. The luminosity function $f_L(L)$, and also $L_{\max}$ and $L_{\min}$, may depend on D. For example, pulsars at large distance from the galactic plane tend to be older, and probably have a luminosity function different from that of young pulsars near the galactic plane. However, for the purpose of this paper, we assume a universal luminosity function, i.e. $f_L(L)$, $L_{\min}$ and $L_{\max}$ do not depend on D.

As a first example we discuss a power-law distribution for the luminosity function:

$$f_L(L)\Delta L \propto \begin{cases} L^\alpha \Delta L & \text{for } L_{\min} < L < L_{\max} \\ \\ 0 & \text{for } L > L_{\max} \text{ or } L < L_{\min}. \end{cases} \tag{1.8}$$

We will consider three values for α, viz. $\alpha = (0, -1, -2)$.

We also consider a luminosity function in the form derived for normal pulsars by Faucher-Giguère & Kaspi (2006):

$$f(x)\Delta x \propto \exp\left[-\frac{(x-\mu_x)^2}{2{\sigma_x}^2}\right]\Delta x \quad \text{where} \quad x \equiv \log L \tag{1.9}$$

which we rewrite as

$$f_L(L)\Delta L = f(x)\frac{dx}{dL}dL \propto \exp\left[-\frac{(\log L - \mu_x)^2}{2{\sigma_x}^2}\right]\frac{1}{L}dL \tag{1.10}$$

where $\mu_x = -1.1$ and $\sigma_L = 0.9$ (both numbers referring to the log of the luminosity in $\mathrm{mJy\,kpc^2}$). We follow Verbiest et al. (2014) in applying this same distribution to millisecond pulsars.

1.2.4 Notation for probabilities

We denote joint probabilites with capital P, in particular the joint probability of measured parallax ϖ' and actual distance D is written $P(\varpi', D)$, and the joint probability for these quantities plus

Table 1.1: Parameters of PSR J0218+4232 used in this paper

specific for PSR J0218+4232			reference
coordinates	l, b	$139°51, -17°53$	
period, -derivative	P,$\dot{P}$	$2.323\,\mathrm{ms},\ 7.739 \times 10^{-20}$	(1)
parallax	ϖ', σ	$0.16 \pm 0.09\,\mathrm{mas}$	(2)
flux 1400 Mhz	S', σ_S	$0.9 \pm 0.2\,\mathrm{mJy}$	(3)
flux 0.1-100 GeV	S_γ	$4.56 \times 10^{-11}\mathrm{erg\,s^{-1}cm^{-2}}$	(4)
generic for millisecond pulsars			reference
in Eq.1.6	R_o, H, h	$8.5\,\mathrm{kpc}$,$0.2R_o$,$500\,\mathrm{pc}$	(5)
Eq.1.10 L_{1400}	μ_x, σ_x	$-1.1, 0.9^a$	(6)
Eq.1.10 L_γ	μ_x, σ_x	$32.7, 1.4^b$	(7)

Notes: [a] actually derived for normal pulsars; both numbers refer to the log of the luminosity in $\mathrm{mJy\,kpc^2}$; [b] both numbers refer to the log of the gamma-ray luminosity in erg/s.
References are: (1) – Hobbs et al. [2004], (2) – Du et al. [2014], (3) – Kramer et al. [1998] (4) – Abdo et al. [2013], (5) – Lorimer et al. [2006], (6) – Faucher-Giguère & Kaspi [2006] and Hooper & Mohlabeng [2016].

measured flux S' and luminosity L as $P(\varpi', D, S', L)$. These joint probabilities may be turned into conditional probabilities with Bayes' theorem. This leads to normalization constants which we denote as follows. If the joint probability is

$$P \propto F(\varpi', D, S', L) \tag{1.11}$$

with F a function of the variables indicated, then the conditional probability

$$\begin{aligned} p &= C_x(a,b)F(\varpi', D, S', L); \quad x \in \{\varpi', D, S', L\} \\ &\text{with} \quad C_x(a,b)^{-1} \equiv \int_a^b F(\varpi', D, S', L)dx \end{aligned} \tag{1.12}$$

Our notation for conditional probabilities is such that

$$p_x(x|a, b\ldots) \tag{1.13}$$

gives the (normalized) probability of x for given (e.g. measured) values for $a, b, \ldots$.

We will use 95% credibility intervals on the posterior probability density. This credibility interval is computed from the one-dimensional posterior probability density $p_x(x)$, where x is the distance or the luminosity, as the shortest interval containing 95% of the total probability:

$$\int_{x_l}^{x_u} p_x(x)dx = 0.95 \int_0^\infty p_x(x)dx \qquad \text{with} \ \ p_x(x_l) = p_x(x_u) \tag{1.14}$$

This equation holds when $x_u < x_{\max}$; when $x_u = x_{\max}$, the condition $p_x(x_l) = p_x(x_u)$ is dropped.

1.2.5 Sample millisecond pulsar

In the Figures which illustrate probabilties involving the galactocentric distribution Eq.1.6 we will use the parameters for PSR J0218+4232, as listed in Table 1.1.

1.3 Distance derived from measured parallax and assumed distance distribution

Due to the measurement error, different distances D may lead to the same measured parallax ϖ'. With the number of objects at distance D given by $f_D(D)$, and the probability of measuring parallax ϖ' at actual distance D by $g_D(\varpi'|D)$, the joint probability of a object to have a distance D and a measured parallax ϖ' is distributed according to

$$P_D(\varpi', D)\Delta\varpi'\,\Delta D = g_D(\varpi'|D)\, f_D(D)\Delta\varpi'\,\Delta D \tag{1.15}$$

and the conditional probability that the actual distance is in a range ΔD around D when the measured parallax is ϖ' follows with Eq.1.12:

$$p_D(D|\varpi')\Delta D = C_D(0,\infty)P_D(\varpi', D)\Delta D \tag{1.16}$$

In principle, only the product $P_D = g_D f_D$ must be normalizable with respect to D; in practice it is often useful to normalize the functions g_D and f_D separately as well, with respect to D and ϖ', respectively. Eqs.1.15 and 1.16 show that a probability distribution for the distance can be derived for a measured parallax of a single object only if a spatial distribution $f_D(D)$ of the class of objects is known or assumed.

For a uniform prior, i.e. $f_D(D) =$ constant in the range $D_{\min} < D < D_{\max}$, Eqs.1.14-1.15 lead to the result

$$p_D(D|\varpi') = C_D(D_{\min}, D_{\max})g_D(\varpi'|D) \tag{1.17}$$

Thus, for a uniform prior, the probability of measuring ϖ' when the real distance is D is the same as the probability that the real distance is D when the measured parallax is ϖ', apart from a normalization constant. To prevent the normalization constant from going to infinity, the prior may have to be limited to a maximum distance.

1.3.1 Finite homogeneous distribution in space

Entering Eqs.1.2, 1.4, 1.5 into Eq.1.16, we obtain with Eq.1.12:

$$p_D(D|\varpi') = \begin{cases} C_D(0, D_{\max})D^2 \exp\left[-\frac{(1/D-\varpi')^2}{2\sigma^2}\right]; & D < D_{\max} \\ \\ 0; \quad D > D_{\max} \end{cases} \tag{1.18}$$

In Fig.1.1 we plot $p_D(D|\varpi')$ according to Eq.1.18, computing $C_D(0, D_{\max})$ numerically, for a measured parallax $\varpi' = 0.2\,\mathrm{mas}$, maximum distance $D_{\max} = 10\,\mathrm{kpc}$ and $\sigma = 0.03\,\mathrm{mas}$. Fig.1.2 illustrates the effect of varying measurement accuracies. As the error decreases, the most probable distance closes in to the nominal measured value $1/\varpi'$, but the probability distribution of the actual distances remains asymmetric, i.e. non-gaussian, even for small measurement errors.

To show that our approach is in agreement with that of Lutz & Kelker (1973), we note that for a homogeneous distribution in space $f_\varpi(\varpi)\Delta\varpi = f_D(D)\Delta D \propto D^2\Delta D$, hence $f_\varpi(\varpi) \propto \varpi^{-2}d(1/\varpi)/d\varpi \propto \varpi^{-4}$. This allows us to write the joint probability of a pulsar to have measured

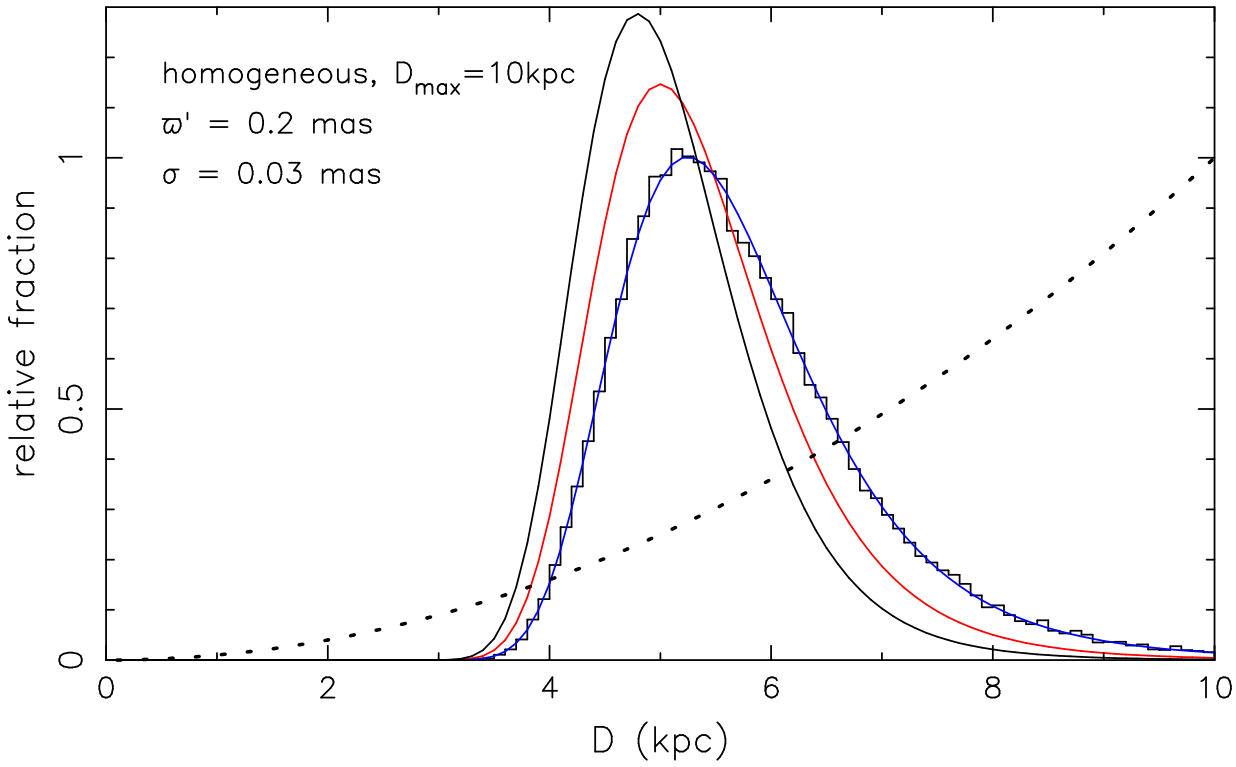

Figure 1.1: The probability distribution of actual distances for a measured parallax for objects distributed homogeneously in a finite sphere; for values of ϖ', σ and $D_{\max}$ as indicated. The blue line represents Eq.1.18. The histogram gives the results of a Monte Carlo simulation which retains objects with $0.198 < \varpi' < 0.202$. The black and red line represent modified versions of Eq.1.18 according to Faucher-Giguère & Kaspi (2006) and Verbiest et al. (2012), respectively. The intrinsic distribution given by Eqs.1.4,1.5 is shown as a dashed line. All curves are normalized to the same area under the curve

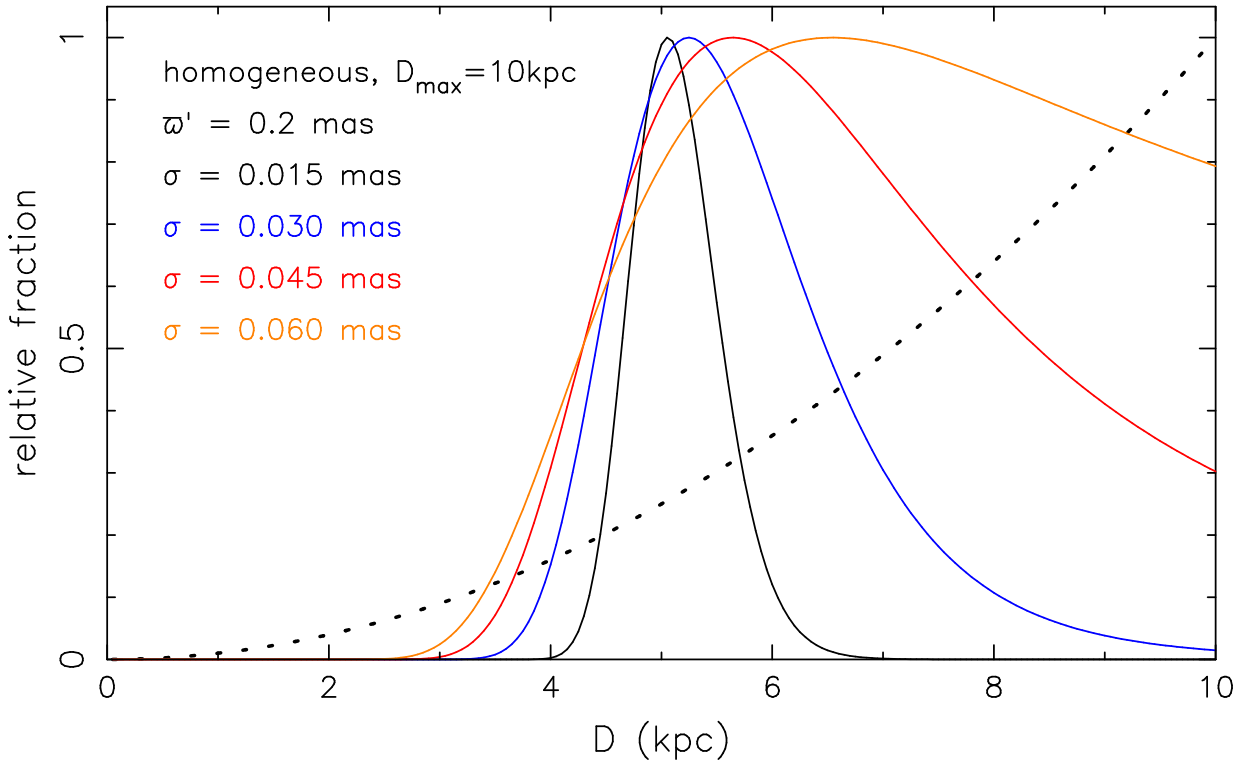

Figure 1.2: The probability distribution of actual distances for a measured parallax $\varpi' = 0.2\,\mathrm{mas}$ for various measurement errors σ, for objects distributed homogeneously in a sphere with radius $D_{\mathrm{max}} = 10\,\mathrm{kpc}$. The intrinsic distribution given by Eqs.1.4,1.5 is shown as a dashed line. The curves are normalized to the same maximum value

parallax ϖ' and actual parallax ϖ analogous to Eq.1.15 as

$$\begin{aligned} P_\varpi(\varpi', \varpi)\Delta\varpi'\Delta\varpi &= g_\varpi(\varpi'|\varpi)\Delta\varpi'\, f_\varpi(\varpi)\Delta\varpi \\ &\propto \frac{\Delta\varpi}{\varpi^4} g(\varpi'|\varpi)\,\Delta\varpi' \end{aligned} \tag{1.19}$$

thus confirming the ϖ^{-4} dependence found by Lutz & Kelker.

1.3.2 Galactocentric distribution

Entering Eqs.1.2, 1.4, 1.6 into Eq.1.16, we obtain with Eq.1.12:

$$\begin{aligned} p_D(D|\varpi') &= C_D(0,\infty) D^2\, R^{1.9} \exp\left[-\frac{|z(D,b)|}{h} - \frac{R(D,l,b)}{H}\right] \\ &\quad \times \exp\left[-\frac{(1/D - \varpi')^2}{2\sigma^2}\right] \end{aligned} \tag{1.20}$$

Fig.1.3 illustrates this distribution for the parameters of PSR J0218+4232.

1.3.3 Earlier studies

Previous authors have given different expressions for $p_D(D|\varpi')$. To understand the difference between our Eqs.1.18,1.20 and these expressions, we consider the measurement process expressed in Eq.1.15. Consider a class of objects distributed in space according to $f_D(D)$ (Eq.1.4). The measurement process starts with the selection of one object whose parallax we wish to measure. This corresponds to taking a draw from the $f_D(D)$ distribution. Then the parallax is measured. The measurement refers to the unique distance D of the selected object, i.e. the selection from $g_D(\varpi'|D)$ is taken for a unique and fixed value of D.

We illustrate this separation between object selection and parallax measurement with a Monte Carlo experiment, as follows. We choose a distance D randomly from a D^2 distribution (corresponding to a homogeneous distribution in a sphere) with maximum distance 10 kpc; for the distance D a measured parallax ϖ' is drawn randomly from a Gaussian distribution according to Eq.1.2 with $\sigma = 0.03$ mas. We retain the distance if $0.198 < \varpi'(\mathrm{mas}) < 0.202$, and repeat the procedure until 50 000 distances are retained. The binned distribution of the distances D of the retained objects is normalized and also plotted in Fig.1.1. It agrees with Eq.1.18. In analogous fashion we perform a Monte-Carlo experiment for the galactocentric distribution, for parameters of the millisecond pulsar PSR J0218+4232, and show in Fig.1.3 that the result agrees with the analytic solution given by Eq.1.20.

Faucher-Giguère & Kaspi (2006) write the probability of distance D for a measured parallax ϖ' as (see their Eq. 2):

$$p(D|\varpi') = \frac{C}{D^2}\,\frac{1}{\sqrt{2\pi}\sigma}\exp\left[-\frac{(1/D - \varpi')^2}{2\sigma^2}\right] \tag{1.21}$$

where C (in our notation) is the normalization constant. In doing so they make two, related, errors. First, they interpret the right hand side of Eq.1.1 as giving the probability that the real parallax is ϖ when the measured value is ϖ', when in fact it gives the probability of measuring

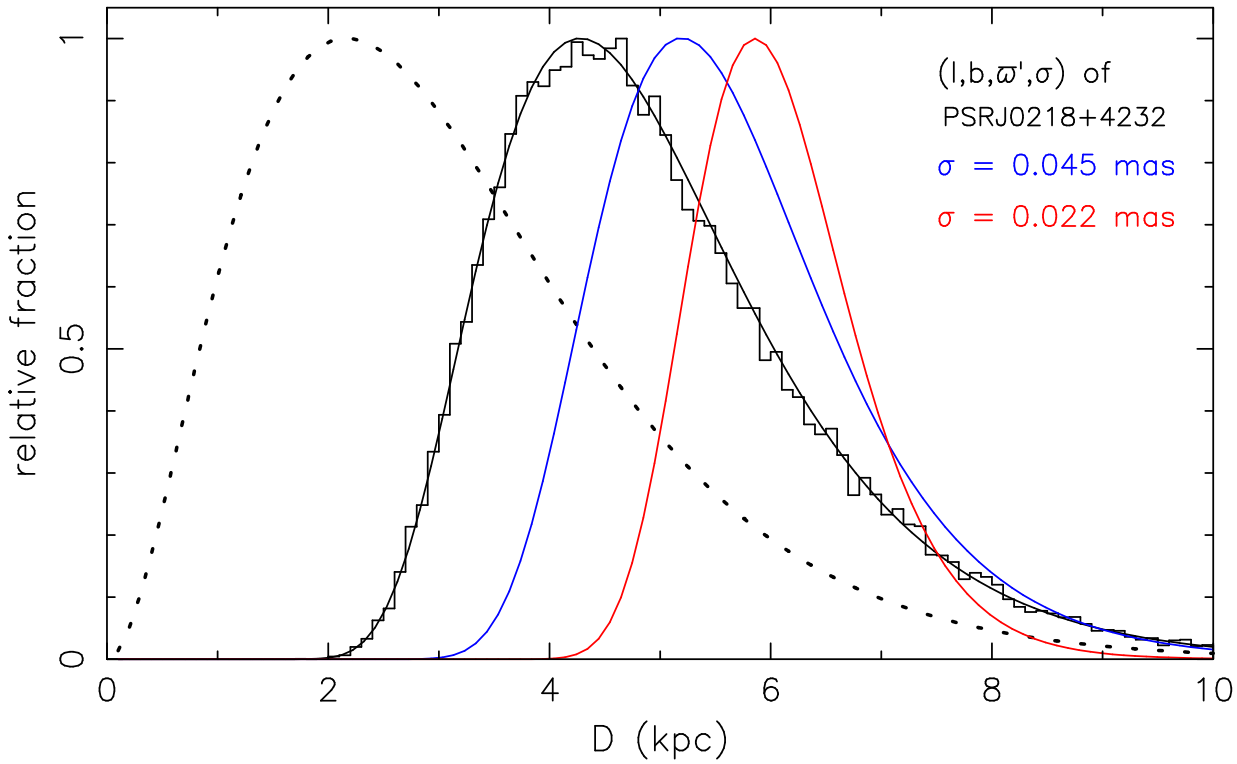

Figure 1.3: For an assumed galactocentric distribution of objects, the distribution as a function of distance to Earth is given by Eqs.1.4,1.6, illustrated for the direction towards PSR J0218+4232 with the dotted line. The black smooth line gives the probability distribution of actual distances in this direction for the measured parallax of this pulsar, according to Eq.1.20, in the approximation $C_D(0,\infty) \simeq C_D(0, D_{\rm max})$, $D_{\rm max} = 10\,$kpc. The histogram gives the results of a Monte Carlo simulation which retains objects with $0.14 < \varpi' < 0.18$. The blue and red lines give the analytic distributions for hypothetically smaller measurement errors but the same value for ϖ'. The curves are normalized to the same maximum value

ϖ' when the real parallax is ϖ. As we explain in Sect.1.1, this is incorrect, and arises from confusing the frequentist and Bayesian methods. Second, by interpreting the right hand side of Eq.1.1 as a probability density for ϖ, they add the factor $|d\varpi/dD| = 1/D^2$ in converting this to a probability density for D; and ignore the spatial density $f(D)$. As may be seen from Eqs.1.2, 1.14 and 1.15 this corresponds effectively to assuming $f(D) \propto 1/D^2$. The effect of this double error for a homogeneous spatial distribution is to replace the D^2 factor in our Eqs.1.18 with D^{-2}, and is illustrated in Fig.1.1.

Verbiest et al. (2012) and Verbiest & Lorimer (2014) make the same errors as Faucher-Giguère and Kaspi (2006), but correctly include $f(D)$ into the probability density $P_D(D|\varpi')$. The net effect of this is to remove the D^2 factor in our Eqs.1.18 and 1.20, which correponds to the assumption of a uniform distance distribution $f_D = 1$. The result is illustrated in Fig.1.1 for a homogeneous spatial distribution.

Francis (2014) argues that the distance probability distribution is a Gaussian centered on the real value, because it collapses to the real value when the measurement error goes to zero. The effect of the spatial distribution prior $D^2\mathcal{F}$ does diminish when the parallax measurement error becomes smaller, because a smaller range of D leads to a smaller variation of the prior $D^2\mathcal{F}$. Thus, for smaller errors the distance probability distribution narrows towards the correct distance. However, even for small errors, the distance probability function remains asymmetric (Figs.1.2 and 1.3). Indeed, Eq.3.2 from Francis (2014) is wrong, and confuses the frequentist and Bayesian approach, as does his conclusion that the distance distribution is irrelevant for the derivation of the probability density for the distance.

1.4 Distance and luminosity from parallax and flux, with assumed distance and luminosity distributions

We now consider sources for which parallax and flux have been measured, and the spatial distribution and luminosity function are known or assumed. The joint probability for D, ϖ', L, S' may be written with Eqs.1.2,1.4,1.3 as

$$P(D,\varpi',L,S') \propto g_D(\varpi'|D) f_D(D) g_S(S'|S[L,D]) f_L(L) = \frac{1}{\sqrt{2\pi}\,\sigma} \exp\left[-\frac{(1/D-\varpi')^2}{2\sigma^2}\right] D^2\mathcal{F}(D)\times \frac{1}{\sqrt{2\pi}\,\sigma_S} \exp\left[-\frac{(L/[L_o D^2]-S')^2}{2{\sigma_S}^2}\right] f_L(L) \tag{1.22}$$

For fixed values of ϖ', σ, S' and σ_S, and for a chosen luminosity function $f_L(L)$, this joint probability can be computed for each combination of D and L. We show contours of equal probability in the D, L-plane in Fig.1.4, as applicable to PSR J0218+4232. The maximum probabilities lie at distances well below the nominal distance $D' = 1/\varpi'$ and at luminosities well below the nominal luminosity $L' = L_o S'/{\varpi'}^2$. This is due to the luminosity functions, that peak at values well below L', and thus favour low luminosities, hence small distances, as far as the measurement uncertainties allow.

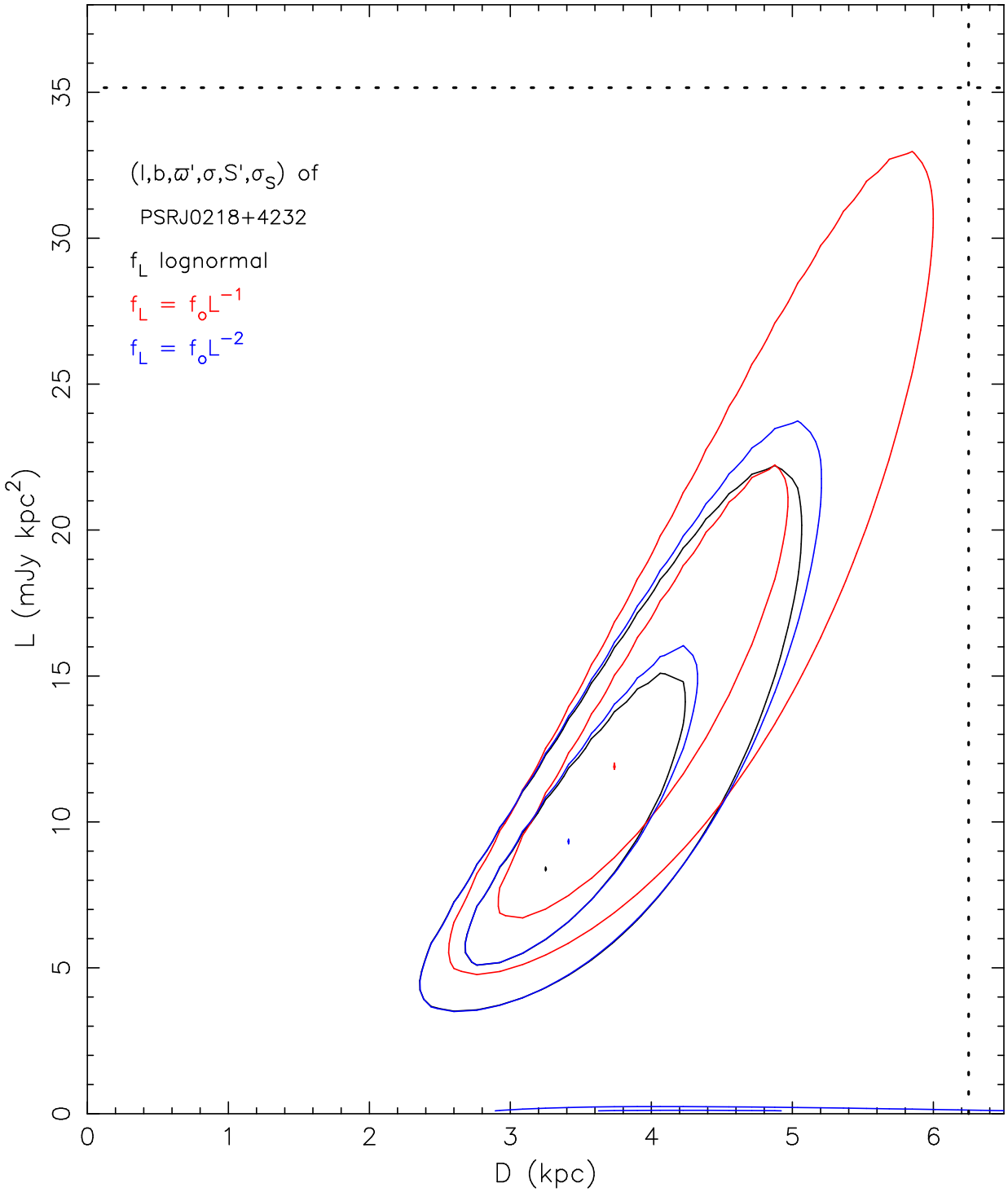

Figure 1.4: Contours of equal joint probability $P(D, \varpi', L, S')$, for the direction, parallax, flux, and measurement errors of PSR J0218+4232, for two power-law and for the lognormal luminosity functions. For each luminosity function we show the maximum, and contours containing 68% and 95% of the integrated probability. The contours for the power-law luminosity function with index -2 have two branches, one at very low luminosities, and one at higher luminosities; part of the latter is indistinguishable from the contours for the the lognormal luminosity function. The vertical and horizontal dashed lines show the nominal values for distance $D = 1/\varpi'$ and luminosity $L' = S'/{\varpi'}^2$, respectively

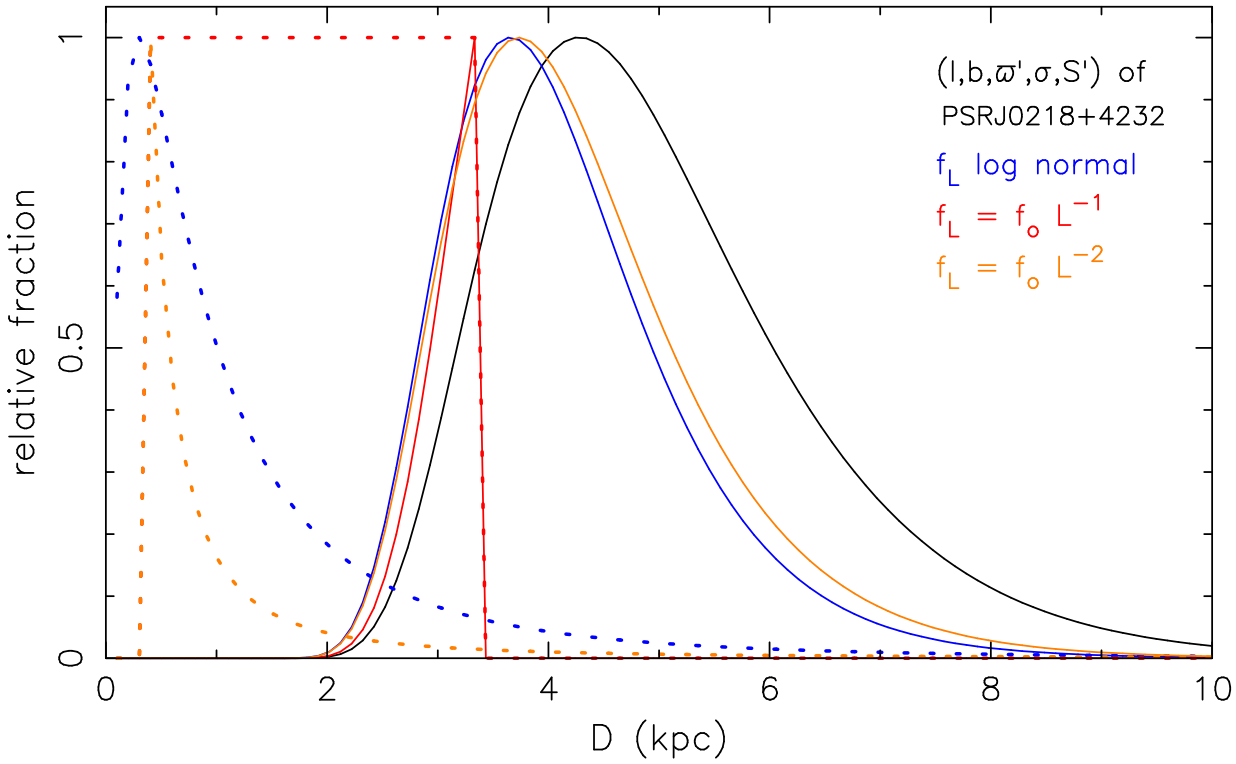

Figure 1.5: The distance probability function determined from parallax and accurate flux, with known spatial and luminosity distributions. The black line gives the values based on parallax only (reproducing the black line in Fig.1.3). For a lognormal luminosity function, the dashed blue line shows the extra term $D^2 f_L(L_o D^2 S')$ and the blue solid line the overall distribution according to Eq.1.24, for values appropriate for PSR J0218+4232. The dashed and solid red and brown lines idem for power-law luminosity functions both with $L_{\rm min} = 0.1\,{\rm mjy\,kpc^2}$, and $L_{\rm max} = 10\,{\rm mJy\,kpc^2}$ for $\alpha = -1$, and $L_{\rm max} = 100\,{\rm mJy\,kpc^2}$ for $\alpha = -2$, respectively. All curves are normalized to their maximum value.

In Fig. 1.4 we did not apply cutoffs to the power-law luminosity functions at low or high luminosity. As may be seen from Eq.1.22 such cutoffs do not change the form of the contours of $P(D, \varpi', L, S')$, but only the normalization, in the range $L_{\rm min} < L < L_{\rm max}$. Outside this range $P(D, \varpi', L, S') = 0$.

1.4.1 Distances

Suppose that we are interested in the probability distribution for distances only. We note that, for a finite measurement error, a range of luminosities contributes to the probability of measuring S'. By integrating over the luminosity, we find the joint probability of D, ϖ', S'

$$P(D, \varpi', S') \propto g_D(\varpi'|D) f_D(D) \int g_S(S'|S[L, D]) f_L(L) dL =$$

$$g_D(\varpi'|D) f_D(D) \int g_S(S'|S[L, D]) f_L(L_o D^2 S))\, L_o D^2 dS \qquad (1.23)$$

where we use the fact that $g_D(D)$ and $f_D(D)$ do not depend on L.

In many applications, the flux is measured much more accurately than the parallax, in the sense that $\sigma_S/S \ll 1$. In that case, for a measurement error distribution g_S according to Eq.1.3, only values of S close to S' contribute to the integral over S in Eq.1.23, and f_L is close to constant in that small interval. Thus the factor $f_L(L_o D^2 S) L_o D^2 = f_L(L_o D^2 S') L_o D^2$ may be written outside of the integral, and the remaining integral $\int g_S(S'|S) dS = 1$. With Bayes' theorem we then obtain (cf. Eqs.1.12, 1.13):

$$\begin{aligned} p_D(D|\varpi', S') &= C_D(0, D_{\max}) D^2 \mathcal{F}(D) \times \\ &\quad \exp\left[-\frac{(1/D - \varpi')^2}{2\sigma^2}\right] L_o D^2 f_L(L_o D^2 S') \end{aligned} \tag{1.24}$$

Apart from normalization, the only difference with Eqs.1.18 and 1.20 is the extra term $D^2 f_L(L_o D^2 S')$. For $f_L \propto L^{-1}$, the extra term $D^2 f_L$ is constant, and thus $p_D(D|\varpi', S')$ (Eq.1.24) is identical to $p_D(D|\varpi')$, except for a normalization constant, provided $L_{\min} < L < L_{\max}$.

In Fig.1.5 we apply eq. 1.24 to PSR J0218+4232, for three luminosity functions, where we set the uncertainty of the measured flux to zero, for illustrative purpose .

For the power-law luminosity function Eq.1.8 with $\alpha = -1$ we fix minimum and maximum luminosities at $0.1\,\mathrm{mJy\,kpc^2}$ and $10\,\mathrm{mJy\,kpc^2}$, respectively. The accurate flux then leads to minimum and maximum distances at: $D_{\min} = \sqrt{L_{\min}/L_o S'} = 0.33\,\mathrm{kpc}$ and $D_{\max} = \sqrt{L_{\max}/L_o S'} = 3.3\,\mathrm{kpc}$. For this luminosity function $p_D(D|\varpi', S') \propto p_D(D|\varpi')$ in the range $L_{\min} < L < L_{\max}$.

For a steeper power law with $\alpha = -2$, the extra term $D^2 f_L \propto D^{-2}$ enhances the probability of lower distances and lowers the probability of large distances. We show this for $L_{\max} = 100\,\mathrm{mJy\,kpc^2}$.

In Fig.1.5 we also show Eq.1.24 for the lognormal distribution, applied to PSR J0218+4232, which apart from the normalization is rather similar to the result for a power-law luminosity distribution with $\alpha = -2$.

For all three luminosity functions, the lower range of allowed distances is determined mainly by the parallax and its error.

1.4.2 Distances: earlier derivations

Verbiest et al. (2012) use the lognormal luminosity function Eq.1.10. Entering this in Eq.1.24 we obtain

$$\begin{aligned} p_D(D|\varpi', S') &= C_D(0, D_{\max}) D^2 \mathcal{F}(D) \exp\left[-\frac{(1/D - \varpi')^2}{2\sigma^2}\right] \times \\ &\quad \exp\left[-\frac{(\log\left[L_o D^2 S'\right] - \mu_x)^2}{2{\sigma_x}^2}\right] \frac{1}{S'} \end{aligned} \tag{1.25}$$

Comparing this with Eq.26 of Verbiest et al. (2012), we see that the $1/S'$ term in Eq.1.25 is there replaced with $1/D$. This variant arises because their Eq. 25 has $d\lambda/dD$ instead of the correct $d\lambda/dS'$, analogous to the error leading to Eq.1.21. As a result, the probability of actual distance for measured parallax and flux given by Verbiest et al. (2012, their Eq. 27), has a weighting factor $1/D^3$, absent in the correct version of our Eq.1.25 (and omits the weighting factor $1/S'$, which however drops out in the normalization).

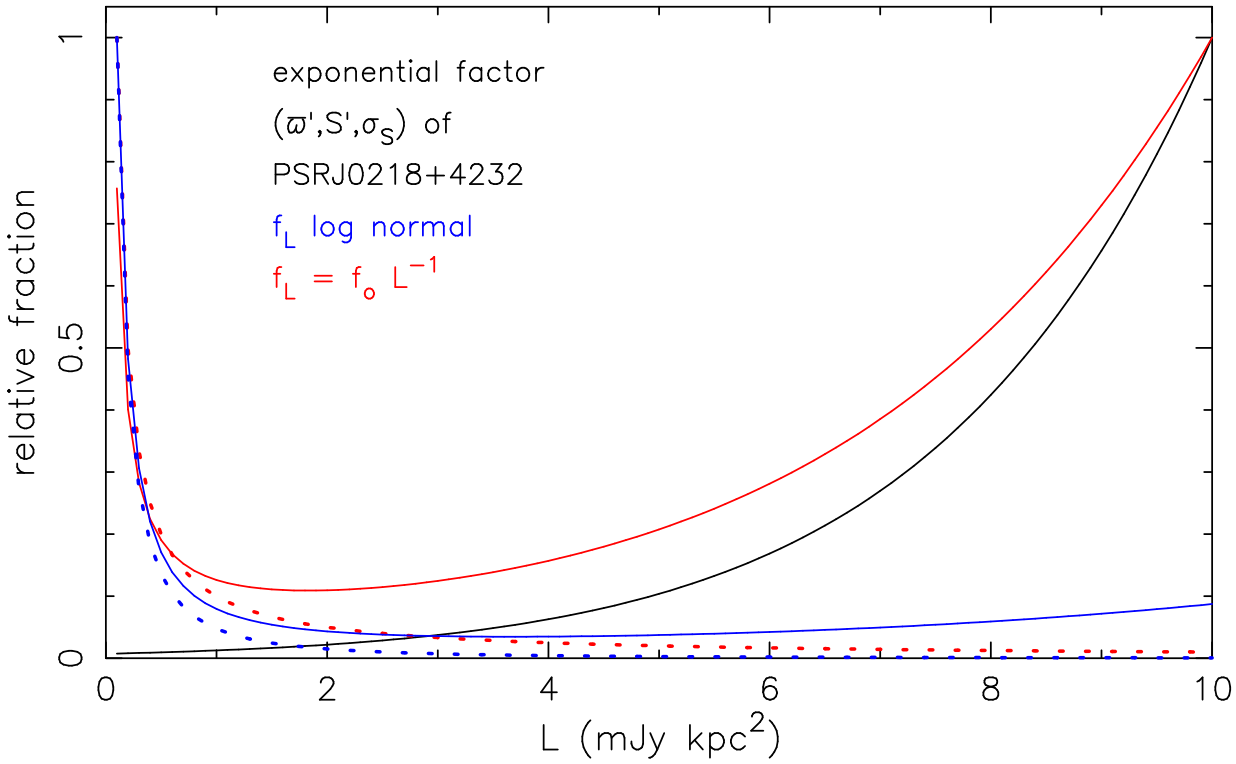

Figure 1.6: The luminosity probability function determined from accurate parallax and uncertain flux (values for PSR J0218+4232), with two assumed luminosity distributions. The black line gives the exponential factor in Eq.1.28. The dashed red line shows a power-law luminosity function, and the solid red line the product of this with the exponential. The blue lines idem for a lognormal luminosity function. Because of the accurate distance, this luminosity probability function is valid for any spatial distribution

1.4.3 Luminosities

In the case where we are interested in luminosities only, we write the joint probability of L, ϖ' and S', averaged over distances D, by integrating Eq.1.22 over D. Substituting $D = \varpi^{-1}$, and $D_{\max} = 1/\varpi_{\min}$ this leads to

$$P(L,\varpi',S') \propto f_L(L)\int_{\varpi_{\min}}^{\infty} \frac{\varpi^{-2}\mathcal{F}(\frac{1}{\varpi})}{\sqrt{2\pi}\,\sigma}\exp\left[-\frac{(\varpi-\varpi')^2}{2\sigma^2}\right]\times \frac{1}{\sqrt{2\pi}\sigma_S}\exp\left[-\frac{(L\varpi^2/L_o - S')^2}{2{\sigma_S}^2}\right]\varpi^{-2}d\varpi \quad (1.26)$$

1.4.3.1 Luminosities with accurate distance

We first consider the case where the distance is well known, in the sense that $\sigma/\varpi \ll 1$. Only terms with $\varpi \simeq \varpi'$ contribute to the integral over ϖ in Eq.1.26, which may be rewritten as

$$P(L,\varpi',S') \propto f_L(L)\varpi'^{-4}\mathcal{F}\left(\frac{1}{\varpi'}\right)\exp\left[-\frac{(L\varpi'^2/L_o - S')^2}{2{\sigma_S}^2}\right]\times \int_{\varpi_{\min}}^{\infty}\frac{1}{\sqrt{2\pi}\,\sigma}\exp\left[-\frac{(\varpi-\varpi')^2}{2\sigma^2}\right]\times d\varpi \quad (1.27)$$

The integral is a constant for a given $\varpi_{\rm min} \equiv 1/D_{\rm max}$, and approaches unity when σ/ϖ' approached zero, provided $\varpi' > \varpi_{\rm min}$, i.e. provided that the nominal distance $D' \equiv 1/\varpi'$ satisfies $D' < D_{\rm max}$. We then have

$$\begin{aligned} p_L(L|\varpi', S') &= C_L(L_{\rm min}, L_{\rm max}) {\varpi'}^{-4} \mathcal{F}(\frac{1}{\varpi'}) f_L(L) \\ &\quad \times \exp\left[-\frac{[L - L'(\varpi', S')]^2}{2\sigma_S(\varpi')^2}\right] \\ \text{where} \qquad & L'(\varpi', S') = \frac{L_o S'}{{\varpi'}^2}; \quad \sigma'_S(\varpi') = \frac{L_o \sigma_s}{{\varpi'}^2} \end{aligned} \tag{1.28}$$

Because the integral over L implicit in $C_L(L_{\rm min}, L_{\rm max})$ does not depend on D, the factor $D^4\mathcal{F} = {\varpi'}^{-4}\mathcal{F}(1/\varpi')$ may be dropped from this equation. Specifically, this implies that $p_L(L|\varpi', S')$ does not depend on the spatial distribution. Eq.1.28 can be interpreted directly, as follows. For an accurate distance $D = 1/\varpi'$, the number of sources scales with $D^2\mathcal{F}$. An extra factor D^2 is due to the conversion of a flux interval ΔS to a luminosity interval ΔL. The probability of luminosity L is given by the probability of the corresponding flux $S = L/(L_o D^2)$, weighted with the luminosity function f_L. The weighting factor f_L in general may cause the most probable luminosity to differ from the nominal luminosity $L' = L_o D^2 S'$ – analogous to the way in which the weighting factor f_D causes the most probable distance to differ from the nominal distance $D' = 1/\varpi'$ in Eqs.1.18 and Eq.1.20.

The effect of the competition between the luminosity function f_L and the exponential term in Eq.1.28 can be quite dramatic, as illustrated in Fig.1.6. As an example we consider PSR J0218+4232, assuming for illustrative purpose that its parallax is exact. With $L_o = 1$, its nominal luminosity is $L' = L_o S'/{\varpi'}^2 \simeq 35\,{\rm mJy\,kpc^2}$, and $\sigma'_S \simeq 8\,{\rm mJy\,kpc^2}$. In the luminosity range considered, $0.1 < L({\rm mJykpc^2}) < 10$, the exponential factor in Eq.1.28 increases by a factor 130 between the low and the high luminosity limit. The relatively flat luminosity function $f_L \propto L^{-1}$ decreases by a factor 100 in the same range. As a result, the overal luminosity probability peaks both at $0.1\,{\rm mJy\,kpc^2}$, and – less steeply – at $10\,{\rm mJy\,kpc^2}$.

The peak at the high luminosity limit is lowered for a luminosity function that drops faster towards high luminosities, as illustrated in Fig.1.6 for the lognormal distribution Eq.1.10. For a power law $f_L \propto L^{-2}$ the peak at $10\,{\rm mJy\,kpc^2}$ disappears. On the other hand, if the flux measurement error is halved from its actual value to $\sigma_S = 0.1\,{\rm mJy}$, both power-law distributions and the lognormal distribution all combine with the exponential function to give a peak only at $10\,{\rm mJy\,kpc^2}$ in the relative probability.

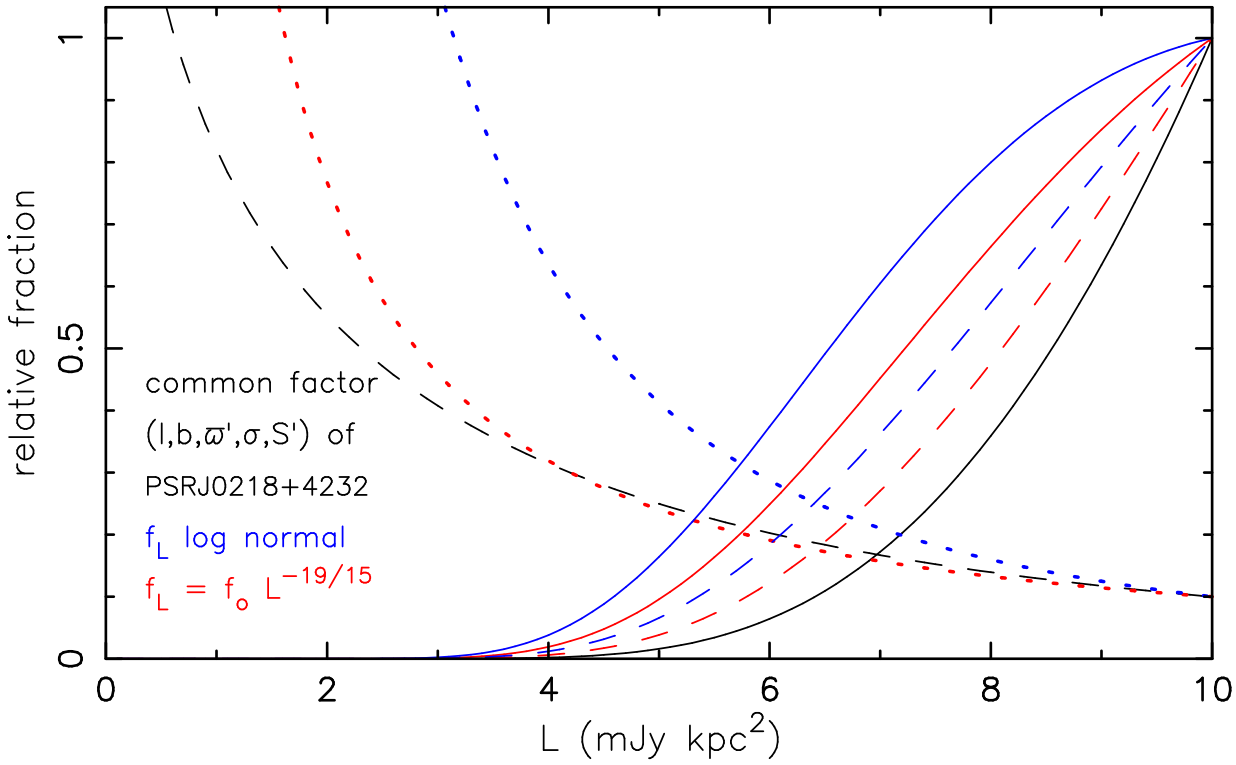

Figure 1.7: The luminosity probability function determined from uncertain parallax and accurate flux (values for PSR J0218+4232). The black solid line shows the exponential factor in Eq.1.30, multiplied with $L^{1.5}$, the black dashed line shows $\mathcal{F}$. In blue, the dotted curve shows the lognormal luminosity distribution, the dashed and solid curves the corresponding luminosity probability functions for homogeneous and galactocentric spatial distributions, respectively. In red, idem for the power-law luminosity function. All curves are normalized to a value 1 at 10 kpc, except those for the luminosity functions and for $\mathcal{F}$, normalized to a value of 0.1 at 10 kpc

1.4.3.2 Luminosities with accurate flux

To compute the integral in Eq.1.26 in the limit $\sigma_s/S' \ll 1$, we first make the substitution $\varpi^2 = uL_o/L$, hence $2\varpi d\varpi = du\, L_o/L$. Only terms with $u \simeq S'$ contribute to the integral, hence

$$\begin{aligned} P(L,\varpi',S') \quad &\propto \quad f_L(L)x^{-5}\mathcal{F}\left(\frac{1}{x}\right)\exp\left[-\frac{(x-\varpi')^2}{2\sigma^2}\right]\times \\ &\qquad \int_{u_{\min}}^{\infty}\exp\left[-\frac{(u-S')^2}{2{\sigma_S}^2}\right]du\,\frac{L_o}{L} \\ \text{where} \qquad &x=\sqrt{\frac{L_oS'}{L}};\quad \text{and}\quad u_{\min}={\varpi_{\min}}^2\frac{L}{L_o} \end{aligned} \tag{1.29}$$

The integral depends on L, via $u_{\min}$. However, provided that $S' > u_{\min}$, i.e. $L < L_o{D_{\max}}^2S'$, the integral approaches unity when σ_s/S' approaches zero. For $L > L_o{D_{\max}}^2S'$ the integral approaches zero in the same limit. Thus

$$p_L(L|\varpi',S') = \begin{cases} C_L(L_{\min},L_{\max})f_L(L)\left(\frac{L}{L_oS'}\right)^{5/2}\frac{L_o}{L}\mathcal{F}\left(\sqrt{\frac{L}{L_oS'}}\right)\times \\ \quad \exp\left[-\frac{(\sqrt{L_oS'/L}-\varpi')^2}{2\sigma^2}\right] \text{ for } L < L_o{D_{\max}}^2S' \\ \\ 0 \quad \text{for} \quad L > L_o{D_{\max}}^2S' \end{cases} \tag{1.30}$$

Because the integral over L implicit in $C_L(L_{\min},L_{\max})$ does not depend on L_o or S', the factor $L_o(L_oS')^{-5/2}$ may be omitted from Eq.1.30.

For the flux and parallax of PSR J0218+4232, the exponential factor in Eq.1.30 increases with L up to $10\,\mathrm{mJy\,kpc^2}$ (and beyond), and this increase is amplified by the factor $L^{1.5}$. In contrast, the luminosity functions increase towards the minimum luminosity of $0.1\,\mathrm{mJy\,kpc^2}$. The combined effect of these two factors is shown in Fig.1.7. The luminosity probability for the galactocentric distribution observed in the direction of PSR J0218+4232, has a stronger contribution at luminosities below $10\,\mathrm{mJy\,kpc^2}$ than the homogeneous distribution. This is due to the rise of $\mathcal{F}$ towards lower distances, hence lower luminosities.

1.4.3.3 Can we do without the luminosity function?

Since the luminosity is given by $L = L_oD^2S'$, one may wonder whether, in the case of accurate flux, the probability of luminosity follows the probability of distance squared:

$$p_L(L|\varpi',S') \stackrel{?}{=} K\,p_{D^2}(D^2|\varpi') \tag{1.31}$$

where K is a proportionality constant. The answer is no. This is most easily seen if we consider a standard candle, where the luminosity function is unity for $L = L_S$ and zero for all other luminosities $L \neq L_S$. An accurate flux then implies that only one distance is possible, viz. the one for which $L_oS'D^2 = L_S$, whereas the right hand side of Eq.1.31 gives a non-zero value for a range of distances.

More generally, at fixed flux S' a different part of the luminosity function f_L is sampled at different distances, and thus the luminosity function is indispensable in the determination of probabilities.

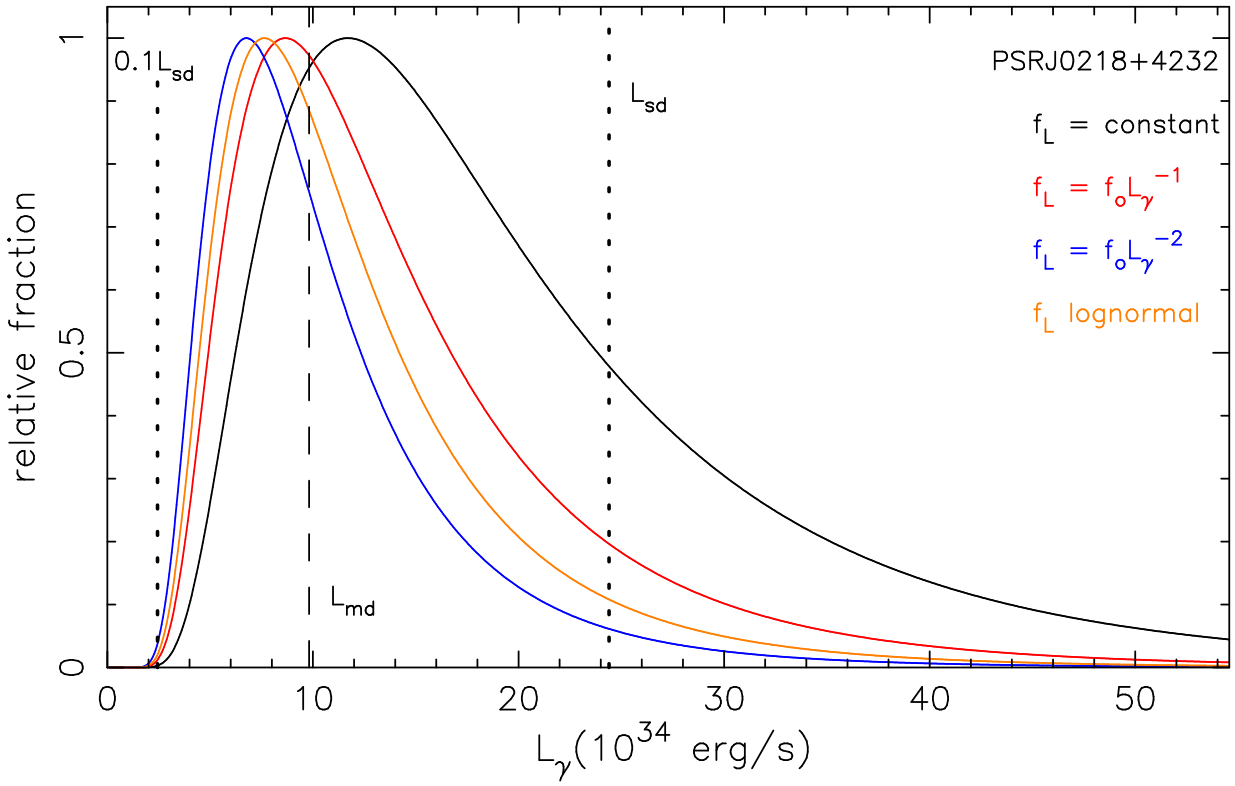

Figure 1.8: The gamma-ray luminosity probability function determined from the parallax with error and accurate gamma-ray flux of PSR J0218+4232, for three different assumed power-law and one lognormal gamma-ray luminosity functions. The realistic distance prior (Eqs. 1.4, 1.6) is assumed. $L_{\rm sd}$ (Eq. 1.32), and $0.1L_{\rm sd}$ are indicated with vertical dotted lines, $L_{\rm md}$ (Eq. 1.34) is indicated with a vertical dashed line.

The invalidity of Eq.1.31 implies that the probability density function of the luminosity can be given only when the luminosity function is known or assumed, or alternatively when also the parallax is very accurate.

1.5 The distance and gamma-ray luminosity of PSR J0218+4232

An upper limit to the rotation-powered gamma-ray luminosity L_γ is given by the spindown luminosity $L_{\rm sd}$

$$L_{\rm sd} \equiv \frac{4\pi^2 I \dot{P}}{P^3} \simeq 2.44 \times 10^{35} {\rm erg/s} \tag{1.32}$$

where the numerical value is for PSR J0218+4232 (see Table 1.1), with an assumed moment of inertia $I = 10^{45} {\rm g\,cm^2}$ for the neutron star. It should be noted that the moment of inertia I of the neutron star PSR J0218+4232 is uncertain, as its mass and radius are uncertain.

As reference values we use the nominal gamma-ray luminosity, at the nominal distance $D_{\rm n} \equiv 1/\varpi' = 6.25\,{\rm kpc}$:

$$L_{\rm n} \equiv 4\pi \frac{1}{\varpi'^2} S_\gamma = 2.1 \times 10^{35} {\rm erg/s} = 0.87 L_{\rm sd} \tag{1.33}$$

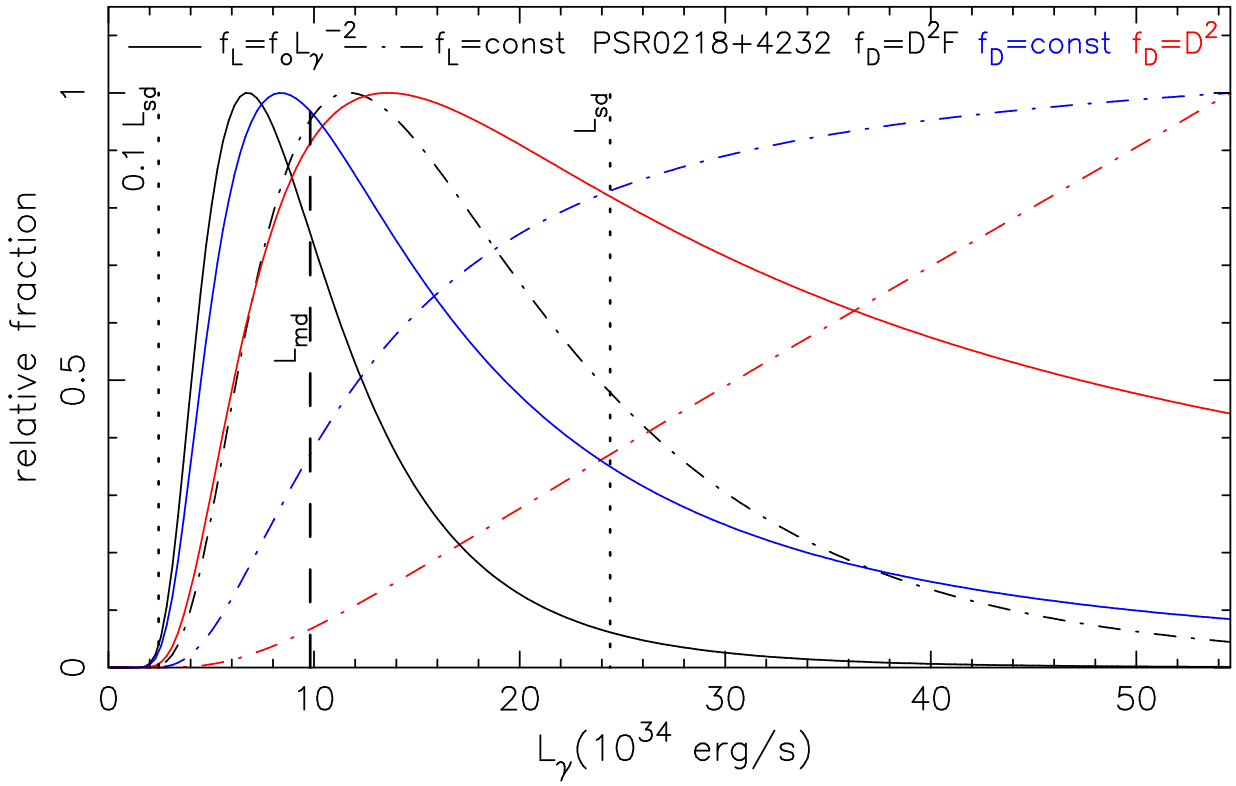

Figure 1.9: The gamma-ray luminosity probability function determined from the parallax with error and accurate gamma-ray flux of PSR J0218+4232, for three different distance priors and two different luminosity priors. $L_{\rm sd}$ (Eq. 1.32), and $0.1L_{\rm sd}$ are indicated with vertical dotted lines, $L_{\rm md}$ (Eq. 1.34) is indicated with a vertical dashed line.

Table 1.2: The most probable distance $D_{\rm mp}$ and 95% credibility interval for different distance and luminosity priors for PSR J0218+4232.

Priors		$D_{\rm mp}$	$D_l - D_u$ (a)	$D_l - D_u$ (b)
f_D	f_L	(kpc)	(kpc)	(kpc)
const	–	6.25	3.75 – 10.0	–
D^2	–	10.0	4.62 – 10.0	–
$D^2\mathcal{F}$	–	4.28	2.65 – 7.82	–
$D^2\mathcal{F}$	lognorm	3.99	2.51 – 7.15	2.71 – 6.38
$D^2\mathcal{F}$	const	5.05	3.08 – 8.95	3.39 – 6.69
$D^2\mathcal{F}$	L^{-1}	4.28	2.65 – 7.82	2.97 – 6.59
$D^2\mathcal{F}$	L^{-2}	3.74	2.39 – 6.65	2.50 – 6.15

Notes: All distance priors have $D_{\rm max} = 10$ kpc; $\mathcal{F}$ refers to eq. 1.6. The luminosity priors are for gamma rays. A dash means no priors applied: note that this is different from using a uniform prior f_L = constant. (a) No upper bound imposed on luminosity prior. (b) Maximum luminosity is $L_{\rm sd}$.

and the luminosity at the most probable distance according to Eq.1.19, $D_{\rm md} = 4.28\,$kpc

$$L_{\rm md} \equiv 4\pi {D_{\rm md}}^2\, S_\gamma = 9.8 \times 10^{34} {\rm erg/s} = 0.40 L_{\rm sd} \tag{1.34}$$

Note that the gamma-ray luminosity is defined for isotropic emission (i.e. $S_o = 4\pi$), which the gamma pulsations show to be false.

As noted in the previous section, the probability distribution of luminosity for measured parallax with error and accurate flux, can be given only when a luminosity function is known or assumed.

The effect of using different priors is illustrated in Figures 1.8 and 1.9 and in Tables 1.2 and 1.3.

Table 1.2 shows that use of a realistic distance prior, $f_D \propto D^2\mathcal{F}$ with $\mathcal{F}$ given by Eq. 1.6, reduces the most probable distance to a value smaller than for f_D uniform or spatially homogeneous, also when f_L is implemented. Application of realistic luminosity priors narrows the 95% distance credibility interval, in particular when an upper bound to L_γ is set equal to $L_{\rm sd}$. In this case the upper limit of the credibility interval is close to the nominal distance of 6.25 kpc.

Figure 1.8 shows the probability density functions of L_γ for the realistic distance prior $f_D \propto D^2\mathcal{F}$ with $\mathcal{F}$ given by Eq. 1.6. For each luminosity prior the probability that $L_\gamma < L_{\rm sd}$ is very small, < 0.001, and the most probable luminosity $L_{\rm mp}$ is well above $0.1L_{\rm sd}$ and well below $L_{\rm sd}$. For steeper luminosiy functions the probability density function is pushed to lower luminosities, as expected (see Table 1.3).

The influence of the distance prior is much more significant. The unrealistic distance priors, combined with the large uncertainty in the parallax, lead to unreallistically high $L_\gamma > L_{sd}$, especially for the uniform luminosity prior.

Table 1.3: The most probable gamma-ray luminosity $L_{\rm mp}$ and 95% credibility interval for different distance and luminosity priors for PSR J0218+4232.

Priors		$L_{\rm mp}$	$L_l - L_u$	$\int_{L_{\rm sd}}^{\infty} p_L(L)dL$
f_D	f_L	$(L_{\rm sd})$	$(L_{\rm sd})$	
–	–	0.87	–	–
D^2	–	2.24	0.70 – 2.24	0.86
const	const	2.24	0.48 – 2.24	0.72
D^2	L^{-2}	0.56	0.24 – 2.14	0.51
$D^2\mathcal{F}$	const	0.48	0.17 – 1.72	0.26
$D^2\mathcal{F}$	L^{-1}	0.36	0.13 – 1.32	0.12
$D^2\mathcal{F}$	L^{-2}	0.28	0.11 – 0.96	0.04
$D^2\mathcal{F}$	lognorm	0.31	0.12 – 1.11	0.07

Notes: A dash means no priors applied: note that this is different from using a uniform prior. All distance priors have upper boundary $D_{\rm max} = 10$ kpc: $\mathcal{F}$ refers to eq. 1.6.

1.6 Conclusions and discussion

A homogeneous spatial distribution is useful for pedagogical purposes in explaining the importance of a prior in deriving a distance probability distribution from a measured parallax. For realistic investigations, however, a homogeneous spatial distribution is rather misleading. In particular, for a homogeneous spatial distribution, the number of sources increases with distance, and a measured parallax will more often correspond to a large distance which is measured too low, than to a small distance measured too high. In this case, a parallax more often underestimates the actual distance, especially for large measurement uncertainties (see Fig.1.2). In a realistic galactic distribution, as observed from Earth, a parallax tends to overestimate the distance, however, at distances where the intrinsic source distribution decreases with distance (Fig.1.3). This is often the case, for example in directions away from the galactic center and / or away from the galactic plane.

Both analytically and via a Monte Carlo simulation, we show that a prior for the spatial distribution must be used, also in the study of a single object, for the determination of the distance probability density. Similarly, when parallax and flux measurements with their errors are combined to derive probability density distributions for distances and luminosities, priors are necessary for both spatial and luminosity distributions. The nominal distance $D' = 1/\varpi'$ and luminosity $L' = L_o S/{\varpi'}^2$ may be very different from the most probable values (see Fig.1.4), unless both measurement erors are small. This is the consequence of the predominance of low luminosities in the luminosity functions that we use: for each flux the higher probability of a low luminosity translates into a higher probability of a lower distance – in as far as the parallax measurement allows this. In the case of PSR J0218+4232, for example, the most probable distance as derived fom the parallax only is at 4.28 kpc (Fig.1.5). When parallax and radio flux are both used, the most probable distance drops to 3.74 kpc and 3.42 kpc for power-law luminosity functions with index $\alpha = -1$ and $\alpha = -2$, respectively; and to 3.25 kpc for the lognormal luminosity distribution

(Fig.1.4). Clearly, the quality of the estimates of distance and luminosity is enhanced by the use of realistic prior distributions with respect to the nominal estimates based on measurement only. On the other hand, it is important to keep in mind that wrong priors may deteriorate the estimate.

In particular the use of the spatial homogeneous prior is harmful in the case of an uncertain parallax: it shifts the value for most probable distance or luminosity to the upper boundary on the prior (see second line in Tables 2 and 3). In contrast, the realistic distance prior gives an estimate for the gamma-ray luminosity inside the physically motivated region ($L_{\rm mp} < L_{\rm sd}$) even when no additional restrictions on the luminosity function are imposed. An application of the lognormal luminosity prior gives an estimate for distance and gamma-ray luminosity which is in between two values obtained if we apply power law with $\alpha = -1$ and $\alpha = -2$.

It may be noted, in particular for the power-law luminosity function, that the luminosity function may have a different form at different luminosities (for an example, see Eq.17 of Faucher-Giguère & Kaspi 2006.) This is easily implemented in the formalism described in the previous Sections. More complicated is the – probably realistic – case where the luminosity function depends on the position in the Galaxy. For millisecond pulsars this is unlikely. Ordinary pulsars at large z, however, are on average older than pulsars close to the galactic plane, and may well have lower luminosities, if the pulsar luminosity depends on its period and / or period derivative. For the study of such pulsars an evolutionary model is indispensable in the determination of their distances and luminosities.

In the study of a single object, the priors of spatial and luminosity distributions must be known. In the study of a larger number of objects, however, these distributions can and indeed should be derived from prior observations. In general one may still wish to describe these distributions with a number of parameters, e.g. H and h in Eq.1.6, α in Eq.1.8, or μ_x and σ_x in Eq.1.10. For a sufficiently large number of pulsars, the evolutionary model can also be tested. At the moment, such studies are hampered by the lack of reliable large ($> 1\,$kpc) distances.

Ceterum censeo Carthaginem delendam esse.

– Cato maior

Chapter 2

The observed velocities of young pulsars

Frank Verbunt, Andrei Igoshev, Eric Cator

A&A, 2017
accepted

Abstract

We argue that comparison with observations of theoretical models for the velocity distribution of pulsars must be done directly with the observed quantities, i.e. parallax and the two components of proper motion. We develop a formalism to do so, and apply it to pulsars with accurate VLBI measurements. We find that a distribution with two maxwellians improves significantly on a single maxwellian. The 'mixed' model takes into account that pulsars move away from their place of birth, a narrow region around the galactic plane. The best model has 42% of the pulsars in a maxwellian with average velocity $\sigma\sqrt{8/\pi} = 120\,\mathrm{km/s}$, and 58% in a maxwellian with average velocity 540 km/s. About 5% of the pulsars has a velocity at birth less than 60 km/s. For the youngest pulsars ($\tau_c < 10\,\mathrm{Myr}$), these numbers are 32% with 130 km/s, 68% with 520 km/s, and 3%, with appreciable uncertainties.

2.1 Introduction

The study of the velocities of pulsars is interesting on its own account, as a pointer to the formation process of a neutron star, but also has ramifications beyond this. In particular, some neutron stars are found in binaries and in globular clusters, as accreting X-ray sources or as pulsars. These neutron stars were born with velocities less than the escape velocity from the binary or from the cluster.

Neutron stars that have the same velocities as their progenitors, move with the rotation of the galaxy, with small velocities with respect to the local standard of rest (LSR), unless their progenitor is a member of a close binary or a runaway star. To investigate the velocities that neutron star acquires at birth in addition to the progenitor velocity, one therefore investigates their velocity v with respect to the LSR.

This investigation is complicated for pulsars with large velocities as these are affected by an acceleration in the galactic potential that varies between their place of birth and their current location, and because their current LSR differs from the LSR at their place of birth. Thus the current v of a pulsar differs from the v at birth. If the age and full space velocities were known, we could solve this complication by integrating the pulsar orbit back in time, but proper motion studies only provide 2 of the 3 velocity components, and ages of pulsars are usually uncertain. By limiting the study to young pulsars, one may reduce the effect of these complications. As well described by Brisken et al. (2003a, in particular Sect.5.1), correlations between spin-axis and velocity, between luminosity and velocity, and/or between velocity and distance to the Galactic Plane, among others, introduce selection effects in the observations. Such selection effects can only be corrected for in a full population study. Even so, determining the observed v distribution is a useful step toward a full population study, and various efforts have been published (see Table 2.5).

Arzoumanian et al. (2002) compare synthesized model populations with the observed periods, period derivatives, dispersion measures, fluxes, and the absolute values of galactic latitudes and of proper motions. They conclude that the velocity distribution of pulsars is bimodal, with a low-velocity and a high-velocity component.

Brisken et al. (2003a) investigate the velocity component v_l in the direction of galactic longitude. Their study is based on interferometric proper motion measurements (mostly their own). For each pulsar, they compute a probability distribution $P(D)$ for the distance D (based on the parallax or on the dispersion measure DM, allowing for the limited accuracy in converting DM to D) and combine this with the probability function $P(\mu_l)$ for the proper motion μ_l (allowing for measurement uncertainty) to compute the probability distribution $P(v_l)$. The set of $P(v_l)$ is fitted with a model in which this distribution is described by two zero-centred Gaussian distributions, representing a slow and a fast component.

Hobbs et al. (2005) construct velocity distributions $P(v_{1\mathrm{D}})$ where $v_{1\mathrm{D}}$ is either v_l or v_b and $P(v_{2\mathrm{D}})$ where $v_{2\mathrm{D}} \equiv \sqrt{{v_l}^2 + {v_b}^2}$ for a larger sample of pulsars, including measurements based on timing. v_b is the velocity component in the direction of latitude. Hobbs et al. assume that these observed $v_{1\mathrm{D}}$ and $v_{2\mathrm{D}}$ distributions are projections of an isotropic velocity distribution $P(v)$, and then reconstruct $P(v)$ by using a `clean` algorithm to deconvolve $P(v_{1\mathrm{D}})$ and $P(v_{2\mathrm{D}})$. The advantage of this method is that it is non-parametric, i.e. it does not assume a prescribed form for $P(v)$. The reconstructed form turns out to be well described by a maxwellian, with $\sigma = 265\,\mathrm{km/s}$.

Faucher-Giguère & Kaspi (2006) extend the method of Brisken et al. (2003a) in two ways. First they consider a variety of models for the distribution of v_l, and second they extend the maximum-likelihood model with a Bayesian analysis of probability ratios for the comparison of different models.

Whereas these studies agree that the space (i.e. 3-D) velocities of neutron stars are high, averaging as much as 450 km/s, they differ on the fraction of low-velocity neutron stars. Hobbs et

al. (2005) argue that the low-velocity tail of the pulsar velocity distribution is due to projection effects, and that very few pulsars have space velocities below 60 km/s. (For a maxwellian with $\sigma = 265\,\mathrm{km/s}$ the fraction is 0.003.) In the acceptable models discussed by Faucher-Giguère & Kaspi (2006) the derived fraction of pulsars with space velocities less than 60 km/s varies from 0.012 (for a two-component Gaussian) to 0.135 (for the Paczyński distribution).

One reason for us to make a new study of the pulsar velocities is to resolve the differences between the predicted numbers of low-velocity pulsars in these recent studies. We note that among nine very accurate pulsar velocities $v_\perp$ ($= \sqrt{{v_l}^2 + {v_b}^2}$) listed by Brisken et al. (2002, Table 5), two are smaller than 40 km/s. The probability of finding two such low-$v_\perp$ pulsars in a sample of nine is 0.004 for an isotropic maxwellian with $\sigma = 265\,\mathrm{km/s}$. This suggests that the pulsar velocities may be overestimated by Hobbs et al. (2005).

A second reason for a new study is the development by Verbiest et al. (2012), of a Bayesian method to combine different distance indicators into a single probability distribution $P(D)$ for each pulsar. The main distance indicator is the parallax, where the Lutz-Kelker (1973) effect is taken into account, with the galactic pulsar distribution as a prior. For the study of pulsar velocities we correct some errors in the equations given by Verbiest et al. (2012) for use of the parallax (see Igoshev et al. 2016 and Bailer-Jones 2015), and add the measurements of the proper motions.

The third and final reason for our new study of pulsar velocities is the increased number of accurately measured proper motions and parallaxes (see Table 2.2).

In Section 2.2 we describe the master list of observed proper motions that we use in our study. We describe the ingredients of the likelihood function for pulsars and their use in determining the parameters of the velocity distribution in Sect. 2.3, and apply these to various models: a single isotropic maxwellian in Sect. 2.4, the sum of two isotropic maxwellians in Sect. 2.5, and a mixture of one or two isotropic and semi-isotropic maxwellians in Sect. 2.7. (In the semi-isotropic maxwellian distribution velocities towards the galactic plane are excluded, as explained in Sect. 2.6.)

Before we proceed, we describe the notation we use: we differentiate between the actual (and generally unknown) properties of the pulsar, and the measured (or nominal) values, by indicating the latter with a prime ($'$). The actual proper motion is the sum of three components: one due to the peculiar velocity of the pulsar, one due to the difference between the local standards of rest of the pulsar and of the Sun, and one due to the peculiar motion of the Sun (Eqs. 2.6 - 2.9). The measured parallax and proper motion differs from the actual values due to measurement errors (Eqs. 2.1 - 2.3), and may be skewed due non-uniform distributions of positions and velocities (Fig. 2.2). For convenience, our notation is summarized in Table2.1.

2.2 Data

To obtain a master list of pulsars with measured proper motions, we start by collating articles with proper motion measurements. The ATNF Catalogue, version 1.54[1] (Manchester et al. 2005), was very helpful in this.

[1] www.atnf.csiro.au/research/pulsar/psrcat

Table 2.1: Notation used in this paper

actual (unknown) values			
parallax, distance	ϖ	$D = 1/\varpi$	
		equatorial	galactic
peculiar velocity	v	v_α, v_δ, v_r	v_l, v_b, v_r
peculiar proper motion	$\mu_v = v/D$	$\mu_{\alpha*,v} = v_\alpha/D$	$\mu_{l*,v} = v_l/D$
		$\mu_{\delta,v} = v_\delta/D$	$\mu_{b,v} = v_b/D$
	$v_\perp = \sqrt{{v_\alpha}^2 + {v_\delta}^2} = \sqrt{{v_l}^2 + {v_b}^2}$		
proper motion:	$\mu_{\alpha*} = \mu_{\alpha*,G} + \mu_{\alpha*,v}$;	$\mu_\delta = \mu_{\delta,G} + \mu_{\delta,v}$	
measured (nominal) values			
parallax, distance	ϖ'	$D' = 1/\varpi'$	
velocity[a]	v'	$v'_\alpha, v'_\delta, v'_r$	v'_l, v'_b, v'_r
proper motion[a]	μ'	$\mu'_{\alpha*} = v'_\alpha/D$	$\mu'_{l*} = v'_l/D$
		$\mu'_\delta = v'_\delta/D$	$\mu'_b = v'_b/D$
	$v'_\perp = \sqrt{{v'_\alpha}^2 + {v'_\delta}^2} = \sqrt{{v'_l}^2 + {v'_b}^2}$		

Notes: [a] note that the measured values differ from the actual values not only due to measurement error, but also due to correction for galactic rotation

Brisken et al. (2000) note that VLBI measurements of proper motions need to be corrected for ionospheric refraction. We therefore do not use articles with proper motions from VLBI published before 2000. To select first-born, single pulsars we reject recycled pulsars (i.e. those with $\dot{P} < 5 \times 10^{-18}\mathrm{s\,s^{-1}}$), pulsars in binaries, and pulsars in globular clusters.

In this first application of our new method we prefer to use relatively accurate measurements. We therefore omit pulsars with distances determined only from dispersion measures, and pulsars with proper motions determined from pulse timing. In both cases, the errors are at least an order of magnitude larger than the errors obtained with VLBI, and often only correspond to (upper or lower) limits. Distances from dispersion measures have uncertainties dominated by systematic effects, with highly non-gaussian distributions. (For pulsars distances and dispersion measures, see e.g. Yao et al. 2017; for proper motions from timing, see Hobbs et al. 2004.) We also omit proper motions of pulsars derived from displacements in X-ray or optical images, which are relative to other objects in the field of view. The conversion to absolute proper motions in the ICRS adds significantly to the error.

This leaves us with the VLBI measurements of the articles listed in Table 2.2. Although the measurement of the proper motion components are not independent of each other, the covariance value is only provided by Brisken et al. [2003a] who give no parallax values. We therefore ignore covariances between $\mu'_{\alpha*}$ and μ'_δ. In the majority of the measurements, the errors are symmetric, and where asymmetric, the difference is small. We simplify our analysis by taking the largest error when errors are asymmetric. (Test calculations in which the smallest error is taken give the same results.)

The resulting master list of observed proper motions in equatorial coordinates is given in Table 2.6. Note that the proper motions in this Table are the observed proper motions $\mu'_{\alpha*}$ and

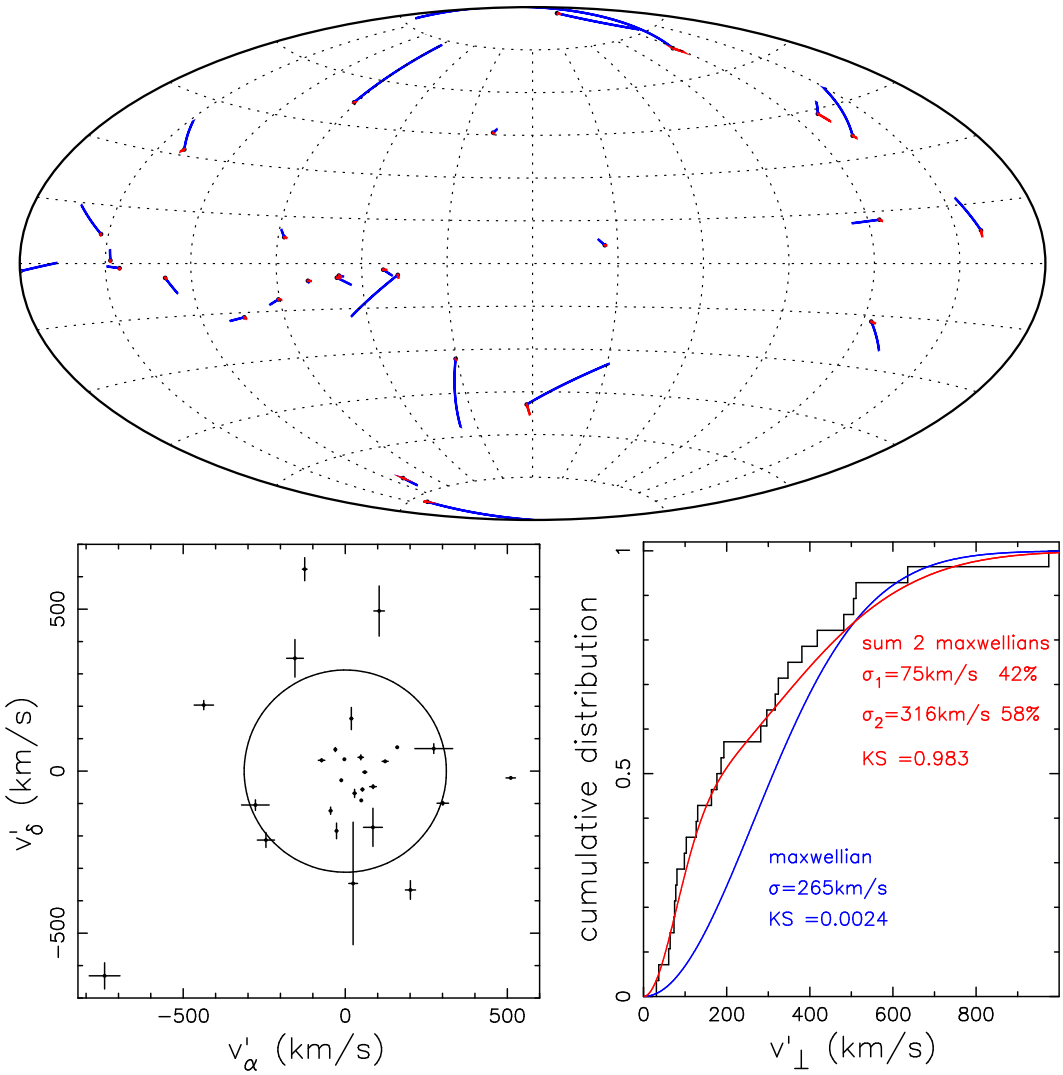

Figure 2.1: Illustrations of data from our master list of pulsars Table 2.6. Top: celestial distribution in galactic coordinates. The blue lines show the observed proper motion μ' and the red lines the correction due to galactic rotation (for nominal distance D'), in 0.5 Myr. Below left: nominal velocities in the celestial plane. The circle indicates the median value for $v_\perp$ for the projection of a maxwellian: $\sqrt{2\ln 2}\,\sigma$, for $\sigma = 265\,\mathrm{km/s}$. Below right: cumulative distributions of the observed $v'_\perp$, and of $v_\perp$, blue: according to Hobbs et al. (2005), red: according to our best solution, with the p-value according to a one-sided Kolmogorov-Smirnov test that the observed distribution is drawn from the theoretical one.

Table 2.2: Sources for proper motions in our master list

S	source		N	n
1	Brisken et al. (2002)	Table 4	6	2
2	Brisken et al. [2003b]	Table 3	1	1
3	Chatterjee et al. (2001)	Table 2	1	1
4	Chatterjee et al. (2004)	Table 1	1	1
5	Deller et al. (2009)	Table 3	4	2
6	Chatterjee et al. (2009)	Table 2	12	9
7	Kirsten et al. (2015)	Table 5	3	3
		total:	28	19

Notes: S source indicator, N number of entries used (isolated pulsars with parallax measurements), n with age less than 10 Myr. Later measurements may replace earlier ones; the source actually used is indicated in Table 2.6

μ'_δ, not corrected for galactic rotation and peculiar solar velocity. The celestial distribution, measured proper motions and nominal velocities of the pulsars in our master list are illustrated in Fig.2.1. From the top figure we learn that the correction for galactic motion in general is small. The lower figures add to our suspicion that a single maxwellian with $\sigma = 265\,\mathrm{km/s}$ seriously underestimates the number of pulsars with low velocities.

2.3 Ingredients

To determine the pulsar velocity distribution we use the measured values of the parallax ϖ' and of the two components of the proper motion $\mu'_{\alpha*}$ and μ'_δ. The conditional probabilities of obtaining these measured values when the actual values are $\varpi = 1/D$, $\mu_{\alpha*}$ and μ_δ can be written separately as

$$g_D(\varpi'|D)\Delta\varpi' = \frac{1}{\sqrt{2\pi}\sigma_\varpi}\exp\left[-\frac{(1/D-\varpi')^2}{2{\sigma_\varpi}^2}\right]\Delta\varpi' \tag{2.1}$$

$$g_\alpha(\mu'_{\alpha*}|\mu_{\alpha*})\Delta\mu'_{\alpha*} = \frac{1}{\sqrt{2\pi}\sigma_\alpha}\exp\left[-\frac{(\mu_{\alpha*}-\mu'_{\alpha*})^2}{2{\sigma_\alpha}^2}\right]\Delta\mu'_{\alpha*} \tag{2.2}$$

$$g_\delta(\mu'_\delta|\mu_\delta)\Delta\mu'_\delta = \frac{1}{\sqrt{2\pi}\sigma_\delta}\exp\left[-\frac{(\mu_\delta-\mu'_\delta)^2}{2{\sigma_\delta}^2}\right]\Delta\mu'_\delta \tag{2.3}$$

where σ_ϖ, σ_α and σ_δ are the measurement errors for the parallax and for the two components of the proper motion, respectively.

To obtain the joint probability of the measured and actual values, these equations must be complemented with the equations indicating the probability density functions of the actual distance and proper motion.

The probability density $f_D(D)$ of the distance D of the pulsar to the Earth for a galactocentric pulsar distribution is given by Verbiest et al. (2012). In the notation of Igoshev et al. (2016):

$$f_D(D) \propto D^2 R^{1.9}\exp\left[-\frac{|z(D,b)|}{h}-\frac{R(D,l,b)}{H}\right] \equiv D^2\mathcal{F}(D) \tag{2.4}$$

Table 2.3: Values of constants defining coordinate transformations and velocity corrections

Galactic pole, longitude node	
$\alpha_{\rm GP} = 192°85948 \quad \delta_{\rm GP} = 27°12825 \quad l_\Omega = 32°93192$	a
Peculiar velocity Sun	
$U = 10.0\,{\rm km/s} \quad V = 5.3\,{\rm km/s} \quad W = 7.2\,{\rm km/s}$	b
Galactic rotation	
$v_R(R_o) = v_R(R) = 220\,{\rm km/s}$	b
Distance galactic center, scales pulsar distribution	
$R_o = 8.5\,{\rm kpc} \quad h = 0.33\ {\rm kpc} \quad H = 1.7\ {\rm kpc}$	c

Notes: For explanation of these constants see Appendix 2.A and Sect. 2.B. a: from Perryman et al. 1997, b: from Dehnen & Binney 1998, c: from Verbiest et al. (2012).

with

$$z = D \sin b; \text{ and } R = \sqrt{{R_o}^2 + (D\cos b)^2 - 2D\cos b\, R_o \cos l} \tag{2.5}$$

where R and R_o are the galactocentric distance of the pulsar and the Sun, respectively, projected on the galactic plane. Through $\mathcal{F}(D)$ also $f_D(D)$ is a function of galactic coordinates l, b.

The proper motion of a pulsar $\mu_{\alpha*}, \mu_\delta$ is the sum of the proper motion of its standard of rest with respect to the Sun $\mu_{\alpha*,G}, \mu_{\delta,G}$ and the proper motion caused by its velocity with respect to its local standard of rest $\mu_{\alpha*,v}, \mu_{\delta,v}$:

$$\mu_{\alpha*} = \mu_{\alpha*,G} + \mu_{\alpha*,v}; \quad \mu_\delta = \mu_{\delta,G} + \mu_{\delta,v} \tag{2.6}$$

The derivation of $\mu_{\alpha*,G}$ and $\mu_{\delta,G}$ is described in Appendices 2.A and 2.B. The velocity of the local standard of rest is assumed to be the galactic rotation velocity, $v_R(R_o)$ for the Sun and $v_R(R)$ for the pulsar. The peculiar velocity of the Sun is [U,V,W], where the components are respectively in the direction from the Sun towards the galactic centre, in the direction of the galactic rotation, and perpendicular to the galactic plane. In galactic coordinates

$$D\,\mu_{l*,G} = U\sin l - [V + v_R(R_o)]\cos l + v_R(R)\cos(\theta + l) \tag{2.7}$$

and

$$D\,\mu_{b,G} = \Big[U\cos l + [V + v_R(R_o)]\sin l - v_R(R)\sin(\theta + l)\Big]\sin b - W\cos b \tag{2.8}$$

The angle $(\theta + l)$ is computed from:

$$\tan(\theta + l) = \frac{R_o \sin l}{R_o \cos l - D\cos b} \tag{2.9}$$

The values for [U,V,W], v_R and R_o that we use are listed in Table 2.3. To compare velocities expressed in km/s with proper motions expressed in mas/yr, we use the conversion

$$v({\rm km/s}) = 4.74\,\mu({\rm mas/yr})\,D({\rm kpc}) \tag{2.10}$$

The pair $\mu_{l*,G}, \mu_{b,G}$, is converted to the pair in equatorial coordinates $\mu_{\alpha*,G}, \mu_{\delta,G}$ with the rotation given by Eqs.2.62,2.63. Note that $\mu_{l*,G}$ and $\mu_{b,G}$ depend on the (unknown) distance.

This is the reason that Table 2.6 gives the observed proper motions, not corrected for galactic rotation and solar motion.

$\mu_{\alpha*,v}$ and $\mu_{\delta,v}$ depend on the peculiar velocity v of the pulsar and on the direction of this velocity.

2.3.1 Best solution and fiducial intervals

In the following sections we will discuss a number of models, and for each model compute a likelihood $L_i(\vec{\sigma})$ for an individual pulsar labelled i, as a function of the parameter vector $\vec{\sigma}$. We then construct the deviance $\mathcal{L}$ with

$$\mathcal{L}(\vec{\sigma}) = -2\sum_{i=1}^{N} \ln L_i(\vec{\sigma}) \tag{2.11}$$

where N is the number of pulsars. $\vec{\sigma}_{\rm opt}$ is the parameter vector for which Eq. 2.11 reaches its minimum. We write differences with the optimal solution as

$$\Delta\mathcal{L}(\vec{\sigma}) \equiv \mathcal{L}(\vec{\sigma}) - \mathcal{L}(\vec{\sigma}_{\rm opt}) \tag{2.12}$$

For appropriate choices of L_i these differences approximate a χ^2 distribution. For a parameter vector consisting of a single parameter, we estimate its 68% range by determining for which values Eq. 2.12 is equal to 1. To determine the range of values if the vector parameter has three parameters, we proceed as follows. We fix the value of one parameter at an offset from the optimal value, and then determine the combination of the two other parameters that gives the lowest value for $\Delta\mathcal{L}(\vec{\sigma})$. We vary the offset until this lowest value is 1. Repeating this for each of the three parameters for positive and negative offsets from the best values gives the ranges listed in Table 2.4.

Note that the best parameter values and the fiducial ranges determined this way do not depend on the normalization of L_i: a constant multiplicative factor x to any L_i leads to a constant additive factor $-2\ln x$ in Eq. 2.11 and drops out in Eq. 2.12.

We will also use the deviance to compare different models, using

$$d\mathcal{L} \equiv \mathcal{L}^a(\vec{\sigma}^a_{\rm opt}) - \mathcal{L}^b(\vec{\sigma}^b_{\rm opt}) \tag{2.13}$$

where indices a and b refer to the different models. The distribution of $d\mathcal{L}$ approximates a χ^2 distribution less well than $\Delta\mathcal{L}$, but we will use this difference as a rough indication of relative merit of models.

2.4 Maxwellian velocity distribution

The maxwellian velocity distribution is characterised by a single parameter σ:

$$f(v,\sigma)dv = \sqrt{\frac{2}{\pi}}\frac{v^2}{\sigma^3}\exp\left[-\frac{v^2}{2\sigma^2}\right]dv; \quad (0 < v < \infty) \tag{2.14}$$

In the isotropic case, the maxwellian may be decomposed in three independent gaussians in any three mutually perpendicular directions. We choose the directions of increasing right ascension,

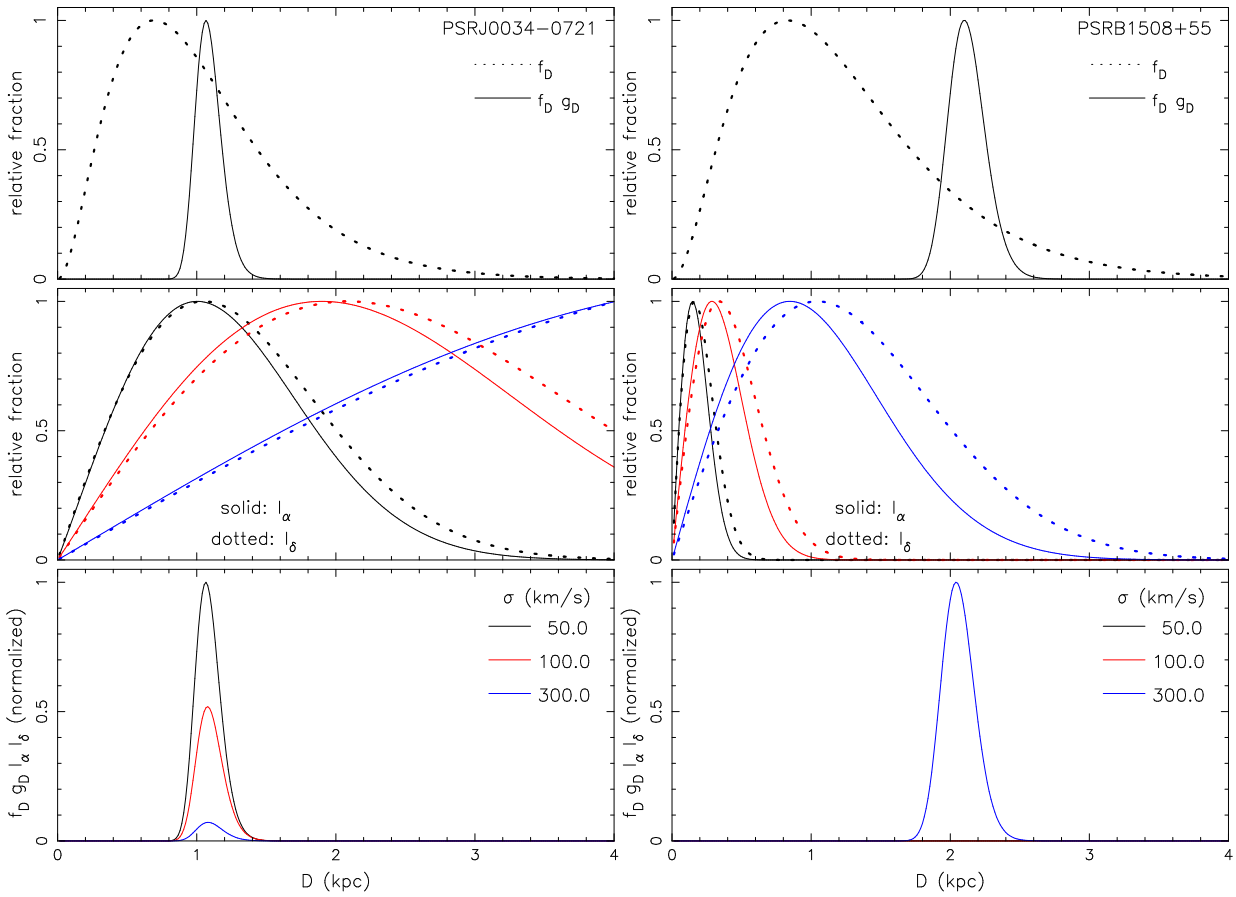

Figure 2.2: Illustration for two pulsars of the contributions to the integrand of the likelihood $L_{\mathrm{maxw}}(\sigma)$ (Eq. 2.19) of the separate factors $f_D(D)g_D(\varpi'|D)$ (top graphs; Eqs. 2.1,2.4), I_α and I_δ (middle graphs). Each curve has been normalized separately to maximum unity. I_α and I_δ are shown for for three values σ of the maxwellian (Eq. 2.14). The lower graphs show the integrand of the likelihood $L_{\mathrm{maxw}}(\sigma)$ for three values of σ, as a function of distance, normalized to the highest maximum of the three. The measurements of PSR J0034−0721 (left) favour a low value of σ. Those of PSR B1508+55 (right) require a high value of σ, and the integrands for $\sigma = 50$ and 100 km/s are indistinguishable from zero in this graph.

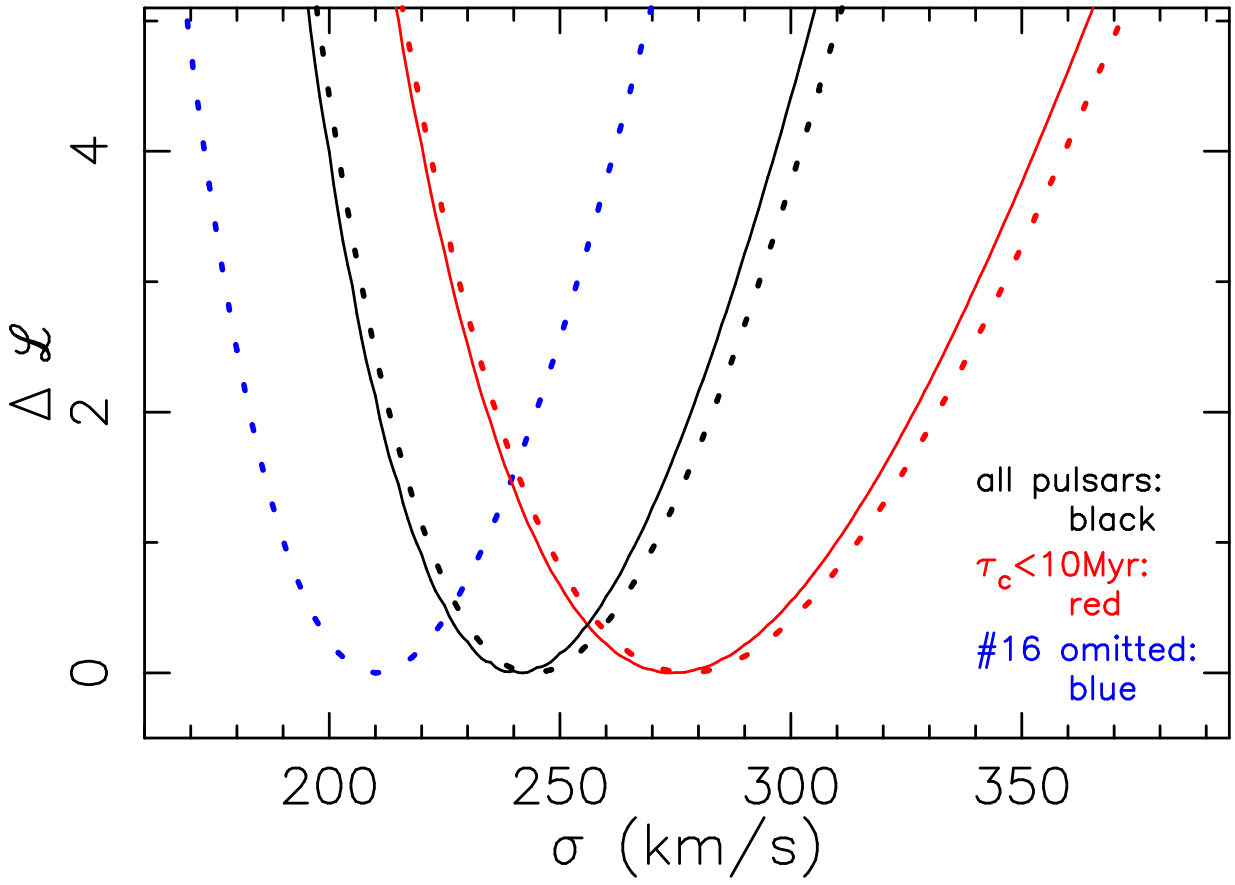

Figure 2.3: Variation of $\mathcal{L}$ with velocity distribution parameter σ for the model with a single isotropic maxwellian (dotted lines), and for the mixed model in which most pulsars have an assumed semi-isotropic velocity distribution (solid lines). The colour coding indicates the pulsar sample: all 28 pulsars in our master list, the 27 pulsars remaining after removing PSR B1508+55, and the 19 youngest ($\tau < 10$ Myr) pulsars.

increasing declination, and the radial direction. This enables us to write the joint probability of measured values ϖ', $\mu'_{\alpha*}$, μ'_δ and actual values D, $v_\alpha = D\mu_{\alpha*,v}$ and $v_\delta = D\mu_{\delta,v}$ as

$$P_{\rm maxw}(\varpi', \mu'_{\alpha*}, \mu'_\delta, D, v_\alpha, v_\delta, v_r) = G(v_\alpha, \sigma)G(v_\delta, \sigma)G(v_r, \sigma)$$

$$\begin{aligned} &\times \quad \frac{f_D(D)}{\int_0^{D_{\rm max}} f_D(D)dD}\,\frac{1}{\sigma_\varpi\sqrt{2\pi}}\exp\left[-\frac{(1/D-\varpi')^2}{2{\sigma_\varpi}^2}\right] \\ &\times \quad \frac{1}{\sigma_\alpha\sqrt{2\pi}}\exp\left[-\frac{(\mu_{\alpha*,G}(D)+v_\alpha/D-\mu'_{\alpha*})^2}{2{\sigma_\alpha}^2}\right] \\ &\times \quad \frac{1}{\sigma_\delta\sqrt{2\pi}}\exp\left[-\frac{(\mu_{\delta,G}(D)+v_\delta/D-\mu'_{\delta})^2}{2{\sigma_\delta}^2}\right] \end{aligned} \tag{2.15}$$

where

$$G(v,\sigma) = \frac{1}{\sigma\sqrt{2\pi}}\exp\left[-\frac{v^2}{2\sigma^2}\right]; \quad (-\infty < v < \infty) \tag{2.16}$$

To obtain the value of σ which gives the most likely correspondence with the measurements, we must take into account contributions to the likelihood of all distances and velocities. We therefore define the likelihood for the maxwellian as

$$L_{\rm maxw}(\sigma) = \int_o^{D_{\rm max}}\int_{-\infty}^{\infty}\int_{-\infty}^{\infty}\int_{-\infty}^{\infty} P_{\rm maxw}dv_\alpha dv_\delta dv_r dD \tag{2.17}$$

The radial velocities occur only in $G(v_r,\sigma)$, and thus the integral over v_r can be computed separately: $\int_{-\infty}^{\infty} G(v_r,\sigma)dv_r = 1$. The integrals over v_α and v_δ are more involved, but can also be solved analytically. Thus, for v_α

$$\int_{-\infty}^{\infty}\exp\left\{-\frac{1}{2}\left[\frac{{v_\alpha}^2}{\sigma^2}+\frac{\left(v_\alpha+D(\mu_{\alpha*,G}-\mu'_{\alpha*})\right)^2}{D^2{\sigma_\alpha}^2}\right]\right\}dv_\alpha =$$

$$\sqrt{2\pi}\left(\frac{1}{\sigma^2}+\frac{1}{D^2{\sigma_\alpha}^2}\right)^{-1/2}\exp\left[-\frac{1}{2}\frac{D^2(\mu_{\alpha*,G}-\mu'_{\alpha*})^2}{\sigma^2+D^2{\sigma_\alpha}^2}\right] \tag{2.18}$$

and analogously for v_δ. Taken together these results lead to

$$L_{\rm maxw}(\sigma) = \mathcal{C}\int_0^{D_{\rm max}} f_D(D)\exp\left[-\frac{(1/D-\varpi')^2}{2{\sigma_\varpi}^2}\right]\mathcal{I}_\alpha\mathcal{I}_\delta dD \tag{2.19}$$

where

$$\begin{aligned} \mathcal{C} &\equiv \left[(2\pi)^{3/2}\sigma_\varpi\sigma_\alpha\sigma_\delta\int_0^{D_{\rm max}} f_D(D)dD\right]^{-1} \\ \mathcal{I}_\alpha &\equiv \left(1+\frac{\sigma^2}{D^2{\sigma_\alpha}^2}\right)^{-1/2}\exp\left[-\frac{1}{2}\frac{(D\,\mu_{\alpha*,G}-D\,\mu'_{\alpha*})^2}{\sigma^2+D^2{\sigma_\alpha}^2}\right] \\ \mathcal{I}_\delta &\equiv \left(1+\frac{\sigma^2}{D^2{\sigma_\delta}^2}\right)^{-1/2}\exp\left[-\frac{1}{2}\frac{(D\,\mu_{\delta,G}-D\,\mu'_{\delta})^2}{\sigma^2+D^2{\sigma_\delta}^2}\right] \end{aligned}$$

The integral over distances in Eq. 2.19 is computed numerically, out to $D_{\max} = 10\,\mathrm{kpc}$. $\mathcal{C}$ ensures that each distribution in Eq. 2.15 is normalized to unity; in the computations $\mathcal{C}$ may be ignored, as it only adds a constant in the deviance (Eq. 2.11) and drops out in Eq. 2.12.

To illustrate the effect of the various factors in the integrand of Eq. 2.19 we show these separately in Fig. 2.2, for two pulsars. For a fixed velocity, the proper motion scales inversely with the distance. The large parallax of PSR 0034−0721, combined with its relatively small proper motion, favours a maxwellian with a small average velocity, but still allows a maxwellian with a high average velocity as this has a finite tail at low velocities. In contrast, the smaller parallax of PSR B1508+55 combined with its large proper motion, demands a maxwellian with a large average velocity, because high velocities have vanishingly low probability in a maxwellian with a low average velocity.

Labelling the likelihoods of Eq. 2.19 for each of N pulsars with i, we compute the deviance $\mathcal{L}$ with Eq. 2.11. $\Delta\mathcal{L}(\sigma)$ (Eq. 2.12) is shown for three pulsar samples in Figure 2.3. The sample of all 28 pulsars in our master list (Table 2.6) leads to $\sigma_{\mathrm{opt}} \simeq 244\,\mathrm{km/s}$, with a range of about 50 km/s found from $\Delta\mathcal{L} = 1$; see Table 2.4. To illustrate the influence of a single pulsar, we also show $\Delta\mathcal{L}(\sigma)$ for the sample of 27 pulsars remaining after removing PSR B1508+55, the pulsar with the worst likelihood for $\sigma = 245\,\mathrm{km/s}$. This sample has $\sigma_{\mathrm{opt}} \simeq 210\,\mathrm{km/s}$. The reason for this shift is evident from Fig. 2.2: the measurements of PSR B1508+55 require a large value of σ. Removing any one of the 27 other pulsars from the full sample leads to a much smaller shift.

The pulsar velocities of young pulsars, less affected by acceleration in the galactic gravitational field, are more indicative of the pulsar velocities at birth, and therefore we also investigate the sample of the 19 youngest pulsars with characteristic age $\tau_c < 10\,\mathrm{Myr}$. This leads to a higher optimal distribution parameter $\sigma_{\mathrm{opt}} \simeq 280\,\mathrm{km/s}$. The smaller number of pulsars also leads to a wider range of σ for which $\Delta\mathcal{L}(\sigma) < 1$. An upper limit to τ_c of 5 Myr leads to the same σ_{opt} as for 10 Myr, but further widens the uncertainty range. Removing PSR B1508+55 from the sample of young pulsars reduces the optimal distribution sample to $\sigma_{\mathrm{opt}} \simeq 235\,\mathrm{km/s}$.

Figures 2.1 and 2.2 indicate that a single maxwellian is not a good description of the velocity distribution of young radio pulsars. We are therefore not unduly worried about the shifts in σ_{opt} between the different samples, but move on to investigate more promising models.

2.5 Sum of two maxwellians

We investigate a velocity distribution which is the sum of two maxwellians, one to explain the lower observed velocities, and one for the higher velocities. Defining the vector of parameters $\vec{\sigma} = [\sigma_1, \sigma_2, w]$ we write

$$f_v(v, \vec{\sigma})dv = \sqrt{\frac{2}{\pi}} v^2 \left[\frac{w}{\sigma_1^3} \exp\left(-\frac{1}{2}\frac{v^2}{\sigma_1^2}\right) + \frac{(1-w)}{\sigma_2^3} \exp\left(-\frac{1}{2}\frac{v^2}{\sigma_2^2}\right) \right] dv \tag{2.20}$$

The likelihood for the sum of two maxwellians is the sum of the likelihoods of the two maxwellians: in analogy with Eq. 2.19 we have

$$L_{2\mathrm{maxw}}(\vec{\sigma}) = wL_{\mathrm{maxw}}(\sigma_1) + (1-w)L_{\mathrm{maxw}}(\sigma_2) \tag{2.21}$$

We compute $L_{\rm maxw}(\sigma)$ on a grid of values of σ, in steps of 1 km/s, and use the subroutine `AMOEBA` of Press et al. (1986) , which implements the downhill simplex method of Nelder and Mead, to obtain the optimal values of w, σ_1 and σ_2 for which $\mathcal{L}$, computed from Eq. 2.21 with Eq. 2.11, has its minimum. The results are listed in Table 2.4, and illustated in Figs. 2.4.

To decide on the significance of the second maxwellian, we note that it adds two parameters to the model with one maxwellian, and compute the deviance difference $d\mathcal{L}$ with Eq. 2.13. We first investigate the sample of all 28 pulsars in our master list (sample A). For this sample, $d\mathcal{L} = -14$, indicating that the addition of a second maxwellian is very significant ($\Delta\chi^2 = -14$ corresponds to a 99.8% confidence level for 2 added parameters). The low-velocity component represents between 29% and 54% of the pulsar population. Fig. 2.4 shows that the values of σ_1 and σ_2 are mildly correlated with w: a larger (smaller) fraction of the low-velocity component leads to larger (smaller) values of σ_1 and σ_2. The shift, however, lies well within the error range of σ_1 and σ_2; the main effect of the correlation between σ_1 and σ_2 is to mitigate the drop of pulsar numbers with velocities between σ_1 and σ_2.

The sample of 19 pulsars in our list with characteristic age $\tau_c < 10\,$Myr (sample Y) leads to the same result, but with somewhat lager error margins for the parameters $\vec{\sigma}$. For these young pulsars, the evidence for a second maxwellian is still significant ($\Delta\chi^2 = -6$ is 95% confidence).

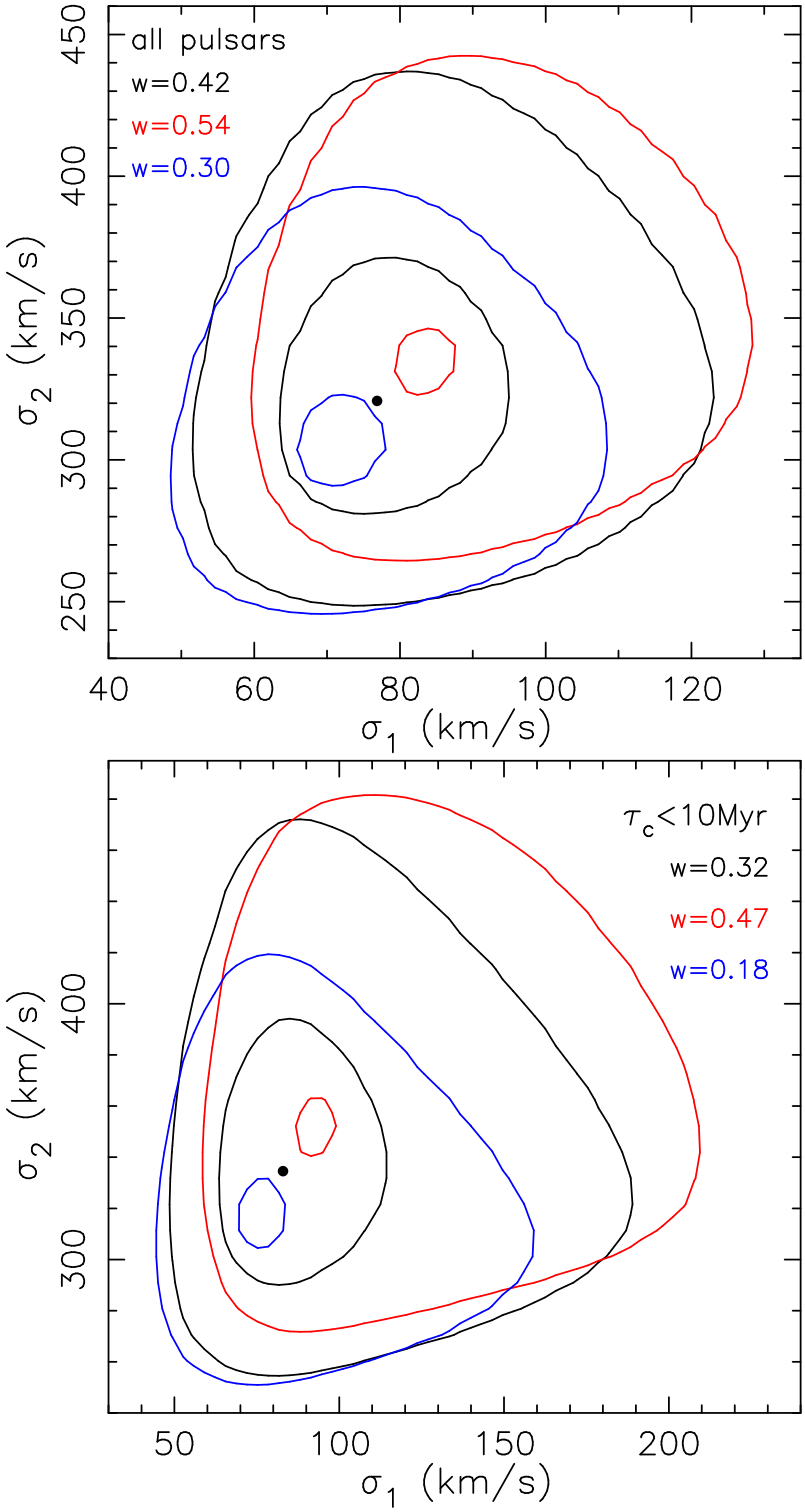

Figure 2.4: Contours of $\mathcal{L}(\vec{\sigma})$ in three σ_1, σ_2 planes with fixed w, for the model with two isotropic maxwellians. Contours of constant $\Delta\mathcal{L}(\vec{\sigma})$ (Eq. 2.12) are shown for values 1 and 4, in each plane, The best solution is indicated with •. Top: all pulsars. $\vec{\sigma}_{\rm opt}$ =(77km/s, 321km/s, 0.42). Below: pulsars with $\tau_c < 10\,$Myr. $\vec{\sigma}_{\rm opt}$ =(83km/s, 335km/s, 0.32).

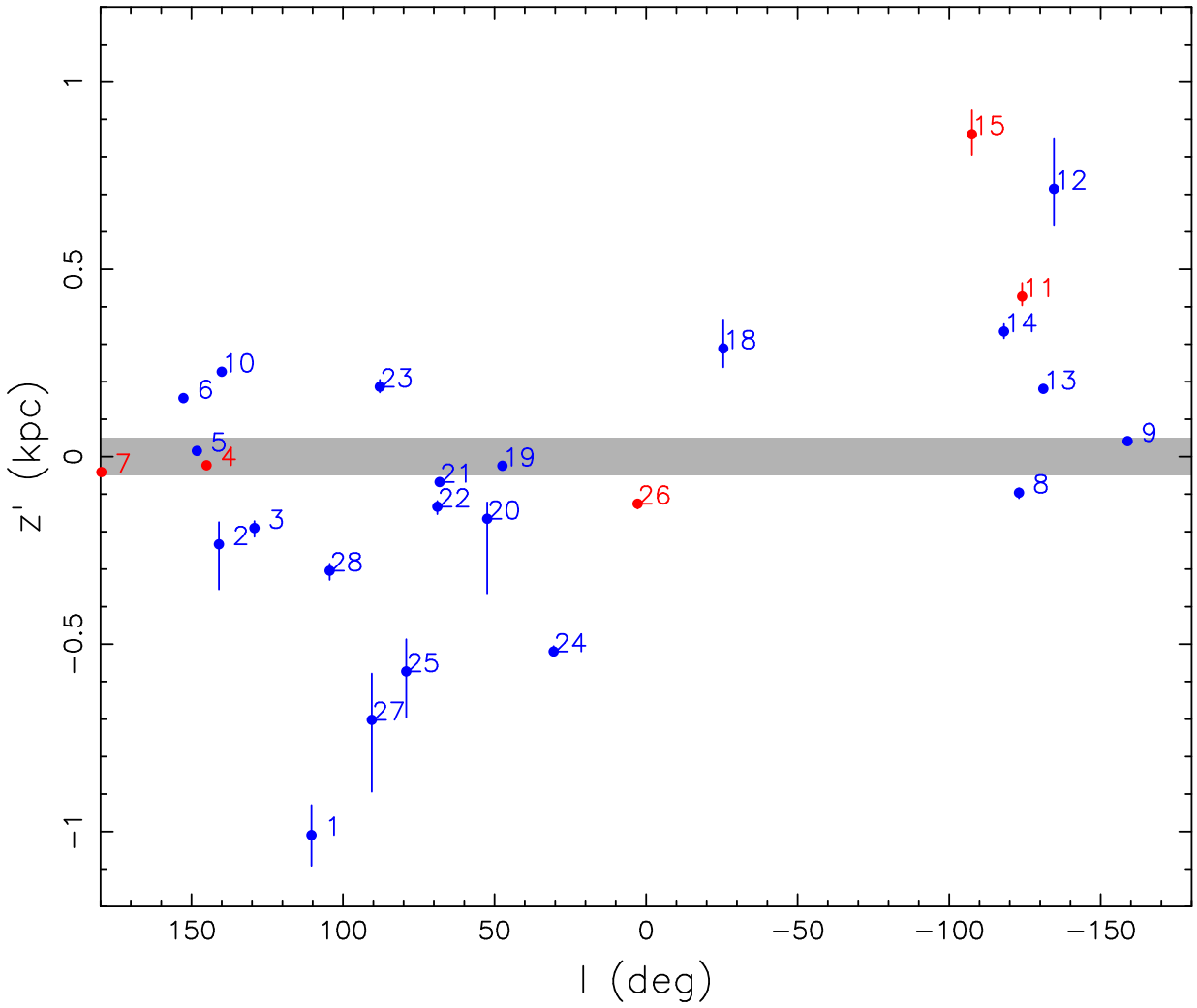

Figure 2.5: Nominal distance from the Galactic plane $z' = \sin b/\varpi'$, range $\sin b/(\varpi' \pm \sigma_\varpi)$, as a function of longitude. The blue points indicate pulsars nominally moving away from the plane, i.e. z' and $v'_z = \mu'_b \cos b/\varpi'$ have the same sign; the red points are pulsars nominally moving towards the plane. The grey band indicates the scale height of 50 pc of O-stars. The numbers refer to the sequence number in Table 2.6. Numbers 16 at $z' = 1.6$ kpc and 17 at 5.5 kpc, respectively, are outside the frame, and both are moving away from the galactic plane.

2.6 Semi-isotropic maxwellian velocity distribution

The isotropic maxwellian velocity distribution has a major advantage in enabling us to compute three out of four integrals in Eq. 2.17 analytically. However, once the pulsar has moved away from the galactic plane, we have more information, that we will put to use in this Section: the pulsar velocity must be directed away from its place of birth, which for sufficiently large $|z|$ implies that $v_z > 0$ when $z > 0$ and $v_z < 0$ when $z < 0$. For these pulsars we assume an intrinsic distribution for the velocity which is an isotropic distribrution from which the velocities towards the galactic plane have been removed: and refer to this distribution as semi-isotropic.

To quantify 'sufficiently large' we show the nominal values of distance to the galactic plane $z' = D' \sin b$ in Fig. 2.5, together with a band indicating the scale height of O stars, as a proxy for the place of birth of pulsars. Five pulsars in our list of 28 are moving towards the galactic plane. Two of these, PSR B0329+54 (#4 in our master list) and PSR J0538+2817 (#7) are within the region where pulsars are born, and thus may well be moving towards the plane. PSR J2144−3933 (#26) is the oldest pulsar in our sample, and may well be a returning pulsar. PSR B0818−13 (#11) and PSR B1237+25 (#15) are too young – assuming their characteristic age is indicative of their real age – to have reversed motion, and their motion towards the galactic plane must be apparent. We may write v_z as (see Fig. 2.10)

$$v_z = D\mu_b \cos b + v_r \sin b \tag{2.22}$$

hence a pulsar is moving away from the plane if

$$z v_z > 0 \,\text{if}\, v_r > \frac{-\mu_b \cos b}{\varpi \sin b} \tag{2.23}$$

Entering the nominal values ϖ' and μ'_b, we obtain $v_r > 120$ km/s (#11) and $v_r > 12\,\text{km/s}$ (#15), indicating that these pulsars may well be moving as expected: away from the plane.

In computing for the case of semi-isotropic maxwellians, we choose axes parallel to the (local) direction of right ascension and declination, and along the line of sight, and write the spatial velocity as

$$\vec{v} = (v_\alpha, v_\delta, v_r) = (v \sin\xi_1 \cos\xi_2, v \sin\xi_1 \sin\xi_2, v \cos\xi_1) \tag{2.24}$$

where

$$0 \le \xi_1 \le \pi; \qquad 0 \le \xi_2 \le 2\pi$$

To determine which velocities lead to v_z away from the galactic plane, we first convert the velocities to galactic coordinates using Eqs. 2.44, 2.45:

$$(v_l, v_b, v_r) = (v \sin\xi_1 \cos(\xi_2 - \phi), v \sin\xi_1 \sin(\xi_2 - \phi), v \cos\xi_1) \tag{2.25}$$

where ϕ is given by Eq. 2.46. Entering v_b and v_r from Eq. 2.25 into Eq. 2.22 we obtain

$$v_z = v[\sin\xi_1 \sin(\xi_2 - \phi) \cos b + \cos\xi_1 \sin b] \tag{2.26}$$

Note that the sign of v_z *does not depend on the speed* v. The condition $v_z > 0$ if $b > 0$ and $v_z < 0$ if $b < 0$ may be written

$$\sin(\xi_2 - \phi) > \frac{-\tan b}{\tan\xi_1} \tag{2.27}$$

We rewrite the joint probability of Eq. 2.15 for the semi-isotropic case as

$$P_{\rm sim}(\varpi', \mu'_{\alpha*}, \mu'_\delta, D, v, \xi_1, \xi_2) = 0 \qquad \text{if} \quad zv_z < 0$$

$$\begin{aligned} P_{\rm sim}(\varpi', \mu'_{\alpha*}, \mu'_\delta, D, v, \xi_1, \xi_2) = \mathcal{C} \exp\left[-\frac{(1/D - \varpi')^2}{2{\sigma_\varpi}^2}\right] \\ \times \quad \exp\left[-\frac{(\mu_{\alpha*,G}(D) + v\sin\xi_1\cos\xi_2/D - \mu'_{\alpha*})^2}{2{\sigma_\alpha}^2}\right] \\ \times \quad \exp\left[-\frac{(\mu_{\delta,G}(D) + v\sin\xi_1\sin\xi_2/D - \mu'_\delta)^2}{2{\sigma_\delta}^2}\right] \\ \times \quad f_D(D)\sin\xi_1\, 2\sqrt{\frac{2}{\pi}}\frac{v^2}{\sigma^3}\exp\left[-\frac{v^2}{2\sigma^2}\right] \quad \text{if} \quad zv_z > 0 \end{aligned} \tag{2.28}$$

where $\mathcal{C}$ is defined with Eq. 2.19, and a factor 2 is added to normalize the semi-maxwellian. The likelihood for the semi-isotropic maxwellian follows:

$$L_{\rm sim}(\sigma) = \int_o^{D_{\rm max}} \int_0^{2\pi} \int_0^{\pi} \int_0^{\infty} P_{\rm sim} dv d\xi_1 d\xi_2 dD \tag{2.29}$$

Eq. 2.26 shows that the condition that v_z is in the correct direction is determined by the angles ξ_1 and ξ_2 and does not depend on v, and this allows the integral in Eq. 2.29 over the velocity to be done analytically. The integrals over the angles and distance are done numerically. Details are given in Appendix 2.C.

Table 2.4: Results of the model calculations for all 28 pulsars in our master list (A), and for the 19 youngest pulsars ($\tau_c < 10\,\mathrm{Myr}$, Y).

	sample	single maxwellian			two maxwellians					v_l Gaussian	
	N	σ (km/s)	range	$d\mathcal{L}$	σ_1 (km/s)	range	σ_2 (km/s)	range	w (%)	range	$d\mathcal{L}$	σ (km/s)	range
isotropic models	A 28	244	221-271	$\equiv 0$	77	62-97	321	278-375	42	29-54	-14	240	209-279
mixed models	A 22+6	239	219-267	-18	75	61-95	316	276-369	42	30-55	-33		
isotropic models	Y 19	277	247-314	$\equiv 0$	83	62-117	335	287-398	32	17-47	-6	263	223-314
mixed models	Y 14+5	273	245-310	-16	82	61-115	328	285-391	32	17-48	-22		

Notes: For the mixed models we give separately the number of pulsars from a semi-isotropic and an isotropic distribution (see Table 2.6). For each model we give the best parameters and their approximate 68% range determined by setting Eq. 2.12 to unity. Within each sample we also give the differences in deviance $d\mathcal{L}$ (Eq. 2.13) between each model and the model with a single isotropic maxwellian, which gives an indication of their relative merits.

2.7 The mixed model

In our mixed model we assume that the pulsars in the grey band in Fig.2.5 (#4,5,7,9,19) and the oldest pulsar (#26) are drawn from an isotropic velocity distribution, whereas all others are drawn from a semi-isotropic distribution, in which the velocities towards the galactic plane are excluded. The distribution parameter σ for the semi-isotropic distribution is equal to the σ for the isotropic distribution. In analogy with Eqs. 2.11 we define the deviance for the mixed model as

$$\mathcal{L}_{\rm mixed}(\sigma) = -2\left(\sum_i \ln L_{{\rm sim},i}(\sigma) + \sum_j \ln L_{{\rm maxw},j}(\sigma)\right) \tag{2.30}$$

where the sums over i and over j are for the pulsars whose velocity is drawn from a semi-isotropic distribution and an isotropic distribution, respectively. The best value for σ is the value for which Eq. 2.30 reaches its minimum, and its range is determined from $\Delta\mathcal{L} = 1$. The results are given in Table 2.4 and Fig. 2.3, and are not very different from those for the single isotropic maxwellian, both for sample A of all pulsars, and for sample Y for the youngest pulsars. For the $d\mathcal{L}$ value it is seen that the mixed model is a significant improvement on the isotropic model. We return to this below, for the more interesting case of two maxwellians.

In a more realistic model the semi-isotropic distribution is composed of two semi-maxwellians, with the same distribution parameters $\vec{\sigma}$ as the two isotropic maxwellians that compose the isotropic distribution.

In analogy with Eqs. 2.21 we now have

$$L_{\rm 2sim}(\vec{\sigma}) = wL_{\rm sim}(\sigma_1) + (1-w)L_{\rm sim}(\sigma_2) \tag{2.31}$$

and in analogy with Eqs. 2.30

$$\mathcal{L}_{\rm 2mixed}(\vec{\sigma}) = -2\left(\sum_i \ln L_{{\rm 2sim},i}(\vec{\sigma}) + \sum_j \ln L_{{\rm 2maxw},j}(\vec{\sigma})\right) \tag{2.32}$$

where the sums over i and over j are for the pulsars whose velocity is drawn from a semi-isotropic distribution and an isotropic distribution, respectively. We use the subroutine `AMOEBA` of Press et al. (1986) to obtain the optimal values of w, σ_1 and σ_2 for which $\mathcal{L}_{\rm 2mixed}$ has its minimum, and $\Delta\mathcal{L} = 1$ for the range of these parameters. The results are given in Table 2.4 and Fig. 2.6.

The best values and the ranges for σ_1, σ_2 and w for the semi-isotropic model are not significantly different from those of the isotropic model. Contour plots in the σ_1-σ_2 planes also are not significantly different from those for the model with two isotropic maxwellians shown in Figs. 2.4.

The factor 2 in (the last line of) Eq. 2.28 ensures that the semi-maxwellian is normalized to unity. As remarked above, a constant multiplicative factor for any likelihood drops out in Eqs. 2.12, and thus does not affect the best solution and its range(s) within one model. However, to compare between models one must use the same normalizations of the separate distributions between the different models, and this requires the factor 2 in Eq. 2.28. The $d\mathcal{L}$ values listed in Table 2.4 show that the mixed model is a highly significant improvement above the isotropic maxwellian model, for the full sample A, and that it is still significant for sample Y of young pulsars.

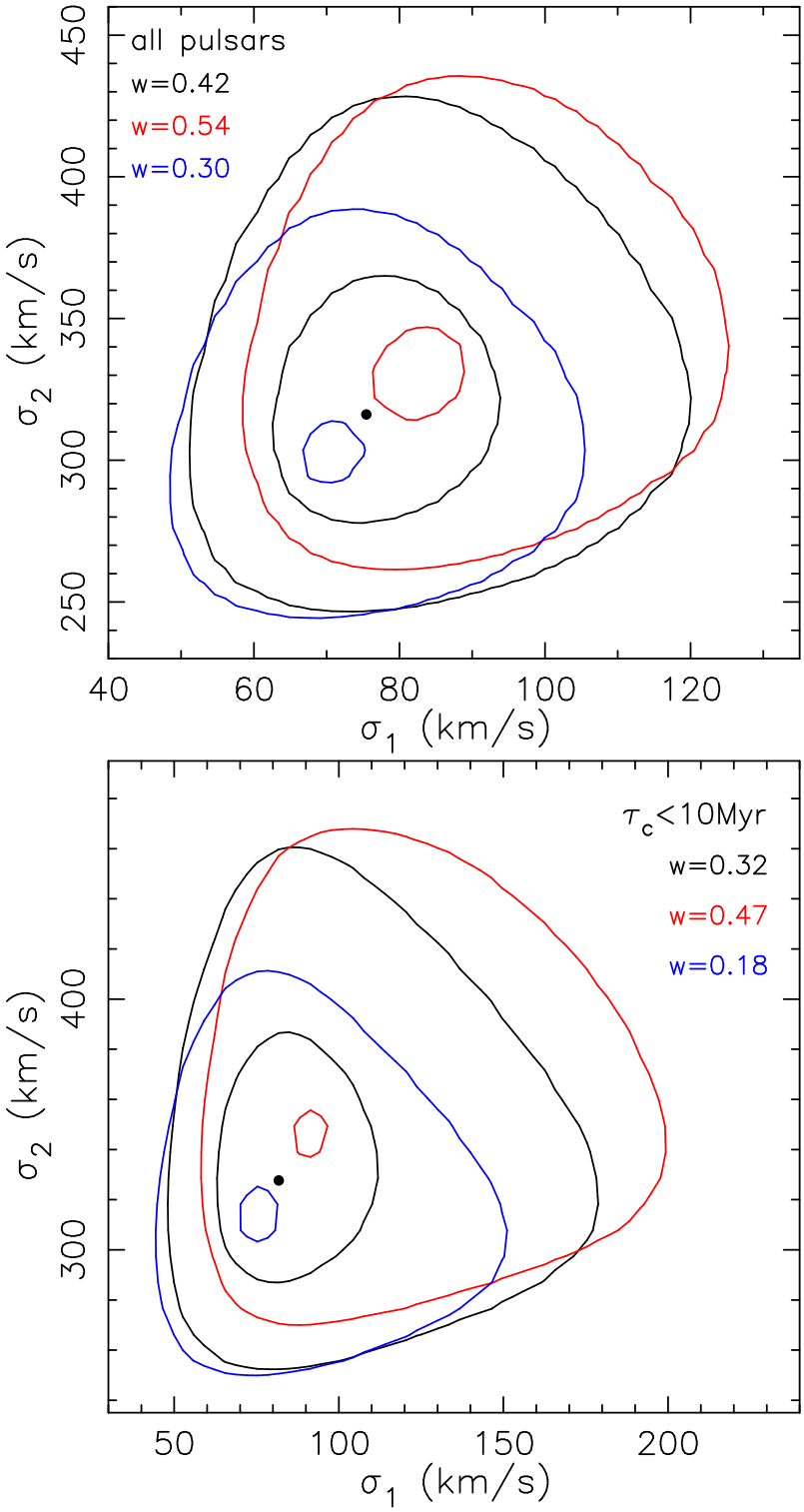

Figure 2.6: As Figs. 2.4, now for the mixed model. $\vec{\sigma}_{\rm opt}$ for all pulsars and for the youngest pulsars are listed in Table 2.4.

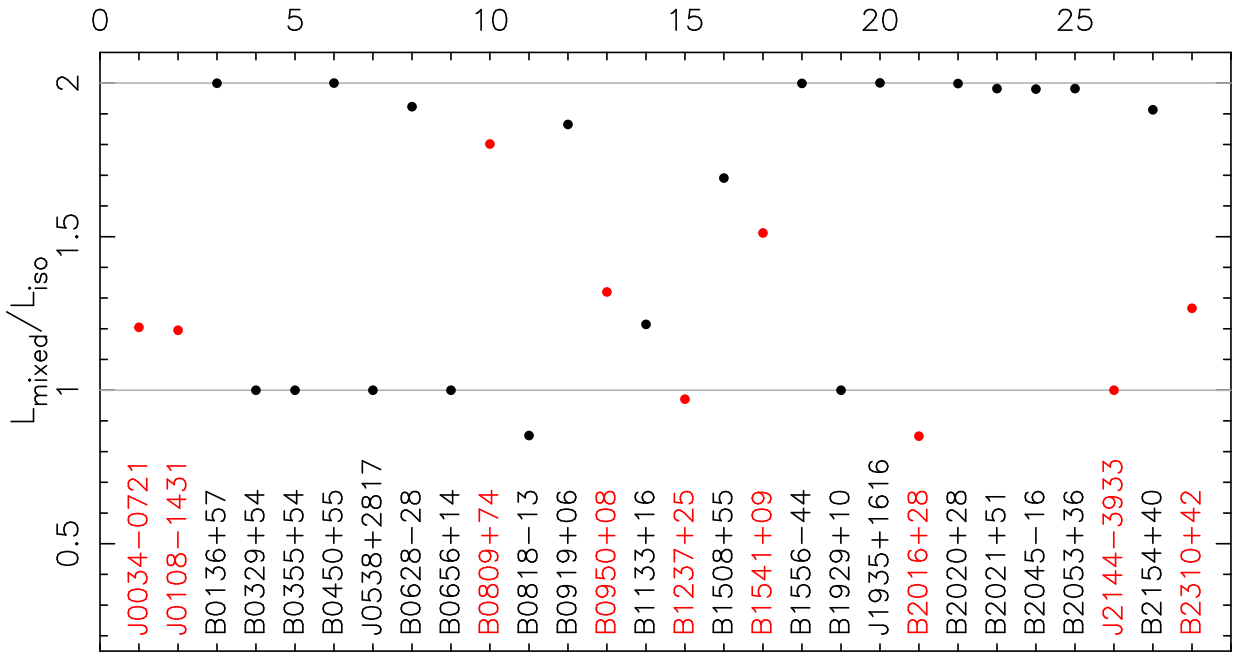

FIGURE 2.7: For each pulsar the ratio of the likelihoods in the mixed and isotropic models is shown. The red colour indicates old pulsars, with $\tau_c > 10\,\mathrm{Myr}$. To illustrate the pure effect of the normalization of the velocity distribution, we use the same parameters $\vec{\sigma}$ =(76km/s, 318km/s, 0.32) for both likelihoods. Use of $\vec{\sigma}_{\mathrm{opt}}$ for each model separately gives rise to small shifts.

It is interesting to look at this is some more detail. Suppose for the moment that the contributions to the integral of Eq. 2.17 are zero for v_z velocities towards the plane, then the only difference between $L_{2\mathrm{maxw}}(\vec{\sigma})$ and $L_{2\mathrm{mixed}}(\vec{\sigma})$ is the multiplicative factor 2 in Eq. 2.28. In sample A for all pulsars, this affects only the 22 pulsars for which a semi-maxwellian applies, and leads to an added term in Eq. 2.32 equal to $-2 \times 22 \times \ln 2 \simeq -30.5$. In sample Y 14 of the young pulsars are affected, leading to an added term $-2 \times 14 \times \ln 2 \simeq -19.4$. The actual differences $d\mathcal{L}$ in deviance between the mixed models and purely isotropic models are smaller than this, which indicates that v_z velocities towards the plane *do* contribute to the integral of Eq. 2.17, also for pulsars for which such velocities are not expected. This implies that the isotropic model overestimates the likelihoods for these pulsars. PSR B0818−13 (#11) is a case in point: its apparent v'_z velocity is towards the plane (Fig. 2.5), and thus v_z velocities towards the plane may be expected to contribute noticeably to integral Eq. 2.17.

In Fig. 2.7 we show the ratio of the likelihoods for the mixed and isotropic two-maxwellian model for each pulsar separately. The six pulsars whose velocities are drawn from an isotropic velocity distribution also in the mixed model by definition have a ratio of one of the likelihoods for the mixed and isotropic two-maxwellian model. The eleven pulsars with ratios closest to the maximum possible, $1.8 < L_{\mathrm{mixed}}/L_{\mathrm{iso}} < 2$ say, are all young. For these pulsars, almost all velocities contributing to L_i in the isotropic model contribute also in the mixed model. For 11 pulsars (sample A) or 3 pulsars (sample Y) the velocity range that contributes to L_i is restricted by the condition that v_z be away from the galactic plane, as shown by the difference of their $L_{\mathrm{mixed}}/L_{\mathrm{iso}}$ from the normalization factor 2.

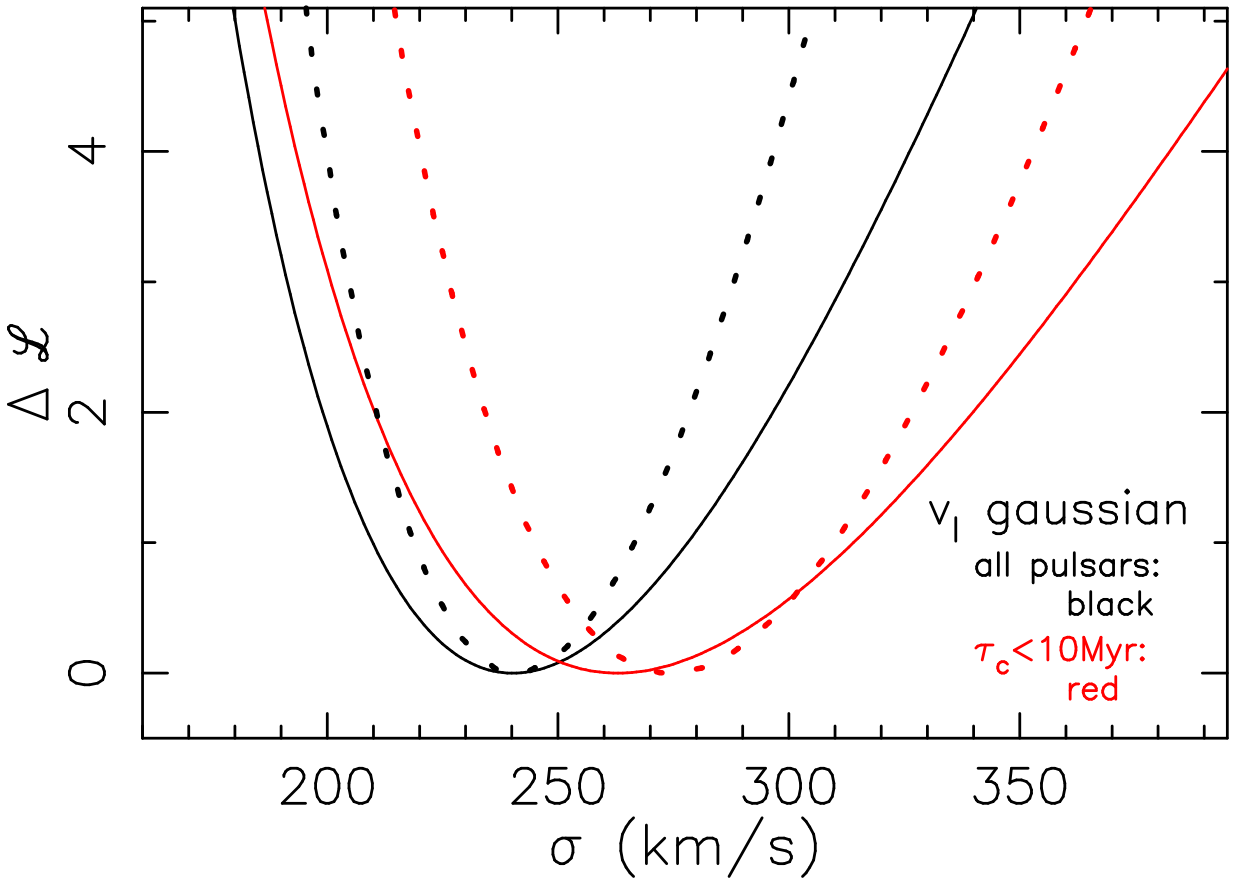

Figure 2.8: Variation of $\mathcal{L}$ with σ when only measurements of the parallax ϖ' and of the proper motion μ'_{l*} in the direction of galactic longitude are used (solid lines). For comparison the results for the mixed model, that uses parallaxes and both proper motions $\mu_{\alpha*}, \mu_\delta$ are also shown (dotted lines).

2.8 The distribution of longitudinal velocities

For comparison with earlier studies we also determine the model parameter σ by only using the measurements of the parallax and the measurements μ'_{l*} of the proper motion in the direction of galactic longitude. For this we choose the coordinates in the directions of galactic longitude and latitude, and radial. We rewrite Eqs. 2.15 and 2.17 as

$$\begin{aligned} P_{\rm gauss}(\varpi', \mu'_{l*}, D, v_l, v_b, v_r) = \mathcal{C}_l f_D(D) G(v_l, \sigma) G(v_b, \sigma) G(v_r, \sigma) \\ \times \quad \exp\left[-\frac{(1/D - \varpi')^2}{2{\sigma_\varpi}^2}\right] \\ \times \quad \exp\left[-\frac{(\mu_{l*,G}(D) + v_l/D - \mu'_{l*})^2}{2{\sigma_l}^2}\right] \end{aligned} \tag{2.33}$$

where

$$\mathcal{C}_l \equiv \left[2\pi\sigma_\varpi\sigma_l \int_0^{D_{\rm max}} f_D(D) dD\right]^{-1}$$

Table 2.5: Comparison of the results of our best model with those obtained in some earlier studies

	single maxwellian		two maxwellians					
	σ	range	σ_1	range	σ_2	range	w	range
reference	(km/s)		(km/s)		(km/s)		(%)	
Arzoumanian et al. (2002)[a]	290	260-320	90	75-110	500	350-750	40	20-60
Brisken et al. (2003a)			99		294		20	
Hobbs et al. (2005)	265	239- 291						
Faucher-Giguère & Kaspi (2006)	290	260-320	160	130-180	780	640-930	90	87-100
mixed model sample A	239	219-267	75	60-95	316	276-368	42	30-52

Notes: [a]Arzoumanian et al. (2002) fit gaussians; comparison of their Eq. 1 with our Eq. 2.20 shows that these are components of maxwellians. Thus, their σ values may be compared directly with those in the other papers, contrary to the statement by Brisken et al. (2003a, below their Eq. 3).

and

$$L_{\rm gauss}(\sigma) = \int_o^{D_{\rm max}} \int_{-\infty}^{\infty} \int_{-\infty}^{\infty} \int_{-\infty}^{\infty} P_{\rm gauss} dv_l dv_b dv_r dD \tag{2.34}$$

μ_{l*} and its error σ_μ are obtained from $\mu_{\alpha*}$, μ_δ and their errors with Eq. 2.44. The integrals over v_b and v_r are decoupled from the other integrals, and equal to 1. Eq. 2.34 is rewritten:

$$L_{\rm gauss}(\sigma) = \mathcal{C}_l \int_o^{D_{\rm max}} f_D(D) \exp\left[-\frac{(1/D - \varpi')^2}{2{\sigma_\varpi}^2}\right] \mathcal{I}_l \, dD \tag{2.35}$$

where

$$\mathcal{I}_l \equiv \left(1 + \frac{\sigma^2}{D^2 {\sigma_l}^2}\right)^{-1/2} \exp\left[-\frac{1}{2}\frac{(D\,\mu_{l*,G} - D\,\mu'_{l*})^2}{\sigma^2 + D^2{\sigma_l}^2}\right]$$

Note that in this case, there is no difference between the isotropic and mixed model, because v_z does not affect v_l. We compute the deviance (Eq. 2.11) with Eq. 2.35 , to determine the values $\sigma_{\rm opt}$ for which the deviance reaches its minimum, and their range from $\Delta\mathcal{L} = 1$. The results are listed in Table 2.4 and shown in Fig. 2.8. Interestingly, PSR B1508+55 is not an outlier in v_l: its proper motion is almost completely in the direction of galactic latitude (see Fig. 2.1). For sample A (all pulsars), $\sigma_{\rm opt}$ is the same as for the isotropic or semi-isotropic single maxwellian; for sample Y (youngest pulsars) it is marginally lower. The limitation to only one component of the proper motion leads to a reduced accuracy of $\sigma_{\rm opt}$, as expected. As a consequence the superposition of two gaussians (i.e. components of two maxwellians in the direction of galactic longitude) does not improve significantly over the single maxwellian description ($\vec{\sigma} = 109\,\mathrm{km/s}, 277\,\mathrm{km/s}, 0.27$, $d\mathcal{L} = 1$).

2.9 Conclusions and discussion

Previous work derived the velocity distribution of pulsars from the observed distances and proper motions, and then compared this distribution with model distributions. This reduces the information present in the observations, complicates error propagation, and has lead to wrong likelihood

definitions. The uncertainties in the proper motions determined from timing are two to three orders of magnitude larger than those of the proper motions in our master list, that are determined from VLBI. The larger number of such proper motions (less than one order of magnitude) does not make up for their larger uncertainties, so that inclusion of these proper motions does not significantly improve the analysis. The use of distances determined from dispersion measures further complicates the analysis, because the related distance uncertainties are dominated by systematic effects, and cannot be described with a gaussian, even in approximation.

Our approach is more reliable because we a) derive predictions for the observed parameters (parallax and proper motion) from the model, and compare these directly with the relevant measurements, b) only use VLBI determinations from after 2000 of both parallax and proper motion, whose uncertainties are well described with gaussians, and c) include the intrinsic galactic distribution of pulsars (as expressed in $f_D(D)$, Eq. 2.4). Our mixed model furthermore takes into account that velocity component v_z perpendicular to the galactic plane of a young pulsar well away from that plane must be in the direction away from the plane.

Applying this to the pulsars in our master list, we find that the description of the velocity distribution of the pulsars with two maxwellians improves significantly on the description with a single maxwellian. Our model describing v_l with a single gaussian gives a similar value for σ as the (mixed or isotropic) single maxwellian, as expected for an isotropic velocity distribution. Comparison with earlier results, compiled in Table 2.5, shows that our more accurate method leads to more accurately determined model parameters. We show in Fig. 2.1 that our best solution corresponds well with the observed distribution of $v_\perp$. One would be tempted to conclude that our whole analysis apparatus can be replaced with a straightforward fit of the cumulative $v_\perp$ according to the model to the observed cumulative data for $v'_\perp$! The reasons for the succes of the simpler method are the relatively small errors in the parallax, which limit the importance of $f_D(D)$, and the smallness of the correction for galactic rotation with respect to the observed proper motions: $\mu_{\alpha*,G} \ll \mu'_{\alpha*}$ and $\mu_{\delta,G} \ll \mu'_\delta$ (Fig. 2.1). Indeed, ignoring the corrections for galactic rotation hardly affects the results (Verbunt & Cator 2017). Corrections for galactic motion matter only for distances much larger than those of the pulsars in our master list.

With the exception of Brisken et al. (2003a), who do not give error estimates, all previous authors find significantly higher velocities for the high-velocity component than we do. The compilation in Table 2.5 illustrates that the fraction of pulsars in the high-velocity component (i.e. $1 - w$) is inversely related to the characteristic velocity of that component. A small number of erroneously very high velocities leads to a high value of σ_2. Because the combination of $\sigma_2 > 500\,\mathrm{km/s}$ with a low value of w, i.e. high $1 - w$, would lead to a much higher fraction of pulsars with $v_\perp > 370\,\mathrm{km/s}$, say, than observed, the high value of σ_2 forces a high value of w. We suggest that the higher velocities derived by previous authors are affected by the inclusion of unreliable distances determined from dispersion measures. In the case of Arzoumanian et al. (2002) we note that all parallaxes are from before 2000, i.e. not corrected for differential ionospheric refraction. As Hartman (1997) has shown, underestimating velocity errors leads to overestimating velocities.

The analysis by Hobbs et al. (2005) is based on the nominal velocities $v'_\perp = \mu'_\perp/\varpi'$, and does not take into account the large errors in both distances and proper motions of their sample.

These errors blur the intrinsic distribution. We suggest that this prevents Hobbs et al. from recognising the presence of low velocities, and from recovering a bimodal velocity distribution in their analysis. The best model with two velocity components by Faucher-Giguère & Kaspi (2006) allows $w = 1$, i.e. the second component is not significant. Our analysis in Sect. 2.8 suggests that this is due to their small sample size (34 pulsars, of which only 8 have a measured parallax).

Our results imply that the velocity contrast between the low- and high-velocity components is a factor 3 to 6, and that 30 to 50% of the pulsars arise from the low-velocity component. It has been suggested (Podsiadlowksi et al. 2004) that pulsars formed from small iron cores or via electron capture would have a lower kick velocity than those formed from higher-mass core collapse, which may lead to a bimodal velocity distribution of pulsars. The existence of a class of neutron stars with low birth velocity has been derived from the properties of Be X-ray binaries (Pfahl et al. 2002) and the properties of millisecond pulsars binaries (Van den Heuvel 2004).

The fact that some pulsars are born in binaries and others from single stars will also affect the velocity distribution of single pulsars. Whether the observed bimodal velocity distribution reflects these different origins can be investigated in a population synthesis.

One of the goals of our work was to determine the fraction of pulsars with velocities small enough to remain bound to a globular cluster, or in a binary. In Fig. 2.9 we show the fraction of pulsars with velocity less than v as a function of v. For a typical escape velocity of a globular cluster, 60 km/s say, it is seen that this fraction is about 5% in our best model (mixed, for sample A). It varies from about 3% to about 7.5% in the range of σ_1. At these low velocities, the fraction of pulsars is dominated completely by the low-velocity component, and therefore varies linearly with w for fixed σ_1 and σ_2.

Finally, we mention two reasons why the determination of pulsar velocities from a local sample may lead to an underestimate of the average velocity. The first one is galactic drift: motion in the galactic gravitational potential leads to reduction of the velocity of a pulsar that moves away from the center of the galaxy, and an increase if it moves towards the center. Thus if pulsars with an origin closer to the galactic center contribute more to the locally observed sample than pulsars with an origin further out, the locally measured velocity distribution underestimates the distribution at birth (Hansen & Phinney 1997). The second reason is related to the velocity perpendicular to the plane: pulsars with a high $|v_z|$ move further from the plane, and thus must have a higher luminosity to be detected. In a flux-limited sample this leads to an over-representation of the low-velocity pulsars. These effects can be studied best in a population synthesis that takes these and other selection effects into account. Since such a synthesis involves also a larger number of parameters, a first step would be the measurement of more pulsar distances and proper motions.

2.A Transformations of equatorial to galactic coordinates

For the convenience of the reader we summarise the equations for coordinate transformations that we use. Lane (1979) gives (two of the three) equations for conversion from galactic to equatorial for B1950.0. He notes that the equatorial coordinates of the galactic pole $\alpha_{\rm GP}$, $\delta_{\rm GP}$ and the galactic longitude l_Ω of the node where the galactic plane ($b = 0$) crosses the equator, define the coordinate transformation and thus also the equatorial coordinates of the centre $l = b = 0$. Note

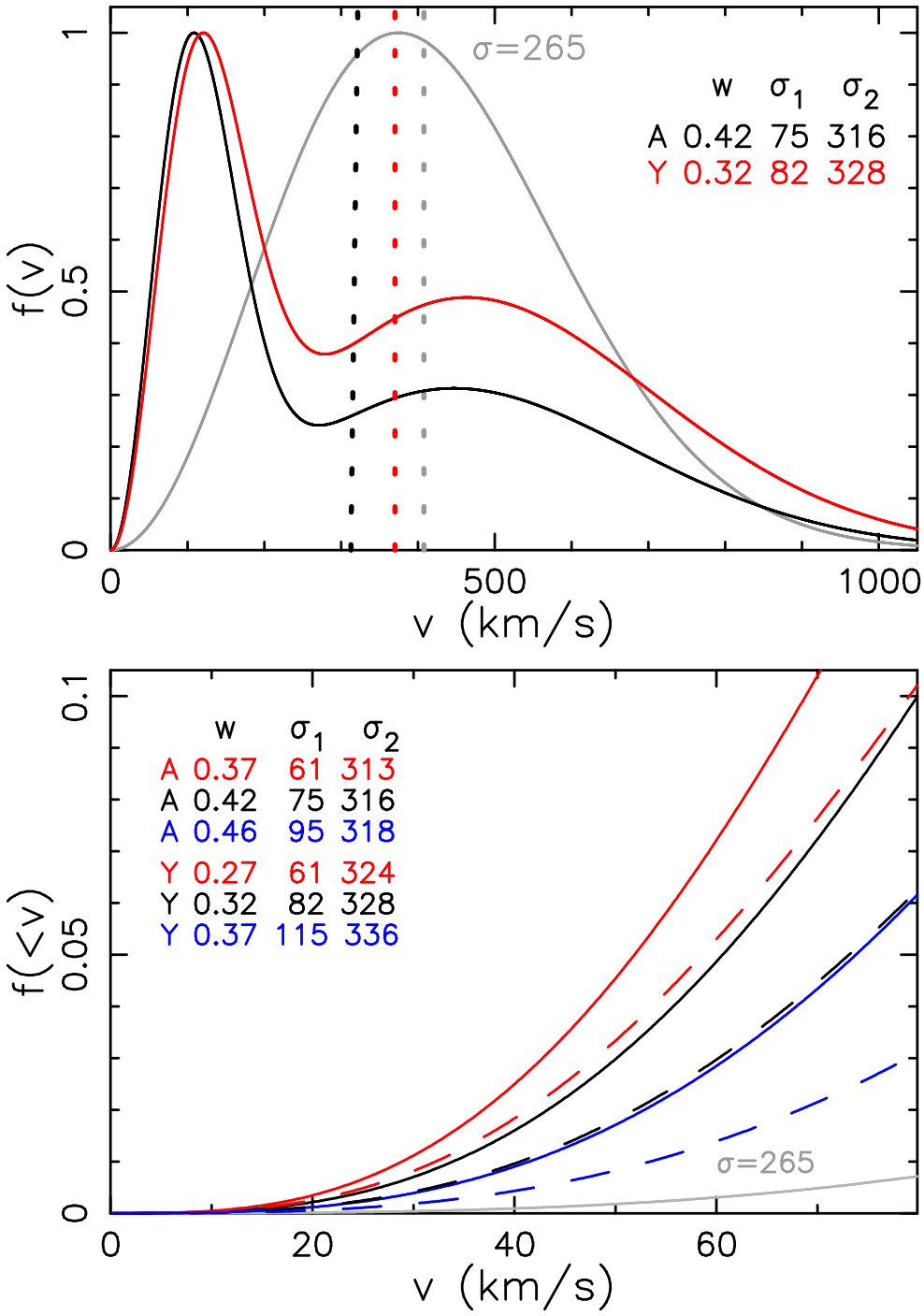

Figure 2.9: Top: our best velocity distribution for all pulsars and for the youngest pulsars, together with a single maxwellian. The vertical dotted lines indicates the median velocities: 313, 370 and 408 km/s. Below: fraction $f(< v)$ of pulsars with velocity less than v, for the best mixed model for all pulsars (black), and for the lowest and highest value in the range of σ_1 (red,blue). Solid lines: all pulsars; dashed lines: pulsars with $\tau_c < 10\,\mathrm{Myr}$. In grey we show the fraction for a single maxwellian (Hobbs et a. 2005).

that this centre does not coincide exactly with the actual centre of the galaxy (e.g. as defined by Sgr A*). We give all three equations, rewriting them slightly to show explicitly the role of $\alpha_{\rm GP}$, $\delta_{\rm GP}$, and l_Ω. The coordinate transformation is composed of three rotations: one around the galactic z-axis to bring the galactic centre to the node (this replaces l with $l-l_\Omega$), one around the equatorial z-axis to bring the spring node to the node (this replaces α with $\alpha-\alpha_\Omega = \alpha-(\alpha_{\rm GP}+\frac{\pi}{2})$, and finally around the now common x-axis over an angle $\frac{\pi}{2}-\delta_{\rm GP}$ to align the galactic pole with the equatorial pole. The resulting equations are (see also Lane 1979).

$$\cos(\alpha-\alpha_{\rm GP}-\frac{\pi}{2})\cos\delta = \cos(l-l_\Omega)\cos b \tag{2.36}$$

$$\begin{aligned}\sin(\alpha-\alpha_{\rm GP}-\frac{\pi}{2})\cos\delta &= \cos(\frac{\pi}{2}-\delta_{\rm GP})\sin(l-l_\Omega)\cos b \\ &\quad -\sin(\frac{\pi}{2}-\delta_{\rm GP})\sin b\end{aligned} \tag{2.37}$$

$$\begin{aligned}\sin\delta &= \sin(\frac{\pi}{2}-\delta_{\rm GP})\sin(l-l_\Omega)\cos b \\ &\quad +\cos(\frac{\pi}{2}-\delta_{\rm GP})\sin b\end{aligned} \tag{2.38}$$

To find the equatorial coordinates $\alpha_{\rm GC}$, $\delta_{\rm GC}$ for the centre of the coordinate system, we enter $l=b=0$ and combine eqs. 2.36,2.37 to find:

$$\tan(\alpha_{\rm GC}-\alpha_{\rm GP}-\frac{\pi}{2}) = \frac{\cos(\frac{\pi}{2}-\delta_{\rm GP})\sin(-l_\Omega)}{\cos(-l_\Omega)} \tag{2.39}$$

$$\sin\delta_{\rm GC} = \sin(\frac{\pi}{2}-\delta_{\rm GP})\sin(-l_\Omega) \tag{2.40}$$

Perryman et al. (1997) give the pole and node longitude for J2000.0 as

$$\alpha_{\rm GP} = 192^\circ 85948, \quad \delta_{\rm GP} = 27^\circ 12825, \quad l_\Omega = 32^\circ 93192 \tag{2.41}$$

and with Eqs. 2.36,2.37,2.38, these define the coordinate transformation for J2000.0 in the ICRS system. Entering these values in Eqs. 2.39, 2.40 we find

$$\alpha_{\rm GC} = 266^\circ 40500, \quad \delta_{\rm GC} = -28^\circ 93617 \tag{2.42}$$

For later reference we combine Eqs. 2.36, 2.37 for the galactic center $l=b=0$ into

$$\tan(-l_\Omega) = \frac{\sin(\alpha_{\rm GC}-\alpha_{\rm GP}-\frac{\pi}{2})/\cos(\frac{\pi}{2}-\delta_{\rm GP})}{\cos(\alpha_{\rm GC}-\alpha_{\rm GP}-\frac{\pi}{2})} \tag{2.43}$$

and note that entering the coordinates for pole and centre from Eqs. 2.41, 2.42 in Eq. 2.43 we re-obtain l_Ω correctly.

The next step is to determine the transformation of the proper motions. This is done by Smart (1938, chapter 1.41), who notes that it corresponds to a rotation over an angle ϕ between the local directions of the lines of constant l and constant α, or equivalently between the lines of constant b and constant δ. With the notation $\mu_{l*} \equiv \mu_l \cos b$ and $\mu_{\alpha*} \equiv \mu_\alpha \cos\delta$ we write Smart's Eqs. 4,5 as

$$\mu_{l*} = \mu_{\alpha*}\cos\phi + \mu_\delta \sin\phi \tag{2.44}$$

$$\mu_b = -\mu_{\alpha*}\sin\phi + \mu_\delta\cos\phi \tag{2.45}$$

From spherical trigonometry the angle ϕ is given by

$$\tan\phi = \frac{\sin(\alpha - \alpha_{\rm GP})}{\cos\delta\tan\delta_{\rm GP} - \sin\delta\cos(\alpha - \alpha_{\rm GP})} \tag{2.46}$$

(Smart 1938, Eq.3). The angle ϕ may also be found by taking the time derivative of the equation defining the transformation equatorial coordinates to galactic latitude (cf. Lane 1979)

$$\begin{aligned}\sin b &= \sin\delta\cos(\frac{\pi}{2} - \delta_{\rm GP}) \\ &\quad - \sin(\frac{\pi}{2} - \delta_{\rm GP})\sin(\alpha - \alpha_{\rm GP} - \frac{\pi}{2})\cos\delta\end{aligned} \tag{2.47}$$

and equating the result to Eq. 2.45.

For galactic to equatorial we may write analogously to Eqs.2.44 and 2.45:

$$\mu_{\alpha *} = \mu_{l*}\cos\phi_2 + \mu_b\sin\phi_2 \tag{2.48}$$

$$\mu_\delta = -\mu_{l*}\sin\phi_2 + \mu_b\cos\phi_2 \tag{2.49}$$

We equate the time derivative of Eq. 2.38 to Eq.2.49 to obtain

$$\tan\phi_2 = \frac{-\cos(l - l_\Omega)}{\cot(\frac{\pi}{2} - \delta_{\rm GP})\cos b - \sin(l - l_\Omega)\sin b} \tag{2.50}$$

Applied to the same source, $\phi = -\phi_2$, and thus either angle may be computed with Eq.2.46 or with Eq.2.50.

2.B Proper motions and velocity corrections

The space velocity of a star in the Galaxy may be decomposed into the average space velocity of its surroundings and its velocity with respect to this average, i.e. its peculiar velocity. The velocity of the local standard of rest for the Sun is its galactic rotation velocity, $v_R(R_o)$, where R_o is the distance to the galactic centre. The peculiar velocity of the Sun is usually written [U,V,W], where the components are respectively in the direction from the Sun towards the galactic centre, in the direction of the galactic rotation, and perpendicular to the galactic plane. The total velocity of the Sun may thus be written

$$\vec{v}_\odot = [U, V + v_R(R_o), W] \tag{2.51}$$

For a pulsar in the galactic plane, with $b = 0$, the velocity of the local standard of rest is also given by the rotation velocity $v_R(R)$ around the centre of the galaxy, at the galactocentric distance of the pulsar R (see Fig. 2.10). This velocity is in the plane of the galaxy, in the direction perpendicular to the line connection the pulsar to the galactic center. For a pulsar far from the plane, the meaning of the Local Standard of Rest is less obvious, because the halo stars do not participate in the rotation of the disk. The birthplace of the neutron star is (with the few exceptions mentioned above) in the galactic plane, therefore we use for its local standard of rest the galactic rotation $\vec{v}_{\rm R}(R)$ of its projection on the galactic plane. The total velocity of a pulsar at distance D and galactic coordinates l, b, may be written in the same coordinate frame as used for the Sun (see Figure 2.10):

$$\vec{v}_p = [U_p + v_R(R)\sin\theta, V_p + v_R(R)\cos\theta, W_p] \tag{2.52}$$

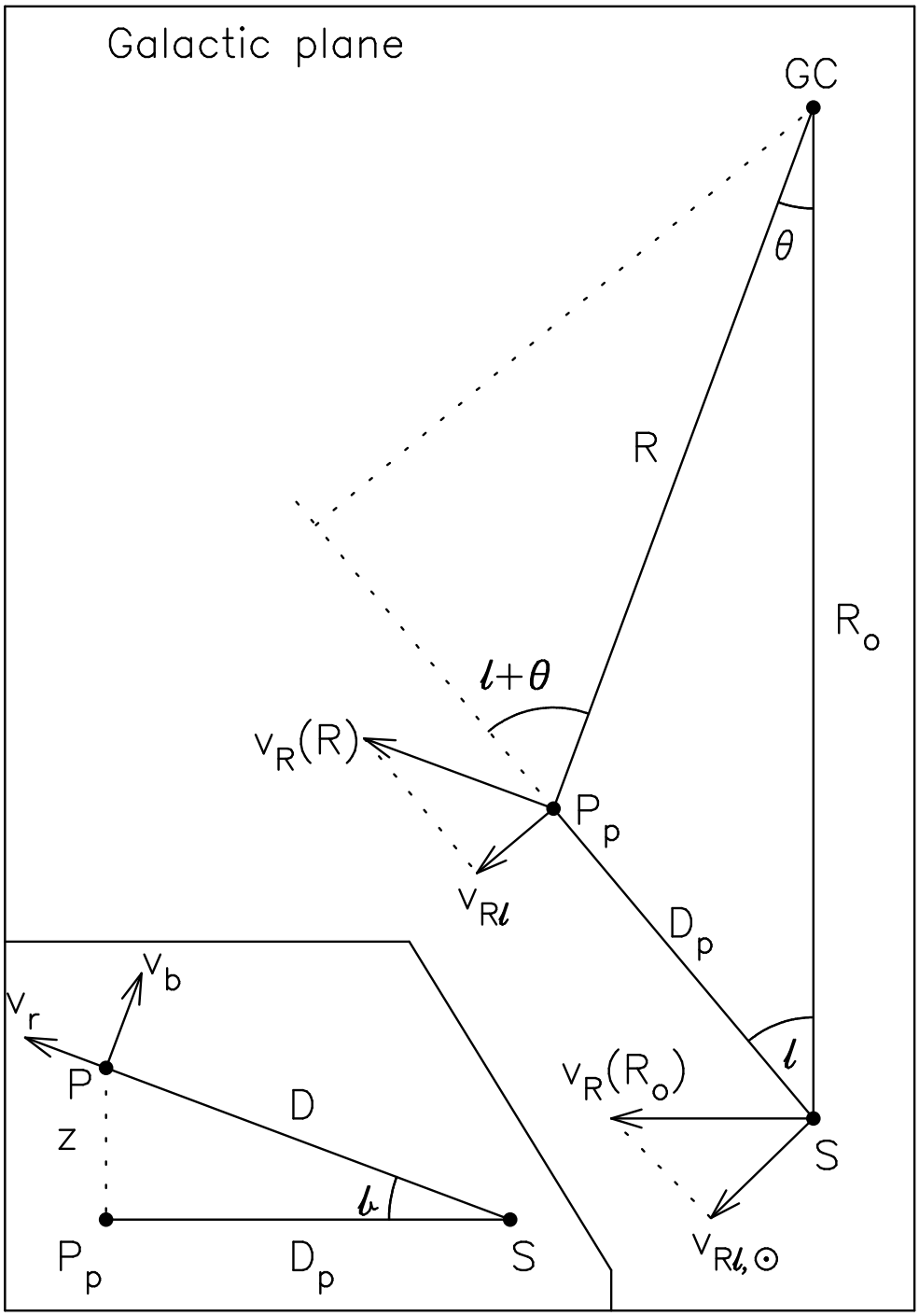

Figure 2.10: Definition of angles and distances in the galactic plane ($z = 0$), and (inset) of the projected distance D_p to the pulsar. S is the Sun, GC the galactic centre, P the pulsar and P_p the projection of the pulsar position on the galactic plane.

with $[U_p, V_p, W_p]$ the peculiar velocity of the pulsar. To obtain the velocity in the l-direction, we write the unit vector in this direction as:

$$\vec{l} = [-\sin l, \cos l, 0] \tag{2.53}$$

Thus the observed relative velocity in the longitude direction is

$$\vec{l} \cdot (\vec{v}_p - \vec{v}_\odot) = (\mu_{l*,v} + \mu_{l*,G})D \equiv \mu_{l*} D \tag{2.54}$$

where the peculiar velocity in the longitude direction is

$$v_l \equiv \mu_{l*} D \equiv -U_p \sin l + V_p \cos l \tag{2.55}$$

and the correction for galactic rotation and solar peculiar velocity is

$$\mu_{l*,G}\, D \equiv U \sin l - [V + v_R(R_o)] \cos l + v_R(R) \cos(\theta + l) \tag{2.56}$$

The angle $(\theta + l)$ may be computed from (see Fig. 2.10):

$$\tan(\theta + l) = \frac{R_o \sin l}{R_o \cos l - D_p} = \frac{R_o \sin l}{R_o \cos l - D \cos b} \tag{2.57}$$

with D_p the projected distance towards the pulsar. Eq. 2.7 follows from Eqs. 2.54-2.57.

The unit vector in the b-direction may be written

$$\vec{b} = [-\sin b \cos l, -\sin b \sin l, \cos b] \tag{2.58}$$

and the relative velocity in this direction

$$\vec{b} \cdot (\vec{v}_p - \vec{v}_\odot) = (\mu_{b,v} + \mu_{b,G})D \equiv \mu_b D \tag{2.59}$$

with

$$v_b \equiv \mu_{b,G}\, D = -U_p \sin b \cos l - V_p \sin b \sin l + W_p \cos b \tag{2.60}$$

and

$$\begin{aligned} \mu_{b,G} D \;\; = \;\; & U \sin b \cos l + [V + v_R(R_o)] \sin b \sin l - W \cos b \\ & - v_R(R) \sin(\theta + l) \sin b \end{aligned} \tag{2.61}$$

For a pulsar in direction l, b, we can compute $\mu_{l*,G}$ and $\mu_{b,G}$, as a function of distance D from Eqs.2.56, 2.57 and 2.61. Because the rotation of the sum of two vectors is equal to the sum of two rotated vectors, symbolically: $\mathcal{R}(\vec{a} + \vec{\Delta a}) = \mathcal{R}(\vec{a}) + \mathcal{R}(\Delta\vec{a})$, we may rotate the corrections with Eqs.2.44, 2.45. Hence:

$$\mu_{\alpha*,G} = \mu_{l*,G} \cos\phi_2 + \mu_{b,G} \sin\phi_2 \tag{2.62}$$

$$\mu_{\delta,G} = -\mu_{l*,G} \sin\phi_2 + \mu_{b,G} \cos\phi_2 \tag{2.63}$$

where ϕ_2 is given by Eq.2.50.

2.C Numerical evalution of the likelihood in for a semi-anisotropic maxwellian

To integrate Eq. 2.29, we first separate the terms involving the velocity and define

$$\begin{aligned} I_v &= e^{-A_3}\int_0^\infty v^2 e^{-A_1 v^2 - A_2 v} dv \quad \text{where} \\ A_1 &\equiv \frac{1}{2\sigma^2} + \frac{1}{2}\left(\frac{\sin\xi_1\cos\xi_2}{D\sigma_\alpha}\right)^2 + \frac{1}{2}\left(\frac{\sin\xi_1\sin\xi_2}{D\sigma_\delta}\right)^2 \\ A_2 &\equiv \frac{\sin\xi_1}{D}\left[\frac{(\mu_{\alpha*,G}-\mu'_{\alpha*})\cos\xi_2}{{\sigma_\alpha}^2} + \frac{(\mu_{\delta,G}-\mu'_\delta)\sin\xi_2}{{\sigma_\delta}^2}\right] \\ A_3 &\equiv \frac{(\mu_{\alpha*,G}-\mu'_{\alpha*})^2}{2{\sigma_\alpha}^2} + \frac{(\mu_{\delta,G}-\mu'_\delta)^2}{2{\sigma_\delta}^2} \end{aligned} \tag{2.64}$$

The result of this integral is

$$I_v = \frac{A_2 e^{-A_3}}{4{A_1}^2}\left[\sqrt{\pi}e^{E^2}\left(\frac{1}{2E}+E\right)\mathrm{erfc}(E)-1\right]; \quad E \equiv \frac{A_2}{2\sqrt{A_1}} \tag{2.65}$$

Entering this in Eq. 2.29, we obtain:

$$\begin{aligned} L_{\rm sim}(\sigma) &= \int_o^{D_{\rm max}}\int_0^{2\pi}\int_0^{\pi} \mathcal{C} f_D(D)\exp\left[-\frac{(1/D-\varpi')^2}{2{\sigma_\varpi}^2}\right] \\ &\times \sin\xi_1\, 2\sqrt{\frac{2}{\pi}}\frac{1}{\sigma^3} I_v(D,\xi_1,\xi_2) d\xi_1 d\xi_2 dD \end{aligned} \tag{2.66}$$

Returning to Eq. 2.28, we note that for fixed distance D, velocity v and angle ξ_1, $P_{\rm sim}$ reaches it maximum when the arguments of the exponents that include the proper motions are zero. The value of ξ_2 for which this is the case follows from

$$\tan\xi_{2m} = \frac{\mu'_{\alpha*} - \mu_{\alpha*.G}(D)}{\mu'_\delta - \mu_{\delta,G}(D)} \tag{2.67}$$

Because this angle is the same for every v, the same value of ξ_2 also maximizes the integrand of Eq. 2.66. The integration of Eq. 2.66 is done in three steps. First we fix D and ξ_1, and determine the range of ξ_2 from the condition Eq. 2.27 (or equivalently by testing with Eq. 2.26 that v_z is in the right direction). We divide this range in three parts, one given by $(\xi_{2m}-h)$ to $(\xi_{2m}+h)$, and the other two dividing the remaining range, and integrate over ξ_2 in each part separately with a 64-node gaussian quadrature. We find that $h = 2\pi/70$ leads to accurate results. Second, we integrate over ξ_1 with one 64-node gaussian quadrature. Finally, we integrate over D, in steps of 100 pc, for $D_{\rm max} = 10$ kpc.

We compute $L_{\rm maxw-si}(\sigma)$ on a grid of values of σ, in steps of 5 km/s, interpolate linearly to get a grid with steps of 1 km/s.

2.D Master list

Table 2.6: Master list of the pulsars used in our study.

	B-name	J-name		l	b	ϖ'	σ_ϖ	$\mu'_{\alpha*}$	σ_α	μ'_δ	σ_δ	τ_c	ref
				(°)	(°)	(mas)		(mas/yr)		(mas/yr)		(Myr)	
1		J0034−0721		110.42	−69.82	0.93	0.08	10.37	0.08	−11.13	0.16	36.7	6
2		J0108−1431		140.93	−76.82	4.17	1.42	75.05	2.26	−152.54	1.65	166.4	5
3	B0136+57	J0139+5814		129.22	−4.04	0.37	0.04	−19.11	0.07	−16.60	0.07	0.4	6
4	B0329+54	J0332+5434	i	145.00	−1.22	0.94	0.11	17.00	0.27	−9.48	0.37	5.5	1
5	B0355+54	J0358+5413	i	148.19	0.81	0.91	0.16	9.20	0.18	8.17	0.39	0.6	4
6	B0450+55	J0454+5543		152.62	7.55	0.84	0.05	53.34	0.06	−17.56	0.14	2.3	6
7		J0538+2817	i	179.72	−1.69	0.72	0.12	−23.57	0.10	52.87	0.10	0.6	6
8	B0628-28	J0630−2834		236.95	−16.76	3.01	0.41	−46.30	0.99	21.26	0.52	2.8	5
9	B0656+14	J0659+1414	i	201.11	8.26	3.47	0.36	44.07	0.63	−2.40	0.29	0.1	2
10	B0809+74	J0814+7429		140.00	31.62	2.31	0.04	24.02	0.09	−43.96	0.35	122.0	1
11	B0818-13	J0820−1350		235.89	12.59	0.51	0.04	21.64	0.09	−39.44	0.05	9.3	6
12	B0919+06	J0922+0638		225.42	36.39	0.83	0.13	18.35	0.06	86.56	0.12	0.5	3
13	B0950+08	J0953+0755		228.91	43.70	3.82	0.07	−2.09	0.08	29.46	0.07	17.5	1
14	B1133+16	J1136+1551		241.90	69.20	2.80	0.16	−73.95	0.38	368.05	0.28	5.0	1
15	B1237+25	J1239+2453		252.45	86.54	1.16	0.08	−106.82	0.17	49.92	0.18	22.9	1
16	B1508+55	J1509+5531		91.33	52.29	0.47	0.03	−73.64	0.05	−62.65	0.09	2.3	6
17	B1541+09	J1543+0929		17.81	45.78	0.13	0.02	−7.61	0.06	−2.87	0.07	27.5	6
18	B1556-44	J1559−4438		334.54	6.37	0.38	0.08	1.52	0.14	13.15	0.05	4.0	5
19	B1929+10	J1932+1059	i	47.38	−3.88	2.78	0.06	94.06	0.09	43.24	0.17	3.1	7
20		J1935+1616		52.44	−2.09	0.22	0.12	1.13	0.13	−16.09	0.15	0.9	6
21	B2016+28	J2018+2839		68.10	−3.98	1.03	0.10	−2.64	0.21	−6.17	0.38	59.8	1
22	B2020+28	J2022+2854		68.86	−4.67	0.61	0.08	−3.46	0.17	−23.73	0.21	2.9	7

Table 2.6: Master list of the pulsars used in our study.

	B-name	J-name		l	b	ϖ'	σ_ϖ	$\mu'_{\alpha*}$	σ_α	μ'_δ	σ_δ	τ_c	ref
				(°)	(°)	(mas)		(mas/yr)		(mas/yr)		(Myr)	
23	B2021+51	J2022+5154		87.86	8.38	0.78	0.07	−5.03	0.27	10.96	0.17	2.7	7
24	B2045-16	J2048−1616		30.51	−33.08	1.05	0.03	113.16	0.02	−4.60	0.28	2.8	6
25	B2053+36	J2055+3630		79.13	−5.59	0.17	0.03	1.04	0.04	−2.46	0.13	9.5	6
26		J2144−3933	i	2.79	−49.47	6.05	0.56	−57.89	0.88	−155.90	0.54	272.3	5
27	B2154+40	J2157+4017		90.49	−11.34	0.28	0.06	16.13	0.10	4.12	0.12	7.1	6
28	B2310+42	J2313+4253		104.41	−16.42	0.93	0.07	24.15	0.10	5.95	0.13	49.3	6

Notes: The last column gives the reference in Table 2.2 from which the parallax with error (columns 7,8), and the proper motions with their errors (columns 9-12) are taken. In the case of asymmetric errors we take the larger one. Columns 11 gives the characteristic age $\tau_c \equiv P/(2\dot{P})$. An i in column 5 indicates that the model velocity distribution for this pulsar is isotropic in the models that mix isotropic and semi-isotropic velocity distributions.

Chapter 3

The observed velocities of millisecond radio pulsars

Andrei Igoshev

A&A, 2017
submitted

Abstract

Observed samples of BeX and double neutron stars indicate that some neutron stars receive a natal kick with magnitude ≤ 50 km/s. A neutron star formed through this channel has to be present among the millisecond radio pulsars as well.

This work studies the observed velocity distribution of millisecond radio pulsars, and represents it as systematic rotation around the Galactic centre (asymmetric drift) plus some extra speed above this value normally distributed in each direction. An analysis using the parametric maximum likelihood method, shows the velocity distribution of the millisecond radio pulsars is bimodal. The isotropic component at 38 ± 13 km/s (95% confidence interval) represents 66% of the population with velocities close to the velocity dispersion of thin disk population and corresponding virtually to no natal kick at the moment of the neutron star formation. The high-velocity component is anisotropic and represents a third of the population which limits the parameter estimate precision. The values are $\sigma_x = 132 \pm 74$ km/s, $\sigma_y = 20^{+60}_{-19}$ km/s and $\sigma_z = 150 \pm 92$ km/s (95% confidence interval). This component rotates with an average velocity $\langle v_{\rm MSP} \rangle = 105 \pm 39$ km/s.

3.1 Introduction

A significant fraction of BeX stars has low eccentricities [Pfahl et al., 2002] which imply a natal kick ≤ 50 km/s for neutron stars. The double neutron stars show correlation between the spin

period and eccentricity [Faulkner et al., 2005] which is possible only if the second neutron star received a kick with the Maxwellian velocity dispersion ≤ 50 km/s [Dewi et al., 2005; Tauris et al., 2017]. The systemic velocities of these objects also indicate their low kick velocity [Tauris et al., 2017].

The study of young radio pulsars [Arzoumanian et al., 2002; Verbunt et al., 2017] show that its velocity distribution is bimodal with a low and a high-velocity component.

The systemic velocity of the millisecond radio pulsars (MSPs hereafter) is related to the kick velocity of the neutron star, and thus the MSP population can also be a mixture of low and high-velocity objects. The aim of this article is to study this.

Our study considers two effects: (1) velocity anisotropy, (2) asymmetric drift.

Any old Galactic population demonstrates a strong velocity anisotropy with $\sigma_x : \sigma_y : \sigma_z = 2.2 : 1.4 : 1$ (Dehnen & Binney 1998; σ stands for the second central moment of the velocity distribution, x is in the direction to the Galactic centre, y is in direction of the local Galactic rotation and z is in vertical direction). Such a large ratio between vertical and horizontal velocity components can mimic a presence of the low-velocity subpopulation if only an isotropic velocity distribution is considered.

Moreover, the old (virialised) population rotates slower about the Galaxy [Toscano et al., 1999; Mihalas & Binney, 1981]. The speed of this rotation depends on the properties of the natal kick as well. The effect is called the asymmetric drift.

An additional motivation to study the velocity distribution of MSP is related to the fact that these objects are much more rotationally stable comparatively to a population of normal radio pulsars [Desvignes et al., 2016]. This property makes it possible to measure the parallax and proper motion with high accuracy by the timing technique. The MSPs are prominent detectors for the low-frequency gravitational waves, that is why a growing number of MSP is observed with extraordinary precision on timespan of decades [Matthews et al., 2016].

The article is structured as follows: Section 3.2 describes the literature sources and selection criteria used to prepare a catalogue of MSP parallaxes and proper motions. In Section 3.3, the maximum likelihood method is explained. This section is mathematically intensive and can be omitted for the first reading. Section 3.4 models the data to better understand the limitations of the maximum likelihood approach and to interpret the result correctly. The results of the analysis are gathered in the Section 3.5. In Section 3.6, the properties of the high and low-velocity MSP subpopulations are compared.

3.2 Data

To prepare the master list the ATNF pulsar catalogue version 1.55 [Manchester et al., 2005] [1] is used. The analysis is restricted to MSPs (period derivatives less than 5×10^{-18} s/s) with measured proper motion and parallaxes outside globular clusters.

The sources of measurements are compiled in Table 3.1 and the values are given in Table 3.A. The pulsar positions and direction of the proper motions are shown in Figure 3.1. In a case when alternative error estimates are provided e.g. Deller et al. [2013] or Yan et al. [2013] I gather values

[1] The catalogue web-site is http://www.atnf.csiro.au/research/pulsar/psrcat

Table 3.1: Sources for proper motions in the master list

S	source (interferometric measurements)		N
1	Deller et al. [2012]	Table 2	1
2	Deller et al. [2013]	Table 2	1
3	Deller et al. [2016]	Table 2	2
4	Du et al. [2014]	Table 2	1
5	Yan et al. [2013]	Table 2	1
	Total:	6	
	source (timing measurements)		
6	Bassa et al. [2016b]	Table 1	1
7	Desvignes et al. [2016]	Tables 2-12	10
8	Ferdman et al. [2014]	Table 2	1
9	Fonseca et al. [2014]	Table 2	1
10	Freire et al. [2012]	Table 1	1
11	Guillemot et al. [2016]	Table 3	11
12	Matthews et al. [2016]	Table 2	19
13	Ng et al. [2014]	Table 5	1
14	Reardon et al. [2016]	Tables A1-A4	7
15	Stovall et al. [2014]	Table 4	1
	Total:	59	

Notes: S source indicator, N number of entries used.

obtained by a standard least-square method, preferably with the best treatment of the ionosphere. The covariance values for parallax and proper motion are neglected because Yan et al. [2013] is the only literature source which gives these estimates. All MSPs with distance estimates based on white dwarf optical magnitude (e.g. PSR J0614-3329 by Bassa et al. 2016a) are excluded from our master list because the model for distance uncertainty, in this case, is too complicated. Radial velocities are not considered.

When the measured parallax appears to be zero or negative as for PSR J1910+1256 from the article by Matthews et al. [2016] only the standard deviation is cited as an upper limit.

3.3 Method

The estimation of velocity distribution parameters and model selection are performed utilising the maximum likelihood technique described in Verbunt et al. [2017]. This section is structured as follows: First, the mathematics related to a derivation of the actual proper motion is summarised. Second, the isotropic and anisotropic velocity distributions are defined. Third, an algorithm which makes it possible to compute the likelihood for the anisotropic velocity distribution numerically is described. Fourth, the likelihood for composite models is introduced. Fifth, the model selection and estimation of the confidence intervals are described.

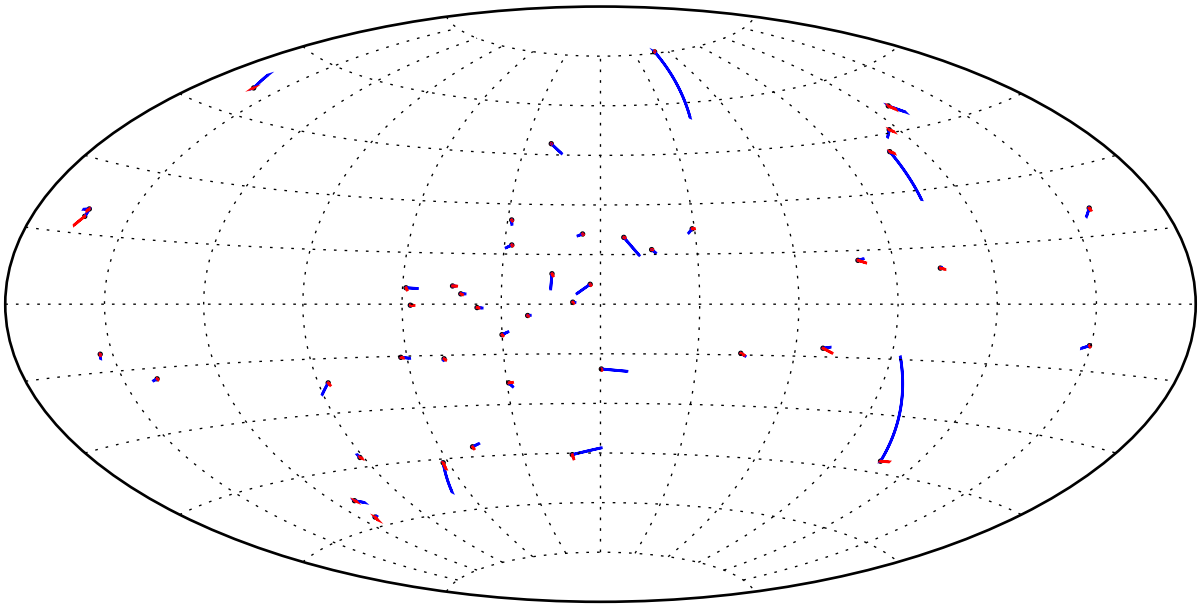

Figure 3.1: Celestial distribution of the pulsars with measured proper motions, in galactic coordinates. Blue lines show vectors for the direction of the proper motion (displacement of the pulsar during 0.5 Myr). Red lines show the value for the correction due to the galactic rotation, the systematic rotation of the MSP population is fixed at $\langle v_{\mathrm{MSP}} \rangle = 220$ km/s.

Table 3.2: The numerical values used in the analysis

$R_\odot = 8.5$ kpc	$H = 1.7$ kpc	$h = 0.5$ kpc
$v_R(R_\odot) = 220$ km/s		
$U = 10$ km/s	$V = 5.3$ km/s	$W = 7.2$ km/s
Integration		
$D_{\max} = 10$ kpc	$v_{\max} = 2000$ km/s	

The method from articles Igoshev et al. [2016] and Verbunt et al. [2017] is adapted to the values and models suitable for MSPs.

The transversal velocity is a composite measurement which consists of a parallax ϖ' and a proper motion $\mu'_{\alpha*}$, μ'_δ in two orthogonal directions for the right ascension and declination (if the measurement is performed in the equatorial coordinate system) or $\mu'_{\lambda*}$, μ'_β for the latitude and longitude respectively (if the measurement is performed in the ecliptic coordinate system). The exact equations for probabilities are written in Verbunt et al. [2017]. The numerical values are summarized in Table 3.2.

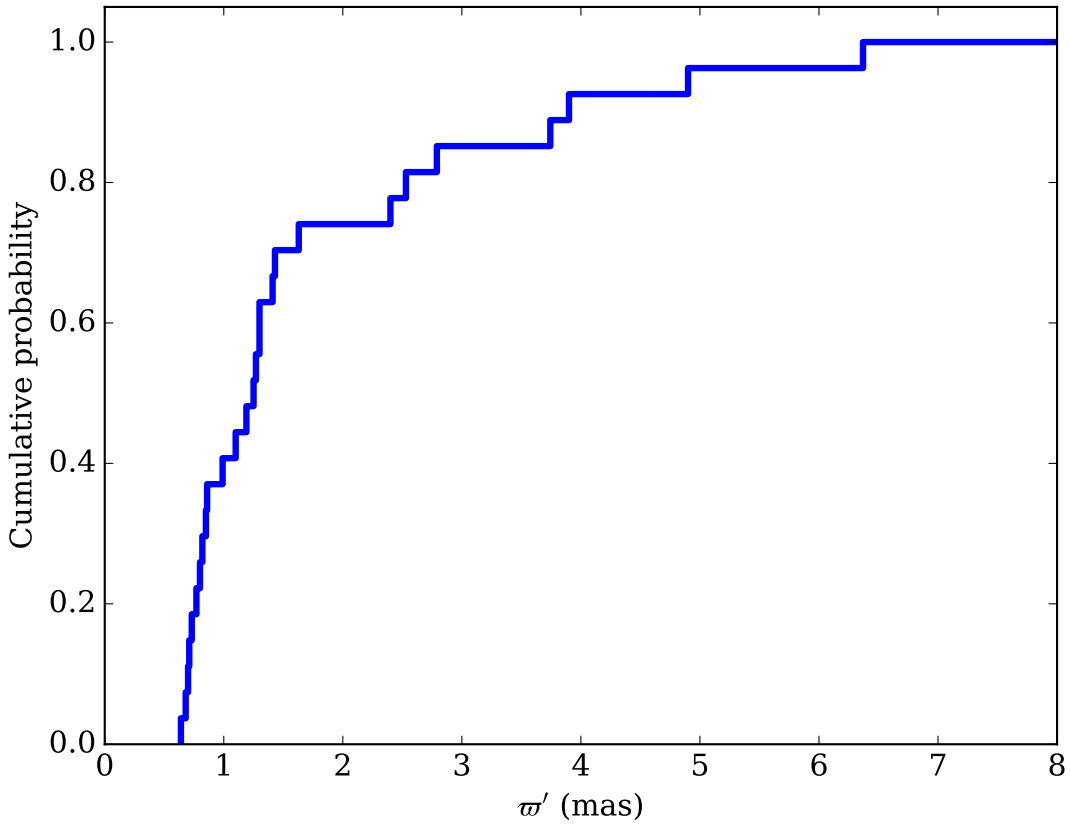

Figure 3.2: The cumulative distribution of the parallaxes for the sample of MSPs with $\varpi'/\sigma_{\varpi} > 3$.

3.3.1 Actual proper motion

The actual proper motions $\mu_{\alpha*}$ and μ_δ are the angular speeds relative to the solar motion[2] Thus three terms compose the actual proper motion: (1) the solar motion in the Galaxy, (2) the slower cojoint rotation of the old virialised population about the Galaxy and (3) an individual speed of pulsar above the MSP systematic rotation. The latter term can be represented as a Gaussian in each of the main axes of the Galactic coordinate system to take anisotropy into account $\mu_{\alpha*,v}$ and $\mu_{\delta,v}$. The first two terms form together the asymmetric drift $\mu_{\alpha*,G}$ and $\mu_{\delta,G}$:

$$\mu_{\alpha*} = \mu_{\alpha*,G} + \mu_{\alpha*,v};\;\; \mu_\delta = \mu_{\delta,G} + \mu_{\delta,v}; \tag{3.1}$$

The proper motion is related to the distance and velocity as:

$$\mu = \frac{v}{D} \;\;\Rightarrow\;\; \mu[\mathrm{mas/yr}] = \frac{v[\mathrm{km/s}]}{4.74D[\mathrm{kpc}]} \tag{3.2}$$

The precise speed of the asymmetric drift is unknown because the velocity of the MSP cojoint rotation $\langle v_{\mathrm{MSP}}\rangle$ depends on the natal kick, that is why this parameter is fitted together with σ_x, σ_y and σ_z. The drift term is written as:

$$\mu_{l*,G}D = U\sin l - (V + v_R(R_\odot))\cos l + \langle v_{\mathrm{MSP}}\rangle\cos(\theta + l) \tag{3.3}$$

and

$$\begin{aligned}\mu_{b,G}D = {} & U\sin b\cos l + (V + v_R(R_\odot))\sin b\sin l \\ & - \langle v_{\mathrm{MSP}}\rangle\sin(\theta + l)\sin b - W\cos b\end{aligned} \tag{3.4}$$

See Appendix 3.B for derivations. These equations differ from analogous ones obtained for young radio pulsars (for them $\langle v_{\mathrm{MSP}}\rangle = v_R(R_\odot)$). The angle $\theta + l$ can be computed as:

$$\tan(\theta + l) = \frac{R_\odot\sin l}{R_\odot\cos l - D\cos b} \tag{3.5}$$

The following equations convert $\mu_{l*,G}$ and $\mu_{b,G}$ into the coordinate system of the observation:

$$\mu_{\alpha*,G} = \mu_{l*,G}\cos\tilde{\chi} + \mu_{b,G}\sin\tilde{\chi} \tag{3.6}$$

$$\mu_{\delta,G} = -\mu_{l*,G}\sin\tilde{\chi} + \mu_{b,G}\cos\tilde{\chi} \tag{3.7}$$

where angle $\tilde{\chi}$ is the local angle between the galactic coordinate system and the coordinate system of the observation, see Appendix C for details. The values for the $\mu_{\alpha*,v}$ and $\mu_{\delta,v}$ are written based on actual velocities v_x, v_y, v_z in the Cartesian coordinate system and actual distance D as:

$$\begin{aligned}\mu_{\alpha*,v} = {} & (v_z\cos b - v_y\sin b\sin l - v_x\sin b\cos l)\frac{\sin\tilde{\chi}}{D} \\ & + (v_y\cos l - v_x\sin l)\frac{\cos\tilde{\chi}}{D}\end{aligned} \tag{3.8}$$

$$\begin{aligned}\mu_{\delta,v} = {} & (v_z\cos b - v_y\sin b\sin l - v_x\sin b\cos l)\frac{\cos\tilde{\chi}}{D} \\ & - (v_y\cos l - v_x\sin l)\frac{\sin\tilde{\chi}}{D}\end{aligned} \tag{3.9}$$

[2]In what follows I use $\mu'_{\alpha*}$ and μ'_δ to label the quantities both in equatorial and ecliptic coordinate system. The actual algorithm takes these differences into account.

3.3.2 Isotropic maxwellian distribution

The isotropic maxwellian velocity distribution is defined by a single parameter σ:

$$f(v,\sigma)dv = \frac{v^2}{\sqrt{8\pi^3}\sigma^3}\exp\left[-\frac{1}{2}\frac{v^2}{\sigma^2}\right]dv \tag{3.10}$$

with $v = \sqrt{v_x^2 + v_y^2 + v_z^2}$. In this case, the likelihood for a particular pulsar i is written as:

$$\begin{aligned} L^i_{\text{iso, maxw}}(\sigma) = 2\int_0^{D_{\max}} f_D(D)\exp\left[-\frac{(1/D-\varpi')^2}{2{\sigma_D}^2}\right] \\ \times \left(1+\frac{\sigma^2}{D^2{\sigma_\alpha}^2}\right)^{-1/2}\exp\left[-\frac{1}{2}\frac{(D\,\mu_{\alpha*,G}-D\,\mu'_{\alpha*})^2}{\sigma^2+D^2{\sigma_\alpha}^2}\right] \\ \times \left(1+\frac{\sigma^2}{D^2{\sigma_\delta}^2}\right)^{-1/2}\exp\left[-\frac{1}{2}\frac{(D\,\mu_{\delta,G}-D\,\mu'_{\delta})^2}{\sigma^2+D^2{\sigma_\delta}^2}\right]dD. \end{aligned} \tag{3.11}$$

see Verbunt et al. [2017] for detailed derivation, the normalisation factor $\mathcal{C}$ is discarded here. The total log-likelihood for the whole sample is:

$$\log L_{\text{iso, maxw}}(\sigma) = \sum_{i=1}^{N_{\text{puls}}} \log L^i_{\text{iso, maxw}}(\sigma) \tag{3.12}$$

The maximum of the likelihood is found with the Nelder-Mead method [Press et al., 2002].

3.3.3 Anisotropic maxwellian distribution

The local instantaneous velocity distribution of MSPs is anisotropic because of the properties of motion in the Galactic gravitational potential, see Dehnen & Binney [1998]. The anisotropic velocity distribution is defined as follows:

$$\begin{aligned} f(v_x,v_y,v_z,\sigma_x,\sigma_y,\sigma_z)dv_xdv_ydv_z = G(v_x,\sigma_x) \\ G(v_y,\sigma_y)G(v_z,\sigma_z)dv_xdv_ydv_z \end{aligned} \tag{3.13}$$

where

$$G(v,\sigma)dv = \frac{1}{\sqrt{2\pi}\sigma}\exp\left[-\frac{v^2}{2\sigma^2}\right]dv \tag{3.14}$$

is the gaussian distribution. This form converges to the isotropic maxwellian velocity distribution when $\sigma_x = \sigma_y = \sigma_z$.

A combination of equations describing the measurements, intrinsic probability for distance and the velocity eq. (3.13) makes it possible to write the joint probability as:

$$P_{\rm anis}(\varpi', \mu'_{\alpha*}, \mu'_\delta, D, v_x, v_y, v_z) dD dv_x dv_y dv_z \propto f_D(D) \frac{dD}{\sigma_x \sigma_y \sigma_z}$$
$$\times \exp\left[-\frac{1}{2}\left(\frac{v_x^2}{\sigma_x^2} + \frac{v_y^2}{\sigma_y^2} + \frac{v_z^2}{\sigma_z^2}\right)\right] \exp\left[-\frac{(1/D - \varpi')^2}{2\sigma_\varpi^2}\right]$$
$$\times \exp\left[-\frac{(\mu_{\alpha*,G}(D) + \mu_{\alpha*,v} - \mu'_{\alpha*})^2}{2\sigma_\alpha^2}\right]$$
$$\times \exp\left[-\frac{(\mu_{\delta,G}(D) + \mu_{\delta,v} - \mu'_\delta)^2}{2\sigma_\delta^2}\right] dv_x dv_y dv_z \tag{3.15}$$

The individual velocity components v_x, v_y, v_z and D are not measured. To obtain the likelihood for an individual pulsar, I integrate over these variables:

$$L^i_{\rm anis,\,maxw}(\sigma_x, \sigma_y, \sigma_z) = \int_0^{D_{\rm max}} \int_{-\infty}^{\infty} \int_{-\infty}^{\infty} \int_{-\infty}^{\infty} P_{\rm anis} dD dv_x dv_y dv_z \tag{3.16}$$

The total likelihood for parameters σ_x, σ_y and σ_z is:

$$\log L_{\rm anis,\,maxw}(\sigma_x, \sigma_y, \sigma_z) = \sum_{i=1}^{N_{\rm puls}} \log L^i_{\rm anis,\,maxw}(\sigma_x, \sigma_y, \sigma_z) \tag{3.17}$$

3.3.4 Practical calculations of the likelihood for an anisotropic velocity distribution

The four integrals in eq. (3.16) are hard to compute numerically because the exponentials in eq. (3.15) decay very fast when actual $\mu_{\alpha*,v}$ and $\mu_{\delta,v}$ are far from the measurements $\mu'_{\alpha*}$ and μ'_δ. Also, four-dimensional integration on grid requires significant computer power since a number of points is proportional to $N^4_{\rm grid}$.

Because of these reasons, I describe an advanced numerical algorithm which makes it possible to compute the likelihood function in a reasonable time. First, the polar coordinate system is introduced where one integration is performed analytically.

The polar coordinate system is:

$$\left.\begin{array}{rcl} v_\alpha &=& v \sin\xi_1 \cos\xi_2 \\ v_\delta &=& v \sin\xi_1 \sin\xi_2 \\ v_r &=& v \cos\xi_1 \end{array}\right\} \tag{3.18}$$

where ξ_1 is an angle between the radial direction and an orientation of the actual velocity and ξ_2 is the position angle on the sky. The Jacobian of transformation from the Cartesian coordinate system to these coordinates is $dv_x dv_y dv_z = v^2 \sin\xi_1 dv d\xi_1 d\xi_2$. Therefore the anisotropic velocity distribution can be written, see Appendix E for details:

$$f(v, \xi_1, \xi_2, \sigma_x, \sigma_y, \sigma_z) v^2 \sin\xi_1 dv d\xi_1 d\xi_2 = \frac{v^2 \sin\xi_1}{\sqrt{8\pi^3}\sigma_x \sigma_y \sigma_z}$$

$$\exp\left[-\frac{1}{2}\frac{v^2\Theta(\xi_1,\xi_2)}{2\sigma_x^2\sigma_y^2\sigma_z^2}\right]dvd\xi_1d\xi_2 \tag{3.19}$$

where function $\Theta(\xi_1,\xi_2)$ describes the anisotropy. In the case of isotropy $\Theta(\xi_1,\xi_2)=\sigma^4$ does not depend on the velocity vector orientation. For an anisotropic case the function $\Theta(\xi_1,\xi_2)$ can be written as:

$$\Theta(\xi_1,\xi_2)=\sigma_y^2\sigma_z^2v_x^2(\xi_1,\xi_2)+\sigma_x^2\sigma_z^2v_y^2(\xi_1,\xi_2)+\sigma_x^2\sigma_y^2v_z^2(\xi_1,\xi_2) \tag{3.20}$$

In the polar coordinate system the joint probability can be written as:

$$\begin{aligned}P_{\rm anis}(\varpi',\mu'_{\alpha*},\mu'_\delta,D,v,\xi_1,\xi_2)v^2\sin\xi_1dDdvd\xi_1d\psi_2\propto f_D(D)\\ \times\frac{v^2\sin\xi_1}{\sigma_x\sigma_y\sigma_z}\exp\left[-\frac{1}{2}\frac{v^2\Theta(\psi_1,\psi_2)}{\sigma_x^2\sigma_y^2\sigma_z^2}\right]\exp\left[-\frac{(1/D-\varpi')^2}{2\sigma_\varpi^2}\right]\\ \times\exp\left[-\frac{(\mu_{\alpha*,G}+\sin\xi_1\cos\xi_2v/D-\mu'_{\alpha*})^2}{2\sigma_\alpha^2}\right]\\ \times\exp\left[-\frac{(\mu_{\delta,G}+\sin\xi_1\sin\xi_2v/D-\mu'_\delta)^2}{2\sigma_\delta^2}\right]\end{aligned} \tag{3.21}$$

This equation can be integrated analytically over the absolute magnitude of the velocity v. To do so, I combine different terms in the power of the exponential to get an integral in the following form:

$$I_k(D,\xi_1,\xi_2)=\exp\left(-A_3\right)\int_0^{v_{\rm max}}v^2\exp\left(-A_1v^2-A_2v\right)dv \tag{3.22}$$

with auxiliary variables:

$$A_1=\frac{\Theta(\xi_1,\xi_2)}{2\sigma_x^2\sigma_y^2\sigma_z^2}+\frac{\sin^2\xi_1\cos^2\xi_2}{2\sigma_\alpha^2D^2}+\frac{\sin^2\xi_1\sin^2\xi_2}{2\sigma_\delta^2D^2} \tag{3.23}$$

$$A_2=\frac{(\mu_{\alpha*G}-\mu'_{\alpha*})}{\sigma_\alpha^2D}\sin\xi_1\cos\xi_2+\frac{(\mu_{\delta G}-\mu'_\delta)}{\sigma_\delta^2D}\sin\xi_1\sin\xi_2 \tag{3.24}$$

$$A_3=\frac{(\mu_{\alpha*G}-\mu'_{\alpha*})^2}{2\sigma_\alpha^2}+\frac{(\mu_{\delta G}-\mu_\delta)^2}{2\sigma_\delta^2} \tag{3.25}$$

The result of the integration is:

$$\begin{aligned}I_k(D,\xi_1,\xi_2)=\frac{1}{8A_1^{5/2}}\exp\left(-A_3+\frac{A_2^2}{4A_1}\right)\left[2\sqrt{A}\left(A_2-2A_1v\right)\right.\\ \left.+\sqrt{\pi}(2A_1+A_2^2){\rm erf}\left(\sqrt{A_1}v+\frac{A_2}{2\sqrt{A_1}}\right)\right]\Bigg|_0^{v_{\rm max}}\end{aligned} \tag{3.26}$$

The likelihood for an individual object i is written now as:

$$\begin{aligned}L^i_{\rm anis,\,maxw}(\sigma_x,\sigma_y,\sigma_z)=\int_0^{D_{\rm max}}g_D(\varpi'|D)f_D(D)\\ \times\int_0^\pi\frac{\sin\xi_1}{\sigma_x\sigma_y\sigma_z}\int_0^{2\pi}I_k(D,\xi_1,\xi_2)d\xi_2\xi_1dD\end{aligned} \tag{3.27}$$

The normalisation in this equation is chosen such a way that $L^i_{\mathrm{anis,\,maxw}}(\sigma,\sigma,\sigma) = L^i_{\mathrm{iso,\,maxw}}(\sigma)$ which allows direct model comparison. The integrals over ξ_1 and ξ_2 are hard to compute numerically with a regular grid. The function under the integrals peaks sharply around the positional angle of the measured proper motion and decays exponentially. To deal with this difficulty, I split the integral over ξ_2 into three separate integrals:

$$\int_0^{2\pi} I_k(D,\xi_1,\xi_2)d\xi_2 = \int_0^{\xi_n-h_n} I_k(D,\xi_1,\xi_2)d\xi_2$$

$$+\int_{\xi_n-h_n}^{\xi_n+h_n} I_k(D,\xi_1,\xi_2) + \int_{\xi_n+h_n}^{2\pi} I_k(D,\xi_1,\xi_2)d\xi_2 \tag{3.28}$$

where ξ_n is chosen for each step of the distance integration as:

$$\tan\xi_n = \frac{\mu'_\delta - \mu_{\delta,G}}{\mu'_{\alpha*} - \mu_{\alpha*G}} \tag{3.29}$$

In trial calculations the optimal value for parameter h_n is found to be $h_n \approx \pi/200$. This value works well, except for PSR J1909-3744 because its fractional error in proper motion direction is tiny (an order of magnitude smaller than for other pulsars in the article by Reardon et al. 2016). It is probably related the T2 binary model used in the timing analysis of this pulsar. When the entire sample including J1909-3744 is analysed using the isotropic model, it gives a very similar result to the analysis of the sample excluding this object. It is essential for the model comparison to obtain the same likelihood in the numerical and analytical integration. It is difficult to trust such a small confidence interval derived based on the timing tecnhique because even in the case of the interferometric observations the errors are larger. That is why the pulsar is excluded from the complete analysis. The integration is performed using the Gauss quadrature method with $N = 64$ for each of three integration intervals and each of numerical integrals.

3.3.5 Sum of two maxwellian distributions

A model for a sum of two isotropic maxwellian distributions is written as:

$$f(v,\vec{\sigma})dv = \frac{v^2}{\sqrt{8\pi^3}}\left[\frac{w}{\sigma_1^3}\exp\left[-\frac{1}{2}\frac{v^2}{\sigma_1^2}\right] + \frac{1-w}{\sigma_2^3}\exp\left[-\frac{1}{2}\frac{v^2}{\sigma_2^2}\right]\right]dv \tag{3.30}$$

where w defines a contribution of the first maxwellian to the total velocity distribution. It is possible to define the total likelihood as:

$$\log L_{\mathrm{sum\,iso,\,maxw}}(\vec{\sigma}) = \sum_{i=1}^{N_{\mathrm{puls}}} \log\Big[wL^i_{\mathrm{iso,\,maxw}}(\sigma_1)$$

$$+(1-w)L^i_{\mathrm{iso,\,maxw}}(\sigma_2)\Big] \tag{3.31}$$

where $\vec{\sigma} = [w,\sigma_1,\sigma_2]$. A combination of the isotropic and anisotropic velocity distribution can be written as:

$$f(\vec{v},\vec{\sigma})dv_x dv_y dv_z = \left\{\frac{w}{\sqrt{8\pi^3}\sigma_x\sigma_y\sigma_z}\exp\left[-\frac{v_x^2}{2\sigma_x^2} - \frac{v_y^2}{2\sigma_y^2} - \frac{v_z^2}{2\sigma_z^2}\right]\right.$$

$$+\frac{1-w}{\sqrt{8\pi^3\sigma^3}}\exp\left[-\frac{1}{2}\frac{v_x^2+v_y^2+v_z^2}{\sigma^2}\right]\Bigg\}dv_x dv_y dv_z \tag{3.32}$$

It corresponds to the total likelihood:

$$\log L_{\text{sum iso+anis, maxw}}(\vec{\sigma}) = \sum_{i=1}^{N_{\text{puls}}} \log\Big[wL^i_{\text{anis, maxw}}(\sigma_x,\sigma_y,\sigma_z) + (1-w)L^i_{\text{iso, maxw}}(\sigma_x)\Big] \tag{3.33}$$

with $\vec{\sigma} = [w, \sigma_x, \sigma_y, \sigma_z, \sigma]$. The values $\sigma_x, \sigma_y, \sigma_z$ describe the velocity dispersion for each major axis for fraction w of the total population while the value σ is for the velocity dispersion of $(1-w)$ fraction of the total population. In the limit case of $[w, \sigma, \sigma, \sigma, \sigma]$ it gives exactly the same result as single isotropic maxwellian.

3.3.6 Confidence interval and model selection

The likelihood ratio test is used to estimate the confidence interval. In case of a single maxwellian, I quote the 95% probability interval:

$$2\log L(\sigma^*) - 2\log L(\sigma) = 3.84 \tag{3.34}$$

where σ^* is the optimum value. This estimate is based on a mathematical fact that a ratio of two log-likelihoods follows approximately the χ^2 distribution.

For a sum of two maxwellians the Hessian matrix is computed numerically:

$$H_{ij}(\vec{m}^*) = \frac{\partial^2}{\partial m_i \partial m_j} L(\vec{m}^*) \tag{3.35}$$

where $\vec{m}^*$ is a vector of optimum values found in the maximum likelihood technique. The mixed second derivative is computed numerically using the central second order finite difference with a suitable step in each direction. In this case the 95% confidence interval is:

$$\vec{m}^* \pm \frac{1.96}{\sqrt{-H(\vec{m}^*)}} \tag{3.36}$$

where $\sqrt{-H(\vec{m}^*)}$ is the square root of the diagonal elements for the inverse Hessian matrix. This approach provides an estimate of symmetric errors.

In a case when symmetric errors are too large and point outside of the parameter domain, the likelihood ratio eq. (3.34) is used to estimate the asymmetric error interval in one particular direction.

To compare two models such as single maxwellian and a sum of two maxwellians we apply the Akaike informational criterion (AIC, see e.g. Liddle 2007):

$$AIC = -2\log L(\vec{m}^*) - 2k \tag{3.37}$$

where k is a number of estimated parameters. The model with the minimum value of AIC is preferable and a difference in AIC more than five can be considered as a strong (probability 0.08) and more than ten as a decisive (probability 0.007) evidence in favour of a particular model.

3.4 Tests of the maximum likelihood method for isotropic and anisotropic velocity distribution

To test the method, I prepare nine synthetic catalogues (each with 27 objects). The positions of test particles are drawn from the radial and vertical distribution typical for the young radio pulsars [Verbiest et al., 2012]. The initial velocities are drawn from a isotropic maxwellian with $\sigma =$ 200 km/s. The motion of particles is integrated in the gravitational potential `MWPotential2014` [Bovy & Rix, 2013] using the `Galpy` code[3] by Bovy [2015]. From this dataset binaries with distances which can be measured at $4\sigma_{\varpi}$ level to the corresponding observational errors in the original catalogue with age 0.72 Gyr (arbitrary choice) are selected. The Cartesian coordinates and velocities of each object are converted to l, b, $\varpi' = 1/D'$ and $\mu'_{\alpha*}, \mu'_{\delta}$. The observational uncertainties normally distributed with the standard deviation as in the original catalogue are added to the actual parallaxes and proper motions.

Each synthetic sample is analysed utilising all the maximum likelihood methods introduced in the previous section. The method based on the intrinsic isotropic velocity distribution consisting of two maxwellians *found no second component in 9 out of 10 cases.* In a single case when the algorithm discovers bimodality, the AIC is not enough to prefer a model with two maxwellians comparatively to model with a single maxwellian. The method based on the anisotropic maxwellian distribution always provides a better quality of the fit than a model which includes two isotropic maxwellians (AIC $= 14.4 - 24.8$) and finds correct values for $\sigma_x, \sigma_y, \sigma_z$ and $\langle v_{\rm MSP} \rangle$, see Figure 3.3. It means that the anisotropic maxwellian distribution is a good model for the local velocity distribution in dynamical equilibrium.

The simulation procedure includes neither a detection probability nor a luminosity function. This is not a real restriction, however, because strong spatial selection is present. MSPs end up in the synthetic catalogue only if their parallaxes large enough to be measured at $4\sigma_{\varpi}$ level to a corresponding observational uncertainty. In any realistic population synthesis, e.g. Story et al. [2007], the MSP luminosity does not correlate with the pulsar velocity. So, random objects from a small vicinity of the Sun are assigned with properties and added to the sample.

3.5 Results

The results of all maximum likelihood methods are summarised in the Table 3.3. The models are labelled with letters to facilitate the discussion. The maximum likelihood method is applied only to a part of the sample with $\varpi'/\sigma_{\varpi} > 3$, (see Discussion 3.6.1).

The single maxwellian velocity distribution (model A) is used as a baseline to compare all other models. The speed estimate obtained with a single maxwellian is in perfect agreement with earlier studies of the MSP ensemble by Toscano et al. [1999]. The isotropic velocity distributions are shown in Figure 3.4. The Galactic escape velocity limits these distributions. An addition of the following effects improves the likelihood: bimodality (model B, AIC = 13.24), asymmetric drift for each component (model C comparatively to B, AIC=2.88), the anisotropy of the high-velocity component (model E comparatively to C, AIC=2.38). In total, model E which consists of

[3] http://github.com/jobovy/galpy

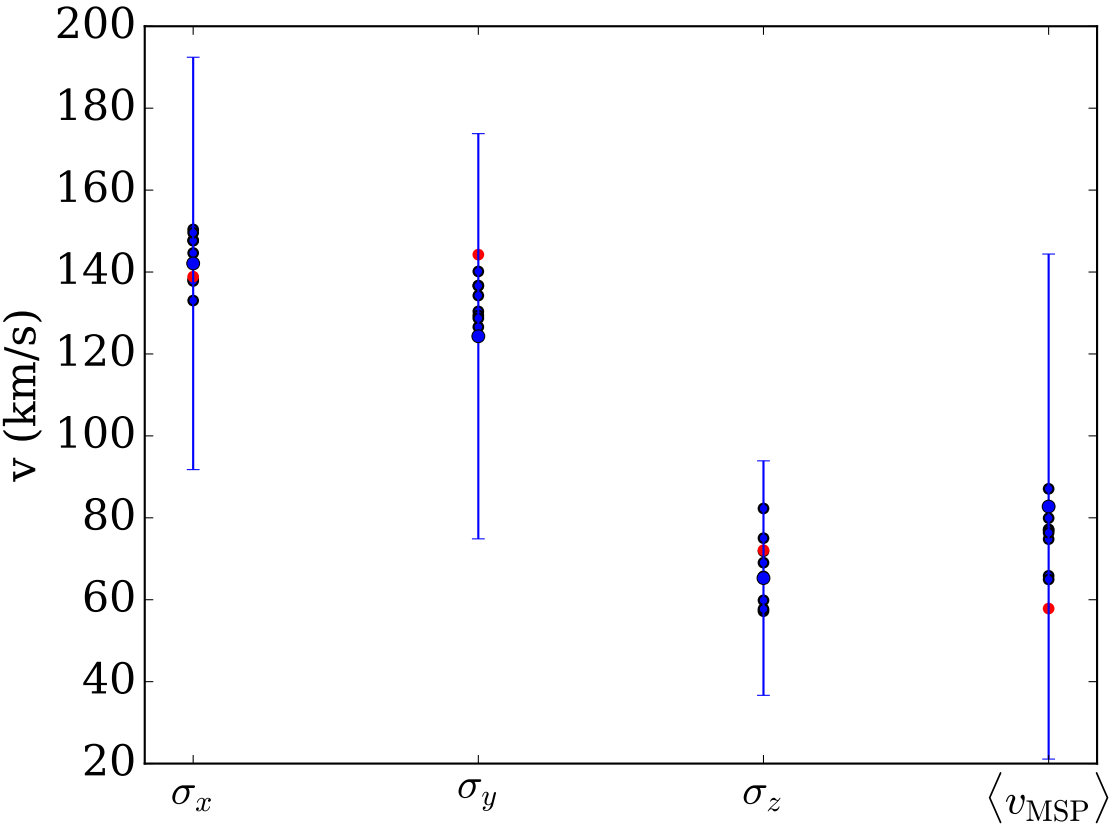

Figure 3.3: The estimates obtained with the maximum likelihood method for nine synthetic catalogues with 95 % (blue dots) confidential interval estimated using the first catalogue. The red dots show an estimate of the parameters obtained directly for synthetic velocities.

66% of objects drawn from the isotropic maxwellian velocity distribution with $\sigma = 38$ km/s and 34% of objects drawn from an anisotropic maxwellian distribution describes the MSP velocities much better (AIC=5.26) than a sum of two isotropic maxwellians (model B) with fixed rotational speed $\langle v_{\rm MSP} \rangle = 220$ km/s.

Models which fit the $\langle v_{\rm MSP} \rangle$ value do not include any physics, nevertheless the estimate of this value is in excellent agreement with what can be expected from the Galactic dynamic. When σ is small, the value of $\langle v_{\rm MSP} \rangle$ is close to $v_R(R_\odot)$.

As it is clear from the tests performed for synthetic catalogues, the false bimodality does not appear in the result of the maximum likelihood analysis even if the real anisotropic velocity distribution is fitted with an isotropic model. Therefore, I conclude that the bimodality of the velocity distribution is the most prominent effect which dominates the MSP distribution.

Table 3.3: he results of the maximum likelihood optimisations for different velocity models. The 95% confidence interval for model parameters is quoted, $\langle v \rangle$ stands for $\langle v_{\rm MSP} \rangle$. A,...,E are the model labels.

	Components of the model									$-L$
	Isotropic Maxwellian		Isotropic Maxwellian			Anisotropic Maxwell				
	σ range (km/s)	$\langle v \rangle$ range (km/s)	σ range (km/s)	$\langle v \rangle$ range (km/s)	w range %	σ_x range (km/s)	σ_y range (km/s)	σ_z range (km/s)	$\langle v \rangle$ range (km/s)	
A	85 70-106	220 fixed	—	—	—	—	—	—	—	491.10
B	181 43-319	220 fixed	50 29-71	220 fixed	82 50-97	—	—	—	—	482.48
C	156 41-271	196 166-226	50 35-65	37 0-257	86 50-100	—	—	—	—	479.04
D	—	—	—	—	—	97 68-194	106 71-141	29 3-55	167 127-207	484.54
E	—	—	38 25-51	220 fixed	66 46-86	132 58-206	20 1-80	150 58-242	105 66-144	476.85

Some more complicated models are tested. None of them provides sufficiently better or realistic fit to be included in the results. A model with fixed $\sigma_x = \sigma_y$ values provides a worse fit and give $\langle v_{\rm MSP} \rangle < 0$. A model with a sum of two anisotropic maxwellian gives likelihood difference $2\Delta \log L = 2.4$ (AIC = -3.6) with model E which is not enough to justify an addition of a few more parameters. The value for σ_y is also quite low in that model $\sigma_y = 42$ km/s.

3.6 Discussion

3.6.1 Quality of the timing parallax

The quality of the parallax measurement is crucial for the analysis of the velocity distribution. Objects with overestimated parallax (underestimated errors) appears to be much faster than they are.

Moreover, when the anisotropic velocity distribution is fitted for all the pulsars with measured parallax (including objects with $\varpi'/\sigma_\varpi < 3$) and proper motion, a strange answer with $\sigma_z = 3 \pm 2$ km/s keeps appearing. Such a low value cannot possibly occur in the Galaxy because the natural velocity dispersion for the stars is $15 - 30$ km/s. The millisecond radio pulsars receive an extra kick which should increase the spread in velocity and is extremely unlikely to decrease it.

Already the analysis of individual likelihoods reveals the puzzling nature of this result, see Figure 3.5. The pulsars which testify for the extremely low value of the σ_z (from J1853+1303 till J1923+2515) are concentrated in the same part of the sky. This position in the sky is very close to the galactic centre direction. A check for the coordinate transformation did not reveal any problem. The measurements for distance and proper motion of these pulsars came from different sources.

The effect can be explained as follows. When the measurements of poor quality are introduced, the error distribution might deviate from the assumed Gaussian, and larger distances (up to bulge of the Galaxy) are possible for these pulsars, e.g. J1903+0327 has DM = 297.5 cm^{-3} pc. At such large distances the vertical component of the velocity cannot be measured (leads to $\mu_b \approx 0$), while the horizontal component appears because of the asymmetric drift.

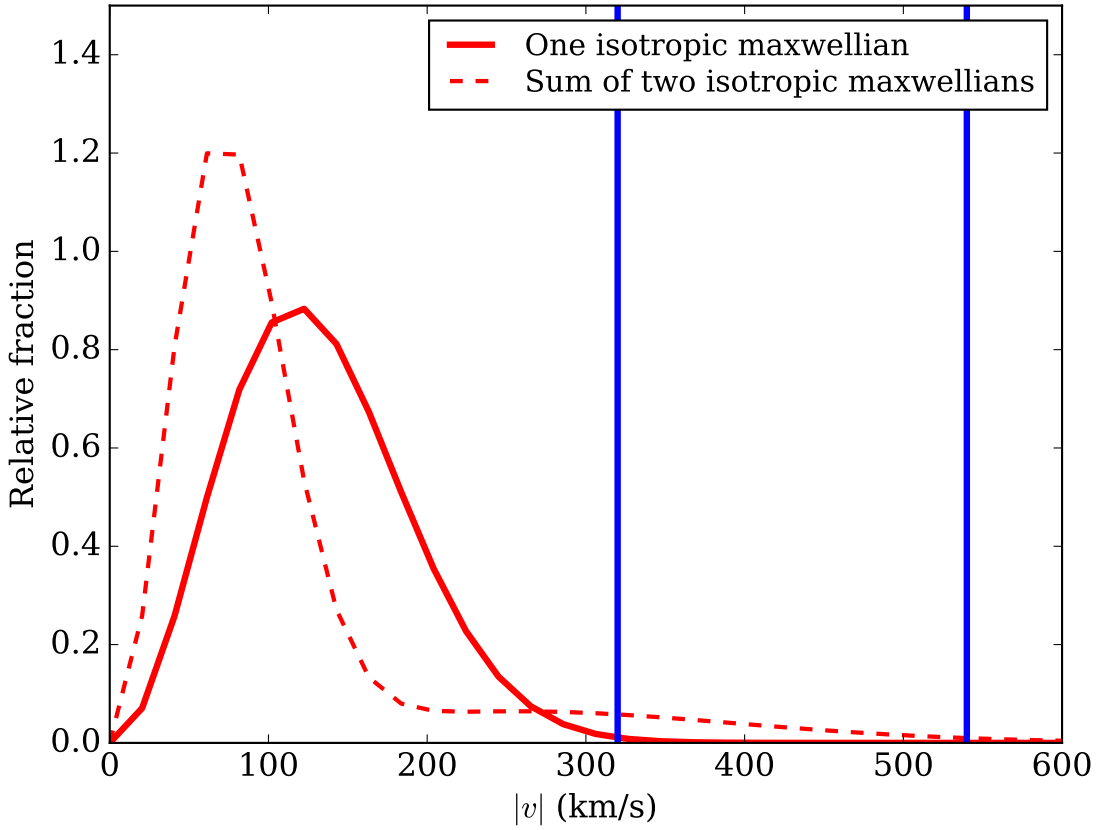

Figure 3.4: Results of the maximum likelihood method for two isotropic velocity distributions. The solid red line shows the single isotropic maxwellian with $\sigma = 83$ km/s, the dashed red line shows sum of two isotropic maxwellians with $w = 0.16$, $\sigma_1 = 183$ and $\sigma_2 = 50$ km/s. The blue line shows the extra velocity which is required to escape from the Galaxy in the Solar vicinity for the direction of the Galactic rotation (320 km/s) and in orthogonal direction (544 km/s) [Smith et al., 2007].

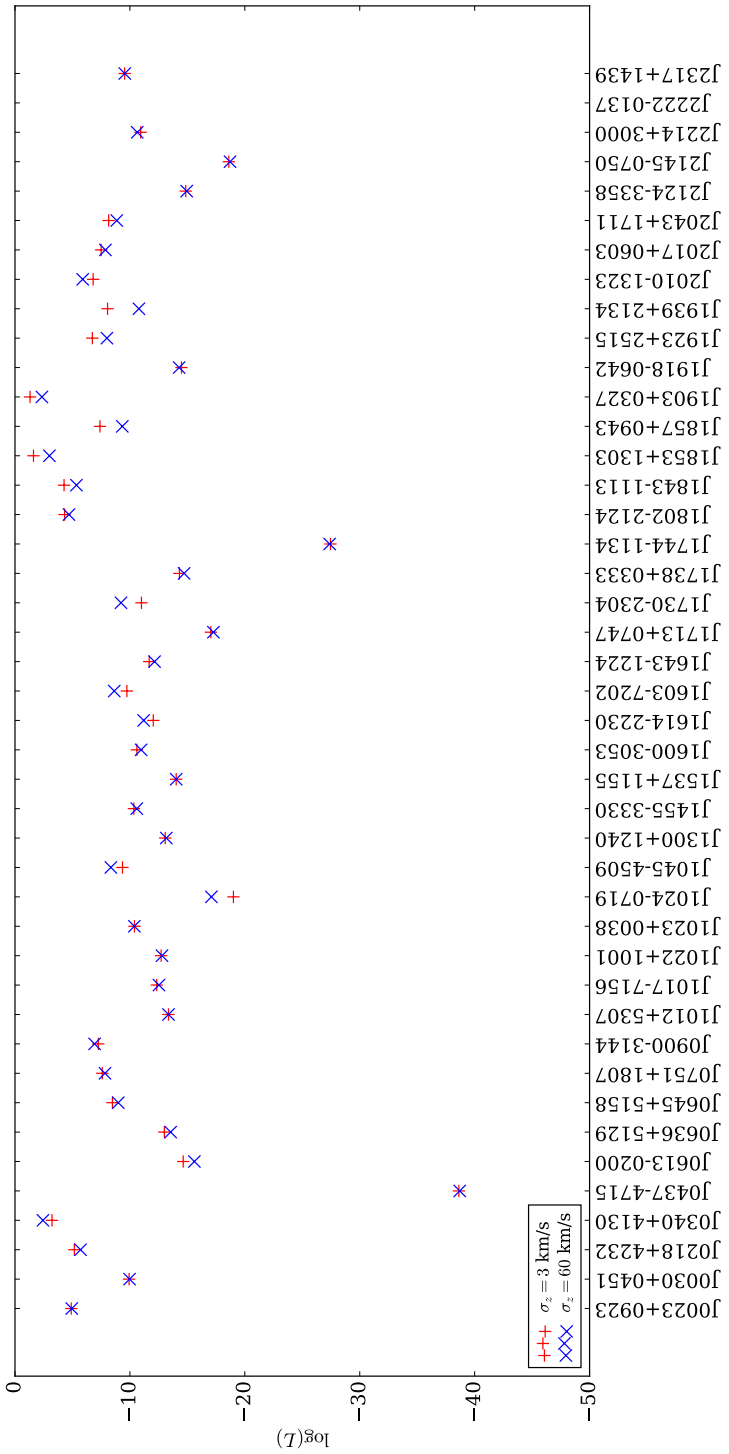

Figure 3.5: The contribution of individual pulsars to the total likelihood for the single anisotropic maxwellian velocity distribution with $\sigma_x = 121$, $\sigma_y = 115$ $\langle v_{\rm MSP} \rangle = 177$ fitted for all MSPs including objects with $\varpi'/\sigma_\varpi < 3$. PSR J2222-0137 is outside the plot because of its large $log(L) = -120$. Its likelihood does not favour the extremely low v_z value.

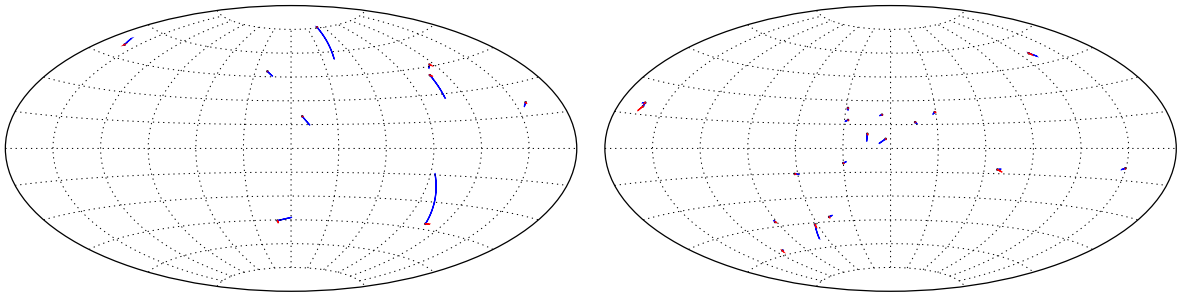

Figure 3.6: The sky location in the Galactic coordinate system and the proper motions (blue line shows the displacement during 0.5 Myr) for MSPs identified as high (left panel) and low (right panel) velocity objects according to the model which includes isotropic and anisotropic maxwellian velocity distribution.

3.6.2 High-velocity objects

The anisotropic velocity distribution in model E is not well defined. The reason for this is that a high-velocity part is represented only by 9 out of 27 MSPs with satisfactory parallax measurements. Figure 3.6 (left panel) shows the location of objects which prefer the anisotropic distribution to isotropic on the sky. These objects are concentrated toward high latitudes as expected for the high-velocity component. There is an absence of sources at $l = 30 - 180$, $b < 0$ which may be due to the small number statistics. This group of MSPs is not otherwise special. All of them, except PSRJ 2124-3358, are in binaries which are very common for MSPs. The secondary components are a helium white dwarf (PSR J0437-4715, J0751+1807, 1012+5307), main sequence star (PSR J1023+0038, J1024-0719), planet (PSR J 1300+1240), carbon-oxygen white dwarf (PSR J1614-2230) and a neutron star (PSR J 1537+1155). The eccentricity varies from few times 10^{-6} for objects with a white dwarf companion, to 0.27368 for the binary neutron star [Fonseca et al., 2014]. The parallax and proper motion measurements are compiled for these objects from different articles and include both timing and interferometric technique. The orbital periods vary from 0.198 days for PSR J10203+0038 till 8.7 days for PSR J1614-2230.

One object PSR J1024-0719 increases σ_z and its uncertainty quite significantly which might be related to its triple origin.

The spin-down distribution is different for the high and low-velocity subpopulations (p value of the Kolmogorov-Smirnov test 0.01). The high-velocity objects have smaller spin-down ages on average, therefore scattering by stars or molecular clouds cannot be responsible for their high velocities. The velocity dispersion of the high-velocity subpopulation is comparable to that for the halo objects (for which see Brown et al. 2010).

3.6.3 Low-velocity objects

The low-velocity MSPs are more numerous than high-velocity ones. The maximum likelihood estimator attributes 18 MSPs to this component. Their location is shown in the sky map Figure 3.6 (right panel). These objects concentrate more toward the Galactic plane as expected except for five pulsars at $|b| > 30$. Four out of five of these objects are at small distances: PSR J0030+0451

(nominal distance $D' = 1/\varpi' = 0.36$ kpc), J1022+1001 ($D' = 0.7$ kpc), J2145-0750 ($D' = 0.63$ kpc), J2222-0137 ($D' = 0.27$ kpc). Their low z's are compatible with the low velocity origin. The notable exception is PSR J2317+1439 with a nominal distance $D' = 1.42$ kpc and $z = 0.9$ kpc. This discrepancy (low systemic velocity and high vertical distance) can be explained if this pulsar has a large radial velocity.

Most MSPs attributed to the low-velocity component are in binaries with a helium or carbon-oxygen white dwarf, with the only exception of PSR J0636+5129 which has an ultra-light component. The eccentricities ranges from 3.4×10^{-7} for J1738+0333 [Freire et al., 2012] till 1.7×10^{-4} for J1600-3053 [Desvignes et al., 2016]. The orbital periods are quite different from the high-velocity population. They range from 0.355 days for J1738+0333 till 147.01728 for J1643-1224. In general, this subpopulation has much longer periods than the high-velocity ones. This may be explained by the fact that a high natal kick preferably destroys binaries with long orbital period, especially ones exceeding ten days. It may also be an explanation of the relation between final orbital period and space velocity suggested by Tauris & Bailes [1996].

3.6.4 Implication for binary stellar evolution

Compared to the velocity distribution which can be derived based on parallax and proper motions of the isolated young radio pulsars, the MSP sample should overrepresent the low-velocity component. If there is a physical channel which leads to formation of such NSs, a fraction of low-velocity MSPs should be larger than the fraction of low-velocity isolated pulsars.

In the young radio pulsars, the low-velocity component can be represented with an isotropic maxwellian distribution with $\sigma = 60 - 95$ km/s (68% interval), see Verbunt et al. [2017]. In the MSP sample the low velocity component has $\sigma = 50$ km/s (C model), or $\sigma = 38$ km/s (E model). Both of these two values correspond to virtually zero natal kick (10-25 km/s) which a significant fraction of the neutron stars receive during the supernova explosion.

It is possible to speculate and try to assign both low-velocity components to the same origin. For brevity, I denote event in which a low-velocity NS is produced as SNLNK. The SNLNK might be attributed to the electron capture supernova explosion or to the accretion induced collapse of a white dwarf. The low-velocity subpopulation is so numerous that it cannot be explained by the number of stripped stars in binaries.

If both low-velocity MSPs and isolated radio pulsars have the same SNLNK origin, the difference between the velocities can be explained because the isolated neutron stars receive an additional Blaauw kick [Blaauw, 1961] of the order a few tens km/s due to the binary disruption and mass loss. Vice versa, any SNLNK in the MSP sample will be scaled down to form the systemic velocity. The proper consideration of the kick influence on the population of MSPs and young radio pulsars requires a binary population synthesis which is outside of the scope of this article.

The fraction of NS formed through the SNLNK channel ($\approx 40\%$; computed back to the initial population) is in agreement with the bimodality observed in Knigge et al. [2011].

3.7 Conclusions

The velocity distribution of MSPs based on new timing and interferometric parallaxes and proper motions is studied, with the maximum likelihood method both for isotropic and anisotropic velocity distributions. The method itself is tested with synthetic catalogues.

It is found that:

- When the data from the kinematic simulations are used to generate the synthetic catalogue, the maximum likelihood method correctly finds the single component distribution and estimates the anisotropy reasonably well.
- The optimum parameter for a single isotropic maxwellian $\sigma = 85$ km/s is in perfect agreement with a previous analysis of the MSP velocity ensemble [Toscano et al., 1999]. This model is not preferable statistically: its probability is 10^{-4}.
- The bimodal velocity distributions fit much better compared to unimodal isotropic and anisotropic distributions. The fraction of the high-velocity component is 0.18 for the isotropic fit and 0.33 for the anisotropic fit.
- The low-velocity component is mostly isotropic with $\sigma = 38 \pm 13$ km/s which is in good agreement with the velocity dispersion of old stars in the disk [Holmberg et al., 2009].
- The high velocity subpopulation orbits the Galactic centre slowly $\langle v_{\rm MSP} \rangle = 105$ km/s (asymmetric drift) while the low-velocity subpopulation has $\langle v_{\rm MSP} \rangle$ comparable with circular velocity of the Sun.
- The high-velocity subpopulation is very diverse and includes binaries with a white dwarf, main sequence, planet and neutron star companions. The maximum orbital period found in this subpopulation is 8.7 days for J1614-2230. On the other hand, the low-velocity subpopulation despite being more numerous is surprisingly homogeneous. Most of MSPs in this subpopulation are in binaries with a white dwarf companion. The maximum orbital period is 147 days for J1643-1224. It is evidence of the anticorrelation between orbital period and the systemic velocity [Tauris & Bailes, 1996].

3.A Master file

The values for the parallax and proper motions for MSPs are presented in Table 3.4.

Table 3.4: The list of MSP with measured parameters. † means that the proper motion measurement is in the ecliptic coordinate system. A number between brakets is the error in the last digit. B/I stands for binary/isolated MSP.

Name	B/I	l	b	P (ms)	$\log\tau$ (yr)	$\mu'_{\alpha*}, \sigma_\alpha$ (mas/yr)	$\mu'_\delta, \sigma_\delta$ (mas/yr)	ϖ', σ_ϖ (mas)	Ref.
J0023+0923	B	111.38	-52.85	3.050	9.63	-13.9(2)†	-1(1)†	0.4(3)	12
J0030+0451	I	113.14	-57.61	4.865	9.88	-5.9(5)	-0.2(11)	2.79(23)	7
J0034-0534	B	111.49	-68.07	1.877	9.78	7.9(8)	-9.9(17)	<7.4	11
J0218+4232	B	139.51	-17.53	2.323	8.68	5.35(5)	-3.74(12)	0.16(9)	4
J0340+4130	I	153.78	-11.02	3.299	9.87	-2.4(8)†	-4(1)†	0.7(7)	12
J0437-4715	B	253.39	-41.96	5.757	9.20	121.4385(20)	-71.4754(20)	6.37(9)	14
J0610-2100	B	227.75	-18.18	3.861	9.70	9.21(6)	16.73(8)	<1.3	11
J0613-0200	B	210.41	-9.30	3.062	9.70	1.822(8)	-10.355(17)	1.25(13)	7
J0614-3329	B	240.50	-21.83	3.149	9.46	0.58(9)	-1.92(12)	<2.2	11
J0636+5129	B	163.91	18.64	2.869	10.13	4.3(9)	2(1)	4.9(6)	15
J0645+5158	I	163.96	20.25	8.853	10.46	2.1(1)†	-7.3(2)†	1.3(3)	12
J0751+1807	B	202.73	21.09	3.479	9.85	-2.73(5)	-13.4(3)	0.82(17)	7
J0900-3144	B	256.16	9.49	11.110	9.56	-1.01(5)	2.02(7)	0.77(44)	7
J1012+5307	B	160.35	50.86	5.256	9.69	2.609(8)	-25.482(11)	0.71(17)	7
J1017-7156	B	291.56	-12.55	2.339	10.22	-7.31(6)	6.76(5)	3.9(12)	13
J1022+1001	B	231.79	51.10	16.453	9.78	-14.86(4)	5.59(3)	1.43(3)	3
J1023+0038	B	243.49	45.78	1.688	9.35	4.76(3)	-17.34(4)	0.731(22)	1
J1024-0719	B	251.70	40.52	5.162	9.64	-35.255(19)	-48.19(4)	0.77(11)	6
J1045-4509	B	280.85	12.25	7.474	9.83	-6.07(9)	5.20(10)	2.2(11)	14
J1231-1411	B	295.53	48.39	3.684	9.41	-62.03(26)	6.2(5)	<1.8	11
J1300+1240	B	311.31	75.41	6.219	8.94	46.44(8)	-84.87(32)	1.41(8)	5
J1455-3330	B	330.72	22.56	7.987	9.72	7.88(5)	-1.90(12)	0.99(22)	11
J1537+1155	B	19.85	48.34	37.904	8.39	1.482(7)	-25.285(12)	0.86(18)	9
J1600-3053	B	344.09	16.45	3.598	9.78	-0.940(19)	-6.94(7)	0.64(7)	7
J1603-7202	B	316.63	-14.50	14.842	10.18	-2.46(4)	-7.33(5)	1.1(8)	14

Table 3.4: The list of MSP with measured parameters. † means that the proper motion measurement is in the ecliptic coordinate system. A number between brakets is the error in the last digit. B/I stands for binary/isolated MSP.

Name	B/I	l	b	P (ms)	$\log\tau$ (yr)	$\mu'_{\alpha*},\sigma_\alpha$ (mas/yr)	$\mu'_\delta,\sigma_\delta$ (mas/yr)	ϖ',σ_ϖ (mas)	Ref.
J1614-2230	B	352.64	20.19	3.151	9.72	3.87(12)	-32.3(7)	1.30(9)	11
J1640+2224	B	41.05	38.27	3.163	10.25	4.20(1)†	-10.73(2)†	<0.6	12
J1643-1224	B	5.67	21.22	4.622	9.60	5.94(5)	3.94(18)	1.27(19)	14
J1713+0747	B	28.75	25.22	4.570	9.93	5.260(2)†	-3.442(5)†	0.85(3)	12
J1730-2304	I	3.14	6.02	8.123	9.80	20.7(4)	8.3(83)	1.19(27)	11
J1738+0333	B	27.72	17.74	5.850	9.58	7.037(5)	5.073(12)	0.68(5)	10
J1741+1351	B	37.89	21.64	3.747	9.29	-8.8(1)†	-7.6(2)†	<0.5	12
J1744-1134	I	14.79	9.18	4.075	9.86	18.790(6)	-9.40(3)	2.53(7)	14
J1747-4036	I	350.21	-6.41	1.646	9.30	0.1(8)†	-6(1)†	<0.7	12
J1756-2251	B	6.50	0.95	28.462	8.65	-2.42(8)	<20	1.05(55)	8
J1802-2124	B	8.38	0.61	12.648	9.44	-1.13(12)	-3(4)	1.24(57)	7
J1811-2405	B	7.07	-2.56	2.661	9.50	0.65(14)	-9.1(52)	<0.4	11
J1843-1113	I	22.05	-3.40	1.846	9.49	-1.91(7)	-3.2(3)	0.69(33)	7
J1853+1303	B	44.87	5.37	4.092	9.87	-1.82(15)†	-2.9(4)†	0.1(5)	12
J1857+0943	B	42.29	3.06	5.362	9.68	-2.649(17)	-5.41(3)	0.70(26)	7
J1903+0327	B	37.34	-1.01	2.150	9.26	-3.5(3)†	-6.2(9)†	0.4(8)	12
J1909-3744	B	359.73	-19.60	2.947	9.52	-9.517(5)	-35.797(17)	0.810(3)	14
J1910+1256	B	46.56	1.80	4.984	9.91	-0.7(1)†	-7.2(2)†	<0.7	12
J1918-0642	B	30.03	-9.12	7.646	9.67	-7.93(2)†	-4.85(9)†	1.1(2)	12
J1923+2515	I	58.95	4.75	3.788	9.80	-9.5(2)†	-12.8(5)†	2.(1)	12
J1939+2134	I	57.51	-0.29	1.558	8.37	0.070(4)	-0.401(5)	0.22(8)	7
J1944+0907	I	47.16	-7.36	5.185	9.68	9.42(13)†	-25.5(4)†	<0.4	12
J1949+3106	B	66.86	2.55	13.138	9.35	13(15)†	10(13)†	<7	12
J1955+2908	B	65.84	0.44	6.133	9.51	-1.8(9)†	-4.4(14)†	<2	12
J2010-1323	I	29.45	-23.54	5.223	10.23	1.16(4)†	-7.3(4)†	0.1(2)	12

Table 3.4: The list of MSP with measured parameters. † means that the proper motion measurement is in the ecliptic coordinate system. A number between brakets is the error in the last digit. B/I stands for binary/isolated MSP.

Name	B/I	l	b	P (ms)	$\log \tau$ (yr)	$\mu'_{\alpha*}, \sigma_\alpha$ (mas/yr)	$\mu'_\delta, \sigma_\delta$ (mas/yr)	ϖ', σ_ϖ (mas)	Ref.
J2017+0603	B	48.62	-16.03	2.896	9.76	2.35(8)	0.17(16)	1.2(5)	11
J2043+1711	B	61.92	-15.31	2.380	9.86	-8.97(7)†	-8.5(1)†	0.8(2)	12
J2124-3358	I	10.93	-45.44	4.931	9.58	-14.14(4)	-50.08(9)	2.4(4)	14
J2145-0750	B	47.78	-42.08	16.052	9.93	-9.46(5)	-9.08(6)	1.63(4)	3
J2214+3000	B	86.86	-21.67	3.119	9.53	20.90(11)	-1.55(15)	1.7(9)	11
J2222-0137	B	62.02	-46.08	32.818	9.95	44.72(2)	-5.64(6)	3.743(10)	2
J2302+4442	B	103.40	-14.00	5.192	9.78	-3.3(6)†	-1(2)†	<2	12
J2302+4442	B	103.40	-14.00	5.192	9.78	-0.05(13)	-5.85(12)	<2.5	11
J2317+1439	B	91.36	-42.36	3.445	10.35	0.19(2)†	3.80(7)†	0.7(2)	12

3.B Asymmetric drift

The velocity drawn from the maxwellian velocity distribution has zero first moments $\langle v_x \rangle = 0$, $\langle v_y \rangle = 0$ and $\langle v_z \rangle = 0$. The MSP originated from a disc population and followed the flat rotational curve in the Galaxy. Therefore, angular momentum conservation requires $\langle v_{\rm MSP} \rangle \neq 0$ as found by Toscano et al. [1999]. The proper motion measurements provide an estimate of the relative velocity because they are performed from the Earth which orbits together with the Sun around the Galactic centre. To correct each actual proper motion for these effects, I derive equations for $\mu_{l,G}$ and $\mu_{b,G}$ starting from three-dimensional velocities.

The local standard of the rest for the Sun moves with the velocity $v_R(R_\odot)$ around the Galactic centre. The Sun has peculiar velocity $[U, V, W]$ with respect to its local standard of rest with component U directed toward the Galactic centre, V in the direction of the Galactic rotation and W perpendicular to the Galactic plane. The MSP moves with average velocity $\langle v_y \rangle = \langle v_{\rm MSP} \rangle$ in the direction of the Galactic rotation. According to these definitions, the total velocity of the Sun can be written as:

$$\vec{v}_\odot = [U, V + v_R(R_\odot), W] \tag{3.38}$$

The total velocity of the MSP:

$$v_p = [v_x + \langle v_{\rm MSP} \rangle \sin\theta, v_y + \langle v_{\rm MSP} \rangle \cos\theta, v_z] \tag{3.39}$$

where θ is the angle between the Sun and the pulsar measured from the Galactic centre.

The measured proper motion in latitudinal direction appears because of the relative motion of the pulsar to the Sun:

$$(\vec{v}_p - \vec{v}_\odot) \cdot \vec{l} = \mu_{l*} D = (\mu_{l*,v} + \mu_{l,G}) D \tag{3.40}$$

where $\vec{l}$ is the first line of the R_G matrix (see Appendix D) which transforms a component of the U, V, W velocity to the l, b, r velocities:

$$\vec{l} = [-\sin l, \cos l, 0]. \tag{3.41}$$

Therefore:

$$\mu_{l,G} D = (\vec{v}_p - \vec{v}_\odot) \cdot \vec{l} - [v_x, v_y, v_z] \cdot \vec{l} \tag{3.42}$$

After some algebra this expression is simplified to:

$$\mu_{l,G} D = U \sin l - (V + v_R(R_\odot)) \cos l + \langle v_{\rm MSP} \rangle \cos(\theta + l) \tag{3.43}$$

In the case of the b component, the equation can be written as:

$$\mu_{b,G} D = (\vec{v}_p - \vec{v}_\odot) \cdot \vec{b} - [v_x, v_y, v_z] \cdot \vec{b} \tag{3.44}$$

with $\vec{b}$ in form:

$$\vec{b} = [-\sin b \cos l, -\sin b \sin l, \cos b] \tag{3.45}$$

After some algebra the result is:

$$\begin{aligned} \mu_{b,G} D = {} & U \sin b \cos l - \langle v_{\rm MSP} \rangle \sin b \sin(\theta + l) \\ & + (V + v_R(R_\odot)) \sin b \sin l - W \cos b \end{aligned} \tag{3.46}$$

3.C Coordinate transformations

For the sake of completeness, I gather here the coordinate transformations which are used in the article. The proper motion measurements are performed in the equatorial or ecliptic coordinates. Therefore, a transformation is necessary to obtain the actual proper motion in the coordinate system of the measurements.

3.C.1 Galactic to the equatorial coordinate system

The equations are derived by Poleski [2013] and Verbunt et al. [2017]. The local angle between the Galactic and the equatorial coordinate system can be computed as:

$$\tan\tilde{\chi} = \frac{-\cos(l - l_\Omega)}{\tan\delta_{\rm GP}\cos b - \sin(l - l_\Omega)\sin b} \tag{3.47}$$

with

$$\delta_{\rm GP}^{(2000)} = 27^\circ.12825\,,\ l_\Omega^{(2000)} = 32^\circ.93192 \tag{3.48}$$

where $\delta_{\rm GP}$ is the equatorial coordinate of the galactic pole and l_Ω is the galactic longitude of the node.

3.C.2 Galactic to the ecliptic coordinate system

The relation between the ecliptic and the Galactic coordinate system can be written in the following form, see e.g. Leinert et al. [1998]:

$$\cos(\lambda - \lambda_{\rm GP} - \pi/2)\cos\beta = \cos(l - l_o)\cos b \tag{3.49}$$

$$\sin(\lambda - \lambda_{\rm GP} - \pi/2)\cos\beta = \sin\beta_{\rm GP}\sin(l - l_o)\cos b - \cos\beta_{\rm GP}\sin b \tag{3.50}$$

$$\sin\beta = \cos\beta_{\rm GP}\sin(l - l_o)\cos b + \sin\beta_{\rm GP}\sin b \tag{3.51}$$

These equations are derived using spherical trigonometry for a triangle with vertices: the Galactic pole, the ecliptic pole and a source. The first equation is derived using the sine rule, the second using the five-part rule, and the third using the cosine rule. If the two last equations are applied to the Galactic centre $l = 0, b = 0$, one finds:

$$\tan l_o = \frac{\cos(\lambda_{\rm GC} - \lambda_{\rm GP})}{\sin(\lambda_{\rm GC} - \lambda_{\rm GP})\sin\beta_{\rm GP}} \tag{3.52}$$

The values for the location of the Galactic pole and centre in the ecliptic coordinate system in 2000 are gathered in Perryman & ESA [1997]:

$$\lambda_{\rm GP} = 180^\circ02322\,,\ \beta_{\rm GP} = 29^\circ81144 \tag{3.53}$$

$$\lambda_{\rm GC} = 266^\circ83952, \quad \beta_{\rm GC} = -5^\circ53632 \tag{3.54}$$

which results in:

$$l_o = 6^\circ.38397 \tag{3.55}$$

The longitude of the node is computed here with a better precision than in Leinert et al. [1998]. To obtain a transformation for proper motion written in the Galactic coordinate system to the ecliptic coordinate system, I differentiate the last equation eq.(3.51) and compare the result to a definition:

$$\mu_\beta = -\mu_l \sin\tilde{\chi} + \mu_b \cos\tilde{\chi} \tag{3.56}$$

which gives:

$$\tan\tilde{\chi} = \frac{-\cos(l - l_O)}{\tan\beta_{\rm GP}\cos b - \sin(l - l_O)\sin b} \tag{3.57}$$

3.D Anisotropic velocity distribution

The function $\Theta(\xi_1, \xi_2)$ can be derived from the following principles. The anisotropic maxwellian distribution is:

$$f(v_x, v_y, v_z, \sigma_x, \sigma_y, \sigma_z)dv_x dv_y dv_z \propto$$
$$\propto \frac{1}{\sqrt{8\pi^3}\sigma_x\sigma_y\sigma_z}\exp\left(-\frac{v_x^2}{2\sigma_x^2} - \frac{v_y^2}{2\sigma_y^2} - \frac{v_z^2}{2\sigma_z^2}\right)dv_x dv_y dv_z \tag{3.58}$$

The use of the common denominator $2\sigma_x^2\sigma_y^2\sigma_z^2$ gives:

$$f(v_x, v_y, v_z, \sigma_x, \sigma_y, \sigma_z)dv_x dv_y dv_z \propto \frac{1}{\sqrt{8\pi^3}\sigma_x\sigma_y\sigma_z}$$
$$\times \exp\left(-\frac{v_x^2\sigma_y^2\sigma_z^2 + v_y^2\sigma_x^2\sigma_z^2 + v_z^2\sigma_x^2\sigma_y^2}{2\sigma_x^2\sigma_y^2\sigma_z^2}\right)dv_x dv_y dv_z \tag{3.59}$$

After the coordinate transformation from the Cartesian Galactic to the spherical system the velocity distribution becomes:

$$f(v_x, v_y, v_z, \sigma_x, \sigma_y, \sigma_z)v^2\sin\xi_1 dv d\xi_1 d\xi_2 \propto \frac{v^2\sin\xi_1}{\sqrt{8\pi^3}\sigma_x\sigma_y\sigma_z}$$
$$\times \exp\left(-\frac{v_x^2\sigma_y^2\sigma_z^2 + v_y^2\sigma_x^2\sigma_z^2 + v_z^2\sigma_x^2\sigma_y^2}{2\sigma_x^2\sigma_y^2\sigma_z^2}\right)dv d\xi_1 d\xi_2 \tag{3.60}$$

Here I use equations for the individual velocity components together with the definition of the spherical coordinate system. In this case the numerator in exponential is written as:

$$\Theta(\xi_1, \xi_2) = \frac{v_x^2\sigma_y^2\sigma_z^2 + v_y^2\sigma_x^2\sigma_z^2 + v_z^2\sigma_x^2\sigma_y^2}{v^2} =$$
$$\sigma_y^2\sigma_z^2[-\sin\xi_1\cos\xi_2(\sin l\cos\tilde{\chi} + \sin b\cos l\sin\tilde{\chi})$$
$$+\sin\xi_1\sin\xi_2(\sin l\sin\tilde{\chi} - \sin b\cos l\cos\tilde{\chi}) + \cos\xi_1\cos b\cos l]^2$$
$$+\sigma_x^2\sigma_z^2[\sin\xi_1\cos\xi_2(\cos l\cos\tilde{\chi} - \sin b\sin l\sin\tilde{\chi})$$
$$+\sin\xi_1\sin\xi_2(-\cos l\sin\tilde{\chi} - \sin b\sin l\cos\tilde{\chi}) + \cos\xi_1\cos b\sin l]^2$$
$$+\sigma_x^2\sigma_y^2[\sin\xi_1\cos\xi_2\cos b\sin\tilde{\chi} + \sin\xi_1\sin\xi_2\cos b\cos\tilde{\chi} + \cos\xi_1\sin b]^2 \tag{3.61}$$

And the velocity distribution becomes:

$$f(v,\xi_1,\xi_2,\sigma_x,\sigma_y,\sigma_z)\,v^2\sin\xi_1 dv d\xi_1 d\xi_2 \propto \frac{v^2\sin\xi_1}{\sqrt{8\pi^3}\sigma_x\sigma_y\sigma_z} \times \exp\left(-\frac{v^2\Theta(\xi_1,\xi_2)}{2\sigma_x^2\sigma_y^2\sigma_z^2}\right) dv d\xi_1 d\xi_2 \tag{3.62}$$

Sieh diese Wolkenlandschaft mit ihren Himmelsstreifen! Beim ersten Blick möchte man meinen, die Tiefe sei dort, wo es am dunkelsten ist, aber gleich nimmt man wahr, daß dieses Dunkle und Weiche nur die Wolken sind und daß der Welraum mit seiner Tiefe erst an den Rändern und Fjorden dieser Wolkengebirge beginnt und ins Unendliche sinkt, darin die Sterne stehen, feierlich und für uns Menschen höchste Sinnbilder der Klarheit und Ordnung. Nicht dort ist die Tiefe der Welt und ihrer Geheimnisse, wo die Wolken und die Schwärze sind, die Tiefe ist im Klaren und Heiteren.

– Herman Hesse, das Glasperlenspiel

Chapter 4

Post fall-back evolution of multipolar magnetic fields and radio pulsar activation

Andrei Igoshev, Justin Elfritz, Sergei Popov

MNRAS, 2017, 462, 4, 3689

Abstract

It has long been unclear if the small-scale magnetic structures on the neutron star (NS) surface could survive the fall-back episode. The study of the Hall cascade [Cumming, Arras, & Zweibel, 2004; Wareing & Hollerbach, 2009] hinted that energy in small scales structures should dissipate on short timescales. Our new 2D magneto-thermal simulations suggest the opposite. For the first ∼10 kyrs after the fall-back episode with accreted mass $10^{-3}M_{\odot}$, the observed NS magnetic field appears dipolar, which is insensitive to the initial magnetic topology. In framework of the Ruderman & Sutherland [1975] vacuum gap model during this interval, non-thermal radiation is strongly suppressed. After this time the initial (i.e. multipolar) structure begins to re-emerge through the NS crust. We distinguish three evolutionary epochs for the re-emergence process: the growth of internal toroidal field, the advection of buried poloidal field, and slow Ohmic diffusion. The efficiency of the first two stages can be enhanced when small-scale magnetic structure is present. The efficient re-emergence of high order harmonics might significantly affect the curvature of the magnetospheric field lines in the emission zone. So, only after few 10^4 yrs would the NS starts shining as a pulsar again, which is in correspondence with radio silence of central compact objects (CCOs). In addition, these results can explain the absence of good candidates for thermally emitting NSs with freshly re-emerged field among radio pulsars (Bogdanov, Ng, & Kaspi 2014), as NSs have time to cool down, and supernova remnants can already dissipate.

4.1 Introduction

Young neutron stars (NSs) are sources with wide ranges of characteristic observables, inferred fundamental parameters, and different energy supplies. The timing, rotational, cooling, and magnetic properties all provide hints to the coupled evolution (see Harding 2013 and references therein). The main classes of NSs include standard radio pulsars (PSRs), the soft gamma repeaters (SGRs) and anomalous X-ray pulsars (AXPs), the nearby cooling NSs called the "Magnificent Seven" (M7), the rotating radio transients (RRATs), and the central compact objects (CCOs) in supernova remnants (SNRs). The evolutionary scenario called the "grand unification for NSs" (GUNS) [Kaspi, 2010; Igoshev, Popov, & Turolla, 2014], attempts to explain this variety of sources. Population synthesis studies have meanwhile yielded fruitful results. Popov et al. [2010] described PSRs, magnetars, and M7 in a unified picture, and these results were later extended and improved by Viganò et al. [2013a] and Gullón et al. [2014, 2015] with models covering larger ranges of parameter space, although CCOs were not included in these studies. The inclusion of CCOs have been discussed in a qualitative manner by Pons, Viganò, & Geppert [2012], but unification within the NS zoo remains problematic. A detailed population synthesis study of all known sub-populations of young NSs has not yet been successful, primarily because the birth process and subsequent evolution of CCO magnetic fields and observed emission remains an open question.

CCOs are young objects with typical ages of the order 10^4 yrs [de Luca, 2008]. These sources are characterized by relatively high surface temperatures and low dipolar (poloidal) fields (inferred from the spin-down period and period derivative). If these observable properties remain roughly unchanged on longer time scales, then we expect to see a significant population of low-field NSs in high-mass X-ray binaries (HMXBs), which have typical ages of $\sim 10^6$ up to a few 10^7 yrs. However as it was demonstrated in a detailed study by Chashkina & Popov [2012] no such systems had been observed. On the other hand, isolated CCOs could remain relatively hot until they have ages on the order 10^5 yrs, but such sources are not observed among nearby cooling NSs [Turolla, 2009], which implies that CCOs might "disappear" after $\sim 10^5$ yrs. The explanation for this disappearance was found in the scenario of field re-emergence after fall-back. Soon after a SN explosion, a significant amount of infalling material can blanket the NS surface due to the reverse shock [Chevalier, 1989], which can bury the NS magnetic field if the amount of material in the fall-back episode exceeds $\sim 10^{-4}$ - $10^{-3}\,M_\odot$ (which is a function of the magnetic field; see e.g. Bernal, Lee, & Page 2010). Following this process, the magnetic field then diffuses slowly back to the NS surface on a time scale $\sim 10^4 - 10^5$ yrs [Ho, 2011; Viganò & Pons, 2012; Bernal, Page, & Lee, 2013]. This screening can also be effective for large surface magnetic fields, leading to the so-called "hidden magnetar" scenario [Geppert, Page, & Zannias, 1999]. Several examples of such objects have been proposed, such as the NS in SNR Kes 79 [Shabaltas & Lai, 2012] and the NS in RCW103 [Popov, Kaurov, & Kaminker, 2015].

As the buried field diffuses through the crust towards the NS surface, one would expect to see an active magnetar or a PSR (Pons et al. 2012, Viganò & Pons 2012). This process is also known as magnetic field re-emergence. In this case, such PSRs would be observed to have a growing dipolar field component. Bogdanov et al. [2014] and Luo et al. [2015] conducted searches for evolved CCOs which would be observed as PSRs, but no such sources have been detected. It is

critical to explain the null results of these searches for evolved CCOs among radio pulsars.

In an earlier study, Viganò & Pons [2012] focused mostly on re-emergence of the dipole component. It is an oversimplification to think that the growth of dipolar component alone is enough for activation of pulsar emission. On the contrary, the weak dipolar magnetic field does not generally prevent NS from emitting non-thermal radiation (millisecond pulsars). Therefore it is essential to choose a condition which allows us to distinguish between active and dormant PSRs. The usual criterion for pulsar activity is the proximity of a source to the death line in the period – period derivative diagram. Studies of the pulsar ensemble consider three different aspects of the death line: observational – absence of known pulsars in the right lower corner of the period – period derivative diagram; theoretical – a drop in electric potential at the magnetic polar cap [Ruderman & Sutherland, 1975]; and populational – pile up of pulsars near the death line [Bhattacharya et al., 1992; Gonthier et al., 2002]. The general consensus is that all three of these aspects correspond to the same physical mechanism, but this conclusion is not final yet.

From the ATNF catalogue[1] [Manchester et al., 2005], the observed ensemble of normal radio pulsars is not strictly bounded to the right in the $P - \dot{P}$ diagram. A few pulsars lie below this line (see Fig. 4.1). One such source, J2144-3933, has a spin period 8.5 s [Young, Manchester, & Johnston, 1999]. Although spin-down magnetic fields for CCOs measured by period P and period derivative $\dot{P}$ are small, these objects are still well above the observed death line and should therefore shine as radio pulsars. The theoretical death line based on a pure dipolar magnetic field crosses the centre of the pulsar distribution [Medin & Lai, 2007b] and places some of the CCOs to the pulsar graveyard. To move the death line to its usual location, it is necessary to assume either a misalignment between the rotational and magnetic axes, or the presence of small-scale magnetic fields [Ruderman & Sutherland, 1975]. In pulsar population studies the pile up appears when neither luminosity nor magnetic field decay are assumed, and pulsars spend most of their lives in the region with characteristic ages $\sim 10^8$ yrs with nearly constant P and small $\dot{P}$, thereafter observing the paucity of these sources. Szary et al. [2014] suggested to consider a limit on radio efficiency which helps to avoid pile-up as well.

In the recent study by Szary, Melikidze, & Gil [2015], the small scale magnetic field is modelled with additional dipoles which allows to vary the curvature radius for the open field lines in large range $\sim 10^5 - 10^8$ cm. Subject to strong fall-back, the magnetic pole may be shifted to a new orientation. Therefore, we consider not just an additional small dipole at the polar cap region as it was suggested by Szary et al. [2015], but rather harmonics of high order which can provide the necessary radius of curvature in the NS emission zone.

There is an important theoretical uncertainty concerning evolution of small-scale magnetic structures in NS after a fall-back episode. The analysis of the Hall cascade properties [Cumming et al., 2004; Wareing & Hollerbach, 2009] provided arguments that energy in small scales structures should dissipate rapidly. Here we address this question with numerical modelling. In this paper we extend the first analysis performed by Viganò & Pons [2012] in two important aspects: we analyze and present evolution of high-order multipoles and study the non-thermal emission criterion to obtain an answer to the question if NSs with freshly re-emerged magnetic fields can be observed as radio pulsars or not.

[1] `http://www.atnf.csiro.au/research/pulsar/psrcat`

In §4.2 we briefly describe the numerical model used to conduct our simulations of magnetic field burial and evolution. In §4.3 we discuss simulation results employing a set of different initial conditions which vary in their prescribed multipolar structure. §4.4 contains an explanation of the numerical results in the context of the Hall cascade given our choice of initial conditions. Consequences for observable NS emission are presented in §4.5. Limitations of both the emission model and the numerical code are discussed in §4.6, along with applicability to pulsar searches. We present our conclusions in §4.7.

4.2 Method

We perform our numerical experiments using two dimensional (2D) magneto-thermal simulations which self-consistently evolve the coupled magnetic field and the temperature throughout the NS interior. The numerical model is the popular code developed in Viganò, Pons, & Miralles [2012], which is based on the earlier model of Pons, Miralles, & Geppert [2009]. The magnetic induction equation and the thermal evolution equation are coupled in non-trivial ways via the temperature-dependent electrical conductivity [Aguilera, Pons, & Miralles, 2008a], and it is necessary to evolve these equations as a system in order to correctly reproduce observed NS emission [Pons et al., 2009; Rea et al., 2012; Viganò et al., 2013a]. A brief overview of our numerical scheme is in order, although the interested reader is directed to these earlier studies for a more detailed treatment.

First, we prescribe an appropriate magnetic induction equation. We consider Hall-Ohmic evolution but also impose an advective electric field in our generalized Ohm's Law, such that the full induction equation is

$$\frac{\partial \vec{B}}{\partial t} = -\vec{\nabla} \times [\eta \vec{\nabla} \times \vec{B} + f_h(\vec{\nabla} \times \vec{B}) \times \vec{B} + \vec{v}_{\rm accr} \times \vec{B}]. \tag{4.1}$$

Here $\eta = c^2/4\pi\sigma$ is the magnetic diffusivity, and σ is the local, time-dependent electrical conductivity computed in the electron relaxation approximation. The time-independent Hall prefactor is $f_h = c/4\pi e n_e$ and has only radial dependence via the local electron density n_e. The velocity $\vec{v}_{\rm accr}$ allows us to manually bury the magnetic field during the accretion epoch, and takes the algebraic form

$$\vec{v}_{\rm accr} = -\frac{\dot{m}}{4\pi r^2 \rho(r)} \hat{r}, \tag{4.2}$$

where $\rho(r)$ is the local mass density in the crust. The accretion epoch is $t_{\rm accr} = 1\,{\rm yr}$, beginning at $t = 0$, during which period $10^{-3}\,{\rm M}_\odot$ of material is accreted uniformly onto the NS surface; thus $\dot{m} = 10^{-3}\,{\rm M}_\odot\,{\rm yr}^{-1}$. As already reported by Torres-Forné et al. [2016], this accretion rate is not enough to bury $10^{12}\,{\rm G}$ fields on $\sim$1 yr time scales[2]. However we are concerned with the first Megayear (Myr) of evolution after the field is buried, and not with modelling the transition from the proto-NS era onward. Chevalier [1989], Bernal et al. [2010] and Bernal & Fraija [2016] have already carefully reported on the huge instant accretion rates associated with the hyper-critical

[2]If the accretion rate drops as $\propto t^{-5/3}$, which was suggested by Chevalier [1989], the instant accretion rate in the first few hours is much larger than 10^{-3} ${\rm M}_\odot$/yr. This makes the submergence process possible while keeping the total amount of accreted matter low enough to neglect its influence on the crustal composition.

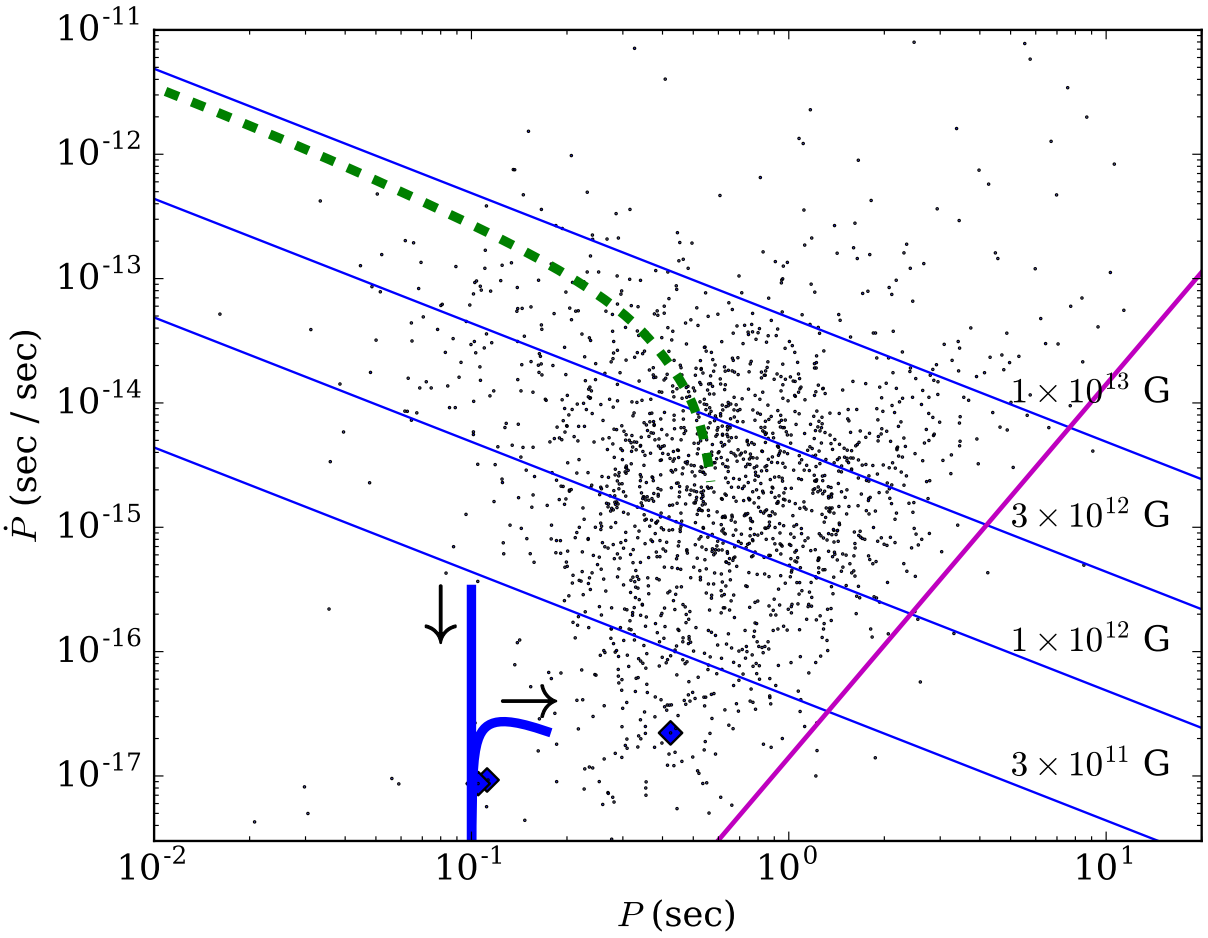

Figure 4.1: $P-\dot{P}$ distribution for normal radio pulsars from the ATNF catalogue [Manchester et al., 2005], and two evolutionary tracks for (a) a non-accreting NS with dipolar magnetic field and aligned quadrupole (dashed green line), and (b) a NS with a pure dipolar magnetic field which was buried with $\dot{M} = 10^{-3} \mathrm{M}_{\odot}\,\mathrm{yr}^{-1}$ during a one year accretion phase (solid blue line). CCOs with measured period and period derivatives are shown as blue diamonds [Halpern & Gotthelf, 2010; Gotthelf, Halpern, & Alford, 2013]. Black arrows indicate the direction of time, magenta solid line indicates the death line [Bhattacharya et al., 1992].

accretion phase, where $\sim 100\,\mathrm{M}_\odot\,/\mathrm{yr}$ can fall back onto the NS surface. Accurately capturing thermal evolution during this era requires understanding the compositional evolution, and how the accreted matter affects e.g. rapid neutrino cooling. However, linking the physical conditions during the supernova explosion to the subsequent hyper-critical phase, and thus to our initial conditions, is beyond the scope of this article. Our phenomenological model in Eq. (4.2) is valid if we assume the hyper-critical accretion phase has already passed, the NS crust has formed, and thus the internal NS structure has been fixed. Thus we consider our Eq. (4.2) sufficient to capture the essential secular signatures of the magnetic re-emergence process. We choose the total accreted mass to be $10^{-3}\,\mathrm{M}_\odot$. Larger total accreted mass can bury the field completely (see e.g. fig. 2 in Geppert et al. [1999] for 0.01 $\mathrm{M}_\odot$), while a smaller total accreted mass can lead to very fast reemergence, which is inconsistent with current CCO observations.

We employ a Skyrme type equation of state (EOS) with SLy nuclear interactions [Douchin & Haensel, 2001]. For densities below neutron drip point we also use the BPS relation [Baym, Bethe, & Pethick, 1971]. We assume a nominal NS mass of $1.40\,\mathrm{M}_\odot$, and our EOS provides a star with radius $R_{NS} = 11.503\,\mathrm{km}$ and a core radius of $R_c = 10.799\,\mathrm{km}$. We restrict our study to fields confined to the NS crust, and consider the NS core to be an ideal superconductor, thus we enforce as inner boundary conditions that tangential electric fields vanish at the crust-core interface ($E_\theta = E_\phi = 0$); Ohmic dissipation timescales are $\sim 10^9$ yrs in the core, and dynamics in the NS core are effectively de-coupled from fundamental observables driven in NS crust [Elfritz et al., 2016], so it is reasonable to ignore the NS core in this study. At the $r = R_{\mathrm{NS}}$ outer boundary we decompose the radial component of the surface field to construct a multipole spectrum, consistent with a potential solution, and valid for both vacuum and force-free magnetospheres (Gralla, Lupsasca, & Philippov 2016).

The specific determination of our initial conditions is discussed separately in Appendix 4.A, but simply put, we prescribe superpositions of multipolar magnetic fields at $t = 0$. We impose a background purely poloidal dipole, and superpose additional multipoles of order l. The initial toroidal field component is taken to be zero. The total magnetic field intensity at the north pole is normalized to $B_{\mathrm{pol}} = 1.5 \times 10^{12}\,\mathrm{G}$, with the dipolar component contributing $0.5 \times 10^{12}\,\mathrm{G}$.

The thermal evolution is computed by the thermal transport equation for local temperature T,

$$c_v \frac{\partial T}{\partial t} - \vec{\nabla} \cdot [\hat{\kappa} \cdot \vec{\nabla} T] = \sum_i Q_i \tag{4.3}$$

where c_v is the local specific heat capacity and $\hat{\kappa}$ is the thermal conductivity tensor. In the right side of Eq. (4.3) we assume no additional sources of heat during the accretion phase for two reasons: first, the accretion process is very short (duration of 1 yr in our simulations) and second, the accretion stage is at the very beginning of the NS evolution when the star is still extremely hot ($\sim 10^{10}\,\mathrm{K}$), and thus any accretion-induced heating due to infalling material is quickly quenched by neutrino emission. Therefore the only non-zero Q_i that we must include are the Joule heating and usual neutrino cooling terms. Our code traces the thermal and magnetic field evolution up to magnetar field strengths, therefore all relevant energy sinks via neutrino cooling are included (see Table 4.3 of Viganò 2013).

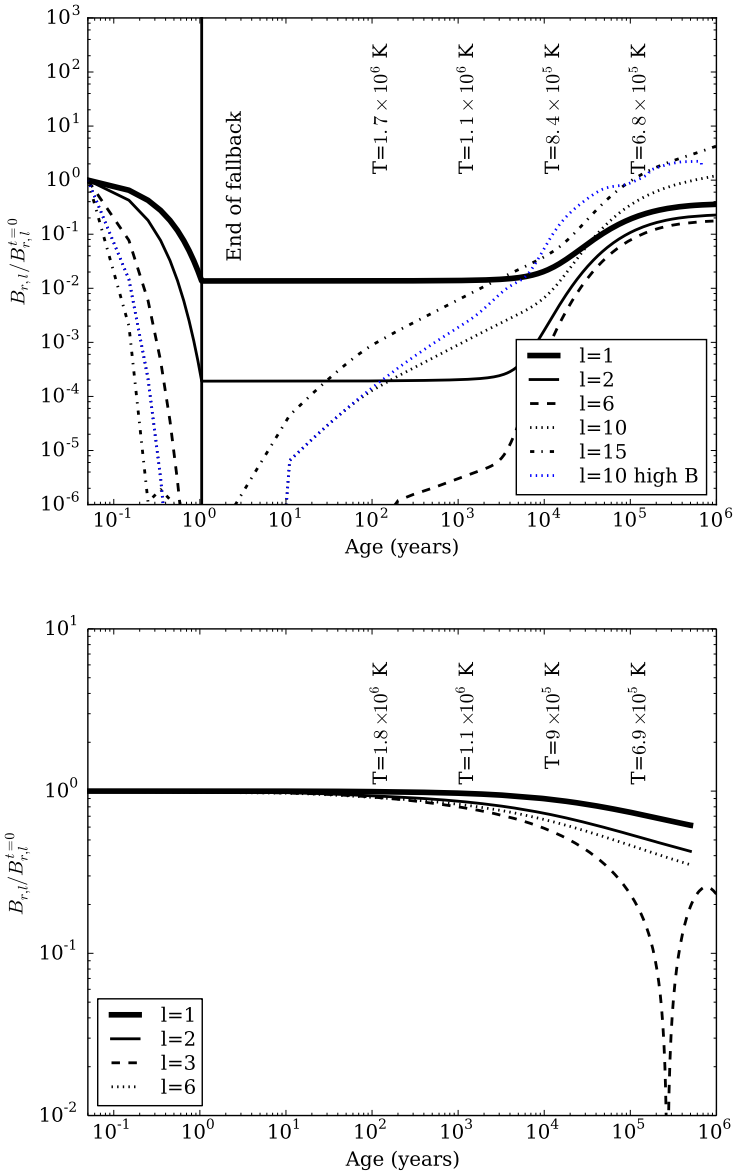

Figure 4.2: Evolution of initially existing components of the surface poloidal magnetic field. *Upper panel*: no fall-back. *Lower panel*: fall-back with the total accreted mass $\delta M = 10^{-3}\,\mathrm{M}_\odot$. In each panel several models with different initial field structure are shown. In every model the field initially consists of the dipole and one additional component. Evolution of the dipole component ($l = 1$, thick solid line) is nearly identical for all models in each panel, and so just one curve for $l = 1$ is shown in both panels. Other curves in each panel correspond to evolution of different components, which initially existed together with the dipole. Labels in legends in each panel mark the component which existed in the inital conditions, and which evolution is shown. Other components in all models, which were not present in the initial conditions and are generated during field evolution, are significantly weaker and are not shown here. The full map of surface multipole expansion is presented for several models in Fig. 4.5. End of the fall-back period is marked in the left panel. In both panels we show several values of surface temperature at different moments. Temperature evolves in identical way in all models in each panel. The blue line in the right panel corresponds to a higher initial field strength of $3 \times 10^{13}\,\mathrm{G}$.

In order to focus on the field evolution during the burial and re-emergence phases, we reduce the inner crust impurity factor to 0.1, such that associated dissipation is suppressed. We use a numerical grid with $n_r = 30$ radial cells through the NS crust, and adjust the number of cells in polar angle to suit the angular variation of the imposed l-pole (varies from 50 - 300 cells). 1 Myr is chosen as the simulation time in each case.

4.3 Results: the re-emergence process

In this section we describe the results from our magneto-thermal simulations for a variety of initial conditions. We compare re-emergence of the imposed multipolar fields, shown alongside identical simulation results without the initial accretion phase (Fig. 4.2).

We start the discussion of the magneto-thermal evolution from a case with no fall-back which was already presented multiple times in the literature, to verify that our results are consistent. The low order harmonics ($l = 1, 2$) decay on the Ohmic timescale, about 1 Myr, see right panel of Fig. 4.2 [Cumming et al., 2004; Pons & Geppert, 2007]. Even though we assume no toroidal magnetic field in our initial conditions, this component is generated and typically saturates at values comparable to the initial poloidal field strength; that is, $B_\phi^{\rm peak} \approx 0.5 - 2.0\, B_{\rm pol}^{t=0}$. The NS cools undisturbed and reaches a temperature around 6.9×10^5 K at $t = 10^5$ years, see temperature labels above the magnetic field curves at Fig. 4.2. This result is in agreement with Aguilera et al. [2008a] for low-mass weakly magnetized NS. The high order harmonic ($l = 6$) decays slightly faster than the dipole and quadruple.

When the fall-back is introduced the evolution of low order multipoles ($l = 1, 2$) does not differ from the earlier published results [Viganò & Pons, 2012]: we found very similar reemergence time scales $\sim 10^5$ yrs, caused by diffusion of the poloidal magnetic field toward the surface. The surface magnetic field is reduced after the fall-back and the internal magnetic field is amplified because of compression by accreted matter [Bernal et al., 2013]. The surface temperature is not sensitive to the short fall-back episode. In simulations where high order harmonics ($l = 6, 10$ or 15) are present with a background dipole, we find the shorter re-emergence time scale of $\sim 10^4$ years. Moreover, the re-emerged field intensity of these higher order harmonics appears to be larger than what was imposed in the initial conditions. This result has important implication for the theory of pulsar emission and is discussed in details in §4.5. During the first few hundred years a strong toroidal magnetic field is formed, up to $B_{\rm tor} \approx 7 \times 10^{12}$ G; see Figs. (4.3,4.4). This toroidal magnetic field has a large multipole number and survives during 10^6 years, showing slow migration toward the crust-core interface. At the surface of the neutron star, additional harmonics are formed on the Hall time scale, see Fig. 4.5, their intensity though does not reach a significant value during the course of our simulations. The presence of high order multipole structure does not affect the bolometric temperature of the NS.

If we choose initial conditions consisting of a dipole and $l = 10$ harmonic with a higher magnetic field, $B = 3 \times 10^{13}$ G, we see very similar behaviour during the toroidal growth stage (compare blue and black dotted lines at left panel of Fig. 4.2), but the stronger Hall drift accelerates the re-emergence process somewhat. The surface multipole expansion Fig. 4.5 shows that more harmonics are generated, due to the Hall cascade, but their intensity is still small compared to

the $l = 1$ and $l = 10$ field components.

We have also performed simulations which include non-zero toroidal field components at $t = 0$, prior to the short fall-back, with the form

$$B_\phi = B_0 \frac{R_0}{r} \left(\frac{2}{\Delta r_{\rm cru}} \right)^4 (r - R_{\rm NS})^2 \left(r - R_c^2 \right) \sin\theta, \tag{4.4}$$

and found no significant difference in the surface multipole expansion in the first 10^6 yrs. Here R_0 and $\Delta r_{\rm cru}$ denote the radial center of the crust and the crustal thickness, respectively. B_0 normalizes the peak field strength. Our series of experiments have shown that with or without the inclusion of an initial toroidal component, the system will in general relax to the configurations shown in Figs. (4.3,4.4) [Gourgouliatos & Cumming, 2014a].

4.4 Theoretical explanation

NS magnetic field evolution in the presence of high-order multipolar structure occurs in three distinct stages, the time scales of which are functions of both the Ohmic diffusion and Hall time scales; these are given by $\tau_{\rm Ohm} = 4\pi\sigma L^2/c^2$ and $\tau_{\rm Hall} = 4\pi e n_e L^2/cB$, respectively, where $L \approx 1\,$km is the characteristic length scale of field variation. The first evolutionary stage is the growth of toroidal field from the standard forward Hall cascade (starting from fall-back until $\sim 1\,\tau_{\rm Hall}$), then advection of the poloidal field towards the surface of the neutron star caused by the poloidal-toroidal coupling in the Hall drift (typically up to $\sim 10\tau_{\rm Hall}$), and finally the diffusion of poloidal field to the surface on the Ohmic time scale. The diffusive epoch depends primarily on the electrical conductivity σ in the NS crust, and typically dominates the evolution beyond $\sim 10^5\,$yrs for our chosen EOS. This final stage weakly depends on the angular structure of the field, but not the field intensity; this evolutionary stage is well-studied in the literature [Cumming et al., 2004; Urpin et al., 1994], and thus we treat only the first two epochs in this section.

4.4.1 The linear toroidal field growth stage.

The early evolution is dominated by the induction of a toroidal magnetic field component, because we supply only poloidal components for the initial field. While an arbitrary toroidal component can easily be imposed (see Viganò & Pons 2012), the long-term NS evolution is not particularly sensitive to its inclusion. We specifically do not prescribe the B_ϕ components from Eq. (4.55) because this simply delays activation of the Hall cascade.

The non-dipolar components of the initial field, from Eqs. (4.53, 4.54) are

$$B_{r,l}(r,\theta) = -\frac{\mu_l^2}{x^2} l(l+1) C_l \Gamma_l(x) P_l(\cos\theta) \tag{4.5}$$

$$B_{\theta,l}(r,\theta) = -\frac{\mu_l^2}{x} C_l \Gamma_l'(x) P_l'(\cos\theta) \tag{4.6}$$

where $x = \mu_l r$ is a normalized radial coordinate. To satisfy boundary conditions we must take $\mu_1 = 2.29$, $\mu_2 = 0.628$, $\mu_3 = 0.313$ and all other $\mu_l \approx 0.273\,{\rm km}^{-1}$ (see Appendix 4.A).

In this early stage of the evolution, the toroidal field evolves according to the non-diffusive Hall induction equation

$$\partial_t B_\phi = -\vec{\nabla} \times \left[f_h (\vec{\nabla} \times \vec{B}_{\rm pol}) \times \vec{B}_{\rm pol} \right]. \tag{4.7}$$

For each multipole l in the poloidal initial conditions, it can be shown that the corresponding azimuthal field grows according to

$$\partial_t B_\phi = -C_l^2 \mu_l^6 \frac{f_h}{x^6} [\psi(x) P_l P_l' + \chi(x) P_l' P_l''], \tag{4.8}$$

where we write the two radial functions $\chi(x)$ and $\psi(x)$ using the Bessel-Riccati differential equation and its derivative as

$$\chi(x) = -2x^3 \Gamma_l \Gamma_l' \tag{4.9}$$

$$\psi(x) = 2xl(l+1)\Gamma_l [x\Gamma_l - l(l+1)\Gamma_l']. \tag{4.10}$$

From consideration of our boundary conditions, it is clear that $\Gamma_l(x)$ is a similar monotonic function for all multipoles, and is thus effectively independent of l. We then Taylor expand Γ about the crust-core interface, keeping up to the linear term. It follows that for typical values, $\Gamma_l \Gamma_l' \approx 2$ for high l. The second term in Eq. (4.8) is the dominant contribution for the $l = 1$ dipole case, whereas the first term dominates for all higher multipoles, due to the quartic dependence on harmonic number l. Thus for a given l, the fastest corresponding toroidal growth obeys

$$\partial_t B_\phi \approx 4 C_l^2 f_h \frac{\mu_l^6}{x^5} l^2 (l+1)^2 P_l P_l', \tag{4.11}$$

illustrating that the toroidal field grows as the odd harmonics $(2l-1, 2l-3, 2l-5, ...)$, due to the $P_l P_l'$ dependence. It makes sense that the expected growth rate scales as $\sim 1/l^2(l+1)^2$, since we impose angular structures of order l as initial conditions, i.e., this is the scale size of our current sheets. The local timescale for large multipoles is therefore

$$\tau_{{\rm Hall},l} \approx \frac{4\pi e n_e}{cB} \frac{L_0^2}{l^2(l+1)^2} \tag{4.12}$$

where L_0 is the length scale for the background, dipolar field. This analytic approximation is in good agreement with the growth shown in our numerical simulations. In the left panels of Figs. (4.3, 4.4) we see the toroidal field during this linear growth phase for two large-l cases. When the toroidal and poloidal field intensities become comparable, the toroidal growth saturates, and the next stage of evolution is controlled by the toroidal-poloidal coupling.

4.4.2 The toroidal-poloidal coupling.

The toroidal magnetic field component is well developed after a few Hall time scales, which accelerates the evolution of the poloidal field from the coupling equation

$$\partial_t \vec{B}_{\rm pol} = -\vec{\nabla} \times \left[f_H \left(\vec{\nabla} \times \vec{B}_{\rm tor} \right) \times \vec{B}_{\rm pol} \right]. \tag{4.13}$$

As already shown by Viganò [2013], the poloidal equations resemble standard advection equations which contain source terms quadratic in $\vec{B}$. We can write the relation in standard form, as

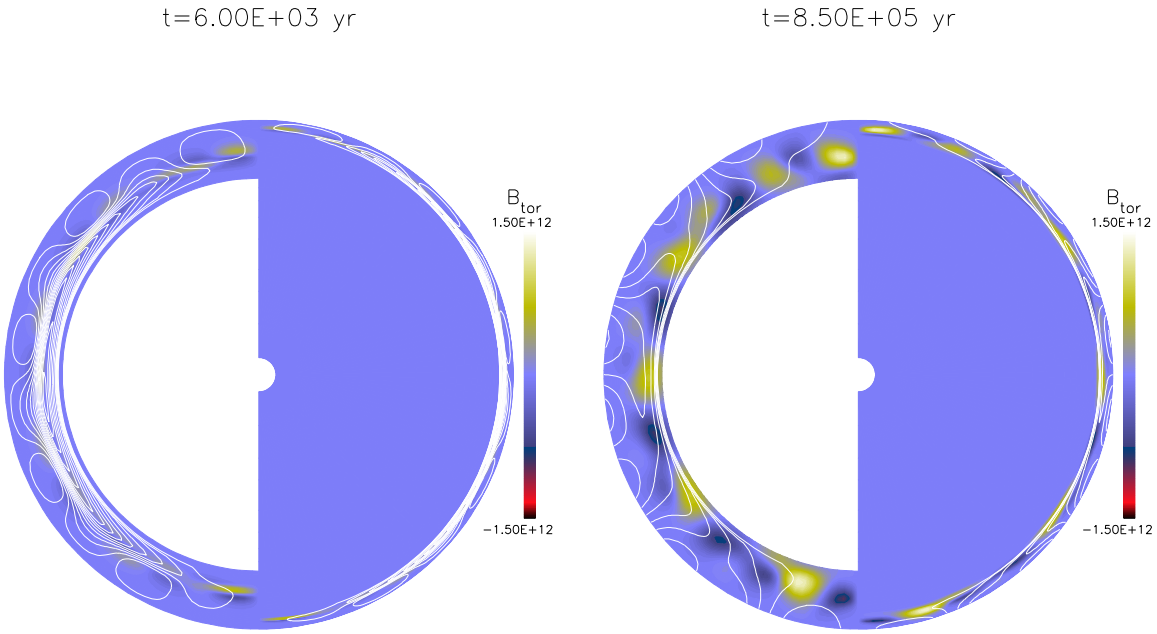

Figure 4.3: The crustal magnetic field configuration at two different times, for initial conditions consisting of dipole and $l = 10$ harmonic. The crust is artificially enlarged in the left halves for clarity. White lines indicate field lines projected into the poloidal plane, and the background color indicates the toroidal field strength.

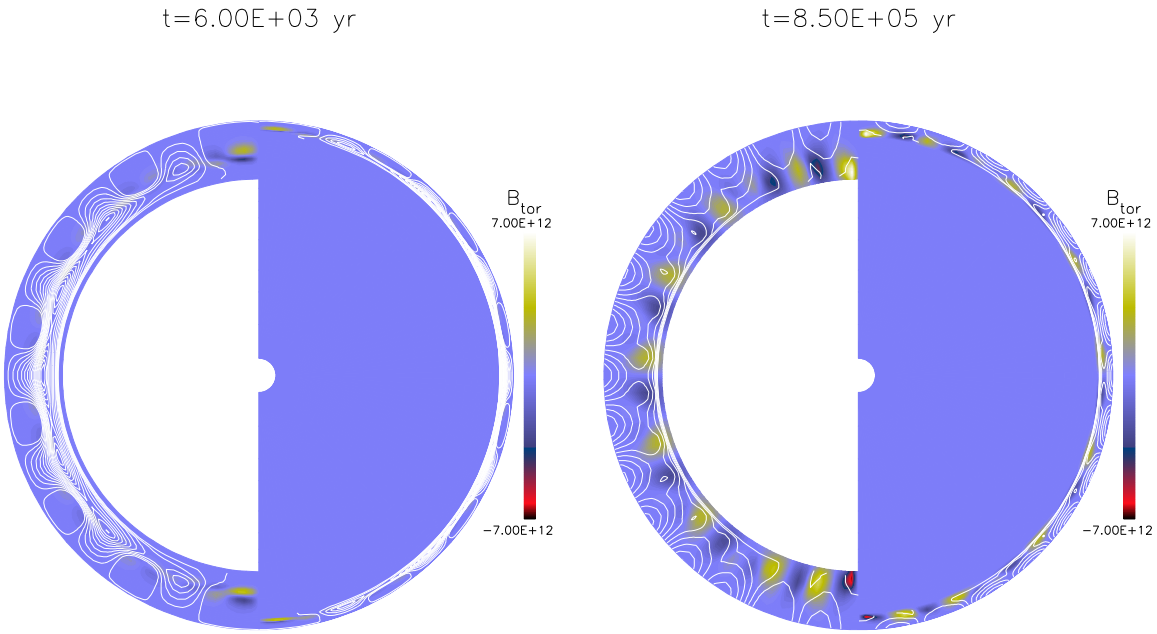

Figure 4.4: The crustal magnetic field configuration at two different times, for initial conditions consisting of dipole and $l = 15$. The crust is artificially enlarged in the left halves for clarity. White lines indicate field lines projected into the poloidal plane, and the background color indicates the toroidal field strength.

$$\left(\partial_t + \vec{v}_e \cdot \vec{\nabla}\right) \vec{B}_{\rm pol} = \left(\vec{B} \cdot \vec{\nabla}\right) \vec{v}_{e,{\rm pol}} \tag{4.14}$$

where $\vec{v}_e = -f_H \vec{\nabla} \times \vec{B}$ is the electron velocity. Clearly the left-hand side of Eq. (4.14) is an advective derivative on the poloidal field, while the right-hand side provides nonlinear feedback on the field depending on the configuration of the current system. The result is that the buried magnetic field advects towards the NS surface, and does so on faster time scales than for pure Ohmic diffusion.

We can exploit the ordered multipolar structure in $\hat{\theta}$ to estimate the re-emergence time scale. There is no such periodicity in the radial direction, so we Fourier transform Eq. (4.13) in $\hat{\theta}$ in the limit $\nabla \rightarrow i\,\vec{k}_\theta$, where $\vec{k}$ is the usual wave vector. We also Fourier transform in time such that $\partial_t \rightarrow -i\,\omega$, and search for exponentially growing solutions. After some algebra, one may compute the re-emergence speed $v_{\rm re-em}$ via the group velocity, as

$$v_{\rm re-em} = \left| \frac{d\omega}{dk_\theta} \right| \approx v_0 \cdot l \cdot B_\phi \tag{4.15}$$

with $v_0 = 2\,f_H / R_{\rm NS}$. This estimate shows that higher-order multipoles re-emerge at the NS surface earlier than e.g. a buried dipole component. There are important observational implications to this. The re-emergence time is then easily inferred based on the burial depth $\Delta\, r_{\rm burial}$:

$$\Delta\, t_{\rm re-em} \approx \frac{\Delta\, r_{\rm burial}}{v_0 \cdot l \cdot B_\phi}. \tag{4.16}$$

In general the peak B_ϕ value at saturation – which is responsible for advecting the poloidal field to the surface – is comparable to the initial field strength $B_0 = 1.5 \times 10^{12}$ G. Using $R_{\rm NS} = 11.5$ km and $f_H \approx 2\,{\rm km\,Myr^{-1}}\,10^{-12}\,{\rm G^{-1}}$, with a 0.35 km burial depth (half the crust thickness), it follows that the re-emergence time scale is roughly

$$\Delta\, t_{\rm re-em} \approx \frac{670}{l}\,{\rm kyrs}. \tag{4.17}$$

This approximation agrees well with the re-emergence time scales found in Fig. 4.2, within a factor of ∼2 – 5.

It is important to note that our choice of simulation inputs constrains the physics. The simulated re-emergence process is elastic, in the sense that the parity of re-emergent poloidal field is determined by the imposed initial conditions. In our experiments we have tested various combinations of odd-even and odd-odd harmonics (see §4.3), and for $t > \Delta\, t_{\rm re-em}$ the spectral decomposition at the NS surface strongly resembles the supplied initial conditions (Fig. 4.5). The reason is that we are concerned with relatively weak field intensity at birth, $\sim 10^{12}$ G, and thus the nonlinear Hall drift is also somewhat weak. Therefore the Hall drift cannot efficiently accelerate Ohmic dissipation of the high-l structure on sub-Myr time scales.

4.5 Consequences for non-thermal emission

Our objects have $B \sim 10^{12}$ G and periods $P \sim$0.1-0.3 sec, in correspondence with recent studies of initial periods (Popov & Turolla 2012a; Igoshev & Popov 2013). In this region of the P – $\dot{P}$ plane the efficiency of non-thermal emission is strongly controlled by the curvature radius of

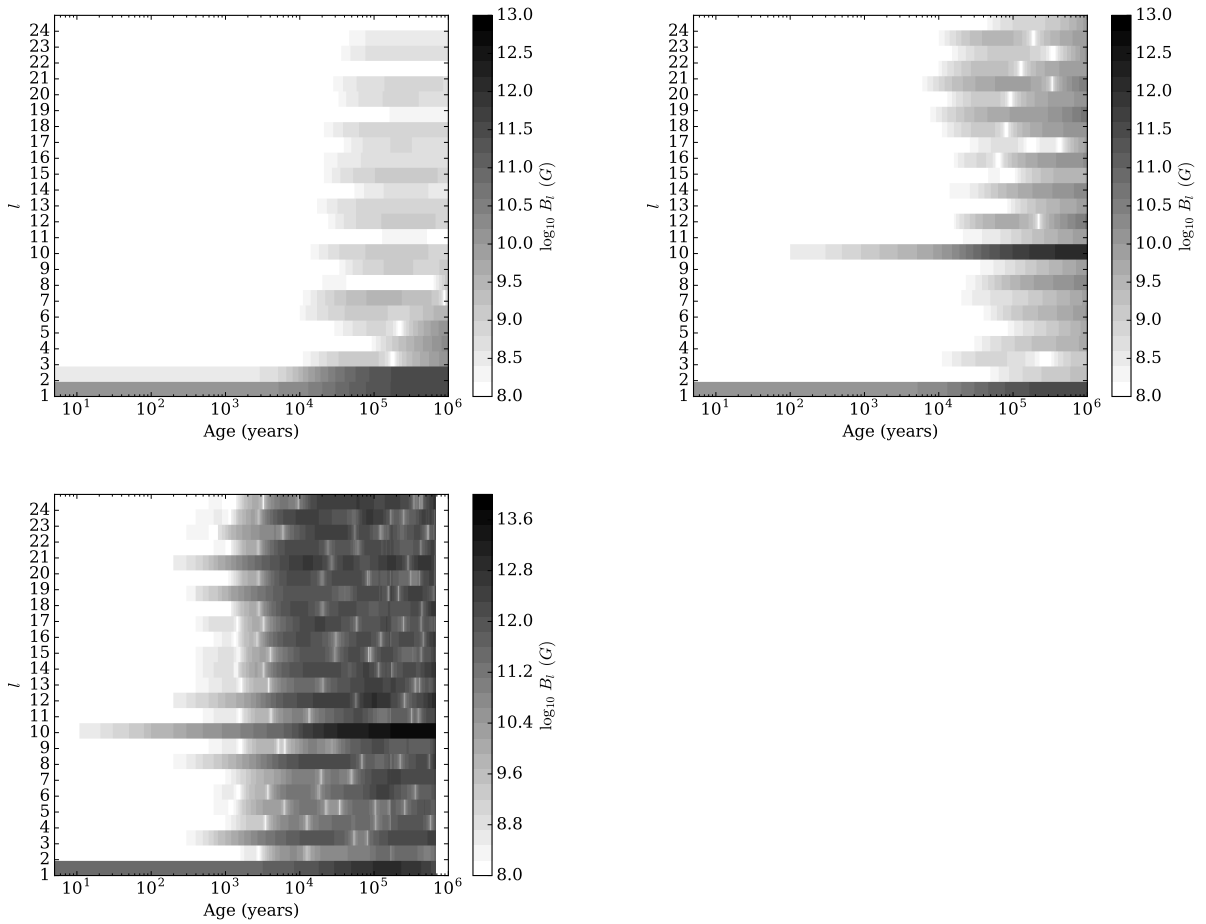

FIGURE 4.5: Surface poloidal magnetic field decomposition versus time (horizontal) and multipole number (vertical). The greyscale shows the strength of individual multipoles. *Top left*: the initial configuration consists of dipole and $l = 2$ harmonic. *Top right*: the initial configuration consists of dipole and $l = 10$ harmonic. *Bottom*: the initial configuration consists of dipole and $l = 10$ harmonic with higher $t = 0$ field strength.

open field lines (see figs. 8,9 in Medin & Lai 2007b for the position of the death line depending on the curvature radius). Curvature radiation is a dominant process which causes the cascade development and determines the emitted power, while the resonant Compton scattering does not play an appreciable role [Timokhin & Harding, 2015].

Our results for field re-emergence, summarized in Fig. 4.2, have immediate consequences for non-thermal emission of NSs. Sources subject to fall-back, shows primarily dipolar magnetic fields and ages up to 10^3 yrs, have large curvature radii in the open field line region ($\sim 100\, R_{\rm NS}$), and thus produce negligible non-thermal radiation. After $\sim 10^5$ yrs, the large multipolar components dominate close to the surface and decrease the curvature radius, thus triggering non-thermal emission. This causes the neutron star to shine as a pulsar again.

We briefly describe the emission of pulsars (the interested reader is referred to Timokhin 2010; Timokhin & Arons 2013; Timokhin & Harding 2015 for details) in the following steps: electrons or ions (depending on the sign of $\vec{\Omega} \cdot \vec{B}$) are efficiently stripped from the NS surface due to negligible cohesive energy and large temperature [Medin & Lai, 2007b], and are accelerated in the strong electric field (see §4.5.2.1). The particles gain energy γ_e and emit curvature radiation photons with energy $E_{\rm CR}$. If $E_{\rm CR} > E_{\rm crit} = 10^{11}$ eV, then they can produce electron-positron pairs in the magnetic field. These first generation particles (we use the notation of Timokhin & Harding 2015) are once again accelerated, and the electrons or positrons return to bombard the NS surface.

We want to investigate in detail the bottlenecks of this process, which are as follows: (a) the energy gained by electrons in the acceleration potential might not be enough to produce photons capable of electron-positron pair creation (see Section 4.5.2.1) and (b) the photon mean free path in the gap region may be much larger than the physical size of the gap itself (see Section 4.5.2.2).

On one hand we have a model of magnetic field evolution in the crust, which predicts the maximum curvature radius of open field lines (see §4.5.1); on the other hand we have a constraint on this curvature radius for producing non-thermal emission (see §4.5.2). We assume that a NS efficiently emits non-thermal radiation only if the actual curvature radius is smaller than required for pair formation.

4.5.1 Actual curvature radius of open field lines

Since the configuration of the poloidal magnetic field is described completely, we can integrate along the field lines. Close to the NS surface, the assumption of a vacuum magnetosphere is valid, see Gralla et al. [2016]; in the open field line region the plasma density is small when the acceleration potential is not screened, and the assumption of vacuum also works here.

We trace magnetic field lines by numerically solving the usual system of differential equations:

$$\frac{dr}{ds} = \frac{B_r}{|B|} \tag{4.18}$$

$$\frac{d\theta}{ds} = \frac{1}{r}\frac{B_\theta}{|B|}, \tag{4.19}$$

with the footpoints selected uniformly on the surface of neutron star given by $r_{0,i} = R_{\rm NS}$, $\theta_{0,i} = \pi i/500$, for the i^{th} field line. We then select those which reach the light cylinder distance $R_{\rm LC} = cP/(2\pi)$, and we choose $P = 0.1\,$s. To compute the curvature radius ρ, we follow the prescription

from Asseo & Khechinashvili [2002] assuming flat space, since the GR corrections are small. Then

$$\rho(r,\theta) = \frac{1}{|(\vec{b}\cdot\vec{\nabla})\vec{b}|}, \tag{4.20}$$

where $\vec{b}(r,\theta)$ is the unit vector in the direction of the local magnetic field.

4.5.2 Required curvature radius for open field lines

4.5.2.1 Electron acceleration

We start from equation (8) from Ruderman & Sutherland [1975] for the potential difference ΔV between the centre of the polar cap and the edge of the negative current emission region,

$$\Delta V \approx \Omega \frac{(r_{p-})^2}{2c} B_d^s \tag{4.21}$$

where Ω is the angular speed of the neutron star, B_d^s is the dipole component of the magnetic field at the surface and r_{p-} is the size of the polar cap. Although the gap appears to be unstable [Timokhin, 2010], this vacuum acceleration potential can still be used in such studies (Timokhin & Harding 2015; Philippov et al. 2015). In our case the size of the polar cap is determined by the opening angle $\theta_{\max}$ for the last open field line at the light cylinder, from

$$r_{p-} = \theta_{\max} R_{\rm NS}. \tag{4.22}$$

Since the light cylinder radius is $R_{\rm LC} = c/\Omega$, we obtain the potential drop

$$\Delta V \approx \frac{R_{\rm NS}^2 \theta_{\max}^2 B_d^s}{2R_{\rm LC}}, \tag{4.23}$$

which gives the electron Lorentz factor

$$\gamma = \frac{e\Delta V}{m_e c^2} = \frac{eR_{\rm NS}^2}{2R_{\rm LC} m_e c^2}(\theta_{\max}^2 B_d^s) \approx 0.586 \cdot (\theta_{\max}^2 B_d^s), \tag{4.24}$$

where B_d^s has dimensions of G, and we have taken the canonical $R_{\rm NS} = 10\,$km. The value for γ should exceed $\gamma_{\rm crit} \approx 2 \times 10^5$ for electrons to activate the cascade [Ruderman & Sutherland, 1975]. In this model, the acceleration potential does not depend on curvature of open magnetic field lines, and sets no conditions for the NS to exhibit pulsed emission.

The particle accelerated in the electric potential emits curvature radiation photon which can produce new electron-positron pairs in magnetic field. We consider critical values for this process in following section.

4.5.2.2 Required curvature radius based on the mean free path of photons

The curvature radiation photon has energy [Ruderman & Sutherland, 1975]

$$E_{\rm CR} = \frac{3}{2}\gamma^3 \frac{\hbar c}{\rho}, \tag{4.25}$$

where γ is the Lorentz factor of the electrons from Eq. (4.24). The photon effectively produce pairs only if its mean free path in the magnetic field is smaller than the size of the acceleration gap

itself. The initial propagation direction aligns with the local magnetic field, but at some distance it starts to deviate since the magnetic field is curved. The mean free path is determined by the strength of the orthogonal to propagation direction component of the magnetic field ($B_\perp$). We assume that the radius of curvature exceeds the size of the emission zone ($h \approx 0.01R_{\rm NS} - 0.1R_{\rm NS}$) and a linear approximation is valid, such that

$$B_\perp \sim \frac{hB}{\rho} \tag{4.26}$$

where B is the strength of the total magnetic field in the emission region.[3] We start from equation (3.1) in Erber [1966] and find the exponential parameter χ from

$$\chi = \frac{1}{2}\frac{E_{\rm CR}}{m_e c^2}\frac{B_\perp}{B_q} = \frac{3}{4}\frac{\hbar}{m_e c B_q}\frac{\gamma^3 hB}{\rho^2}. \tag{4.27}$$

Here $B_q = 4.414 \times 10^{13}$ G is the Schwinger critical magnetic field. Then, the mean free path is

$$l_{\rm CR} = 2\frac{\hbar^2}{m_e e^2}B_q\frac{\rho}{hB}\frac{1}{T(\chi)}, \tag{4.28}$$

where we have used the approximate form for $T(\chi)$ as in Erber [1966], since in our simulations the parameter χ is far from the asymptotic cases:

$$T(\chi) \approx 0.16\chi^{-1}K^2_{1/3}\left(2/3\chi\right). \tag{4.29}$$

Upon substituting numerical values we obtain

$$\chi = 1.3 \times 10^{-25}\frac{hB}{\rho^2}(\theta^2_{\rm max}B^s_d)^3, \tag{4.30}$$

and the mean free path is

$$l_{\rm CR} = 2.8 \times 10^6\frac{\rho}{hB}\chi\frac{1}{K^2_{1/3}\left(2/3\chi\right)}. \tag{4.31}$$

We want $l_{\rm CR} < h$, otherwise photons freely leave the emission region. This condition sets an upper limit for the curvature radius of the open field lines. In §4.5.3, we solve this equation numerically and find the maximum curvature radius required for an NS to emit as a pulsar.

4.5.3 When does the pulsar shine again?

For all simulations with fall-back, we show in Figs. (4.6, 4.7, 4.8) the actual (black lines) and required (blue and red lines) curvature radius of open field lines. Initially the required maximum curvature radius is larger than the actual one, which means that the NS emits as a pulsar. After the fall-back episode large harmonics are strongly suppressed and the actual curvature radius reached typical for a pure dipole value ($\sim$100 $R_{\rm NS}$). The required curvature radius for effective pairs creation decreases to extremely small values around $0.1R_{\rm NS}$ since the magnetic field is strongly suppressed and $B_\perp$ is not developed enough. During this period the NS does not emit

[3] We repeatedly call the region from the surface to $1.01R_{\rm NS}$ at the magnetic pole as the emission region even though there might be no emission from there.

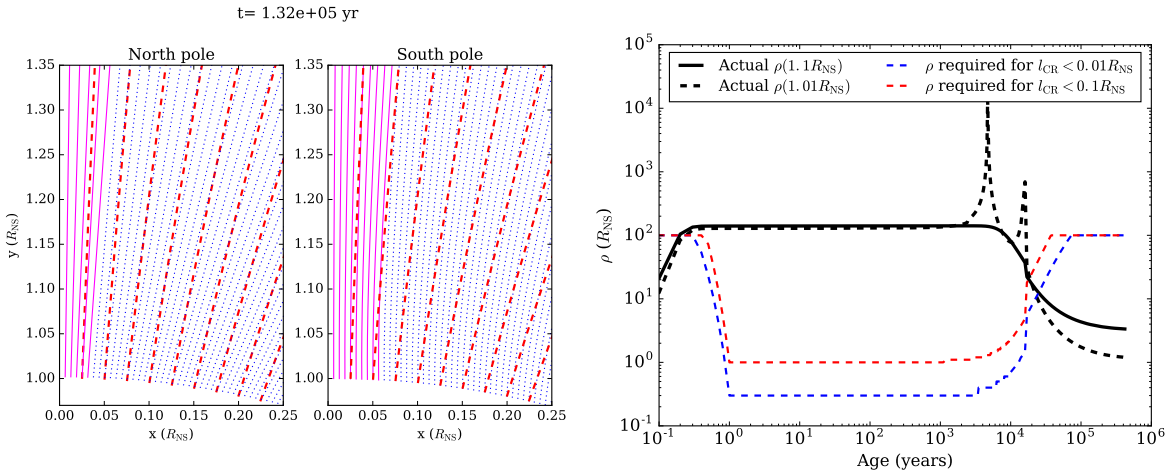

FIGURE 4.6: The structure of magnetic field lines above the NS surface (left panel) for the initial conditions consisting of dipole and $l = 6$ harmonic; north and south poles both shown. The dashed red lines show purely dipolar magnetic field lines at the pole, dotted are for closed and solid are for open field lines. The right panel shows the maximum curvature radius for open field lines for the same initial configuration (black line). Other lines show theoretical predictions: blue dashed line for typical height of the emission zone $h = 0.01R_{\rm NS}$; red dashed line is for larger height of the emission zone $h = 0.1R_{\rm NS}$.

non-thermal radiation. It is still visible as a source of pure thermal radiation with temperatures around 10^6 K (see temperature labels at Fig. 4.2).

Depending on the initial field configuration the actual curvature radius of open field lines starts to decrease at $\sim 10^4$ yrs for initial dipole and $l = 6$ harmonic and ~ 100 yrs for initial dipole and $l = 15$ harmonic. The actual and required curvatures of open field lines intersects at around a few times 10^4 yrs which means that the NS starts efficiently emitting non-thermal radiation.

4.6 Discussion

4.6.1 Some properties of the external magnetic field

The accuracy of our numerical solutions for the crustal magnetic field is restricted by the number of bins in the angular direction. From the standpoint of numerical stability, the required angular resolution must be calculated from consideration of the initial conditions. For the $l = 6$ and the $l = 15$ case, we use 150 and 300 angular cells, respectively. This gives a corresponding angular resolution of 1.2° and 0.6°. We must also consider whether the angular resolution is sufficient from the standpoint of tracing field lines in the emission zone. For real NSs in nature, the size of the polar cap is unknown and undoubtedly varies among sources. We conclude that our chosen resolution is indeed sufficient for the following reason: the magnetospheric field satisfies our outer boundary condition, the Legendre expansion. Technically at the NS surface we perform the expansion up to order $l = 200$, far higher than any order we are interested in modelling. If we were to increase the angular resolution, the dominant coefficients in the multipole expansion stay the same – i.e. the imposed initial conditions – and only the multipole coefficients corresponding

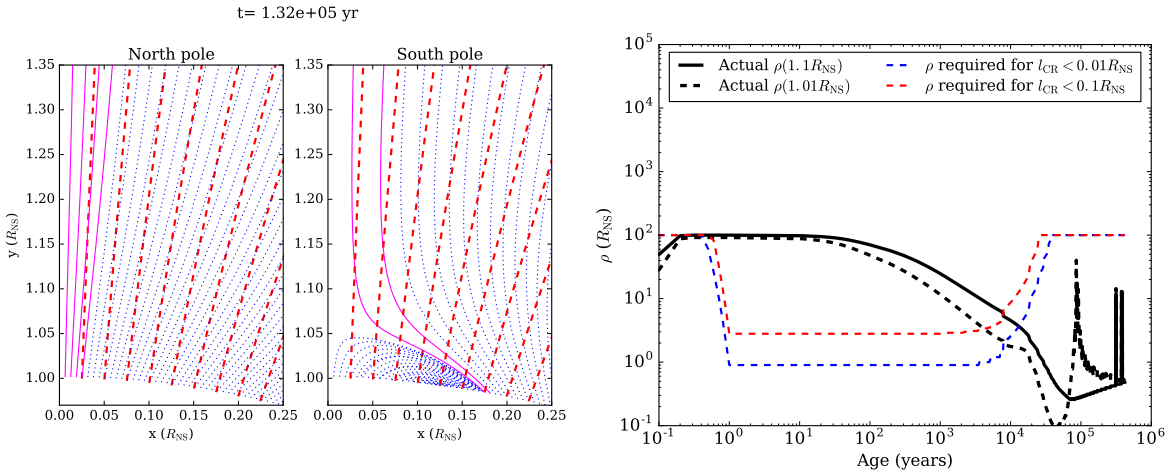

Figure 4.7: The structure of magnetic field lines above the NS surface (left panel) for the initial conditions consisting of dipole and $l = 10$ harmonic; north and south poles both shown. The dashed red lines show purely dipolar magnetic field lines at the pole, dotted are for closed and solid are for open field lines. The right panel shows the maximum curvature radius for open field lines for the same initial configuration (black line). Other lines show theoretical predictions: blue dashed line for typical height of the emission zone $h = 0.01R_{\rm NS}$; red dashed line is for larger height of the emission zone $h = 0.1R_{\rm NS}$.

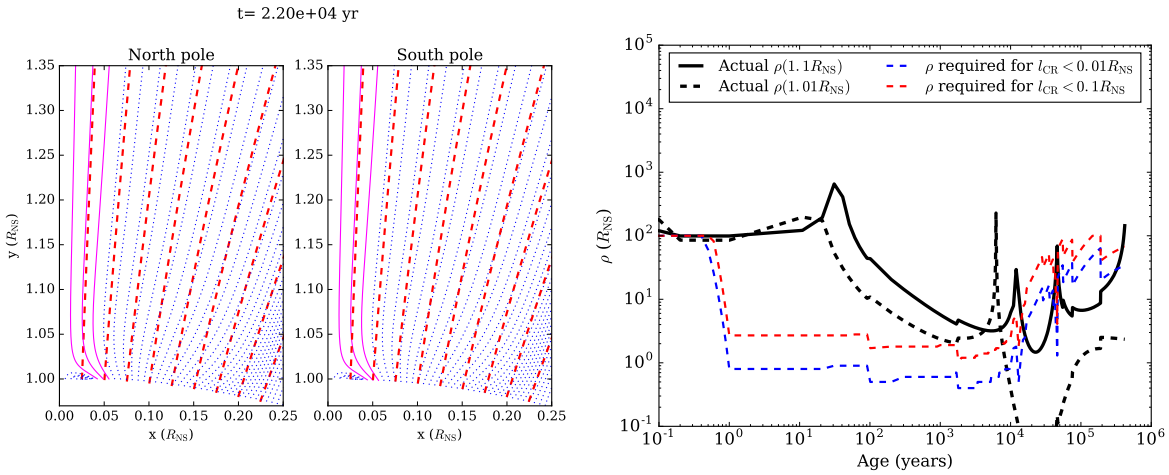

Figure 4.8: The structure of magnetic field lines above the NS surface (left panel; video is available at `http://pulsars.info/videos/l15.mp4`) for the initial conditions consisting of dipole and $l = 15$ harmonic; north and south poles both shown. The dashed red lines show purely dipolar magnetic field lines at the pole, dotted are for closed and solid are for open field lines. The right panel shows the maximum curvature radius for open field lines for the same initial configuration (black line). Other lines show theoretical predictions: blue dashed line for typical height of the emission zone $h = 0.01R_{\rm NS}$; red dashed line is for larger height of the emission zone $h = 0.1R_{\rm NS}$.

to the Nyquist multipole should fluctuate. In addition, since we are not performing detailed simulations of the emission processes, but instead are only considering the magnetic topology in the region, we note that our angular resolution is at worst comparable to the polar cap size r_{p-}. Since our surface expansion conserves $\vec{\nabla} \cdot \vec{B} = 0$ everywhere, we are free to trace the field lines with sub-grid scale resolution if desired.

Another particularly interesting case study is the shifted dipole, which was long-discussed as a plausible explanation for the small curvature radius of open field lines in pulsars [Ruderman et al., 1998]. While our numerical model would require significant modifications in order to model mis-aligned rotational and magnetic axes (see Viganò 2013), we could approximate such a configuration by imposing a smooth spectrum of harmonics as our initial conditions. However, looking at Fig. 4.2, we can immediately conclude that the shifted dipole case would probably not survive the fall-back episode. The low-order multipoles $l = 2, 3, ..., 6$ re-emerge less efficiently than the dipole component, while higher-order multipoles of $l = 10, ..., 15$ re-emerge more efficient than the dipole component. This could lead to the destruction of the shifted dipole and would result in growth of the leading multipole, most likely the highly-structured field components.

4.6.2 Limitations of Ruderman and Sutherland emission model

We are aware that the vacuum gap model does not describe all emission process entirely. The electron work function and the ionic cohesive energy appears to be much smaller that it was expected in the time of Ruderman & Sutherland [1975]. As Medin & Lai [2006a,b] have shown for the case of condensed surfaces, the work function for electrons is roughly 100 eV, and the cohesive energy is ∼500-700 eV for different atmospheric compositions, in the weak magnetic field limit [4]. Then for typical surface temperatures of post-CCO NSs ∼0.5-1×10^6 K, no vacuum gap can be formed because the charge can be supplied at local the Goldreich-Julian rate (Medin & Lai 2007b).

This problem is well-known, and has been already discussed in several papers (Neuhauser, Langanke, & Koonin 1986; Neuhauser, Koonin, & Langanke 1987). The first solution for an extended space-charge limited flow was suggested by Arons & Scharlemann [1979] for the case when large multipoles are present. The authors considered steady flow in the co-rotation frame and identified favourable field line curvature, i.e. in the direction of rotation. Moreover, consideration of the Lense-Thirring effect of frame-dragging [Muslimov & Tsygan, 1992] leads to the conclusion that the presence of free charge carriers at the NS surface cannot tighten the gap. The electric field grows rapidly from the surface of neutron stars and reaches a maximum at a distance of the polar cap size, and then decays. The accelerating potential is slightly different from the classical Ruderman and Sutherland potential.

[4] If a condensate is not formed, which is possible in the case of post-CCO NSs, then the situation is uncertain. However we can assume that the cohesive energy in this case is not exceedingly large. In addition, we want to note that accretion in a fall-back episode of a significant amount of light elements can result in changes in the surface properties, which can suppress opening of the gap. If the magnetosphere is positive above the poles, then for relatively low fields and high temperatures it is much more difficult to form a gap above hydrogen than above an iron surface (see fig. 4 in Medin & Lai 2007a). This can be an additional reason why PSRs do not appear immediately after the field re-emerges to the surface.

However particle acceleration is not the only component of the pulsar emission mechanism. Electron-positron pairs transfer energy to photons, which then produce the next generation of pairs. Therefore it is essential to have a field topology which decreases the photon mean free path to a scale less than the size of the acceleration zone. Detailed physics of the acceleration zone has been considered in many studies, e.g. Beloborodov [2008], Szary [2013], and Szary et al. [2015]. Here we intended only to look at the basic properties of multipolar re-emergence and draw corresponding conclusions about how such magnetic structure is important for non-thermal pulsar emission.

4.6.3 Searches for pulsars with re-emerging magnetic fields

Original models of magnetic re-emergence [Bernal et al., 2010; Ho, 2011; Viganò & Pons, 2012] predicted that for ages $\gtrsim 10^4$ yrs, the NS magnetic field would return to its initial value due to diffusion through the accreted envelope. The main observational feature of an NS at this stage should be its anomalous braking which does not correspond to the standard dipolar radiative braking. This difference can be quantified by means of the braking index, commonly written as

$$n = 2 - \frac{P\ddot{P}}{\dot{P}^2}. \tag{4.32}$$

In the recent work by Ho [2015] the field re-emergence scenario was studied in detail, with the braking index formula written as

$$n = 3 - 2\frac{\dot{B}}{B}\frac{P}{\dot{P}} = 3 - \frac{4}{\gamma_{\rm br}}\frac{\dot{B}}{B^3}P^2. \tag{4.33}$$

The $\gamma_{\rm br}$ in Eq. (4.33) is given by $\gamma_{\rm br} \approx 4\pi^2 R_{\rm NS}^6/(3c^3 I)$, with I being the NS moment of inertia the NS. For typical NS parameters, we can estimate this factor as $\gamma_{\rm br} \approx 10^{-39}\,{\rm G}^{-2}\,{\rm s}$, and plot the braking index from the dipolar component of the total magnetic field. The results are shown in Fig. 4.9. During the re-emergence epoch, shortly after the pulsar begins emitting non thermal radiation, the braking index has extremely negative values. Such extreme values of the braking index can be impossible to measure since impulsive changes in the magnetic field could cause glitch activity according to Ho [2015]. The NS crust easily lose its torque because of coupling with crust-confined magnetic field, whereas the NS core does not. Timing noise of glitches with different magnitudes makes the second period derivative $\ddot{P}$ extremely difficult to measure.

An alternative observational feature is that kinematically old pulsars with relatively weak fields and with braking indices $n < 1$ can be associated with SNRs, and can show significant thermal emission from the NS surface. Indeed, the life-time of a SNR can be up to 10^5 yrs. According to standard cooling models (see, for example, Yakovlev & Pethick 2004) a CCO-like NS stays hot at least for 10^5 yrs, which typically corresponds to the case of light element envelopes. Light elements enhance heat transfer to the stellar surface, and so make such sources hotter and brighter at young ages [Viganò et al., 2013a].

Bogdanov et al. [2014] and Luo et al. [2015] used two different approaches to search for such PSRs with re-emerged magnetic field. In the first paper the authors selected a sample of 8 objects with associated SNRs within the distance $d = 6$ kpc. Kinematic ages of these NSs were estimated to be $\sim$20 – 30 kyrs, based on their positions relative to the SNRs (and based on velocities, if

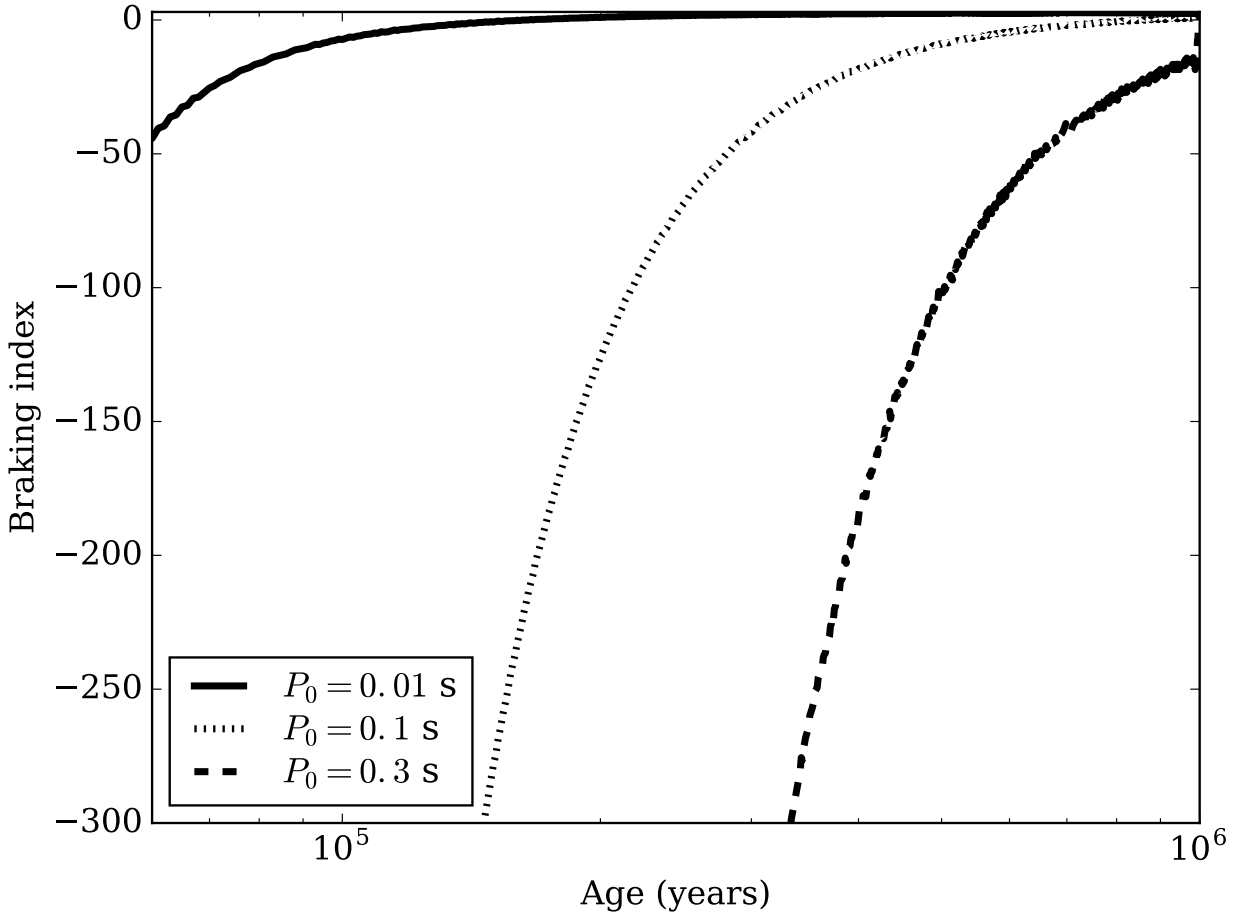

Figure 4.9: Evolution of braking indices based on the dipolar magnetic field component. Curves for different initial periods converge to $n = 3$.

available). *Chandra* and *XMM-Newton* observations put upper limits on (or directly detected) their thermal X-ray emission. The authors concluded that the selected sources do not look like evolved CCOs, and therefore their associations with SNRs might be due to chance. In Luo et al. [2015] a different approach was used. Twelve PSRs were selected according to the following conditions: $B < 10^{11}$ G, $P > 0.05$ s, $z < 100$ pc, where z is distance from the Galactic plane. None of them appeared to be associated with a SNR. Also, none of the sources appeared to have large thermal X-ray luminosity. Typical upper limits for temperature are $\sim$50 – 100 eV. Thus, Bogdanov et al. [2014] and Luo et al. [2015] concluded that the proposed scenario of field re-emergence, and the corresponding appearance of PSRs is not correct. Our study demonstrates that it remains possible to bring the scenario of field evolution after fall-back into correspondence with the results of X-ray searches.

According to the results presented above, it takes $\gtrsim$ 30 kyrs for small scale fields to re-emerge. Only after this time a radio pulsar can begin emitting non-thermal radiation. By this point in time, a NS can cool down below the limits obtained by Bogdanov et al. [2014]; Luo et al. [2015], and the SNR can become too faint to detect. We thus propose that it is necessary to extend the approaches used by Bogdanov et al. [2014] and Luo et al. [2015] to look for colder (and older) NSs which appear as PSRs with recently re-emerged field. Correspondingly, for the 12 sources discussed by Luo et al. [2015], it is necessary to put more stringent limits on ages and temperatures.

For distant sources it can be difficult to probe lower temperatures due to significant interstellar absorption in the soft X-ray band. In this case, a searching strategy based on identification of a NS with a SNR is not very promising. Among the sample studied by Luo et al. [2015], more than one half are farther than 2.5 kpc, making it difficult to detect NSs with such low temperatures. Still, for nearby sources with distances $\lesssim$ 1 – 2 kpc it is possible to improve limits on the surface temperatures down to 30-40 eV with longer *Chandra* exposures (several tens of ksec), or even to detect thermal emission from them according to expectations presented in Fig. 4.2. Correspondingly, with lower temperature limits, the limits on the ages will shift towards larger values, up to $\sim 10^5$ yrs. To increase the size of the sample of objects at distances $\lesssim$ 1 – 2 kpc we can slightly relax ranges of magnetic field and distance from the Galactic plane, in comparison with those used by Luo et al. [2015] This can be done, especially if for particular PSRs there are arguments in favour of their youth (proximity to one of OB associations, etc.).

We have selected radio pulsars from the ATNF catalogue v1.54 (Manchester et al. 2005) and cross-correlated their positions with known OB associations at distances less than 3 kpc from the Sun. The pulsars have been chosen according to criteria similar to those in Luo et al. [2015], but we relax the criteria somewhat. We select only pulsars within 3 kpc from the Sun with heights above the Galactic plane of less than 200 pc, with periods $P > 0.1$ s, and magnetic fields of $< 5 \times 10^{11}$ G. Our sample contains 37 pulsars. Note that in the ATNF, distances to most of these pulsars are estimated from the dispersion measure according to Taylor & Cordes [1993]. We have used several approaches to cross-correlate the pulsar sample with known OB associations, because distances to these agglomerations of stars are not very certain. At first, we use the catalogue of Blaha & Humphreys [1989] (but also see Mel'nik & Efremov 1995). No significant coincidences between the list of pulsars and OB associations have been found, i.e. no pulsar detections within 100 pc

from the centre of OB associations. We then take into account that distances to OB associations might be 20% smaller (Dambis, Mel'nik, & Rastorguev 2001, Mel'nik & Dambis 2009). Taking this into account, we find two pairs of pulsar-OB association: J1107-5907 and J1154-6250.

The first pulsar J1107-5907 is close to the Car OB2 association with an age of ∼4 Myr (Tetzlaff et al. 2010). The characteristic age of the pulsar is very large, $\sim 4.5 \times 10^8$ yrs. The young age of the association and that the pulsar is nearby the association indicates that the pulsar might itself be very young, as only the most massive NS progenitors are expected to explode. Note that this object has also been studied by Luo et al. [2015]. However, they assumed a distance of 1.3 kpc, estimated according to Cordes & Lazio [2002]. With this distance the source does not fall close to the Car OB2. But new estimates based on Schnitzeler [2012] show that the distance is about 1.94 kpc, which is in good correspondence with the ATNF value (1.81 kpc). With this improved distance estimate, the pulsar is close to the OB association, and could thus be related to it when taking into account the uncertainties in distance. The temperature limit given by Luo et al. [2015] is therefore modified, as the source is further away by factor ∼1.5. Since Luo et al. [2015] already estimated the column density $n_{\rm H}$ from DM using the standard relation from He, Ng, & Kaspi [2013], we must only take into account changes in distance. Then the updated temperature limit is ∼67 eV. This is not strict enough to draw clear conclusions, but is notably higher than in Luo et al. [2015]. This temperature of 7.8×10^5 K corresponds to the rising part of the curve in Fig. 4.2. However, 55 eV – 6.4×10^5 K – is already behind the rising part. We suggest that deeper observations of this source are necessary.

The second pulsar is J1154-6250, which can be related to the Cru OB1 association with the age 5-7 Myrs (Tetzlaff et al. 2010). There are no available temperature estimates for this object. With the distance calculated according to Schnitzeler [2012], the source still remains close to the association. The characteristic age of this pulsar is $\sim 8 \times 10^6$ yrs, inconsistent with the age of the association. Thus this source was possibly born with a spin period close to the present day value.

We have also used the list of 25 OB association from Dambis et al. [2001] for which parallax distances are estimated. These distances are not considered to be precise enough (Mel'nik & Dambis 2009; Dambis et al. 2001), and in addition we have not found any pulsar from our list within 100 pc of any of these associations, so we do not comment on it further.

Potentially, a full account of the uncertainties in pulsar distances and OB associations, of different combinations of selection parameters of pulsars, and usage of larger lists of associations could result in new cases of pulsar-association pairs. Such cases must be studied in detail, although that analysis is beyond the scope of this paper. For the purposes of this work, we simply point out examples of pulsars which could in fact be objects with re-emerging magnetic field.

4.7 Conclusions

We have studied, for the first time, the evolution of high-order multipolar fields ($l > 10$) in a self-consistent, 2D magneto-thermal framework, while imposing a short accretion epoch as an initial condition. We confirm re-emergence time scales of $\sim 10^5$ yrs for magnetic field buried by fall-back with accreted mass $10^{-3} M_\odot$ just after NS birth [Viganò & Pons, 2012]. For our relatively weak field strengths, we find that harmonics up to $l = 15$ efficiently re-emerge on time scales comparable

to – or shorter than – the corresponding time scale for the dipolar magnetic field component. We also report that for high-order multipoles the toroidal-poloidal interaction plays an essential role in accelerating magnetic re-emergence.

We have implemented the full Ruderman & Sutherland [1975] formalism for strongly non-dipolar surface fields, and have confirmed that the observable field following the fall-back episode (first $\sim 10^4$ yrs) is extremely weak and also purely dipolar. Such conditions prevent effective conversion of photons into electron-positron pairs. The re-emergence of large multipoles at $3 \times 10^4 - 5 \times 10^4$ yrs decreases the curvature radius in the emission zone. This activates non-thermal emission, and thus the neutron star manifests as a pulsar. The surface temperature at these times is about 7×10^5 K which prevents effective detection.

Although earlier searches for pulsars with re-emerging fields have revealed no plausible candidates [Bogdanov et al., 2014; Luo et al., 2015] we argue that our scenario is still valid, especially because the distances to the pulsars are highly uncertain and some candidates might be hotter than that predicted by Luo et al. [2015]. We develop a new criterion for such searches, namely the small projected distance from an OB association. We have found two candidates, J1107-5907 and J1154-6250, which based on our simulations could be young pulsars currently experiencing magnetic re-emergence.

4.A Initial conditions for crust-confined magnetic fields

We impose magnetic field initial conditions which follow the logic of Aguilera et al. [2008a], but here we expand in more detail for the interested reader. In azimuthally-symmetric spherical 2D ($\partial_\phi \to 0$), the magnetic field may be decomposed into poloidal and toroidal components:

$$\vec{B} = \vec{B}_{\rm pol}\,(r,\theta) + \vec{B}_{\rm tor}\,(\phi) \tag{4.34}$$

Each can then be written in terms of stream functions $\mathcal{S}(r,\theta,t)$ and $\mathcal{T}(r,\theta,t)$:

$$\vec{B}_{\rm pol} = \vec{\nabla} \times (\vec{r} \times \vec{\nabla}\mathcal{S}) \tag{4.35}$$

$$\vec{B}_{\rm tor} = -\vec{r} \times \vec{\nabla}\mathcal{T}. \tag{4.36}$$

We are free to decompose $\mathcal{S}$ and $\mathcal{T}$ in terms of Legendre polynomials, and search for stationary solutions such that

$$\mathcal{S} = \sum_l C_l \frac{P_l(\cos\theta)}{r} \mathcal{S}_l(r) \tag{4.37}$$

where C_l are normalization constants ($\mathcal{T}$ has an identical form). We can then write each magnetic field component as

$$B_r = -\frac{1}{r^2} \sum_l C_l \mathcal{S}_l l(l+1) P_l \tag{4.38}$$

$$B_\theta = -\frac{1}{r} \sum_l C_l P_l' \frac{d\mathcal{S}_l}{dr} \tag{4.39}$$

$$B_\phi = -\frac{1}{r}\sum_l C_l \mathcal{T}_l P_l' \tag{4.40}$$

To determine the radial eigenmodes, we choose so-called force-free initial conditions ($\vec{J}\times\vec{B}=0$), such that the magnetic field components obey

$$\nabla\times\vec{B} = \mu_l \vec{B} \tag{4.41}$$

at $t=0$, where μ_l is the scale length for the radial Stokes functions of order l. The choice of force free condition is simply a convenient method for imposing multipolar structure, but the NS will immediately drift away from such a configuration due to e.g. the presence of density and conductivity gradients in the induction equation. From the radial component of Eq. (4.41), one obtains

$$\mu_l \mathcal{S}_l l(l+1) P_l = \mathcal{T}_l P_l' \cot\theta + \mathcal{T}_l P_l''. \tag{4.42}$$

and it is immediately evident that

$$\mu_l \mathcal{S}_l(r) = -\mathcal{T}_l(r). \tag{4.43}$$

Now considering the azimuthal component of Eq. (4.41) we obtain the Bessel-Riccati differential equation for the poloidal Stokes function

$$x^2\frac{d^2\mathcal{S}_l}{dx^2} + (x^2 - l(l+1))\mathcal{S}_l = 0 \tag{4.44}$$

where $x=\mu_l r$ is a scaled radial coordinate. The general solutions are well-known, and for a given l have the form

$$\Gamma_l(x) = a_l x\cdot j_l(x) + b_l x\cdot n_l(x) \tag{4.45}$$

where a_l, b_l are normalization coefficients, and the functions $j_l(x)$ and $n_l(x)$ can be written using Rayleigh's formula:

$$j_l(x) = (-x)^l\left(\frac{1}{x}\frac{\partial}{\partial x}\right)^l\left[\frac{\sin x}{x}\right] \tag{4.46}$$

$$n_l(x) = -(-x)^l\left(\frac{1}{x}\frac{\partial}{\partial x}\right)^l\left[\frac{\cos x}{x}\right] \tag{4.47}$$

We can write the spherical Bessel functions in a more useful form:

$$j_l(x) = A_l(x)\sin(x) + \beta_l(x)\cos(x) \tag{4.48}$$

$$n_l(x) = -A_l(x)\cos(x) + \beta_l(x)\sin(x) \tag{4.49}$$

where $A_l(x)$ and $\beta_l(x)$ are polynomials in x, which we extract from a Fortran library.

The field must satisfy both the vacuum outer boundary condition and the inner superconducting boundary condition. The simplest choice for the surface boundary condition is that $\mathcal{S}_l(\mu_l R_{\rm NS})=1$, which is satisfied if we choose a_l and b_l as

$$a_l = \frac{\cos(\mu_l R_{\rm NS})}{\mu_l R_{\rm NS}\cdot\beta_l(\mu_l R_{\rm NS})} \tag{4.50}$$

$$b_l = \frac{\sin(\mu_l R_{\rm NS})}{\mu_l R_{\rm NS} \cdot \beta_l(\mu_l R_{\rm NS})}. \tag{4.51}$$

The inner boundary condition requires $\mathcal{S}_l(\mu_l R_c) = 0$, where R_c is the NS core radius. Satisfying this boundary condition then requires that

$$\tan[\mu_l(R_c - R_{NS})] = -\frac{\beta_l(\mu R_c)}{A_l(\mu R_c)}. \tag{4.52}$$

We employ a modified Newton's method to solve Eq. (4.52) numerically to obtain μ_l, and then compute the coefficients a_l and b_l from equations Eqs. (4.50, 4.51). Finally, we construct the solution $\mathcal{S}_l(x)$, and the magnetic field components have the following final forms:

$$B_r = -\frac{1}{r^2}\sum_l l(l+1)C_l\mathcal{S}_l(x)P_l(\cos\theta) \tag{4.53}$$

$$B_\theta = -\frac{1}{r}\sum_l \mu_l C_l \frac{d\mathcal{S}_l(x)}{dx}P_l'(\cos\theta) \tag{4.54}$$

$$B_\phi = +\frac{1}{r}\sum_l \mu_l C_l \mathcal{S}_l(x)P_l'(\cos\theta). \tag{4.55}$$

Chapter 5

How to make a mature accreting magnetar

Andrei Igoshev & Sergei Popov

MNRAS, 2017
accepted

Abstract

Several candidates for accreting magnetars have been proposed recently by different authors. Existence of such systems contradicts the standard magnetic field decay scenario where a large magnetic field of a neutron star reaches $\lesssim$ few $\times 10^{13}$ G at ages $\gtrsim$ 1 Myr. Among other sources, the high mass X-ray binary 4U0114+65 seems to have a strong magnetic field around 10^{14} G. We develop a new Bayesian estimate for the kinematic age and demonstrate that 4U0114+65 has kinematic age 2.4-5 Myr (95% credential interval) since the formation of the neutron star. We discuss which conditions are necessary to explain the potential existence of magnetars in accreting high-mass binaries with ages about few Myrs and larger. Three necessary ingredients are: the Hall attractor to prevent rapid decay of dipolar field, relatively rapid cooling of the crust in order to avoid Ohmic decay due to phonons, and finally, low values of the parameter Q to obtain long Ohmic time scale due to impurities. If age and magnetic field estimates for proposed accreting magnetars are correct, then these systems set the strongest limit on the crust impurity for a selected sample of neutron stars and provide evidence in favour of the Hall attractor.

5.1 Introduction

There are hundreds of known X-ray binaries with accreting neutron stars (NSs) in the Milky Way as well as in near-by galaxies [Liu et al., 2006, 2007; Fabbiano, 2006; Sarazin et al., 2003].

In some cases it is possible to measure magnetic fields of compact objects directly observing electron (or proton) cyclotron lines (see Revnivtsev & Mereghetti 2015 and references therein): $(E_{\rm cyc,e}/{\rm keV}) = 12(B/10^{12}{\rm G})\,(1+z)^{-1}$, where B is the magnetic field, and z – redshift at the line formation region. Typically, measured fields are in the range 10^{11} – 10^{13} G (which is also determined by the energy range available for observational facilities, i.e. much smaller or larger fields correspond to lines out of the range of sensitivity of X-ray spectrometers $\sim 1-100$ keV). However, for majority of NSs the magnetic field can be estimated only with indirect methods based on timing measurements (see Appendix B and, for example, Shi et al. 2015; D'Angelo 2017 and references therein). Among the latter cases there are a few NSs for which estimates argue for magnetar scale fields $\gtrsim 10^{14}$ G [Doroshenko et al., 2010; Reig et al., 2012; Fu & Li, 2012; Ho et al., 2014]. Such NSs have been called *accreting magnetars* (see Appendix A for a list of candidates). Meanwhile alternative approaches, for example based on a new model of settling wind accretion [Shakura et al., 2012] provide modest fields estimates $\sim 10^{13}$ G [Chashkina & Popov, 2012; Popov & Turolla, 2012b; Postnov et al., 2014]. The latter results are in better correspondence with the expected evolution of magnetic fields of NSs, as in modern scenarios initially large fields rapidly decay down to the level typical for normal radio pulsars [Pons et al., 2013; Viganò et al., 2013b].

If an accreting NS is a member of a low-mass X-ray binary system (LMXBs), then its age can be very large — up to billions of years. It is hard to imagine that a NS can still have strong magnetic field at such age. On the other hand when NS has a massive companion (high-mass X-ray binary — HMXB) its age is usually restricted by a few tens of Myrs which is still a large value in comparison with ages of known isolated magnetars [Turolla et al., 2015].

The X-ray pulsar 4U0114+65 is one of the slowest known HMXRBs Reig et al. [1996]. In the recent article by Sanjurjo et al. [2017], the long spin period (9.4 ks) and small emitting area of this sources were explained due to a magnetar scale magnetic field even in the frame of the wind settling accretion. The source is at a significant distance from any star formation region and the Galactic plane which suggests a large kinematic age. The concept of the kinematic age is precious for the studies of the neutron star properties because it measures the time since the supernova explosion which imparts the kick velocity to the system. The estimate of the kinematic age is obtained by backward orbit integration. Such estimate should take into account the uncertainties in the proper motion measurements and unknown birth position. To deal with these we develop the Bayesian approach which allows us to quantify both uncertainties.

Accreting magnetars have been also proposed to explain properties of ultra-luminous X-ray sources (ULXs, see a review in Kaaret et al. 2017) with NSs. The first of such source has been found by Bachetti et al. [2014], later two other examples were discovered by Israel et al. [2017b,a]. To explain both timing and luminosity of such sources a large dipolar magnetic field is required, for example to support the accretion column which allows higher luminosity [Mushtukov et al., 2015].

Known NS-ULXs belong to the class of HMXBs with Roche lobe overflow [Motch et al., 2014], so it can be expected that compact objects in these systems have ages at least about several Myrs [Kaaret et al., 2017; Feng & Kaaret, 2008; Grisé et al., 2011]. In this note we discuss parameters of NSs with which it is possible to obtain accreting magnetars in HMXBs in the framework generally consistent with rapid field decay in young magnetars such as soft gamma-ray repeaters

and anomalous X-ray pulsars.

According to many calculations (see e.g. Mereghetti et al. 2015 and references therein) at ages around few Myr the initially strong ($\sim 10^{15}$ G) dipole magnetic field decays by several orders of magnitude from its initial value. In order to preserve a field $\sim 10^{14}$ G up to ages $\gtrsim$ few Myrs NS should satisfy a few conditions regarding the magnetic field evolution. These are properties of the Hall cascade in the NS crust and material impurity.

This article is structured as follows. In the Section 5.2 we introduce our formalism to describe the magnetic field evolution in a NS and identify the crucial terms responsible for the field evolution during first 10 Myr. Results of the field evolution calculations are presented in Section 5.3. In the Section 5.4 we introduce the Bayesian estimate for the kinematic age and demonstrate that the NS in the accreting magnetar candidate 4U 0114+65 is at least 2 Myr old. In Section 5.5 we discuss some additional topics related to our study. Finally, in the Section 5.6 we summarize our results.

5.2 Model of magnetic field evolution

The instantaneous magnetic field $B(t)$ depends on the initial value B_0 and follows a complicated evolution. To describe it theoretically we start with the formula introduced by Aguilera, Pons, & Miralles [2008b]:

$$B(t) = \frac{B_0 \times \exp(-t/\tau_{\rm ohm})}{1 + (\tau_{\rm Ohm}/\tau_{\rm Hall})[1 - \exp(-t/\tau_{\rm Ohm})]}. \tag{5.1}$$

In this equation two distinct time scales are defined. The first one is related to the Ohmic decay (resistivity in the crust), $\tau_{\rm Ohm}$, and the second one — to the Hall cascade, $\tau_{\rm Hall}$. The Hall evolution is in principle non-dissipative, however it redistributes the magnetic energy from high spatial scale (dipole field) to small scales (multipoles of higher order) which causes the decay of the dipole component and enhances release of magnetic energy. The eq. (5.1) can be modified to include some minimal value of the field, at which the decay is saturated which is usually attributed to the influence of the core magnetic field. As we are not interested in a long-term evolution ($\gtrsim 10^8$ yrs), we do not discuss this topic further, and omit possible saturation field. Note, that both time scales, $\tau_{\rm Ohm}$ and $\tau_{\rm Hall}$, evolve with time and the latter one depends on the magnetic field value itself. Below we write equations for both time scales and choose parameters in such a way to reproduce recent detailed simulations of magneto-thermal evolution in the crust.

The timescale of the Hall evolution is:

$$\tau_{\rm Hall} = \frac{4\pi e n_e L^2}{cB(t)}, \tag{5.2}$$

with n_e is local electron density, e is the elementary charge, B is local instantaneous magnetic field, L is the typical spatial scale of electric currents (it can be, for example, the local pressure height scale, see Cumming et al. 2004), and c is the speed of light. We can also define the Hall timescale using its initial value and the instantaneous magnetic field:

$$\tau_{\rm Hall} = \tau_{\rm Hall,0}\frac{B_0}{B(t)}. \tag{5.3}$$

Here it is assumed that n_e and L are constant.

The Hall cascade can be terminated if so-called *Hall attractor* stage is reached. This stage was proposed by Gourgouliatos & Cumming [2014a,b] and then confirmed by Wood & Hollerbach [2015]. Gourgouliatos & Cumming [2014a] demonstrated that the stage is reached after a few initial Hall time scales. For a NS with initial field $\sim 10^{14}$ G it happens after approximately a few hundred thousand years (up to 1 Myr). In our model we assume that the Hall attractor stage starts after three initial Hall time scales are passed. As soon as the attractor is reached $\tau_{\rm Hall}$ is set to infinity, and the following field evolution proceeds only via Ohmic processes.

The Ohmic decay proceeds on two timescales $\tau_{\rm Ohm,ph}$ due to electron scattering on phonons, and $\tau_{\rm Ohm,Q}$ due to resistivity caused by the crust impurity. The general form to describe the timescale of the Ohmic decay is:

$$\tau_{\rm Ohm} = \frac{4\pi\sigma L^2}{c^2}, \tag{5.4}$$

where σ is the local electric conductivity which depends on resistivity agent.

The local electric conductivity is computed as:

$$\sigma = \frac{\sigma_{\rm Q}\sigma_{\rm ph}}{\sigma_{\rm Q} + \sigma_{\rm ph}}. \tag{5.5}$$

Thus, for the timescales we can write $\tau^{-1}_{\rm Ohm} = \tau^{-1}_{\rm Ohm,ph} + \tau^{-1}_{\rm Ohm,Q}$.

The conductivity due to impurities is described as:

$$\sigma_Q = 4.4 \times 10^{25}{\rm s}^{-1} \left(\frac{\rho_{14}^{1/3}}{Q}\right) \left(\frac{Y_e}{0.05}\right)^{1/3} \left(\frac{Z}{30}\right), \tag{5.6}$$

according to Cumming et al. [2004]. In this equation ρ_{14} is the density in units 10^{14} g cm^{-3}, and Y_e is the electron fraction in the current layer. The parameter Q characterizes how ordered the crystalline structure of the crust is: $Q = n_{\rm ion}^{-1}\Sigma_i\, n_i \times (Z^2 - \langle Z\rangle^2)$. Here Z is ion charge, and n number density.

A large value of $Q \gg 1$ means that the crust composition is strongly non-homogeneous. The electrons are scattered much more often in this case which significantly reduces the conductivity. For parameters of interest we obtain $\tau_{\rm Ohm,Q} = 2 \times 10^6\,{\rm yrs}\,Q^{-1}$, and we use this estimate below for different values of Q.

The phonon conductivity is computed as:

$$\sigma_{\rm ph} = 1.8 \times 10^{25}{\rm s}^{-1} \left(\frac{\rho_{14}^{7/6}}{T_8^2}\right) \left(\frac{Y_e}{0.05}\right)^{5/3}, \tag{5.7}$$

The value T_8 is the temperature of the crust in units 10^8 K. Our choice of parameters is guided by detailed numerical simulations by Pons et al. [2013]. For magnetars the layer in the crust which controls the long-term field evolution is $\rho_{14} = 0.8$. The electron fraction seems to be a factor of 2 larger in Pons et al. [2013] than in Cumming et al. [2004]. The phonon conductivity goes to infinity when the temperature of the crust drops below $T_{\rm U}$. In our calculations we use $T_{\rm U} = 2.6 \times 10^7$ K.

To calculate $\tau_{\rm Ohm,ph}$ we need to know the temperature in the crust. For NSs at the stage of Hall cascade we use the following analytical fit for the crustal temperature calculated by Viganò et al. [2013a]:

$$T = T_1 \exp(-t/\tau_1) + T_2 \exp(-t/\tau_2). \tag{5.8}$$

Parameters T_1, T_2, τ_1, τ_2 depend on the initial magnetic field and on the NS mass (massive NSs in which direct URCA processes are allowed, cool faster). For $B_0 = 10^{15}$ G we take $T_1 = 7 \times 10^8$ K, $\tau_1 = 150$ yrs, $T_2 = 1.5 \times 10^8$ K, $\tau_2 = 2.5 \times 10^6$ yrs. For smaller fields T_2 and τ_2 are smaller (i.e., cooling proceeds more rapidly due to smaller energy release due to field decay). For initial fields $\lesssim$ few 10^{13} G additional heating is not important. As soon as the temperature is determined we calculate the timescale via $\tau_{\rm Ohm,ph} = 2 \times 10^6 {\rm yrs}\, T_8^{-2}$. Magnetars are known sources of thermal X-ray emission which is explained by their high surface temperature. The exact mechanism causing this heating is unknown [Beloborodov & Li, 2016]. One of possible alternatives is the heating produced by crustal electric current Viganò et al. [2013a] which is especially efficient during the Hall cascade.

When the Hall attractor stage is reached rapid dissipation of the magnetic field energy is over, and the crust quickly relaxes to the stage without additional heating. In this case we use an analytical approximation for cooling tracks from Shternin et al. [2011]:

$$T = b \left(\frac{t}{1{\rm yr}}\right)^a \exp(-t/\tau_{\rm c}). \tag{5.9}$$

Parameters are chosen to be: $b = 6.56 \times 10^8$ K, $a = -0.185$, and $\tau_{\rm c} = 8.58 \times 10^5$ yrs. This fits a NS without direct URCA processes in the core.

In eq. (5.1) the instantaneous magnetic field is used in the left and in the right hand side. To express it explicitly we need to solve a quadratic equation:

$$B^2(t) \left(\frac{\tau_{\rm ohm}}{\tau_{\rm Hall,0} B_0}\right) \left[1 - \exp\left(-\frac{t}{\tau_{\rm ohm}}\right)\right] + B(t) - B_0 \exp\left(-\frac{t}{\tau_{\rm ohm}}\right) = 0 \tag{5.10}$$

The solution is:

$$B(t) = \frac{B_0}{2} \left(-\frac{1}{\gamma(t)} + \sqrt{\frac{1}{\gamma^2(t)} + \frac{4\kappa(t)}{\gamma(t)}}\right); \tag{5.11}$$

written by means of the auxiliary variables:

$$\kappa(t) = \exp\left(-\frac{t}{\tau_{\rm Ohm}}\right), \tag{5.12}$$

and

$$\gamma(t) = \left(\frac{\tau_{\rm Ohm}}{\tau_{\rm Hall,0}}\right) [1 - \kappa(t)]\,. \tag{5.13}$$

The exact algorithm that we use is as follows: first, we check whether the Hall attractor is reached i.e. $t > 3\tau_{\rm Hall,0}$. If it is the case we set $\tau_{\rm Hall} = \infty$, otherwise we compute the actual Hall timescale. To avoid an unphysical jump in $B(t)$ at the moment when the Hall attractor starts operating, we substitute new B_0 in eq. (5.11) which is equal to the last moment before the turn-off of the attractor. Second, we compute the temperature according to eq. (5.8) or eq.(5.9) depending on whether the Hall attractor is reached. If the temperature is larger than T_U, we compute $\tau_{\rm ohm,ph}$. If the $T < T_U$ we set $\tau_{\rm ohm,ph} = \infty$. Third we substitute all timescales into eq.(5.11). The instantaneous magnetic field $B(t)$ is computed then at a time grid.

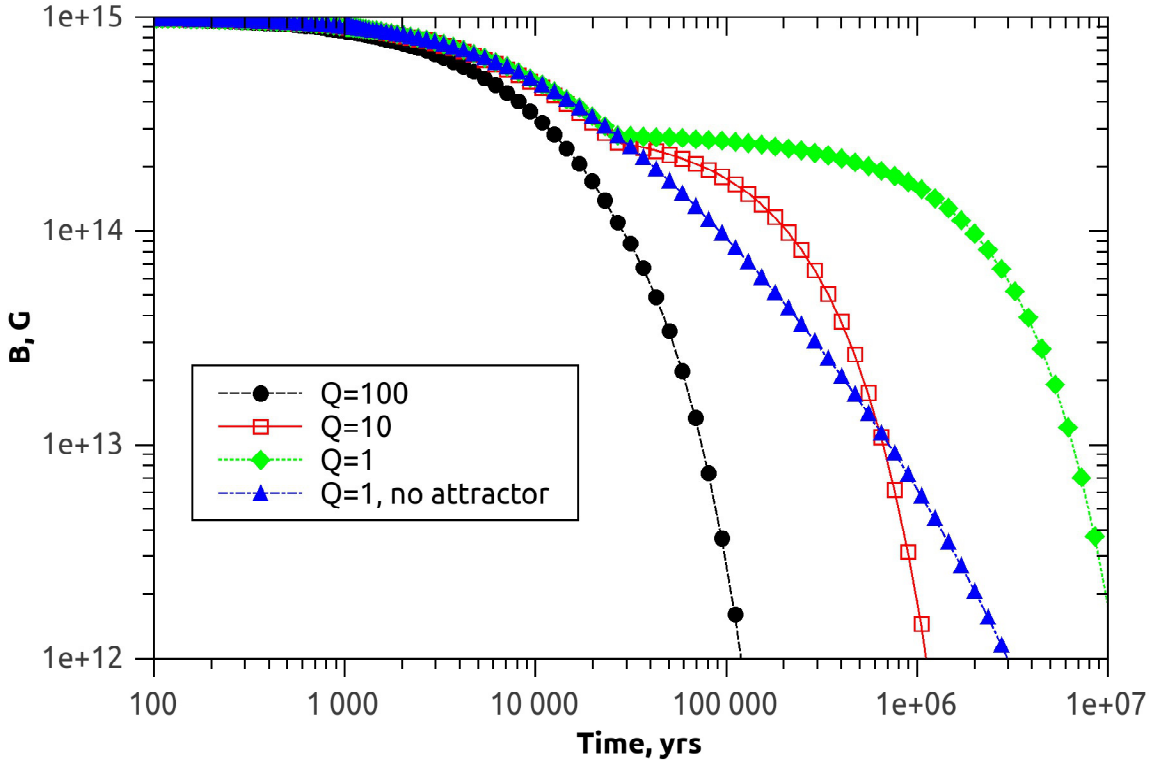

Figure 5.1: Magnetic field decay for several sets of parameters. Initial field $B_0 = 10^{15}$ G. Filled circles, empty squares, and filled diamonds corresponds to the standard case with Hall attractor (since $t = 3\tau_{\rm Hall,0}$) and different values of Q (see the legend). Upward filled triangles correspond to the model with $Q = 1$ and no Hall attractor. In the latter case thermal evolution always proceeds along the track fitted by the sum of two exponents (see text).

5.3 Results of magnetic field evolution calculations

We made runs for different sets of parameters determining the magnetic field evolution. Here we present results for our reference model, in which $\tau_{\rm Hall} = 10^4\,{\rm yrs}\,(10^{15}\,{\rm G}/B)$ and $\tau_{\rm Ohm,ph} = 2\times10^6\,{\rm yrs}\,T_8^{-2}$. In the models with the Hall attractor, we turn it on at $t = 3\tau_{\rm Hall,0} = 3\times10^4\,{\rm yrs}\,(10^{15}\,{\rm G}/B_0)$. We perform our simulations for three values of Q: 1, 10, and 100 and it is kept constant.

In Fig. 5.1 we present results for the initial field $B_0 = 10^{15}$ G. These refer to a NS without direct URCA processes in the core.

In addition to three tracks for different Q, in Fig. 5.1 we also plot a curve for the case without the Hall attractor (upward triangles). This line is calculated with $Q = 1$. However, without termination of the Hall cascade even for low Q it is impossible to save a large field at ages $\gtrsim 1$ Myr. In this case thermal evolution always proceeds according to eq. (5.8), i.e. scattering on phonons is active up to several Myrs (temperature is above $T_{\rm U}$).

We expect that NSs in accreting magnetar systems are at least older than 1 Myr. Thus, as it

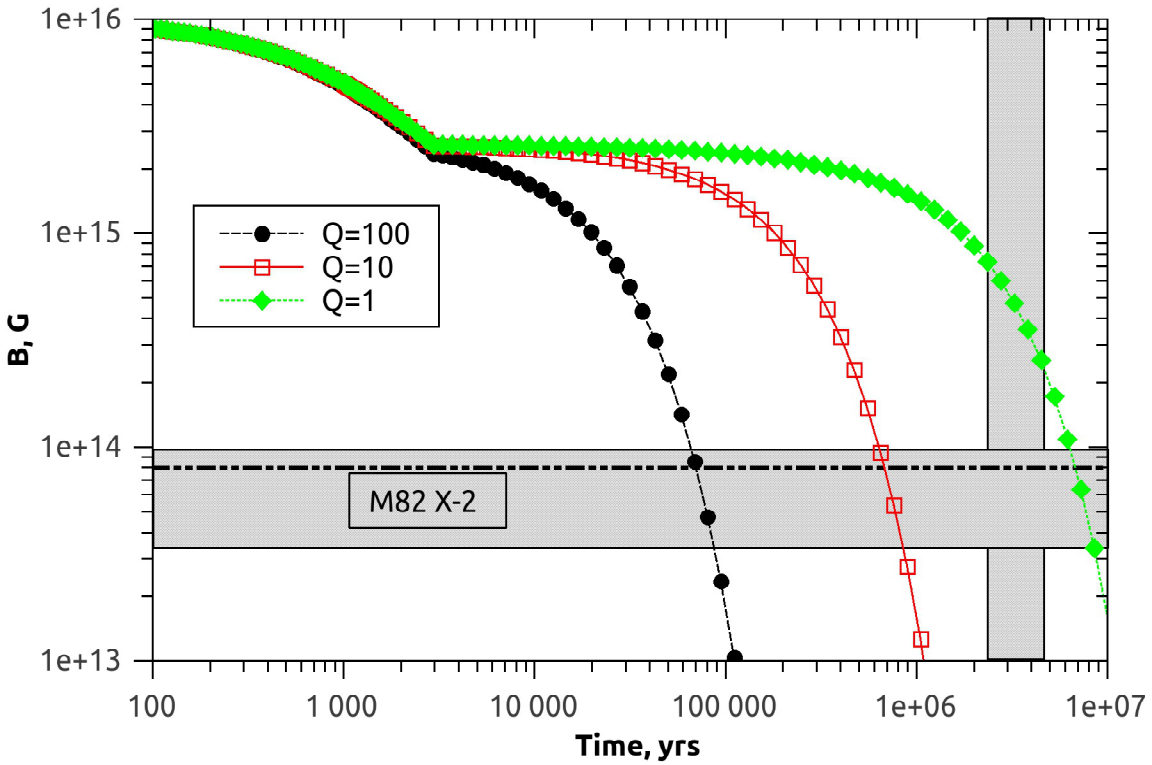

Figure 5.2: Magnetic field decay for several sets of parameters and estimates for known sources. Initial field $B_0 = 10^{16}$ G. Filled circles, empty squares, and filled diamonds corresponds to the standard case with Hall attractor (since $t = 3\tau_{\rm Hall,0}$) and different values of Q (see the legend). Dot-dot-dashed horizontal line corresponds to the magnetic field estimate for the ULX M82 X-2 from Mushtukov et al. (2015): $B = 8 \times 10^{13}$ G. Horizontal grey box corresponds to the field estimate for the NS in 4U 0114+65 by Sanjurjo et al. (2017): $B \sim (3 - 10) \times 10^{13}$ G. Vertical grey box shows credential interval which contains 95% probability for the age of the NS in this source: 2.4-5 Myrs (this work).

is visible from Fig. 5.1, in most of the cases the remaining magnetic field is $\lesssim 10^{13}$ G. However, we can construct an evolutionary track for the field which allows values $\sim 10^{14}$ G several Myrs after the NS formation. Two main ingredients are: the Hall attractor and low Q. In addition, it is necessary that resistivity due to phonons is low (i.e., the crust is colder than $T_{\rm U}$) during most of the evolution (say, after few hundred thousand years).

This combination of parameters is not the expected one, as typically it is assumed (Pons et al. 2013) that Q is large for magnetars, because currents are situated in deep crustal layers in the zone of nuclear pasta, where impurities are important.

For comparison we present in Fig. 5.2 magnetic field evolution for $B_0 = 10^{16}$ G. For such large fields results are not very sensitive to the choice of coefficients in eq. (5.8). This is so because for higher field the Hall attractor stage starts very early, and also at early phases of evolution decay is mostly driven by the Hall term. With respect to Fig. 5.1 curves are shifted not only up, but also to the left, as the initial evolution proceeds much faster for larger fields due to smaller Hall time scale. Later evolution, at ages $\gtrsim 100$ kyrs, is not much changed. Obviously, it is still impossible to explain accreting magnetars without involving the Hall attractor and low values of Q even for very large initial magnetic fields.

To make good estimates of Q or at least to put strict limits on its value, it is necessary to use sources with known ages of NSs. In many cases only very approximate estimates are available from analysis of binary evolution. However, in a few cases it is possible to derive age estimates from kinematics of well-studied binaries in the Galaxy. In the following section we provide such calculations for the X-ray binary 4U 0114+65.

5.4 Age of 4U0114+65

The accreting magnetar candidate 4U 0114+65 is an excellent source to place some limits on the inner crust impurity. The magnetic field of this source was recently estimates as $\sim 10^{14}$ G (see Introduction). Meanwhile, the source is at substantial offset from any star-forming region which is most probably caused by a velocity kick imparted to the system during the first supernova explosion. The large OB association CAS OB8 [Ruprecht et al., 1982; Alter et al., 1970] is 2° away which is comparable with the distance of 4U0114+65 from the Galactic plane ($b = +2°.5635$). At angular separation of one degree an old stellar cluster Pfleiderer 1 with the age 1 Gyr can be found [Kharchenko et al., 2012, 2013; Schmeja et al., 2014a,b]. Clusters of such age are not associated with OB stars. The source is at $\alpha' = 01^h\ 18^m\ 02^s.6974$ δ'=+65° 17′ 29.″830[1] and has effectively an upper limit on parallax $\varpi' = 0.11$ mas set by *Gaia* with its accuracy 0.23 mas in the first data release [Lindegren et al., 2016]. The parallax indicates a distance larger than 4 kpc which is in agreement with photometric distance 7 ± 3.6 [Reig et al., 1996] based on the apparent magnitude $m_v = 11.14$, $E(B-V) = 1.24$ and spectral type of the companion B1Ia. According to the recent three-dimensional map of the Milky Way dust [Green et al., 2015] the measured reddening of $E(B-V) = 1.24$ corresponds to distances in range 3.8-6.0 kpc in the direction to 4U0114+65.

[1]The measured quantities are written with prime here

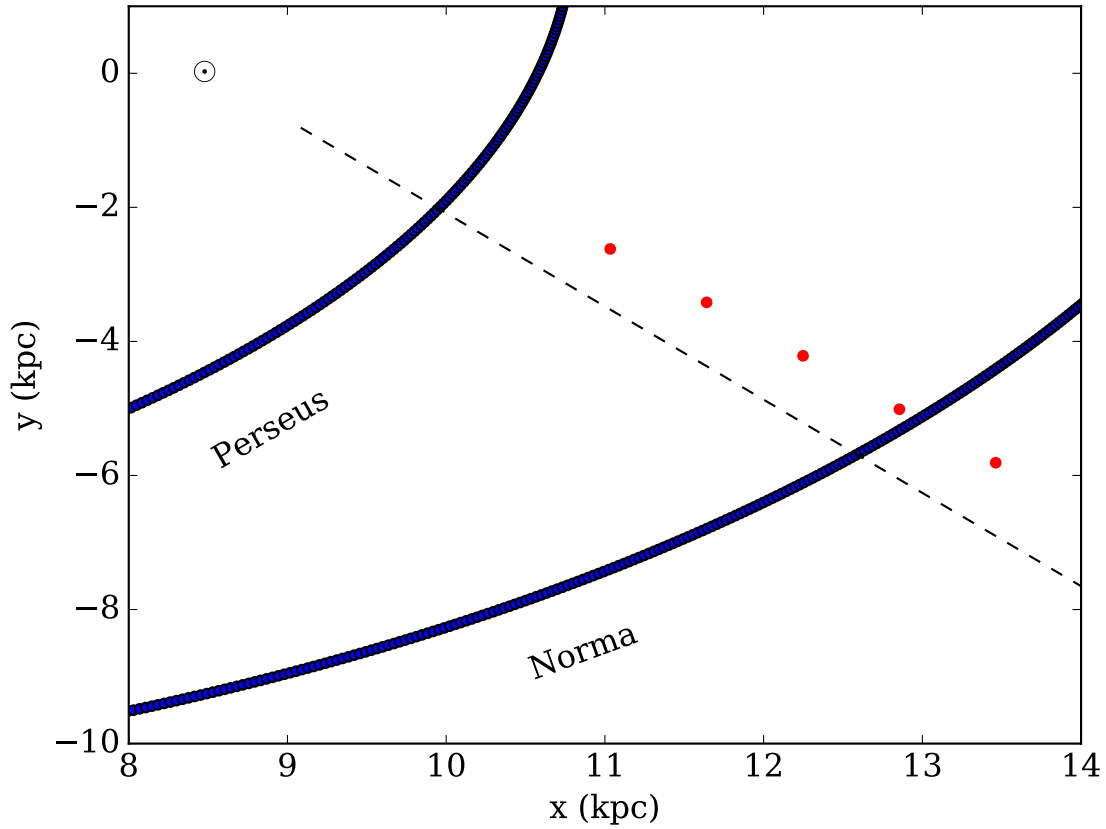

Figure 5.3: The Galactic spiral pattern and the direction toward 4U0114+65 (dashed line). Dots show possible birth positions of the source obtained by back integration in time of its current location, proper motion and radial velocity for different assumed distances D in the range from 4 until 10 kpc from the observer with step 1 kpc. The spiral pattern is valid only for radial distances more than 3 kpc from the Galactic centre.

The system 4U0114+65 has measured proper motion $\mu'_{\alpha*} = -1.4 \pm 1.72$, $\mu'_{\delta} = 3.17 \pm 1.56$ [van Leeuwen, 2007] and the radial velocity $v'_r = -57 \pm 2$ (Pourbaix et al. 2004; Crampton et al. 1985, the observational uncertainty is made larger to take both fits into account). Such proper motion in combination with the angular separation of 2° easily gives the kinematic age of order 2 Myr irrespectively of the source distance.

To better understand the possible origin of the source and its kinematic age we plot the direction to 4U0114+65 on top of the four spiral arms based on Wainscoat et al. [1992] and Georgelin & Georgelin [1976], see Fig. 5.3. Given its distance, the system is most probably originated from the Norma spiral arm. It allows us to get some estimate of the system age. Two approaches are described in the following sections: (1) the classical backward orbit integration for a number of distances; (2) the Bayesian approach.

5.4.1 Backward orbit integration

The kinematic age of a system is usually considered as a time which is required for the system to travel from its birth position (often assumed as the Galactic plane $z = 0$) until its recent location, see e.g. Noutsos et al. [2013]. This approach is justified because majority of B stars are born in a very thin layer close to the Galactic plane (scale height 45 pc according to Reed 2000). It is quite common that some estimate of the object distance is available, but the radial velocity is missing. In our case the distance is unknown, but the radial velocity is perfectly constrained. This is the reason to start the backward orbit integration from different positions along the line of sight from 4 kpc with 1 kpc spacing between separate initial conditions.

The equatorial coordinates, distance, proper motion and the radial velocity uniquely constrain the initial conditions for the orbit integration. The integration is performed by means of the GALPY python package [Bovy, 2015][2] which allows us to perform the coordinate transformation. The binary motion is considered in the second gravitational potential from the paper by Irrgang et al. [2013]. The conversion to natural units used in the GALPY is done assuming the Solar distance $R_\odot = 8.5$ kpc and the Solar velocity $v_\odot = 220$ km/s. The orbit is integrated backward in time until a moment when it either crosses the Galactic plane ($|z| < 10$ pc), or when it approaches the height $z = 100$ pc (two times of the scale height from Reed 2000). The orbit intersections with the Galactic plane for different distances are shown with dots in Fig. 5.3. The Norma spiral arm seems to be the most prominent formation region (see also Reig et al. 1996).

For the whole range of distances the age estimate is exactly the same and it is equal 3.48 Myr. It happens because the intersection time is defined by fraction between z and v_z and a contribution of the radial velocity is constant which makes both z and v_z linearly depend on distance. The intersection with $z = 100$ pc leads to age estimates ranging from 1.97 Myr for smaller distances up to 2.72 Myr for larger distances. The age depends on distance in this case because $z = 100$ pc has different angular size at different distances.

The distance from the Galactic center $R_0 = 13.8$ kpc and azimuth $\phi = 21°.30$ is close to the Norma spiral arm (the GALPY uses the left-handed frame for the orbit integration). The position and velocity found in the backward integration is used then in the next Section as the first guess for the Markov Chain Monte Carlo process.

5.4.2 The Bayesian age estimate

The proper motion of the system 4U0114+65 is measured with a significant uncertainty which leads to a large family of possible orbits. We introduce here the Bayesian approach for the kinematic age estimate. We start from the conditional probability to obtain measurements given the actual values for the birth position $\vec{R}_0 = [R_0, \phi_0, z_0]$ (radial distance R_0, azimuth ϕ_0 and height above the galactic plane z_0), and three dimensional velocity $\vec{v}_0 = [v_{r,0}, v_{T,0}, v_{z,0}]$ (radial $v_{r,0}$, transversal $v_{T,0}$ and vertical $v_{z,0}$) as well as the system age t since the moment of the first supernova explosion. The conditional probability is:

$$p(\mu'_{\alpha*}, \mu'_\delta, v'_r, \alpha', \delta' | \vec{R}_0, \vec{v}_0, t) \propto$$
$$g(\mu'_{\alpha*}|\mu_{\alpha*}) g(\mu'_\delta|\mu_\delta) g(\alpha'|\alpha) g(\delta'|\delta) g(v'_r|v_r) \tag{5.14}$$

[2] http://github.com/jobovy/galpy

where $g(x'|x)$ is a Gaussian in form:

$$g(x'|x) = \frac{1}{\sqrt{2\pi}\sigma_x} \exp\left(-\frac{(x'-x)^2}{2\sigma_x^2}\right). \tag{5.15}$$

The values with prime are used to show measured quantities while values without prime are for actual (unknown) values. The difference between the measured and actual values appears only because of the observational errors. Eq. (5.14) is essentially the likelihood which constrains the possible birth properties of the system such a way that its current sky position, proper motion and the radial velocity are in agreement with observations. In the case of the coordinates α, δ the observational uncertainty is artificially increased up to $1'$ because more accurate precision is not necessary. The posterior can be written as multiplication of the likelihood to prior:

$$P(\vec{R}_0, \vec{v}_0, t|\mu'_{\alpha*}, \mu'_\delta, v'_r, \alpha', \delta') \propto$$

$$p(\mu'_{\alpha*}, \mu'_\delta, v'_r, \alpha', \delta'|\vec{R}_0, \vec{v}_0, t) f(\vec{R}_0, \vec{v}_0, t). \tag{5.16}$$

The normalization is not important here because it is a constant. The prior $f(\vec{R}_0, \vec{v}_0, t)$ is a multiplication of three independent priors: for the Galactic structure $f_G(\vec{R}_0)$ which includes the description of the spiral pattern, for the initial systemic velocity $f_v(\vec{v}_0)$ and a flat Jefferson prior for time in the range from 0.01 Myr till 100 Myr.

The prior for the spiral pattern is:

$$f_G(\vec{R}_0) \propto \frac{1}{\sqrt{2\pi}\sigma_r\sigma_z} \exp\left(-\frac{(R_0 - r_k \exp((\phi_0 - \phi_k)/\kappa_k))}{2\sigma_r^2}\right) \times \exp(-z/\sigma_z) \tag{5.17}$$

This complicated function represents the logarithmic spiral with $r_k = 3.48$ kpc, $\kappa_k = 4.25$ and $\phi_k = 2\pi$ in the case of the outer part of the Norma arm [Wainscoat et al., 1992]. The typical dispersions are selected as $\sigma_r = 0.35$ kpc [Faucher-Giguère & Kaspi, 2006] and $\sigma_z = 0.045$ kpc [Reed, 2000].

The prior for the birth kick velocity is a simple isotropic Maxwellian with reduced $\sigma = 150$ km/s to take into account that binaries can be disrupted and the natal kick velocity of the neutron star is not the systemic velocity of the binary, see e.g. Repetto et al. [2017].

Since we are interested only in the kinematic age, all spatial and dynamical variables are integrated out:

$$P(t) \propto \int ... \int P(\vec{R}_0, \vec{v}_0, t|\mu'_{\alpha*}, \mu'_\delta, v'_r, \alpha', \delta') d^3\vec{R}_0 d^3\vec{v}_0 \tag{5.18}$$

The simplest way to implement this multidimensional integration is to use the Markov chain Monte Carlo sampler. The simulations are performed for 48 walkers and the ensemble size 4000 with first 1000 samples were excluded to allow the process to converge to the stationary distribution. For this process the maximum radial distance was set to 15 kpc and maximum velocity to 300 km/s in each direction. To quantify the posterior distribution the 95% credential interval is computed for samples. Analytically this interval is described as:

$$\int_a^b P(t)dt = 0.95 \tag{5.19}$$

where a and b are the boundaries of the interval. The credential interval ranges from 2.39 Myr till 4.96 Myr. The posterior peaks at 3.90 Myr. A use of the velocity prior in form of Maxwellian with $\sigma = 250$ km/s (typical for isolated neutron stars) extends the credential interval by ≈ 0.5 Myr at both sides: 1.92 Myr to 5.65 Myr with peak at 4.0 Myr.

We conclude this section with the statement that taking into account the age estimates presented above, properties of 4U 0114+65 as an accreting magnetar candidate can be explained with initial fields $\sim 10^{15}$ – 10^{16} G and $Q \sim 1$ – 5, see Fig. 5.2.

5.5 Discussion

Accreting magnetars remain hypothetical sources, i.e. estimates of magnetic field of NSs in candidate systems are not certain. Still, several authors discussed the origin and evolution of such binaries. Above we focused on the magnetic field evolution to study under which conditions the field can remain high enough for the required long time.

For the first time we tried to model NS magnetic field evolution for accreting magnetars in the framework used for studies of standard isolated magnetars. In our analysis we did not include possible influence of accretion on the field decay. If this effect is taken into account (see, for example, Pan et al. 2016) then the field might be even lower than in our estimates. I.e., smaller values of Q might be appropried to fit properties of the systems discussed in this paper. However, NSs in HMXBs are relatively young, and if we are not dealing with ULXs, then the amount of accreted matter is not high enough ($\lesssim$ few $\times 0.001\,M_\odot$) to result in significant additional field decay.

In our calculations we assumed the the Hall attractor stage starts at $t = 3\tau_{\rm Hall,0}$. According to Gourgouliatos & Cumming [2014a] and Wood & Hollerbach [2015] the onset of this stage is not so certain. It can start later. In this case we present conservative estimates, i.e. for later Hall attractor initiation the magnetic field might decay more (see Fig. 5.1 for the case without the Hall attractor). Thus, it is necessary to use even smaller Q to explain accreting magnetars with ages from few Myrs up to few tens of Myrs.

Shao & Li [2015] studied possible evolutionary channels to explain ULXs with NSs. According to this study typical ages of of NSs at the time when the Roche lobe overflow is initiated are about several tens of Myrs. Fragos et al. [2015] came to similar conclusions. The system M82 X-2, according to these authors, is most probably $\lesssim 65$ Myrs old, and the NS progenitor had a mass 8 – $25\,M_\odot$; thus the NS might have an age $\gtrsim$ few tens of Myrs. From Fig. 5.2 it is visible, that with $Q = 1$ we can explain the field estimate for the source M82 X-2 made by Mushtukov et al. [2015] just for age $\lesssim 10^7$ yrs even with $B_0 = 10^{16}$ G. For larger ages it is necessary to use lower values of Q, which can be applicable to normal radio pulsars, but is not considered to be typical for magnetars. Better (and more numerous) estimates of ages of NSs in accreting magnetar candidate systems might help to improve our understanding of their magnetic fields evolution.

5.6 Summary

Accreting magnetars have been proposed as a class by Reig et al. [2012], and later on ULXs with NSs were suggested an possible members of this group [Ekşi et al., 2015]. Despite the fact that evidence in favour of their existence is up to date just indirect, such systems might be formed if a NS remains highly magnetized after tens of Myrs of evolution. It is possible to find a set of parameters which allows this.

To better constrain the NS parameters responsible for the field evolution it is necessary to have better estimates of ages for accreting magnetar candidates. We suggest a new Bayesian estimate of the kinematic ages. Applying this estimate to the accreting magnetar candidate 4U0114+65 with realistic priors we find that its kinematic age is 2.4-5.0 Myr (95% credential interval).

We conclude, that to form an accreting magnetar with an age $\gtrsim$ few Myrs it is necessary to include three main ingredients: the Hall attractor, absence of scattering on phonons after few hundred thousand years, and low ($\lesssim$ few) value of parameter Q which characterizes the role of impurities.

5.A Proposed accreting magnetars

Below we list some of proposed accreting magnetar candidates:

- ULX. NuSTAR J095551+6940.8 (M82 X-2). Ekşi et al. [2015].
- ULX. NGC 5907. Israel et al. [2017a]
- ULX. NGC 7793 P13. Israel et al. [2017b].
- 4U0114+65. Sanjurjo et al. [2017].
- 4U 2206+54. Ikhsanov & Beskrovnaya [2010].
- SXP1062. Fu & Li [2012]
- Swift J045106.8-694803. Klus et al. [2013].

Also a large list of possible candidates can be found in Klus et al. [2014]; Ho et al. [2014] (see also Shi et al. 2015). These candidates are selected on the base of timing properties of X-ray pulsars.

Individual estimates of magnetic field can be very different for a given source as several models (and considerations) can be applied. For example, in the case of M82 X-2, which is the most famous source in the list, estimates range from standard fields $\sim 10^{12}$ G [Christodoulou et al., 2016] up to $\sim 10^{14}$ G [Tsygankov et al., 2016], including the case of normal dipole ($\sim 10^{12}$ G) but strong multipole fields ($\sim 10^{14}$ G) [Tong, 2015].

For several other sources (for example, IGR J16358-4726 and 4U 1954+319, see Enoto et al. 2014) it was noted that basing on the model of standard disc accretion [Ghosh & Lamb, 1979] NSs in these systems might have magnetar-scale dipolar fields. However, more detailed analysis usually demonstrate that sources can be explained with a different model of accretion, in which

there is no necessity of strong magnetic field. Thus, independent measurement of magnetic fields in such sources is of interest for accretion physics.

5.B Magnetic field estimates based on timing properties

Here we briefly remind basics of magnetic field estimates from data on spin period, p, and period derivative, $\dot{p}$. We basically follow Chashkina & Popov [2012].

Magnetic field can be estimated either under so-called hypothesis of equilibrium period, or from period variations (spin-up or spin-down) for a specified model of accretion.

Assuming that the spin period of a NS is equal to its equilibrium period, the magnetic field B for disc accretion can be estimated as follows:

$$B = 2^{-1/4}\pi^{-7/6}k_t^{-7/12}\epsilon^{7/24}p^{7/6}\dot{M}^{1/2}(GM)^{5/6}R^{-3}. \tag{5.20}$$

Here $\dot{M}$ is the accretion rate, M and R are the NS mass and radius, and k_t and ϵ are coefficients of order unity (often used values are $\epsilon = 0.45$, $k_t = 1/3$).

For wind accretion:

$$B = 2\sqrt{\frac{2\eta}{k_t\pi}}p_{\rm orb}^{-1/2}v^{-2}(GM)^{3/2}\dot{M}^{1/2}pR^{-3}. \tag{5.21}$$

Here $p_{\rm orb}$ is the orbital period of a binary, v is the stellar wind velocity, and η is a coefficient of order unity (often it is assumed $\eta = 1/4$).

In the model of settling accretion from stellar wind developed recently by Shakura et al. [2012] a different equation is valid:

$$B = 0.24\times10^{12}\,{\rm G}\,\eta_{\rm s}\left(\frac{p/100{\rm s}}{p_{orb}/10{\rm days}}\right)^{11/12}\dot{M}_{16}^{1/3}\left(v/(10^8\,{\rm cm/s})\right)^{-11/3}, \tag{5.22}$$

where $\eta_{\rm s}$ is a coefficient of order unity. This model is valid for relatively low luminosities, and it was successfully applied to many systems (see, for example, Postnov et al. 2014; Sanjurjo et al. 2017 and references therein).

A NS star can be out of spin-equilibrium if it is rapidly spinning up or down. In this case it is possible to neglect either spin-up or spin-down torque. This allows us to estimate the magnetic field. For example, for disc accretion using the observed values of the maximum spin-up rate, the magnetic field of NS can be estimated as follows:

$$B = \frac{2^4\pi^{7/2}}{\epsilon^{7/4}}\frac{(I\dot{p})^{7/2}}{R^3p^7\dot{M}^3(GM)^{3/2}}, \tag{5.23}$$

where I is the moment of inertia of a NS.

In the case of the maximum spin-down rate the magnetic field of a NS can be estimated as follows:

$$B = \frac{2}{R^3}\left(\frac{I\dot{p}GM}{2\pi k_t}\right)^{1/2}. \tag{5.24}$$

This estimate should be normally considered as a lower limit, since we cannot be sure that no accelerating torque exists at that moment.

Note, that there are many more equations to estimate magnetic field under the hypothesis of spin equilibrium or without it. Description of some of them can be found in Shi et al. [2015].

List of publications

Refereed journals

- **A.P. Igoshev** "The observed velocities of millisecond radio pulsars" A&A, submitted
- **A.P. Igoshev**, S.B. Popov "How to make a mature accreting magnetar" MNRAS 2017, in press
- F. Verbunt, **A.P. Igoshev**, E. Cator "The observed velocity distribution of young pulsars" A&A 2017, in press
- S. Repetto, **A.P. Igoshev**, G. Nelemans "The Galactic distribution of X-ray binaries and its implications for compact object formation and natal kicks" MNRAS 2017, 467, 1, 298-310
- **A.P. Igoshev**, J.G. Elfritz, S.B. Popov "Post fall-back evolution of multipolar magnetic fields and radio pulsar activation" MNRAS 2016, 462, 4, 3689
- **A.P. Igoshev**, F. Verbunt, E. Cator "Distance and luminosity probability distributions derived from parallax and flux with their measurement errors. With application to the millisecond pulsar PSR J0218+4232" A&A 2016, 591, 10
- D.J. Jones, **A.P. Igoshev**, M. Haverkorn "A new method to probe the thermal electron content of the Galaxy through spectral analysis of background sources" MNRAS 2016, 460, 3, 3298-3304
- **A.P. Igoshev** & S.B. Popov "Modified pulsar current analysis: probing magnetic field evolution" MNRAS 2014, 444, 1066
- **A.P. Igoshev** & S.B. Popov "Gaussian mixture model and population synthesis of radio pulsars" MNRAS 2013, 434, 2229
- **A.P. Igoshev** & S.B. Popov "Neutron star's initial spin period distribution" MNRAS 2013, 432, 967

Conference proceedings

- **A.P. Igoshev** & S.B. Popov "Magnetic field decay in normal radio pulsars" AN 2014, 336, 8-9, 831
- **A.P. Igoshev**, S.B. Popov & R. Turolla "Unifying neutron stars: getting to GUNS" AN 2014, 335, 3, 262
- **A.P. Igoshev** & A.F. Kholtygin "Population synthesis of young neutron stars" Proceedings of the International Astronomical Union, 2013, 291, 411
- **A.P. Igoshev** & A.F. Kholtygin "Neutron stars: history of the magnetic field decay" Proceedings of the International Astronomical Union, 2013, 291, 408
- **A.P. Igoshev** & A.F. Kholtygin "Statistics of magnetic fields and fluxes of massive OB stars and the origin of neutron star magnetic fields" AN 2011, 332, 1012
- A.F. Kholtygin, S.N. Fabrika, N.A. Drake & **A.P. Igoshev** "Magnetic fluxes of massive stars: statistics and evolution" Active OB stars: structure, evolution, mass loss, and critical limits, Proceedings of the International Astronomical Union, IAU Symposium, 2011, 272, 198

Bibliography

A. A. Abdo, M. Ajello, A. Allafort, et al., 2013. *ApJS*, 208:17.

D. N. Aguilera, J. A. Pons, & J. A. Miralles, 2008a. *A&A*, 486:255–271.

D. N. Aguilera, J. A. Pons, & J. A. Miralles, 2008b. *ApJ*, 673:L167.

G. Alter, B. Balazs, J. Ruprecht, et al., 1970. *Catalogue of star clusters and associations*.

W. D. Arnett, J. N. Bahcall, R. P. Kirshner, et al., 1989. *ARA&A*, 27:629–700.

J. Arons & E. T. Scharlemann, 1979. *ApJ*, 231:854–879.

Z. Arzoumanian, D. F. Chernoff, & J. M. Cordes, 2002. *ApJ*, 568:289–301.

E. Asseo & D. Khechinashvili, 2002. *MNRAS*, 334:743–759.

M. Bachetti, F. A. Harrison, D. J. Walton, et al., 2014. *Nature*, 514:202–204.

Coryn A L Bailer-Jones, 2015. *PASP*, 127(9):994–1009.

C G Bassa, J Antoniadis, F Camilo, et al., 2016a. *Monthly Notices of the Royal Astronomical Society*, 455(4):3806–3813.

C G Bassa, G H Janssen, B W Stappers, et al., 2016b. *MNRAS*, 460(2):2207–2222.

G. Baym, H. A. Bethe, & C. J. Pethick, 1971. *Nuclear Phys. A*, 175:225–271.

A. M. Beloborodov, 2008. *ApJ*, 683:L41–L44.

A. M. Beloborodov & X. Li, 2016. *ApJ*, 833:261.

C. G. Bernal & N. Fraija, 2016. *ArXiv e-prints*.

C. G. Bernal, W. H. Lee, & D. Page, 2010. *Rev. Mexicana Astron. Astrofis.*, 46:309–322.

C. G. Bernal, D. Page, & W. H. Lee, 2013. *ApJ*, 770:106.

H. A. Bethe & J. R. Wilson, 1985. *ApJ*, 295:14–23.

D. Bhattacharya, R. A. M. J. Wijers, J. W. Hartman, et al., 1992. *A&A*, 254:198–212.

A. Blaauw, 1961. *Bull. Astron. Inst. Netherlands*, 15:265.

C. Blaha & R. M. Humphreys, 1989. *AJ*, 98:1598–1608.

S. Bogdanov, C.-Y. Ng, & V. M. Kaspi, 2014. *ApJ*, 792:L36.

J. Bovy, 2015. *ApJS*, 216:29.

J. Bovy & H.-W. Rix, 2013. *ApJ*, 779:115.

W. F. Brisken, J. M. Benson, A. J. Beasley, et al., 2000. *ApJ*, 541:959–962.

W. F. Brisken, J. M. Benson, W. M. Goss, et al., 2002. *ApJ*, 571:906–917.

W. F. Brisken, A. S. Fruchter, W. M. Goss, et al., 2003a. *AJ*, 126:3090–3098.

W. F. Brisken, S. E. Thorsett, A. Golden, et al., 2003b. *ApJ*, 593:L89–L92.

W. R. Brown, M. J. Geller, S. J. Kenyon, et al., 2010. *AJ*, 139:59–67.

E. M. Burbidge, G. R. Burbidge, W. A. Fowler, et al., 1957. *Reviews of Modern Physics*, 29:547–650.

N. Chamel & P. Haensel, 2008. *Living Reviews in Relativity*, 11:10.

A. Chashkina & S. B. Popov, 2012. *New A*, 17:594–602.

S. Chatterjee, W. F. Brisken, W. H. T. Vlemmings, et al., 2009. *ApJ*, 698:250–265.

S. Chatterjee, J. M. Cordes, T. J. W. Lazio, et al., 2001. *ApJ*, 550:287–296.

S. Chatterjee, J. M. Cordes, W. H. T. Vlemmings, et al., 2004. *ApJ*, 604:339–345.

R. A. Chevalier, 1989. *ApJ*, 346:847–859.

D. M. Christodoulou, D. Kazanas, & S. G. T. Laycock, 2016. *ArXiv e-prints*.

Joseph E. Coleman, 1992. *Annual Review of Biochemistry*, 61(1):897–946. PMID: 1497326.

J. M. Cordes & T. J. W. Lazio, 2002. *ArXiv e-prints*.

D. Crampton, J. B. Hutchings, & A. P. Cowley, 1985. *ApJ*, 299:839–844.

A. Cumming, P. Arras, & E. Zweibel, 2004. *ApJ*, 609:999–1017.

A. K. Dambis, A. M. Mel'nik, & A. S. Rastorguev, 2001. *Astron. Letters*, 27:58–64.

C. R. D'Angelo, 2017. *MNRAS*, 470:3316–3331.

A. de Luca, 2008. In *40 Years of Pulsars: Millisecond Pulsars, Magnetars and More*, editors C. Bassa, Z. Wang, A. Cumming, et al., volume 983 of *American Inst. of Phys. Conf. Series*, pages 311–319.

W. Dehnen & J. J. Binney, 1998. *MNRAS*, 298:387–394.

A T Deller, A M Archibald, W F Brisken, et al., 2012. *ApJ*, 756(2):L25.

A T Deller, J Boyles, D R Lorimer, et al., 2013. *ApJ*, 770(2):145.

A. T. Deller, S. J. Tingay, M. Bailes, et al., 2009. *ApJ*, 701:1243–1257.

A T Deller, S J Vigeland, D L Kaplan, et al., 2016. *ApJ*, 828(1):8.

G Desvignes, R N Caballero, L Lentati, et al., 2016. *MNRAS*, 458(3):3341–3380.

J. D. M. Dewi, P. Podsiadlowski, & O. R. Pols, 2005. *MNRAS*, 363:L71–L75.

V. Doroshenko, A. Santangelo, V. Suleimanov, et al., 2010. *A&A*, 515:A10.

F. Douchin & P. Haensel, 2001. *A&A*, 380:151–167.

Y. Du, J. Yang, R. M. Campbell, et al., 2014. *ApJ*, 782:L38.

Yuanjie Du, Jun Yang, Robert M Campbell, et al., 2014. *ApJ*, 782(2):L38.

K. Y. Ekşi, İ. C. Andaç, S. Çıkıntoğlu, et al., 2015. *MNRAS*, 448:L40–L42.

J. G. Elfritz, J. A. Pons, N. Rea, et al., 2016. *MNRAS*, 456:4461–4474.

T. Enoto, M. Sasano, S. Yamada, et al., 2014. *ApJ*, 786:127.

T. Erber, 1966. *Rev. of Modern Phys.*, 38:626–659.

G. Fabbiano, 2006. *ARA&A*, 44:323–366.

C.-A. Faucher-Giguère & V. M. Kaspi, 2006. *ApJ*, 643:332–355.

A. J. Faulkner, M. Kramer, A. G. Lyne, et al., 2005. *ApJ*, 618:L119–L122.

H. Feng & P. Kaaret, 2008. *ApJ*, 675:1067-1075.

R D Ferdman, I H Stairs, M Kramer, et al., 2014. *MNRAS*, 443(3):2183–2196.

Emmanuel Fonseca, Ingrid H Stairs, & Stephen E Thorsett, 2014. *ApJ*, 787(1):82.

T. Fragos, T. Linden, V. Kalogera, et al., 2015. *ApJ*, 802:L5.

Paulo C C Freire, Norbert Wex, Gilles Esposito-Farèse, et al., 2012. *MNRAS*, 423(4):3328–3343.
L. Fu & X.-D. Li, 2012. *ApJ*, 757:171.
Y. M. Georgelin & Y. P. Georgelin, 1976. *A&A*, 49:57–79.
U. Geppert, D. Page, & T. Zannias, 1999. *A&A*, 345:847–854.
P. Ghosh & F. K. Lamb, 1979. *ApJ*, 232:259–276.
P. L. Gonthier, M. S. Ouellette, J. Berrier, et al., 2002. *ApJ*, 565:482–499.
E. V. Gotthelf & J. P. Halpern, 2009. *ApJ*, 695:L35–L39.
E. V. Gotthelf, J. P. Halpern, & J. Alford, 2013. *ApJ*, 765:58.
K. N. Gourgouliatos & A. Cumming, 2014a. *Phys. Rev. Letters*, 112(17):171101.
K. N. Gourgouliatos & A. Cumming, 2014b. *MNRAS*, 438:1618–1629.
S. E. Gralla, A. Lupsasca, & A. Philippov, 2016. *ArXiv e-prints*.
G. M. Green, E. F. Schlafly, D. P. Finkbeiner, et al., 2015. *ApJ*, 810:25.
F. Grisé, P. Kaaret, M. W. Pakull, et al., 2011. *ApJ*, 734:23.
L Guillemot, D A Smith, H Laffon, et al., 2016. *A&A*, 587:A109.
M. Gullón, J. A. Miralles, D. Viganò, et al., 2014. *MNRAS*, 443:1891–1899.
M. Gullón, J. A. Pons, J. A. Miralles, et al., 2015. *MNRAS*, 454:615–625.
J. P. Halpern & E. V. Gotthelf, 2010. *ApJ*, 709:436–446.
B. M. S. Hansen & E. S. Phinney, 1997. *MNRAS*, 291:569.
A. K. Harding, 2013. *Frontiers of Phys.*, 8:679–692.
J. W. Hartman, 1997. *A&A*, 322:127–130.
C. He, C.-Y. Ng, & V. M. Kaspi, 2013. *ApJ*, 768:64.
A. Hewish, S. J. Bell, J. D. H. Pilkington, et al., 1968. *Nature*, 217:709–713.
W. C. G. Ho, 2011. *MNRAS*, 414:2567–2575.
W. C. G. Ho, 2015. *MNRAS*, 452:845–851.
W. C. G. Ho, H. Klus, M. J. Coe, et al., 2014. *MNRAS*, 437:3664–3669.
G. Hobbs, D. R. Lorimer, A. G. Lyne, et al., 2005. *MNRAS*, 360:974–992.
G. Hobbs, A. G. Lyne, M. Kramer, et al., 2004. *MNRAS*, 353:1311–1344.
J. Holmberg, B. Nordström, & J. Andersen, 2009. *A&A*, 501:941–947.
D. Hooper & G. Mohlabeng, 2016. *J. Cosmology Astropart. Phys.*, 3:049.
A. Igoshev, F. Verbunt, & E. Cator, 2016. *A&A*, 591:A123.
A. P. Igoshev & S. B. Popov, 2013. *MNRAS*, 432:967–972.
A. P. Igoshev, S. B. Popov, & R. Turolla, 2014. *Astronomische Nachrichten*, 335:262–267.
N. R. Ikhsanov & N. G. Beskrovnaya, 2010. *Astrophysics*, 53:237–250.
A. Irrgang, B. Wilcox, E. Tucker, et al., 2013. *A&A*, 549:A137.
G. L. Israel, A. Belfiore, L. Stella, et al., 2017a. *Science*, 355:817–819.
G. L. Israel, A. Papitto, P. Esposito, et al., 2017b. *MNRAS*, 466:L48–L52.
H.-T. Janka, 2012. *Annual Review of Nuclear and Particle Science*, 62:407–451.
H.-T. Janka, 2017. *ApJ*, 837:84.
P. Kaaret, H. Feng, & T. P. Roberts, 2017. *ArXiv e-prints*.
V. M. Kaspi, 2010. *Proc. of the Natl. Acad. of Sci.*, 107:7147–7152.
N. V. Kharchenko, A. E. Piskunov, E. Schilbach, et al., 2012. *A&A*, 543:A156.
N. V. Kharchenko, A. E. Piskunov, E. Schilbach, et al., 2013. *A&A*, 558:A53.

F. Kirsten, W. Vlemmings, R. M. Campbell, et al., 2015. *A&A*, 577:A111.
H. Klus, E. S. Bartlett, A. J. Bird, et al., 2013. *MNRAS*, 428:3607–3617.
H. Klus, W. C. G. Ho, M. J. Coe, et al., 2014. *MNRAS*, 437:3863–3882.
C. Knigge, M. J. Coe, & P. Podsiadlowski, 2011. *Nature*, 479:372–375.
M. Kramer, K. M. Xilouris, D. R. Lorimer, et al., 1998. *ApJ*, 501:270–285.
D. Lai, 2001. In *Physics of Neutron Star Interiors*, editors D. Blaschke, N. K. Glendenning, & A. Sedrakian, volume 578 of *Lecture Notes in Physics, Berlin Springer Verlag*, page 424.
A. P. Lane, 1979. *PASP*, 91:405–407.
C. Leinert, S. Bowyer, L. K. Haikala, et al., 1998. *A&AS*, 127:1–99.
A. R. Liddle, 2007. *MNRAS*, 377:L74–L78.
L. Lindegren, U. Lammers, U. Bastian, et al., 2016. *A&A*, 595:A4.
Q. Z. Liu, J. van Paradijs, & E. P. J. van den Heuvel, 2006. *A&A*, 455:1165–1168.
Q. Z. Liu, J. van Paradijs, & E. P. J. van den Heuvel, 2007. *A&A*, 469:807–810.
D. R. Lorimer, A. J. Faulkner, A. G. Lyne, et al., 2006. *MNRAS*, 372:777–800.
J. Luo, C.-Y. Ng, W. C. G. Ho, et al., 2015. *ApJ*, 808:130.
T. E. Lutz & D. H. Kelker, 1973. *PASP*, 85:573.
R. N. Manchester, G. B. Hobbs, A. Teoh, et al., 2005. *AJ*, 129:1993–2006.
Allison M Matthews, David J Nice, Emmanuel Fonseca, et al., 2016. *ApJ*, 818(1):92.
Z. Medin & D. Lai, 2006a. *Phys. Rev. A*, 74(6):062507.
Z. Medin & D. Lai, 2006b. *Phys. Rev. A*, 74(6):062508.
Z. Medin & D. Lai, 2007a. *Advances in Space Res.*, 40:1466–1471.
Z. Medin & D. Lai, 2007b. *MNRAS*, 382:1833–1852.
A. M. Mel'nik & A. K. Dambis, 2009. *MNRAS*, 400:518–523.
A. M. Mel'nik & Y. N. Efremov, 1995. *Astron. Letters*, 21:10–26.
S. Mereghetti, J. A. Pons, & A. Melatos, 2015. *Space Sci. Rev.*, 191:315–338.
D. Mihalas & J. Binney, 1981. *Galactic astronomy: Structure and kinematics /2nd edition/.*
C. Motch, M. W. Pakull, R. Soria, et al., 2014. *Nature*, 514:198–201.
A. A. Mushtukov, V. F. Suleimanov, S. S. Tsygankov, et al., 2015. *MNRAS*, 454:2539–2548.
A. G. Muslimov & A. I. Tsygan, 1992. *MNRAS*, 255:61–70.
D. Neuhauser, S. E. Koonin, & K. Langanke, 1987. *Phys. Rev. A*, 36:4163–4175.
D. Neuhauser, K. Langanke, & S. E. Koonin, 1986. *Phys. Rev. A*, 33:2084–2086.
C Ng, M Bailes, S D Bates, et al., 2014. *MNRAS*, 439(2):1865–1883.
K. Nomoto, 1984. *ApJ*, 277:791–805.
A. Noutsos, D. H. F. M. Schnitzeler, E. F. Keane, et al., 2013. *MNRAS*, 430:2281–2301.
Y. Y. Pan, L. M. Song, C. M. Zhang, et al., 2016. *MNRAS*, 461:2–5.
M. A. C. Perryman & ESA, editors, 1997. *The HIPPARCOS and TYCHO catalogues. Astrometric and photometric star catalogues derived from the ESA HIPPARCOS Space Astrometry Mission*, volume 1200 of *ESA Special Publication.*
E. Pfahl, S. Rappaport, P. Podsiadlowski, et al., 2002. *ApJ*, 574:364–376.
A. A. Philippov, B. Cerutti, A. Tchekhovskoy, et al., 2015. *ApJ*, 815:L19.
P. Podsiadlowski, N. Langer, A. J. T. Poelarends, et al., 2004. *ApJ*, 612:1044–1051.
R. Poleski, 2013. *ArXiv e-prints.*

J. A. Pons & U. Geppert, 2007. *A&A*, 470:303–315.
J. A. Pons, J. A. Miralles, & U. Geppert, 2009. *A&A*, 496:207–216.
J. A. Pons, D. Viganò, & U. Geppert, 2012. *A&A*, 547:A9.
J. A. Pons, D. Viganò, & N. Rea, 2013. *Nature Physics*, 9:431–434.
S. B. Popov, A. A. Kaurov, & A. D. Kaminker, 2015. *PASA*, 32:e018.
S. B. Popov, J. A. Pons, J. A. Miralles, et al., 2010. *MNRAS*, 401:2675–2686.
S. B. Popov & R. Turolla, 2012a. *Ap&SS*, 341:457–464.
S. B. Popov & R. Turolla, 2012b. *MNRAS*, 421:L127–L131.
K. A. Postnov, N. I. Shakura, A. Y. Kochetkova, et al., 2014. In *European Physical Journal Web of Conferences*, volume 64 of *European Physical Journal Web of Conferences*, page 02002.
D. Pourbaix, A. A. Tokovinin, A. H. Batten, et al., 2004. *A&A*, 424:727–732.
W. H. Press, B. P. Flannery, S. A. Teukolsky, et al., 1986. *Numerical recipes: the art of scientific computing*. Cambridge University Press.
W. H. Press, S. A. Teukolsky, W. T. Vetterling, et al., 2002. *Numerical recipes in C++ : the art of scientific computing*.
N. Rea, J. A. Pons, D. F. Torres, et al., 2012. *ApJ*, 748:L12.
D J Reardon, G Hobbs, W Coles, et al., 2016. *MNRAS*, 455(2):1751–1769.
B. C. Reed, 2000. *AJ*, 120:314–318.
P. Reig, D. Chakrabarty, M. J. Coe, et al., 1996. *A&A*, 311:879–888.
P. Reig, J. M. Torrejón, & P. Blay, 2012. *MNRAS*, 425:595–604.
S. Repetto, A. P. Igoshev, & G. Nelemans, 2017. *MNRAS*, 467:298–310.
M. Revnivtsev & S. Mereghetti, 2015. *Space Sci. Rev.*, 191:293–314.
M. Ruderman, T. Zhu, & K. Chen, 1998. *ApJ*, 492:267–280.
M. A. Ruderman & P. G. Sutherland, 1975. *ApJ*, 196:51–72.
J. Ruprecht, B. Balazs, & R. E. White, 1982. *Bulletin d'Information du Centre de Donnees Stellaires*, 22:132.
A. Sandage & A. Saha, 2002. *AJ*, 123:2047–2069.
G. Sanjurjo, J. M. Torrejon, K. Postnov, et al., 2017. *ArXiv e-prints*.
C. L. Sarazin, A. Kundu, J. A. Irwin, et al., 2003. *ApJ*, 595:743–759.
L. Scheck, H.-T. Janka, T. Foglizzo, et al., 2008. *A&A*, 477:931–952.
S. Schmeja, N. V. Kharchenko, A. E. Piskunov, et al., 2014a. *A&A*, 568:A51.
S. Schmeja, N. V. Kharchenko, A. E. Piskunov, et al., 2014b. *VizieR Online Data Catalog*, 356.
D. H. F. M. Schnitzeler, 2012. *MNRAS*, 427:664–678.
N. Shabaltas & D. Lai, 2012. *ApJ*, 748:148.
N. Shakura, K. Postnov, A. Kochetkova, et al., 2012. *MNRAS*, 420:216–236.
Y. Shao & X.-D. Li, 2015. *ApJ*, 802:131.
C.-S. Shi, S.-N. Zhang, & X.-D. Li, 2015. *ApJ*, 813:91.
P. S. Shternin, D. G. Yakovlev, C. O. Heinke, et al., 2011. *MNRAS*, 412:L108–L112.
W. M. Smart, 1938. *Stellar dynamics*. Cambridge University Press.
M. C. Smith, G. R. Ruchti, A. Helmi, et al., 2007. *MNRAS*, 379:755–772.
S. A. Story, P. L. Gonthier, & A. K. Harding, 2007. *ApJ*, 671:713–726.
K Stovall, R S Lynch, S M Ransom, et al., 2014. *ApJ*, 791(1):67.

A. Szary, 2013. *ArXiv e-prints*.
A. Szary, G. I. Melikidze, & J. Gil, 2015. *MNRAS*, 447:2295–2306.
A. Szary, B. Zhang, G. I. Melikidze, et al., 2014. *ApJ*, 784:59.
T. M. Tauris & M. Bailes, 1996. *A&A*, 315:432–444.
T. M. Tauris, M. Kramer, P. C. C. Freire, et al., 2017. *ArXiv e-prints*.
J. H. Taylor & J. M. Cordes, 1993. *ApJ*, 411:674–684.
N. Tetzlaff, R. Neuhäuser, M. M. Hohle, et al., 2010. *MNRAS*, 402:2369–2387.
A. N. Timokhin, 2010. *MNRAS*, 408:2092–2114.
A. N. Timokhin & J. Arons, 2013. *MNRAS*, 429:20–54.
A. N. Timokhin & A. K. Harding, 2015. *ApJ*, 810:144.
H. Tong, 2015. *Astronomische Nachrichten*, 336:835.
A. Torres-Forné, P. Cerdá-Durán, J. A. Pons, et al., 2016. *MNRAS*, 456:3813–3826.
M. Toscano, J. S. Sandhu, M. Bailes, et al., 1999. *MNRAS*, 307:925–933.
S. S. Tsygankov, A. A. Mushtukov, V. F. Suleimanov, et al., 2016. *MNRAS*, 457:1101–1106.
R. Turolla, 2009. In *Astrophys. and Space Sci. Libr.*, editor W. Becker, volume 357 of *Astrophys. and Space Sci. Libr.*, page 141.
R. Turolla, S. Zane, & A. L. Watts, 2015. *Reports on Progress in Physics*, 78(11):116901.
V. A. Urpin, G. Chanmugam, & Y. Sang, 1994. *ApJ*, 433:780–785.
E. P. J. van den Heuvel, 2004. In *5th INTEGRAL Workshop on the INTEGRAL Universe*, editors V. Schoenfelder, G. Lichti, & C. Winkler, volume 552 of *ESA Special Publication*, page 185.
F. van Leeuwen, 2007. *A&A*, 474:653–664.
J. P. W. Verbiest & D. R. Lorimer, 2014. *MNRAS*, 444:1859–1861.
J. P. W. Verbiest, J. M. Weisberg, A. A. Chael, et al., 2012. *ApJ*, 755:39.
F. Verbunt & E. Cator, 2017. *Journal of Astrophysics and Astronomy*, 38:40.
F. Verbunt, A.P. Igoshev, & E. Cator, 2017. *A&A*.
D. Viganò, 2013. *Magnetic fields in neutron stars*. Ph.D. thesis, University of Alicante.
D. Viganò & J. A. Pons, 2012. *MNRAS*, 425:2487–2492.
D. Viganò, J. A. Pons, & J. A. Miralles, 2012. *Comput. Phys. Communications*, 183:2042–2053.
D. Viganò, N. Rea, J. A. Pons, et al., 2013a. *MNRAS*, 434:123–141.
D. Viganò, N. Rea, J. A. Pons, et al., 2013b. *MNRAS*, 434:123–141.
R. J. Wainscoat, M. Cohen, K. Volk, et al., 1992. *ApJS*, 83:111–146.
C. J. Wareing & R. Hollerbach, 2009. *A&A*, 508:L39–L42.
T. S. Wood & R. Hollerbach, 2015. *Physical Review Letters*, 114(19):191101.
D. G. Yakovlev & C. J. Pethick, 2004. *ARA&A*, 42:169–210.
Zhen Yan, Zhi-Qiang Shen, Jian-Ping Yuan, et al., 2013. *MNRAS*, 433(1):162–169.
J M Yao, R N Manchester, & N Wang, 2017. *ApJ*, 835:29 (32pp).
M. D. Young, R. N. Manchester, & S. Johnston, 1999. *Nature*, 400:848–849.
V. E. Zavlin & G. G. Pavlov, 2002. In *Neutron Stars, Pulsars, and Supernova Remnants*, editors W. Becker, H. Lesch, & J. Trümper, page 263.

Summary and Future prospects

This thesis presents a few studies of the neutron star properties: the natal kick distribution and magnetic field re-emergence process as well as the properties of the neutron star crust. These features shed light on supernova explosion, in particular, possibly two types of supernova are necessary to explain the bimodality in velocity distribution. This bimodality is seen not only among young radio pulsars but also in recycled pulsars and BeX stars. The activation of the pulsar mechanism in the presence of a fall-back after the supernova explosion is described in Chapter 4.

Distances from parallax measurements

The distances to pulsars are essential in studies of the velocity and luminosity. The pulsars are quite far away, and often the quality of the interferometric measurements of parallax is limited. The knowledge of the Galaxy structure helps to restrict such measurements better. Unfortunately, in a previous analysis of the distances derived from parallax measurements, mathematical mistakes were made.

In the first chapter we rederived the correct equation for the Bayesian probability of distance based on parallax and apply it with a prior of the pulsar distribution in the Galaxy. We have tested this equation using Monte Carlo simulations. We also give an equation for the posterior probability of the pulsar luminosity when the flux (radio or gamma-ray) and parallax are measured. Using this equation we show that the most probable intrinsic gamma-ray flux of the J0218+4232 is significantly less than its spin-down energy loss as it is expected from pulsar theory.

Velocity distribution of young radio pulsars

The second chapter concentrates on the velocity distribution of young radio pulsars derived from measured parallaxes and proper motions extending equations obtained in the first chapter. Multiple previous studies considered this problem. Often distances were estimated based on dispersion measure (applied wrongly) and the electron density model of the Galaxy. Such estimates are not accurate.

In this research, we derive the maximum likelihood function for a number of models such as isotropic maxwellian distribution, a sum of two isotropic maxwellian distributions and the semi-isotropic model. We used only high-quality parallax and proper motion measurements obtained by means of the interferometric technique. As a result, we clearly see a presence of low-velocity subpopulation ($\sigma_1 = 77$ km/s) with fraction 0.42 of the total population. The high-velocity subpopulation has $\sigma_2 = 321$ km/s. The total velocity distribution is semi-isotropic: young pulsars in the northern galactic hemisphere have preferably velocities with the positive vertical component.

The velocity distribution of millisecond radio pulsars

The millisecond radio pulsars belong to old population so they should demonstrate velocity anisotropy. The maximum likelihood technique for an anisotropic velocity distribution with slower rotation around the galactic centre is developped. In the third chapter, the method was applied to a catalogue of the parallaxes and proper motions of the millisecond radio pulsars. These measurements were performed both by means of the timing and interferometric technique.

The velocity distribution of the millisecond radio pulsars is also bimodal with low-velocity component nearly isotropic $\sigma = 38$ km/s and fraction 0.66. This large fraction of the low-velocity subpopulation confirms that the natal kicks are bimodal because this fraction is in an excellent agreement with our expectations from the previous chapter about fraction of high to low-velocity components. The high-velocity component shows some indications of anisotropy and rotates slowly $\langle v_{\rm MSP} \rangle = 105$ km/s around the Galactic centre.

Magnetic field re-emergence

The pulsar activation depends strongly on the curvature of the magnetic field in the open line region. Despite their location above the death line the central compact objects are famous for their radio silence. A most probable explanation of such behaviour is that the curvature of open field lines is not enough to activate the pulsar mechanism. On the other hand, the central compact objects go through an episode of fall-back. No simulations of the high order multipoles harmonic re-emergence (responsible for small open field line curvature) were performed before.

In this chapter, we perform simulations of the magneto-thermal evolution of the neutron star with high order harmonics. We find that $l = 3, ..15$ bury deeply in the crust (much deeper than the dipole) during the fall-back episode. In means that for a period of time $\approx 10^4$ years the external magnetic field looks dipolar with high curvature radius of the open field lines (10^8 cm). These harmonics re-emerge after some time. We identified the exact physical mechanism behind this behaviour: generation of strong toroidal magnetic field and consequent interaction between toroidal and poloidal magnetic field. This behaviour suggests that the curvature of the open field line decreases at timescale few $\times 10^4$ years and the neutron star starts operating as a radio pulsar if the integrated fall-back mass is about $10^{-3} M_\odot$.

Ages of accreting magnetar and the crust impurity

Recently a few high mass accreting system were suggested to have magnetar range magnetic field. The typical age of these system is suspected to be more than a few Myr. The kinematic age of one of the best candidates 4U0114+65 is studied by means of the Bayesian method. The neutron star is found to have the kinematic age in range 2.4-5 Myr (95% confidence interval). In order to keep the strong magnetic field at this age the crust impurity parameter Q should be in range 1-5 which in contradiction with previous estimates based on normal magnetars.

Future prospects

The low-velocity component both in the millisecond radio pulsars and the young radio pulsars is most probably have the same origin. It is worth testing with a population synthesis the exact velocity distribution which binaries and isolated radio pulsars acquire as a result of the bimodal natal kick. The result of this binary population synthesis can be compared with the sky distribution of young radio pulsars, X-ray binaries and millisecond radio pulsars. A careful treatment of the observational bias is essential for such studies.

This population synthesis can also include a treatment of a fall-back classifying neutron stars as the central compact objects or radio pulsars depending on fall-back amount and age. Such a population synthesis will provide a much better description of the observed diversity of neutron stars.

Samenvatting

Dit proefschrift beschrijft een aantal studies van de eigenschappen van neutronensterren: de verdeling van zogenaamde natal kicks, het opnieuw verschijnen van magnetische velden en de eigenschappen van de korst van neutronensterren. Deze kenmerken verhelderen wat we weten over supernova explosies. In het bijzonder, het zou zo kunnen zijn dat twee verschillende types van supernova explosies nodig zijn om de bimodaliteit in de snelheidsverdeling te verklaren. Deze bimodaliteit wordt niet alleen waargenomen bij jonge radiopulsars maar ook bij gerecyclede pulsars en BeX sterren. De activering van het pulsar mechanisme in het geval van een terugval na de supernova explosie is beschreven in hoofdstuk 4.

Afstanden van parallax metingen

De afstanden naar pulsars zijn essentieel in studies van hun snelheid en helderheid. De pulsars staan ver weg en vaak is de kwaliteit van interferometrische metingen van parallaxen maar beperkt. De kennis van de structuur van ons sterrenstelsel helpt om zulke metingen beter te kunnen begrenzen. Helaas zijn er wiskundige fouten gemaakt in een voorgaande analyse van de afstanden afgeleid van parallax metingen.

In het eerste hoofdstuk wordt de correcte vergelijking afgeleid voor de Bayesiaanse waarschijnlijkheid van afstanden gebaseerd op parallaxen en wordt deze vergelijking toegepast met een a-priori bepaalde pulsar verdeling in de Melkweg. Wij hebben deze vergelijking getest aan de hand van Monte Carlo simulaties. Wij geven ook een vergelijking voor de a-posteriori waarschijnlijkheid van de helderheid van de pulsars wanneer de flux (radio of gammastraling) en parallax gemeten zijn. Gebruikmakend van deze vergelijking laten we zien dat de meest waarschijnlijke intrinsieke flux van gammastraling van J0218+4232 significant minder is dan het energieverlies door spin-down zoals verwacht in pulsar theorie.

Snelheidsverdeling van jonge radiopulsars

Het tweede hoofdstuk focust op de snelheidsverdeling van jonge radiopulsars afgeleid van gemeten parallaxen en eigenbewegingen, hierbij worden vergelijkingen verkregen in het eerste hoofdstuk

uitgebreid. Verschillende voorgaande studies hebben dit probleem behandeld. Vaak werden afstanden geschat aan de hand van spreidingsmetingen (verkeerd toegepast) en een dichtheidsmodel van elektronen in de Melkweg. Zulke schattingen zijn niet nauwkeurig.

In dit onderzoek leiden wij de maximale waarschijnlijkheidsfunctie af voor een aantal modellen, bijvoorbeeld voor een isotrope Maxwelliaanse verdeling, de som van twee isotrope Maxwelliaanse verdelingen en een semi-isotroop model. Wij hebben alleen parallax en eigenbeweging metingen van hoge kwaliteit gebruikt, verkregen door de interferometrische techniek. Als gevolg daarvan zien we duidelijk de aanwezigheid van een subpopulatie met een lage snelheid ($\sigma_1 = 77$ km/s) met een fractie van 0,42 van de totale populatie. De subpopulatie met een hoge snelheid heeft $\sigma_2 = 321$ km/s. De totale snelheidsverdeling is semi-isotroop: jonge pulsars in het noordelijke Galactische halfrond hebben bij voorkeur snelheden met een positieve verticale component.

De snelheidsverdeling van milliseconde radiopulsars

De milliseconde radiopulsars behoren tot oude populaties en daarom zouden ze een snelheidsanisotropie moeten vertonen. De maximale waarschijnlijkheidstechniek voor een anisotrope snelheidsverdeling met langzamere omwenteling rond het midden van de Melkweg is ontwikkeld. In het derde hoofdstuk is deze methode toegepast op een catalogus van parallaxen en eigenbewegingen van milliseconde radiopulsars. Deze metingen zijn uitgevoerd door middel van de timing en de interferometrische techniek.

De snelheidsverdeling van milliseconde radiopulsars is ook bimodaal, waarbij de lage snelheidscomponent bijna isotroop is, $\sigma = 38$ km/s en de fractie is 0,66. Deze grote fractie van de lage-snelheid subpopulatie bevestigt dat de natal kicks bimodaal zijn omdat deze fractie in uitstekende overkomst is met onze verwachtingen uit het vorige hoofdstuk voor de fractie van de hoge en lage snelheidscomponenten. De hoge snelheidscomponent geeft een indicatie van anisotropie en draait langzaam $v_{\rm MSP} = 105$ km/s rond het Galactisch centrum.

Herverschijning van het magnetisch veld

De pulsar activering hangt sterk af van de kromming van het magnetisch veld in het open-lijn regime. Ondanks hun locatie boven de doodslijn staan de centrale compacte objecten bekend om hun radiostilte. Een meest waarschijnlijke verklaring van dit gedrag is dat de kromming van open veldlijnen niet genoeg is om het pulsar mechanisme te activeren. Aan de andere kant gaan de centrale compacte objecten door een periode van terugval heen. Voor dit onderzoek waren er nog geen simulaties uitgevoerd van de harmonische terugkomst van hoge-orde multipolen.

In dit hoofdstuk voeren wij simulaties uit van de magnetisch-thermische evolutie van de neutronenster met hoge-orde harmonieën. Wij vinden dat $l = 3,..15$ diep in de korst graven (veel dieper dan de dipool) tijdens de terugval periode. Dit betekent dat voor een periode van $\approx 10^4$ jaar het externe magnetische veld er dipolair uit ziet met een grote buigingsstraal van de open veldlijnen (10^8 cm). Deze harmonieën komen na een bepaalde tijd weer terug. Wij identificeerden het exacte natuurkundige mechanisme achter dit gedrag: het ontwikkelen van een sterk toroïdaal magnetisch veld en daaropvolgende interacties tussen het toroïdale en poloïdale magnetisch veld.

Dit gedrag suggereert dat de buiging van de open veldlijnen afneemt op een tijdsschaal van een paar $\times 10^4$ jaar en dat de neutronenster zich begint te gedragen als een radiopulsar wanneer de totale terugval massa ongeveer $10^{-3} M_\odot$ is.

Eeuwen van aangroeiende magnetars en onzuiverheid van de korst

Recentelijk is voorgesteld dat een paar hoge-massa aangroeiende systemen magnetische velden hebben in het magnetar gebied. De typische leeftijd van deze systemen wordt verwacht meer dan een paar miljoen jaar te zijn. De kinematische leeftijd van één van de beste kandidaten, 4U0114+65, is bestudeerd door middel van de Bayesiaanse methode. De neutronenster blijkt de kinematische leeftijd in het interval van 2.4-5 Mjaar (95% betrouwbaarheidsinterval) te hebben. Om op deze leeftijd nog het sterke magnetische veld te houden moet de onzuiverheidsparameter van de korst Q in het interval 1-5 liggen, wat in tegenspraak is met voorgaande schattingen gebaseerd op normale magnetars.

Toekomstperspectieven

De lage snelheidscomponent in zowel de milliseconde pulsars als de jonge radiopulsars heeft waarschijnlijk dezelfde herkomst. Het is het waard om te onderzoeken, door middel van een populatiesynthese, wat de exacte snelheidsverdeling is die dubbelsterren en geïsoleerde radiopulsars verkrijgen als gevolg van de bimodale natal kick. De resultaten van deze populatiesynthese van dubbelsterren kan worden vergeleken met de verdeling aan de hemel van jonge radiopulsars, röntgenstraling dubbelsterren en milliseconde radiopulsars. Een zorgvuldige behandeling van de observationele bias is essentieel voor zulke studies.

Deze populatiesynthese kan ook een behandeling van de terugval bevatten waarbij de neutronensterren geklasseerd worden als de centrale compacte objecten of als radiopulsars, afhankelijk van de hoeveelheid terugval en leeftijd. Zo'n populatiesynthese zal zorgen voor een veel betere beschrijving van de waargenomen diversiteit van neutronensterren.

Заключение

В этой работе собраны несколько исследований о свойствах нейтронных звезд, в частности о распределении начальных толчков скорости и процессе всплытия магнитного поля, а также коры нейтронных звёзд. Все эти исследования позволяют пролить свет на механизм вспышки сверхновой. Бимодальность распределения скоростей радиопульсаров по всей видимости объясняется тем, что существует два типа сверхновых. Эта бимодальность наблюдается не только среди молодых радиопульсаров, но также среди миллисекундных пульсаров и BeX звезд. Активация пульсарного механизма после падения части вещества сверхновой на нейтронную звезду описана в части 4.

Расстояния основанные на измерениях параллакса

Знание расстояний до пульсаров очень важно для изучения их скоростей и светимостей. Достаточно часто пульсары расположены далеко от наблюдателя и поэтому качество параллаксов измеренных посредством интерферометрии ограничено. Использование знания о структуре Галактики позволяет улучшить качество таких измерений. К сожалению, в ряде предыдущих исследований расстояний основанных на измерениях параллакса была допущена математическая ошибка.

В первой главе мы выведем правильное уравнение для Байесовская вероятности расстояния основанного на параллаксах и применим его используя распределение радиопульсаров в галактике в качестве априорной вероятности. Полученное выражение было протестировано с использованием метода Монте Карло. Также мы вывели уравнение для апостериорной распределения светимости радиопульсара если измерен поток (в радио или гамма лучах) и параллакс. Используя это выражение мы показали, что самая вероятная гамма светимость пульсара J0218+4232 значительно меньше чем его кинетическая светимость как и должно быть в соотвествии с теорией излучения радиопульсаров.

Распределение скоростей молодых радиопульсаров

Во второй главе мы сосредотачиваемся на определении распределения скоростей молодых радиопульсаров используя параллаксы и собственные движения. Математические выражения найденные в первой главе составляют основу этого исследования. Распределение скоростей радиопульсаров неоднократно рассматривалось в литературе. В таких ранних исследованиях оценки расстояния как правило основывались на мере дисперсии и модели распределения свободных электронов в Галактике. К сожалению, такие оценки не надежны.

В нашем исследовании мы записываем функцию правдоподобия для нескольких моделей распределения скорости таких как: изотропное максвеловское распределение, сумма двух изотропных максвеловских распределений и семи-изотропное распределение. Мы использовали только измерения параллаксов и собственных движений самого высокого качества полученные с помощью радиоинтерферометрии со сверхдлинными базами. Как результат, мы ясно видим что низкоскоростная популяция ($\sigma = 77$ км/с) составляет 42% от полной популяции молодых радиопульсаров. Высокоскоростная популяция описывается максвелловским распределением с $\sigma = 321$ км/с. Полное распределение по скоростям семи-изотропное: у молодые радиопульсары в северной части галактики положительные вертикальные компоненты скорости.

Распределение скоростей миллисекундных радиопульсаров

Миллисекундные радиопульсары относятся к старому населению Галактики, поэтому они должны иметь анизотропное распределение скоростей. Я записал функцию правдоподобия для анизотропного распределения скоростей для обьектов с медленным вращением вокруг Галактического центра. В третьей главе я применил этот метод к каталогу параллаксов и собственных движений миллисекундных радиопульсаров. Эти измерения были преимущественно получены методом хронометрирования, но среди них есть результаты радиоинтерферометрии со сверхдлинными базами.

Распределение по скоростям у миллисекундных пульсаров также бимодально, низкоскоростная компонента описывается максвелловским распределением с $\sigma = 38$ км/с и составляет 66% от всей популяции. Столь большая часть низкоскоростных объектов подтверждает то, что начальное распределение по скоростям бимодально. 66% согласуется с нашими ожиданиями о количестве низкоскоротных объектов. Распределение по скоростях у высокоскоростных объектов указывает на анизотропию. Скорость их вращения вокруг центра Галактики $\langle v_{\rm MSP} \rangle = 105$ км/с.

Всплытие магнитного поля

Включение пульсарного механизма сильно зависит от кривизны магнитного поля в районе открытых силовых линий. Несмотря на то, что центральные компактные объекты расположены над линией смерти на $P - \dot{P}$, они не излучают в радиодиапазоне. Самое вероятное объяснение состоит в том, что кривизна открытых силовых линий недостаточна для запуска пульсарного механизма. Предполагается, что центральные компактные объекты проходят

через эпизод возвратной аккреции. Тем не менее, к настоящему моменту, не было выполнено ни одного моделирования всплытия магнитного поля содержащего мультиполи высокого порядка. Такие мультиполи позволяют уменьшить радиус открытых силовых линий.

В четвертой главе мы выполнили моделирование магнето-тепловой эволюции нейтронной звезды в присутствии магнитных мультиполей высокого порядка. Мы обнаружили, что $l = 3, \ldots 15$ погружаются глубже в кору (гораздо глубже, чем дипольная компонента) в течении возвратной аккреции. Это значит что на протяжении $\approx 10^4$ лет внешнее магнитное поле похоже на дипольное с большим радиусом кривизны силовых линий (10^8 см). Гармоники высоких порядков всплывают на поверхность через некоторое время. Мы обнаружили физический механизм ответственный за такое поведение: сначала генерируется сильное тороидальное поле и затем происходит взаимодействие между полоидальным и тороидальным полем. Подобное поведение говорит нам о том, что кривизна открытых силовых линий убывает на временах $\times 10^4$ лет и нейтронная звезда становится радиопульсаром, если полная масса возвратной аккреции $\approx 10^{-3} M_\odot$.

Возраста аккрецирующих магнетаров и примеси в коре

Недавно было предложено, что несколько нейтронных звезд в массивных рентгеновских двойных обладают магнетарными магнитными полями. Как правило возраста этих систем превыщают несколько миллионов лет. Мы исследовали кинематический возраст одного из лучших кандидатов 4U0114+65 с использованием Байесовой статистики. Оказалось, что нейтронная звезда родилась 2.4-5 миллионов лет назад (95% доверительный интервал). Чтобы сохранить сильное магнитное поле на таких временах, Q - безразмерный параметр описывающий содержание примесей, должен находится в пределах 1-5, что противоречит предыдущим оценкам основанным на распределении периодов у обычных магнетаров.

Перспективы исследования

Низкоскоростная компонента в распределений скоростей миллисекундных и молодых радиопульсаров скорее всего имеет одно и тоже происхождение. Поэтому сравнение распределения начальных толчков скорости для одиночных и двойных радиопульсаров, полученное посредством популяционного синтеза и результатов настоящего исследования позволит уточнить распределение скоростей радиопульсаров. Результаты популяцонного синтеза двойных могут быть так же сопоставлены с распределением молодых радиопульсаров, рентгеновских двойных и миллисекундных пульсаров на небе. В таком популяционном синтезе очень важно правильно учитывать естественные ограничения вызванные способами наблюдения.

Популяционный синтез может также включать рассмотрение возвратной аккреции и классифицировать нейтронную звезду как центральный компактный объект или радиопульсар в зависимости от аккрецированной массы и возраста. Такой популяционный синтез сделает возможным гораздо более полное описание наблюдаемого многообразия нейтронных звёзд.

Curriculum vitæ

I was born in a small mountainous town Zlatoust in the Ural on 28th March of 1990. I attended the general education school #18. During the school time, I got interested in natural sciences and was keen on studying astronomy. In addition to the general school education, I attended the children's art school #1 specializing in fine arts with a strong interest in the history of fine art. By the 6th year in the school, I got interested in natural sciences which provided unambiguous and general description of the world around with a possibility to test in opposed to fragmented and contradictory worlds descriptions provided by humanities in post-soviet era. The knowledge independent of authority is the main attractiveness of the natural sciences for me. I participated in many school astronomical olympiads at the level of my town, the Chelyabinsk region, and the whole Russia. Based on the results of consistent good participation in the Russian astronomical olympiads (3rd diploma in 2005 and the 2nd diploma in 2006) as well as the result of the winter selection in Saint Petersburg (2005) I was included in the national team. It resulted into travel to the international astronomical olympiad in Bombay (India) where I won the III Diploma. The last few years in the school I performed the meteor observations and submitted the results to the international meteor organization.

The successful participation in the Russian Olympiad gave me a right to enter any Russian university to study astronomy or physics. After some consideration, I have chosen the mathematical and mechanical faculty of the Saint Petersburg State University because of its outstanding program in mathematics and programming. Four years I attended the English language courses to develop an ability to speak and understand English. At the third year of my education, I started the first research project with prof. Alexander Kholtygin about magnetic fluxes of massive stars. At the fifth year, I spent two months at the internship in the Moscow State University working on magnetic field evolution in radio pulsars together with prof. Sergei Popov.

I was graduated from the Saint Petersburg University in 2012 with the specialist diploma in Astronomy with distinction. Since my first travel to India, I always dreamed of writing the Ph.D. thesis abroad. To achieve this dream, I applied to different Ph.D. programs until I got a position in Nijmegen, the Netherlands in June of 2013. During one year between my graduation and start of the contract in the Netherlands, I applied to the graduate program in the Saint Petersburg State University. I passed the exams in English and philosophy which are required for the Ph.D. in

Russia and wrote two articles in close collaboration with Sergei Popov. The subject of my Ph.D. was a logical continuation of all my previous works. I started the Ph.D. program in Radboud University Nijmegen in October 2013 under the supervision of Frank Verbunt.

My Ph.D. included an extensive use of statistics and numerical methods. I worked in collaboration with Eric Cator. During my Ph.D., I initiated a collaboration with Justin Elfritz from the University of Amsterdam. I presented my research results in the Netherlands, UK, Germany, Russia, Spain, and Poland.

During the 2016-2017 I was a chair of the Journal club. I participated actively in the organization of the NAC 2017 in Nijmegen. I start running again after a break in 2015 and run the half-marathon (Nijmegen and Tallinn) and 15 km running race in Nijmegen. I continue the work in astrophysics with a fellowship from the Technion Israel Institute of technology.

Acknowledgments

I want to thank all the people who made my way through the PhD program possible. In particular, I am very grateful to Frank Verbunt for his fruitful ideas and numerous expert advice as well as for his time, patience and efforts which he put into supervision.

Eric, I would like to thank you for leading us through this dark and dangerous forest of statistics. That forest is full of wrong paths which we avoided only because of your guidance.

Gijs, thank you very much for collaborations and encouragement.

Sergei, I am grateful for our long-term cooperation concerning different aspects of neutron stars properties and evolution.

Serena, I am really grateful for our collaboration on "the Galactic distribution of X-ray binaries and its implications for compact object formation and natal kicks" in which I learned a lot about the X-ray binaries and systemic velocities. I want to thank you a lot for all the inspiration, your modus vivendi and much more.

Justin, I thank you a lot for our fruitful collaboration on "Post-fall-back evolution of multipolar magnetic fields and radio pulsar activation". It was a wonderful excuse to be in UvA more often. I learned many things about the magnetic fields and finally got a chance to perform some up to date simulations of the crust confined field evolution.

Thomas B. and Christiaan, I enjoyed a lot our science discussions and side projects especially related to quantum mechanics.

Svea, for our friendship and scientific discussions as well as for the HST proposal.

Alexander M. thanks a lot for our exciting discussions about ULXs, accretion and so on during a time when I was in UvA.

Acknowledgments

Samaya, thank you for letting me be a part of the LOC for the NAC 2017, it was very important experience for me which let me test my limits.

Karolina, I am very grateful for our epistemological correspondence.

Pim, for our running on weekends.

Yulia, for our travel to Tallinn and much more.

Silvia, for our science discussion about the binary population synthesis

Emilio, for our interesting discussions about extraterrestrial life and radio observations.

Reka, danke wel voor onze Nederlandse gespreken.

Michelle, danke wel voor Nederlandse lessen.

Arjen, thank you very much for the help with the translation of the Summary section to Dutch.

Nina, I am very grateful for beauty, our France and Italian travels and music.

Thanks to Cameron, Sara, Payaswini, Michael, Irene, Sander, Rocco and Deanne for being awesome officemates.

Над ним не было ничего уже, кроме неба, — высокого неба, не ясного, но все-таки неизмеримо высокого, с тихо ползущими по нем серыми облаками. «Как тихо, спокойно и торжественно, совсем не так, как я бежал, — подумал князь Андрей, — не так, как мы бежали, кричали и дрались; совсем не так, как с озлобленными и испуганными лицами тащили друг у друга банник француз и артиллерист, — совсем не так ползут облака по этому высокому бесконечному небу. Как же я не видал прежде этого высокого неба? И как я счастлив, что узнал его наконец. Да! все пустое, все обман, кроме этого бесконечного неба.

Л.Н. Толстой – "Война и мир".